Fermi National Accelerator Laboratory

FERMILAB Pub-94/244-E
CDF

Measurement of W + γ and Z + γ Cross Sections in the Electron and Muon Channels in $\sqrt{s}$ = 1.8 TeV $\bar{p}p$ Collisions

The CDF Collaboration

Fermi National Accelerator Laboratory
P.O. Box 500, Batavia, Illinois 60510

August 1994

Submitted to *Physical Review D.*

Operated by Universities Research Association Inc. under Contract No. DE-AC02-76CHO3000 with the United States Department of Energy

Disclaimer

CDF/ANAL/ELECTROWEAK/PUBLIC/2133
FERMILAB-PUB-94/244-E

Measurement of $W + \gamma$ and $Z + \gamma$ Cross Sections in the Electron and Muon Channels in $\sqrt{s} = 1.8$ TeV $\bar{\text{p}}$-p Collisions

The CDF Collaboration

July 22, 1994

Submitted to Physical Review D
August 1, 1994

F. Abe,[12] M. Albrow,[6] D. Amidei,[15] C. Anway-Wiese,[3] G. Apollinari,[23] M. Atac,[6] P. Auchincloss,[22] P. Azzi,[17] N. Bacchetta,[16] A. R. Baden,[8] W. Badgett,[15] M. W. Bailey,[21] A. Bamberger,[6,a] P. de Barbaro,[22] A. Barbaro-Galtieri,[13] V. E. Barnes,[21] B. A. Barnett,[11] G. Ba er,[14] T. Baumann,[8] F. Bedeschi,[20] S. Behrends,[2] S. Belforte,[20] G. Bellettini,[20] J. Bellinger,[28] D. Benjamin,[27] J. Benlloch,[14] J. Bensinger,[2] A. Beretvas,[6] J. P. Berge,[6] S. Bertolucci,[7] K. Biery,[10] S. Bhadra,[9] M. Binkley,[6] D. Bisello,[17] R. Blair,[1] C. Blocker,[2] A. Bodek,[22] V. Bolognesi,[20] A. W. Booth,[6] C. Boswell,[11] G. Brandenburg,[8] D. Brown,[8] E. Buckley-Geer,[6] H. S. Budd,[22] G. Busetto,[17] A. Byon-Wagner,[6] K. L. Byrum,[1] C. Campagnari,[6] M. Campbell,[15] A. Caner,[6] R. Carey,[8] W. Carithers,[13] D. Carlsmith,[28] J. T. Carroll,[6] R. Cashmore,[6,a] A. Castro,[17] Y. Cen,[18] F. Cervelli,[20] K. Chadwick,[6] J. Chapman,[15] G. Chiarelli,[7] W. Chinowsky,[13] S. Cihangir,[6] A. G. Clark,[6] M. Cobal,[20] D. Connor,[18] M. Contreras,[4] J. Cooper,[6] M. Cordelli,[7] D. Crane,[6] J. D. Cunningham,[2] C. Day,[6] F. DeJongh,[6] S. Dell'Agnello,[20] M. Dell'Orso,[20] L. Demortier,[23] B. Denby,[6] P. F. Derwent,[15] T. Devlin,[24] D. DiBitonto,[25] M. Dickson,[22] R. B. Drucker,[13] A. Dunn,[15] K. Einsweiler,[13] J. E. Elias,[6] R. Ely,[13] S. Eno,[4] D. Errede,[9] S. Errede,[9] A. Etchegoyen,[6,a] B. Farhat,[14] M. Frautschi,[16] G. J. Feldman,[8] B. Flaugher,[6] G. W. Foster,[6] M. Franklin,[8] J. Freeman,[6] H. Frisch,[4] T. Fuess,[6] Y. Fukui,[12] A. F. Garfinkel,[21] A. Gauthier,[9] S. Geer,[6] D. W. Gerdes,[15] P. Giannetti,[20] N. Giokaris,[23] P. Giromini,[7] L. Gladney,[18] M. Gold,[16] J. Gonzalez,[18] K. Goulianos,[23] H. Grassmann,[17] G. M. Grieco,[20] R. Grindley,[10] C. Grosso-Pilcher,[4] C. Haber,[13] S. R. Hahn,[6] R. Handler,[28] K. Hara,[26] B. Harral,[18] R. M. Harris,[6] S. A. Hauger,[5] J. Hauser,[3] C. Hawk,[24] T. Hessing,[25] R. Hollebeek,[18] L. Holloway,[9] A. Hölscher,[10] S. Hong,[15] G. Houk,[18] P. Hu,[19] B. Hubbard,[13] B. T. Huffman,[19] R. Hughes,[22] P. Hurst,[8] J. Huth,[6] J. Hylen,[6] M. Incagli,[20] T. Ino,[26] H. Iso,[26] H. Jensen,[6] C. P. Jessop,[8] R. P. Johnson,[6] U. Joshi,[6] T. Kamon,[25] S. Kanda,[26] D. A. Kardelis,[9] I. Karliner,[9] E. Kearns,[8] L. Keeble,[25] R. Kephart,[6] P. Kesten,[2] R. M. Keup,[9] H. Keutelian,[6] D. Kim,[6] S. B. Kim,[15] S. H. Kim,[26] Y. K. Kim,[13] L. Kirsch,[2] K. Kondo,[26] J. Konigsberg,[8] K. Kordas,[10] E. Kovacs,[6] M. Krasberg,[15] S. E. Kuhlmann,[1] E. Kuns,[24] A. T. Laasanen,[21] S. Lammel,[3] J. I. Lamoureux,[28] S. Leone,[20] J. D. Lewis,[6] W. Li,[1] P. Limon,[6] M. Lindgren,[3] T. M. Liss,[9] N. Lockyer,[18] M. Loreti,[17] E. H. Low,[18] D. Lucchesi,[20] C. B. Luchini,[9] P. Lukens,[6] P. Maas,[28] K. Maeshima,[6] M. Mangano,[20] J. P. Marriner,[6] M. Mariotti,[20] R. Markeloff,[28] L. A. Markosky,[28] J. A. J. Matthews,[16] R. Mattingly,[2] P. McIntyre,[25] A. Menzione,[20] E. Meschi,[20] T. Meyer,[25] S. Mikamo,[12] M. Miller,[4] T. Mimashi,[26] S. Miscetti,[7] M. Mishina,[12] S. Miyashita,[26] Y. Morita,[26] S. Moulding,[23] J. Mueller,[24] A. Mukherjee,[6] T. Muller,[3] L. F. Nakae,[2] I. Nakano,[26] C. Nelson,[6] D. Neuberger,[3] C. Newman-Holmes,[6] J. S. T. Ng,[8] M. Ninomiya,[26] L. Nodulman,[1] S. Ogawa,[26] R. Paoletti,[20] V. Papadimitriou,[6] A. Para,[6] E. Pare,[8] S. Park,[6] J. Patrick,[6] G. Pauletta,[20] L. Pescara,[17] T. J. Phillips,[5] A. G. Piacentino,[20] R. Plunkett,[6] L. Pondrom,[28] J. Proudfoot,[1] F. Ptohos,[8] G. Punzi,[20] D. Quarrie,[6] K. Ragan,[10] G. Redlinger,[4] J. Rhoades,[28] M. Roach,[27] F. Rimondi,[6,a] L. Ristori,[20] W. J. Robertson,[5] T. Rodrigo,[6] T. Rohaly,[18] A. Roodman,[4] W. K. Sakumoto,[22] A. Sansoni,[7] R. D. Sard,[9] A. Savoy-Navarro,[6] V. Scarpine,[9] P. Schlabach,[8], E. E. Schmidt,[6] O. Schneider,[13] M. H. Schub,[21] R. Schwitters,[8] G. Sciacca,[20] A. Scribano,[20] S. Segler,[6] S. Seidel,[16] Y. Seiya,[26] G. Sganos,[10] M. Shapiro,[13] N. M. Shaw,[21] M. Sheaff,[28] M. Shochet,[4] J. Siegrist,[13] A. Sill,[22] P. Sinervo,[10] J. Skarha,[11] K. Sliwa,[27] D. A. Smith,[20] F. D. Snider,[11] L. Song,[6] T. Song,[15] M. Spahn,[13] P. Sphicas,[14] A. Spies,[11] R. St. Denis,[8] L. Stanco,[17] A. Stefanini,[20] G. Sullivan,[4] K. Sumorok,[14] R. L. Swartz, Jr.,[9] M. Takano,[26] K. Takikawa,[26] S. Tarem,[2] F. Tartarelli,[20] S. Tether,[14] D. Theriot,[6] P. Tipton,[22] S. Tkaczyk,[6] A. Tollestrup,[6] J. Tonnison,[21] W. Trischuk,[8] Y. Tsay,[4] J. Tseng,[11] N. Turini,[20] F. Ukegawa,[26] D. Underwood,[1] S. Vejcik, III,[15] R. Vidal,[6] M. Vondracek,[9] R. G. Wagner,[1] R. L. Wagner,[6] N. Wainer,[6] R. C. Walker,[22] J. Walsh,[18] A. Warburton,[10] G. Watts,[22] T. Watts,[24] R. Webb,[25] C. Wendt,[28] H. Wenzel,[20] W. C. Wester, III,[13] T. Westhusing,[9] S. N. White,[23] A. B. Wicklund,[1] E. Wicklund,[6] H. H. Williams,[18] B. L. Winer,[22] J. Wolinski,[25] D. Y. Wu,[15] X. Wu,[20] J. Wyss,[17] A. Yagil,[6] K. Yasuoka,[26] Y. Ye,[10] G. P. Yeh,[6] J. Yoh,[6] M. Yokoyama,[26] J. C. Yun,[6] A. Zanetti,[20] F. Zetti,[20] S. Zhang,[15] W. Zhang,[18] S. Zucchelli,[6,a]

[1] *Argonne National Laboratory, Argonne, Illinois 60439*
[2] *Brandeis University, Waltham, Massachusetts 02254*
[3] *University of California at Los Angeles, Los Angeles, California 90024*
[4] *University of Chicago, Chicago, Illinois 60637*
[5] *Duke University, Durham, North Carolina 27706*
[6] *Fermi National Accelerator Laboratory, Batavia, Illinois 60510*
[7] *Laboratori Nazionali di Frascati, Istituto Nazionale di Fisica Nucleare, Frascati, Italy*
[8] *Harvard University, Cambridge, Massachusetts 02138*
[9] *University of Illinois, Urbana, Illinois 61801*
[10] *Institute of Particle Physics, McGill University, Montreal, and University of Toronto, Toronto, Canada*
[11] *The Johns Hopkins University, Baltimore, Maryland 21218*
[12] *National Laboratory for High Energy Physics (KEK), Japan*
[13] *Lawrence Berkeley Laboratory, Berkeley, California 94720*
[14] *Massachusetts Institute of Technology, Cambridge, Massachusetts 02139*
[15] *University of Michigan, Ann Arbor, Michigan 48109*
[16] *University of New Mexico, Albuquerque, New Mexico 87131*
[17] *Universita di Padova, Instituto Nazionale di Fisica Nucleare, Sezione di Padova, I-35131 Padova, Italy*
[18] *University of Pennsylvania, Philadelphia, Pennsylvania 19104*
[19] *University of Pittsburgh, Pittsburgh, Pennsylvania 15260*
[20] *Istituto Nazionale di Fisica Nucleare, University and Scuola Normale Superiore of Pisa, I-56100 Pisa, Italy*
[21] *Purdue University, West Lafayette, Indiana 47907*
[22] *University of Rochester, Rochester, New York 15627*
[23] *Rockefeller University, New York, New York 10021*
[24] *Rutgers University, Piscataway, New Jersey 08854*
[25] *Texas A&M University, College Station, Texas 77843*
[26] *University of Tsukuba, Tsukuba, Ibaraki 305, Japan*
[27] *Tufts University, Medford, Massachusetts 02155*
[28] *University of Wisconsin, Madison, Wisconsin 53706*
[a] *Visitor*

Abstract

The production cross section times decay branching ratio for $W+\gamma$ and $Z+\gamma$ have been measured in $\sqrt{s} = 1.8$ TeV $\bar{\text{p}}$-p collisions. Both inclusive electron and muon W and Z decay data samples obtained from the CDF 1988-89 Tevatron collider run were used. For photons in the central pseudorapidity region of the CDF detector ($|\eta_\gamma| < 1.1$) with transverse energies $E_T^\gamma > 5.0$ GeV and lepton-photon angular separation $\Delta R_{\ell\gamma} > 0.7$, we observe 8 (5) electron (muon) $W\gamma$ candidates and 2 (2) electron (muon) $Z\gamma$ candidates. The extracted numbers $\sigma \cdot B(W\gamma)$ and $\sigma \cdot B(Z\gamma)$ for the electron, muon and $e+\mu$ combined samples are in good agreement with Standard Model predictions. The cross section ratios $W\gamma/W$, $Z\gamma/Z$ and $W\gamma/Z\gamma$, combined with previous CDF measurements of the W/Z cross section ratio provide new tests of the Standard Model. The absence of an excess of events with photons accompanying the production of W and Z bosons is used to extract direct limits on $WW\gamma$, $ZZ\gamma$ and $Z\gamma\gamma$ anomalous couplings. The implications of tree-level $S-$matrix unitarity on our experimental limits and sensitivity to W (Z) form factor scales Λ_W (Λ_Z) are discussed. The limits on $WW\gamma$ anomalous couplings place bounds on the W boson higher-order electromagnetic moments and mean-squared charge radius. The limits on $ZZ\gamma$ anomalous couplings place bounds on the $ZZ\gamma$ transition moments of the Z boson.

PACS numbers: 14.80.Er, 12.10.Dm, 12.50.Fk, 13.38+c

1 INTRODUCTION

The Standard Model (SM) of electroweak interactions unifies the electromagnetic and weak interactions into a single interaction described by the gauge group $SU(2)_L \otimes U(1)_Y$ [1]. The $W^{\pm}$ vector bosons mediate the charged weak currents [2]; the Z^0 and the γ vector bosons mediate the neutral currents [1]. The measurement of $W^{\pm}$, Z^0 and Drell-Yan production cross sections and W and Z leptonic decay properties in $\sqrt{s} = 1.8$ TeV $\bar{\text{p}}$-p collisions test the strength and the nature of these gauge boson couplings to fermions (the quarks and leptons) in the region of the W and Z boson mass scales.

In the context of the SM, the W, Z and γ are viewed as fundamental gauge particles. The experimental measurement of $W + \gamma$ and $Z + \gamma$ di-boson production cross sections and final-state decay kinematics provide tests of the SM predictions of the strength and nature of tri-linear gauge boson couplings between these particles and also yields information on static (transition) electromagnetic multipole moments of the W (Z) bosons, respectively [3, 4]. Large anomalous $WW\gamma$, $ZZ\gamma$ and/or $Z\gamma\gamma$ couplings ($>> \alpha = e^2/4\pi$) may be realized in nature only if the W and Z are composite and have an internal structure. In such a scenario, the W and Z would then be viewed as bound states of as-yet unknown particles, mediating the weak interactions in a role similar to that of rho mesons as mediators of the nuclear forces at low energy. Composite models of the W and Z bosons with large values of anomalous couplings predict cross sections for $W + \gamma$ and $Z + \gamma$ production well above those expected in the Standard Model [4, 5].

The inclusive electron and muon W and Z data samples obtained from the CDF 1988-89 collider run are used as a starting point for this analysis, since the $W\gamma$ and $Z\gamma$ events of interest are a subset of inclusive W and Z boson production. The inclusive W and Z data samples have been previously used for measurements of the inclusive W and Z cross sections in the electron and muon channels [6] and the W/Z cross section ratios [7]. In this analysis, we use the same W and Z event-selection criteria for defining the W and Z bosons in the $W\gamma$ and $Z\gamma$ event sub-samples, but *additionally* require the presence of an isolated, hard central photon accompanying the W or Z boson in each event [8].

One of the hallmarks of the Standard Model is the universal coupling of gauge bosons to fermions [1], lepton universality in the electroweak interactions. This is now well-tested at the W and Z mass scales [9]. It should also be obeyed in the leptonic decay channels for the $W\gamma$ and $Z\gamma$ processes. A comparison of $\sigma \cdot B(W + \gamma)$ and $\sigma \cdot B(Z + \gamma)$ in the electron and muon decay channels provides a cross-check. A comparison of the results for $W\gamma$ with those for $Z\gamma$ provides a consistency check in the search for possible anomalous couplings.

The small integrated luminosity presently available for studying $W\gamma$ and $Z\gamma$ processes implies limited statistical precision. Combining the individual electron and muon $W\gamma$ and $Z\gamma$ cross section results provides enhanced statistical accuracy. The detailed analysis presented here provides the foundation for more precise future measurements with larger integrated luminosity.

The organization of this paper is as follows. The theory of $W\gamma$ and $Z\gamma$ production in the context of the Standard Model, anomalous couplings and associated phenomenological implications is discussed in Section 2. The CDF detector and data collection are described in Section 3. The selection of the electron and muon $W\gamma$ and $Z\gamma$ data samples is discussed in Section 4. The details of the determination of $\sigma \cdot B(W+\gamma)$ and $\sigma \cdot B(Z+\gamma)$ in the electron and muon channels are described in Section 5. The results on three new cross section ratios, $\mathcal{R}(W\gamma/W)_\ell$, $\mathcal{R}(Z\gamma/Z)_\ell$, $\mathcal{R}(W\gamma/Z\gamma)_\ell$ and the inclusive W/Z cross section ratio, $\mathcal{R}(W/Z)_\ell$ are presented in Section 6. Finally, in Section

7, direct limits on $WW\gamma$, $ZZ\gamma$ and $Z\gamma\gamma$ anomalous couplings are presented. For $W\gamma$, the limits on $WW\gamma$ anomalous couplings are related to bounds on the higher-order electromagnetic moments and mean squared charge radius of the W boson. For $Z\gamma$, the limits on $ZZ\gamma$ anomalous couplings are related to bounds on the transition moments of the Z boson. The implications of tree-level $S-$matrix unitarity on our experimental limits and sensitivity to W (Z) form factor (compositeness) scales, Λ_W (Λ_Z) respectively are also discussed. All experimental results are summarized in Section 8.

2 THEORY OF $W\gamma$ AND $Z\gamma$ PRODUCTION

2.1 $W\gamma$ Production

The tree-level Feynman diagrams for $W\gamma$ production and decay are shown in Figs. 1a - 1d. The process of greatest interest here is the $s-$channel tri-linear gauge coupling diagram, Fig. 1c. $W\gamma$ events with different kinematics are produced in processes represented by Figs. 1a, 1b and 1d. The Feynman diagrams shown in Figs. 1a and 1b for the $u-$ and $t-$channel processes are associated with initial-state radiation off of the incoming quark lines. The process shown in Fig. 1d is known as radiative W decay due to final state/inner bremsstrahlung. The amplitudes for each of these processes must be summed coherently in order to produce a matrix element which preserves electromagnetic gauge invariance [10].

For $WW\gamma$ anomalous couplings, the most general effective Lagrangian compatible with Lorentz invariance and electromagnetic gauge invariance for the tree-level processes shown in Figs. 1a - 1d is given by [10, 11]:

$$\begin{aligned}\mathcal{L}_{WW\gamma} &= -ie\Big[W^\dagger_{\mu\nu}W^\mu A^\nu - W^\dagger_\mu A_\nu W^{\mu\nu} \\ &\quad +\kappa_f W^\dagger_\mu W_\nu F^{\mu\nu} + \frac{\lambda_f}{M_W^2}W^\dagger_{\lambda\mu}W^\mu_\nu F^{\nu\lambda} \\ &\quad +\tilde{\kappa}_f W^\dagger_\mu W_\nu F'^{\mu\nu} + \frac{\tilde{\lambda}_f}{M_W^2}W^\dagger_{\lambda\mu}W^\mu_\nu F'^{\nu\lambda}\Big] \qquad (1)\end{aligned}$$

where e is the charge of the proton, A^μ and W^μ are the photon and W^- fields, respectively and

$$W_{\mu\nu} = \partial_\mu W_\nu - \partial_\nu W_\mu \qquad (2)$$

$$F_{\mu\nu} = \partial_\mu A_\nu - \partial_\nu A_\mu \qquad (3)$$

$$F'_{\mu\nu} = \frac{1}{2}\epsilon_{\mu\nu\rho\sigma}F^{\rho\sigma} \qquad (4)$$

and M_W is the W mass. The photon is taken to be on-shell and both the virtual and on-shell W couple to essentially massless fermions allowing $\partial_\mu W^\mu = 0$.

The nature of the $WW\gamma$ vertex for $q\,\bar{q}' \to W^{\pm}\gamma$ can also be equivalently described in terms of the $WW\gamma$ vertex function, which is given by [12]

$$\begin{aligned}\Gamma^{\alpha\beta\mu}(q_1,q_2,P) \;=\; & \mp\frac{1}{2}\Big[(2+\Delta\kappa_f)(q_1-q_2)^{\mu}g^{\alpha\beta} \\ & + \frac{\lambda_f}{M_W^2}\,(q_1-q_2)^{\mu}\,(P^2 g^{\alpha\beta} - 2P^{\alpha}P^{\beta}) \\ & - 4\,P^{\beta}g^{\mu\alpha} \;+\; 2\,(2+\Delta\kappa_f+\lambda_f)\,P^{\alpha}g^{\mu\beta} \\ & + 2\,(\tilde{\kappa}_f+\tilde{\lambda}_f)\,\epsilon^{\mu\alpha\beta\rho}q_{2\rho} \\ & + \frac{\tilde{\lambda}_f}{M_W^2}\,(q_1-q_2)^{\mu}\epsilon^{\alpha\beta\rho\sigma}P_{\rho}\,(q_1-q_2)_{\sigma}\Big] \end{aligned} \tag{5}$$

Here P (q_1) are the four momenta of the incoming (outgoing) W boson (Lorentz indices μ and α respectively), and q_2 is the four momentum of the final state on-shell photon (Lorentz index β). The tree-level Standard Model predictions for the values of the momentum-dependent form factors are $\Delta\kappa_f = \kappa_f - 1 = \lambda_f = \tilde{\kappa}_f = \tilde{\lambda}_f = 0$. The form factors $a_f = \Delta\kappa_f$, λ_f, $\tilde{\kappa}_f$, and $\tilde{\lambda}_f$ are assumed to be of the generalized dipole form [10]:

$$a_f(P^2=\hat{s},\; q_1^2 = M_W^2,\; q_2^2 = 0) \;=\; \frac{a_0}{(1+\hat{s}/\Lambda_W^2)^n} \tag{6}$$

where the dimensionless anomalous couplings $a_0 = \Delta\kappa = \kappa - 1$, λ, $\tilde{\kappa}$, or $\tilde{\lambda}$, with tree-level Standard Model values of $\Delta\kappa = \lambda = \tilde{\kappa} = \tilde{\lambda} = 0$.

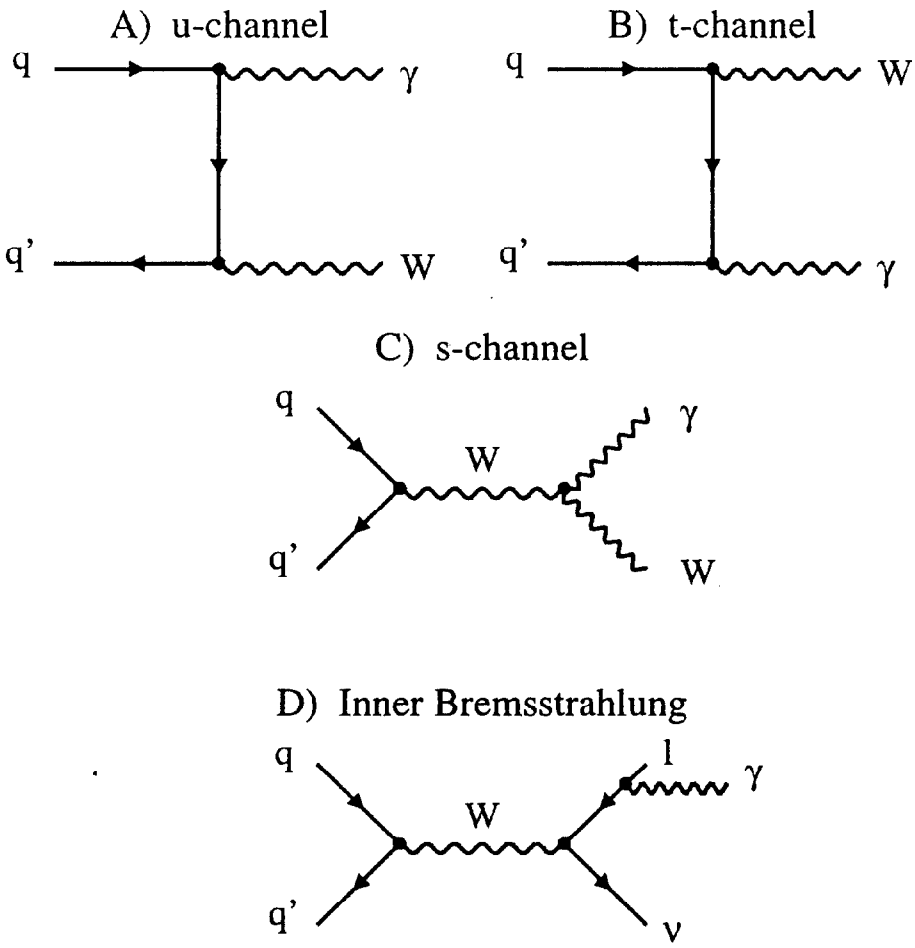

Figure 1: Tree-level $W+\gamma$ Feynman diagrams. (A) $u-$channel $W+\gamma$ initial-state bremsstrahlung diagram. (B) $t-$channel $W+\gamma$ initial-state bremsstrahlung diagram. (C) $s-$channel $W+\gamma$ diagram. (D) final-state inner bremsstrahlung diagram.

The anomalous contributions to the $W\gamma$ helicity amplitudes grow like $\sqrt{\hat{s}}/M_W$ for $\Delta\kappa$, $\tilde{\kappa}$ and $(\sqrt{\hat{s}}/M_W)^2$ for λ, $\tilde{\lambda}$. The form factor scale Λ_W represents the scale at which new physics becomes important in the weak boson sector, due to a composite structure of the W boson. The choice of the exponent $n = 2$ guarantees that unitarity is preserved. If the exponent is sufficiently above the minimum value of 1/2 (1) for $\Delta\kappa_f$, $\tilde{\kappa}_f$ (λ_f, $\tilde{\lambda}_f$) then one ensures that $W\gamma$ production is suppressed at energies $\sqrt{\hat{s}} >> \Lambda_W >> M_W$, where multiple weak boson or resonance phenomena are expected to dominate [11]. The behavior of the form factors (equation 6) is such that they stay essentially constant for $\hat{s} << \Lambda_W^2$ and start to decrease only when the scale Λ_W is reached (or surpassed), in analogy to the behavior associated with the well-known nucleon form factors.

In the static limit (photon energy $\rightarrow$ 0), the anomalous couplings, which are relativistic quantities, are related to the higher-order classical electromagnetic moments of the W boson – the magnetic dipole moment μ_W, electric quadrupole moment Q_W^e, electric dipole moment d_W, magnetic quadrupole moment Q_W^m and the mean-squared charge radius, $<R_W^2>$ (with $\hbar = c = 1$) via:

$$\mu_W = \frac{e}{2M_W}(2 + \Delta\kappa + \lambda) \tag{7}$$

$$Q_W^e = -\frac{e}{M_W^2}(1 + \Delta\kappa - \lambda) \tag{8}$$

$$d_W = \frac{e}{2M_W}(\tilde{\kappa} + \tilde{\lambda}) \tag{9}$$

$$Q_W^m = -\frac{e}{M_W^2}(\tilde{\kappa} - \tilde{\lambda}) \tag{10}$$

$$<R_W^2> = \frac{1}{M_W^2}(1 + \Delta\kappa + \lambda) \tag{11}$$

The sign associated with each of these quantities indicates their orientation relative to the spin direction of the W^+ boson. Note that for an arbitrary spin-S particle, $2S + 1$ $\mathcal{CP}-$conserving electromagnetic moments are allowed [13]. Thus, the electrically charged $W^{\pm}$ vector boson is expected to have *both* a magnetic dipole moment *and* an electric quadrupole moment in the Standard Model [14]. The W electric dipole and magnetic quadrupole moments (the terms in the effective Lagrangian involving the $\tilde{\kappa}$ and $\tilde{\lambda}$ parameters) are $\mathcal{P}-$odd and violate $\mathcal{CP}$ (i.e. violate $\mathcal{T}$). All four anomalous couplings are $\mathcal{C}-$even. Note also that within the context of the Standard Model, only the $\mathcal{CP}-$conserving parameters $\Delta\kappa$ and λ are expected to receive small, non-zero contributions at the one-loop level, of order α [10, 11].

Although all Feynman diagrams must be summed coherently, there are certain kinematic regions in which a subset of these diagrams provides most of the "interesting" signal. For the initial-state radiation processes, the radiation is sharply peaked in angle along the incident quark/anti-quark directions. The vast majority of photons from final-state radiative W decay are co-linear with the decay lepton. Both initial and final state radiation distributions are also sharply peaked at low photon energy, as are the contributions from the $WW\gamma$ vertex graphs. However, in contrast to radiative W decay, the photons from $W + \gamma$ production tend to be emitted at large angles with respect to the W decay lepton and the invariant mass of the $W + \gamma$ system also tends to be greater than the W boson mass. Additional details are described in Appendix A.

2.2 $Z\gamma$ Production

The tree-level Feynman diagrams for $Z\gamma$ production and decay are shown in Figs. 2a - 2d. Since the Z^0 boson, like the photon, is a Majorana particle (i.e. is its own anti-particle) it cannot have any *static* electromagnetic multipole moments. Hence, the SM of electroweak interactions predicts no $ZZ\gamma$ (and also no $Z\gamma\gamma$) tri-linear gauge couplings at the tree-level. The Feynman diagrams for SM $Z\gamma$ production are shown in Figs. 2a - 2c, corresponding to initial state and final state radiation (inner bremsstrahlung). The non-SM Feynman diagram for $ZZ\gamma$ and $Z\gamma\gamma$ anomalous couplings is shown in Fig. 2d. In addition, because of Bose symmetry and energy conservation, at least one of the Z bosons (photons) must be off-shell for non-zero $ZZ\gamma$ ($Z\gamma\gamma$) anomalous couplings, respectively. The SM diagrams for initial and final-state radiation for $Z\gamma$ produce photons sharply peaked in angles about the beam and decay lepton directions, respectively.

Electromagnetic gauge invariance and Lorentz invariance allow four different anomalous couplings. The most general anomalous $Z\gamma Z$ vertex function is given by [15]

$$\begin{aligned}\Gamma^{\alpha\beta\mu}_{Z\gamma Z}(q_1,q_2,P) &= \left(\frac{P^2-q_1^2}{M_Z^2}\right)\left[h_1^Z\left(q_2^\mu g^{\alpha\beta}-q_2^\alpha g^{\mu\beta}\right)\right.\\ &+\frac{h_2^Z}{M_Z^2}P^\alpha\left(P\cdot q_2 g^{\mu\beta}-q_2^\mu P^\beta\right)\\ &\left.+h_3^Z\epsilon^{\mu\alpha\beta\rho}\,q_{2\rho}+\frac{h_4^Z}{M_Z^2}P^\alpha\epsilon^{\mu\beta\rho\sigma}P_\rho q_{2\sigma}\right] \qquad (12)\end{aligned}$$

where M_Z is the Z boson mass, P and q_1 are the incoming and outgoing Z boson four-momenta (Lorentz indices μ and α respectively), and q_2 is the four-momentum of the outgoing (on-shell) photon (Lorentz index β). The most general anomalous $Z\gamma\gamma$ vertex function can be obtained from the $Z\gamma Z$ vertex function by replacing

$$\left(\frac{P^2-q_1^2}{M_Z^2}\right)\;\rightarrow\;\left(\frac{P^2}{M_Z^2}\right)\quad\text{and}\quad h_i^Z\;\rightarrow\;h_i^\gamma,\;\;i=1-4. \qquad (13)$$

The overall $ZZ\gamma$ and $Z\gamma\gamma$ coupling strengths $g_{ZZ\gamma}$ and $g_{Z\gamma\gamma}$ are chosen to be e, where e is the proton charge. The factor of $P^2-q_1^2$ in the $Z\gamma Z$ vertex function is a consequence of Bose symmetry, whereas the factor of P^2 in the $Z\gamma\gamma$ vertex function is a consequence of electromagnetic gauge invariance; note that the $Z\gamma\gamma$ vertex function vanishes identically if both photons are on-shell [16].

The form factors h_i^V $(V=Z,\gamma,\;\;i=1-4)$ are dimensionless functions of q_1^2, q_2^2 and P^2. As in the case for the form factors associated with the $WW\gamma$ vertex function, the values of h_i^V at low energies are constrained by S-matrix unitarity [17]. The $Z+\gamma$ form factors h_i^V are assumed to be of the generalized dipole form [17]:

$$h_i^V(P^2=\hat{s},\;q_1^2=M_Z^2,\;q_2^2=0)\;=\;\frac{h_{i0}^V}{(1+\hat{s}/\Lambda_Z^2)^n} \qquad (14)$$

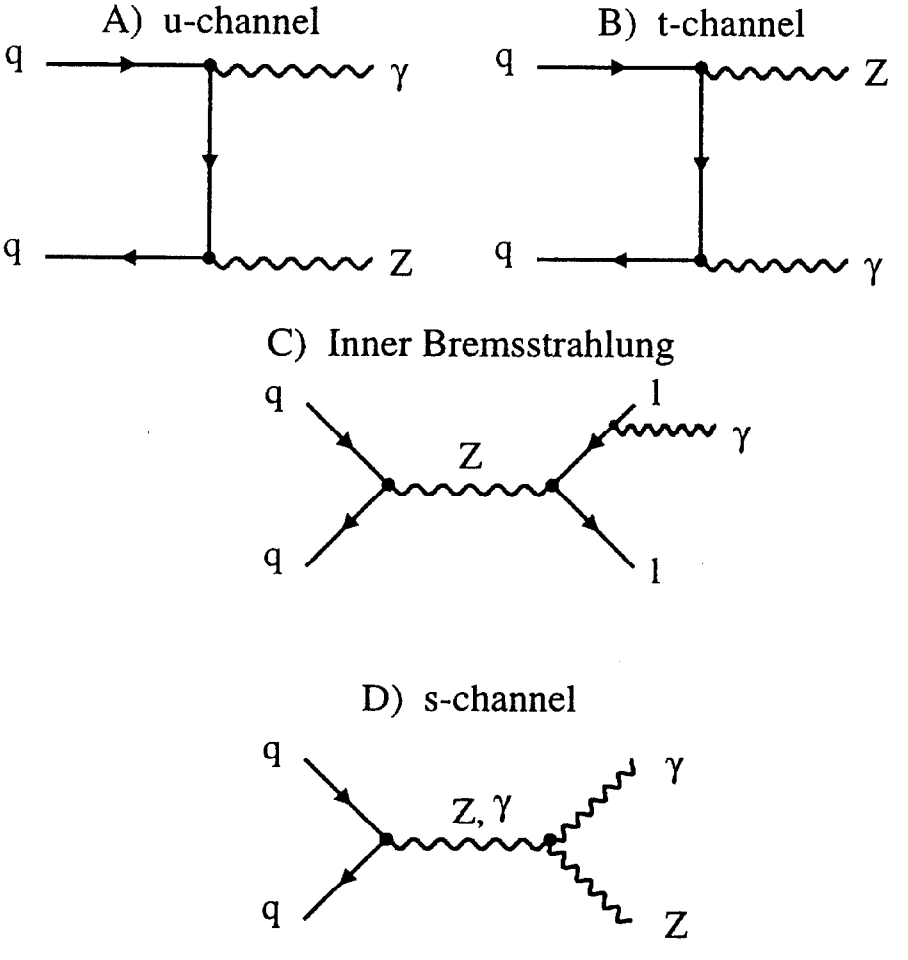

Figure 2: Tree-level $Z + \gamma$ Feynman diagrams. (A) $u-$channel $Z + \gamma$ initial-state bremsstrahlung diagram. (B) $t-$channel $Z + \gamma$ initial-state bremsstrahlung diagram. (C) final-state inner bremsstrahlung diagram. (D) non-SM $s-$channel $Z + \gamma$ diagram.

The anomalous contributions to the $Z\gamma$ helicity amplitudes grow like $(\sqrt{\hat{s}}/M_Z)^3$ for $h^V_{1,3}$ and $(\sqrt{\hat{s}}/M_Z)^5$ for $h^V_{2,4}$. We shall assume that $n = 3$ for $h^V_{1,3}$ and $n = 4$ for $h^V_{2,4}$. These choices guarantee that unitarity is preserved and that terms proportional to $h^V_{20,40}$ have the same high energy behavior as those proportional to $h^V_{10,30}$. If these exponents are sufficiently above their minimum values of 3/2 for $h^V_{1,3}$ and 5/2 for $h^V_{2,4}$ then $Z\gamma$ production is suppressed at energies $\sqrt{\hat{s}} >> \Lambda_Z >> M_Z$, where multiple weak boson or resonance phenomena are expected to dominate [17].

Note that all anomalous couplings are $\mathcal{C}-$odd. The couplings h^V_{30} and h^V_{40} are $\mathcal{CP}-$conserving, whereas h^V_{10} and h^V_{20} violate $\mathcal{CP}$ (i.e. violate $\mathcal{T}$). Within the context of the Standard Model, at the tree-level all couplings h^V_{i0} vanish. However, at the one-loop level, only the $\mathcal{CP}-$conserving couplings h^V_{30} and h^V_{40} are non-zero. However, as in the case of the one-loop SM corrections to the $\mathcal{CP}-$conserving $WW\gamma$ couplings, the higher-order SM contributions to $Z + \gamma$ are also expected to be quite small, *e.g.* $h^Z_{30} \sim 2 \times 10^{-4}$ [18]. Large anomalous contributions to the $\Delta\kappa$ and λ parameters for $W\gamma$, and to h^Z_{30} and h^Z_{40} for $Z\gamma$ are possible if the W and Z bosons are composite objects. This is analogous to the anomalous contributions to the magnetic dipole moments of the proton and neutron, where $\Delta\kappa_p = +1.80$ and $\Delta\kappa_n = -1.91$ originate from quark sub-structure of the nucleon.

Combinations of h^Z_{30} and h^Z_{40} correspond to electric dipole and magnetic quadrupole *transition* moments for the $Z\gamma Z$ process, whereas combinations of h^Z_{10} and h^Z_{20} correspond to magnetic dipole and electric quadrupole *transition* moments. For the case of the transition of an off-shell Z^* with mass $\sqrt{\hat{s}}$ radiating to an on-shell Z and a γ with energy k, the $\mathcal{CP}-$conserving electric dipole ($E1$) and magnetic quadrupole ($M2$) $Z^*Z\gamma$ *transitions*, and the $\mathcal{CP}-$violating magnetic dipole ($M1$) and electric quadrupole ($E2$) $Z^*Z\gamma$ *transitions*, with $k << M_Z$ are given by [19]:

$$E1 = \frac{2e}{M_Z^2}\frac{k}{M_Z}\frac{k^2}{\sqrt{2}}\left(h^Z_{30} - h^Z_{40}\right) + \mathcal{O}(k^4) \text{ terms} \tag{15}$$

$$M2 = \frac{2e}{M_Z^2}k^2\sqrt{\frac{5}{6}}\left(2h^Z_{30}\right) + \mathcal{O}(k^3) \text{ terms} \tag{16}$$

$$M1 = \frac{2e}{M_Z^2}\frac{k}{M_Z}\frac{k^2}{\sqrt{2}}\left(h^Z_{10} - h^Z_{20}\right) + \mathcal{O}(k^4) \text{ terms} \tag{17}$$

$$E2 = \frac{2e}{M_Z^2}k^2\sqrt{\frac{5}{6}}\left(2h^Z_{10}\right) + \mathcal{O}(k^3) \text{ terms} \tag{18}$$

Note that the non-relativistic $Z^*Z\gamma$ transition multipoles have high powers in k because these moments are for a neutral, spin-1 Majorana particle. One power of k is associated with the Bose pre-factor in the $ZZ\gamma$ vertex function.

The expressions for the $Z^*Z\gamma$ transition *moments*, in the static limit ($k \to 0$) are defined with the convention [20]:

$$E1 \equiv -2k\, d_{Z_T} \qquad E2 \equiv \frac{1}{\sqrt{3}}k^2 Q^e_{Z_T} \tag{19}$$

$$M1 \equiv -2k\, \mu_{Z_T} \qquad M2 \equiv \frac{1}{\sqrt{3}}k^2 Q^m_{Z_T} \tag{20}$$

The $\mathcal{CP}-$conserving electric dipole and magnetic quadrupole transition moments, d_{Z_T} and $Q^m_{Z_T}$, and the $\mathcal{CP}-$violating magnetic dipole and electric quadrupole transition moments, μ_{Z_T} and $Q^e_{Z_T}$, to leading order in k (with $\hbar = c = 1$) are given by [19]:

$$d_{Z_T} = -\frac{e}{M_Z}\frac{1}{\sqrt{2}}\frac{k^2}{M_Z^2}\left(h_{30}^Z - h_{40}^Z\right) \quad (21)$$

$$Q_{Z_T}^m = \frac{e}{M_Z^2}\sqrt{10}\,(2h_{30}^Z) \quad (22)$$

$$\mu_{Z_T} = -\frac{e}{M_Z}\frac{1}{\sqrt{2}}\frac{k^2}{M_Z^2}\left(h_{10}^Z - h_{20}^Z\right) \quad (23)$$

$$Q_{Z_T}^e = \frac{e}{M_Z^2}\sqrt{10}\,(2h_{10}^Z) \quad (24)$$

Because the Z has no *static* multipole moments (due to the Majorana nature of the Z) it has no classical equivalent of the charge radius, in contrast to the W. Note also that for $Z\gamma\gamma$ anomalous couplings, the multipole transitions/transition moments for the $\gamma^* Z\gamma$ case are not physically well-defined in the static limit ($k \to 0$) since the γ^* is (very) far off shell [19].

As in the $W\gamma$ case, non-standard $ZZ\gamma$ and $Z\gamma\gamma$ couplings include momentum-dependent form factors which must vanish at large momentum transfer in order to guarantee that S-matrix unitarity is not violated [21]. Limits on the Z anomalous couplings extracted from experimental data therefore depend on the form factor scale Λ_Z which characterizes the energy above which the form factor starts to decrease. The scale Λ_Z is generally assumed to be connected to some novel interactions operative at energies $\approx \Lambda_Z$, and is expected to be at least of order of a few hundred GeV. For $\bar{\text{p}}$-p interactions at $\sqrt{s} = 1.8$ TeV, the dependence of the limits for $WW\gamma$ anomalous couplings on the scale Λ_W is small. The dependence on Λ_Z is much stronger for $ZZ\gamma/Z\gamma\gamma$ anomalous couplings.

As described in Appendix A, the destructive interference between the $s-$channel diagrams involving the $WW\gamma$ vertex and the $u-$ and $t-$channel graphs for the SM $W\gamma$ process results in the radiation amplitude zero. However, no such destructive interference effects are present for the SM $Z\gamma$ process. The ratio of the observed $W\gamma/Z\gamma$ cross section $\times$ branching ratios is expected to be ~ 4 whereas the ratio of the inclusive W/Z cross section $\times$ branching ratios is expected to be ~ 11 for our choice of $W\gamma/Z\gamma$ event selection cuts. For $WW\gamma$ and $ZZ\gamma/Z\gamma\gamma$ anomalous couplings, the $W\gamma$ and $Z\gamma$ cross sections are approximately quadratically dependent on the anomalous parameters. The minimum of the $W+\gamma$ cross section does not occur at the SM values of $\mathcal{CP}-$conserving $WW\gamma$ anomalous couplings, $\Delta\kappa$ and λ due to interference effects and the different $\hat{s}-$dependencies of the various anomalous terms in the overall invariant amplitude $\mathcal{M}_{W\gamma}$. This is also true for the $Z+\gamma$ case.

3 DETECTOR AND DATA COLLECTION

3.1 Introduction

The Tevatron $\bar{\text{p}}$-p collider at Fermilab operated at a center of mass energy of 1.8 TeV and a nominal luminosity of $10^{30}\text{cm}^{-2}\text{sec}^{-1}$ during the 1988-89 run. The Collider Detector at Fermilab (CDF) is a multi-component, 5000-ton detector that covers most of 4π solid angle [22]. A cut-away view of the CDF detector is shown in Fig. 3. The CDF coordinate system defines the positive z axis along the direction travelled by protons. The y axis is vertically upward and the x axis is radially outward from the center of the Tevatron ring. The angles θ and ϕ are the polar and azimuthal angles; the pseudorapidity variable $\eta = -\ln(\tan\theta/2)$. The superconducting solenoid provides a magnetic field

of 1.4116 T for magnetic analysis of charged particles in the central ($\eta < 1.1$) region. Calorimeter coverage extends to within 2.0° of the beam ($|\eta| < 4.2$).

The components of the CDF detector of most interest for this analysis are the beam-beam counters, the central tracking system, the central, plug and forward calorimeters, and the central muon system. The beam-beam counters (BBC) are a plane of scintillation counters located immediately in front of the forward/backward calorimeters at a distance of 5.8 m from the nominal interaction point and covering the beam-fragmentation region in the pseudo-rapidity range $3.2 < |\eta| < 5.9$. These counters provide a minimum-bias trigger for the detector and are also used as the primary luminosity monitor for CDF. The minimum-bias BBC trigger requires at least one counter in each plane to fire within a 15 ns window centered on the beam crossing time.

3.2 Tracking Detectors

The CDF central tracking system is composed of a vertex time projection chamber system [23] (VTPC) located immediately outside the beam pipe and large volume central tracking chamber [24] (CTC) contained within the uniform magnetic field region of the solenoid. The VTPC is used to establish the position of the interaction vertex with an rms resolution of 1mm in the beam (z) direction and to provide tracking information in the region $|\eta| \leq 3.5$. Sense wires provide measurements of track coordinates in the $r - z$ view, cathode pads and small-angle stereo provide measurements in $r - \phi$. The central tracking chamber encloses the VTPC and gives precise track momentum and charge-sign measurements in the region $|\eta| < 1.1$. The CTC is a 3.2 m long cylindrical drift chamber with an outer radius of 1.3 m, consisting of 84 layers of sense wires, grouped into nine alternating axial and stereo superlayers. Five axial superlayers consist of 12 sense wires; four stereo layers have 6 sense wires, tilted at ±3° relative to the beam direction. The rms momentum resolution of the CTC is $\delta p_T/p_T = 0.0020 p_T$ (p_T in GeV/c) for isolated tracks. Imposing the constraint that individual tracks originate from the interaction vertex extends the effective track-fitting region from 1.0 to 1.3 m, resulting in an improved momentum resolution of $\delta p_T/p_T = 0.0011 p_T$.

3.3 Calorimeters

The calorimeters have fine segmentation in eta-phi and are organized into projective towers pointing towards the interaction region. The calorimeters cover all of phi, and extend to $|\eta| < 4.2$. Each calorimeter tower consists of an electromagnetic shower counter in front of a hadronic calorimeter element. In the central region ($|\eta| < 1.1$) the calorimeters are scintillator-based, while the plug and forward calorimeters are gas-based, using proportional tubes and cathode pad readouts. The calorimeters are used to identify electrons and photons by their local kinetic energy deposition in the EM portion of the calorimeter, and to augment muon identification by detection of their minimum ionizing energy deposition signature in the calorimeter. Photons are distinquished from electrons by energy deposition in the EM portion of the calorimeter where no track is incident. The central calorimeter is composed of 15° wedges in ϕ, with a projective tower size of $0.1 \times 15°$ in $\eta \times \phi$. The central electromagnetic calorimeter [25] (CEM) is 18 radiation lengths (0.6 absorption lengths) thick and consists of lead sheets interspersed with polystyrene scintillator, read out through wavelength shifters coupled via light-guides to conventional photomultiplier tubes. The CEM calorimeter has an energy resolution of $\delta E/E = 13.5\%/\sqrt{E_T} \oplus 2\%$ (E in GeV), where E_T (in GeV) is the

transverse energy and the symbol $\oplus$ signifies that the constant term is added in quadrature with the stochastic term.

The central electromagnetic strip chambers [22] (CES) are used to determine shower position and transverse development of an electromagnetic shower at shower maximum ($\sim$ 6.3 radiation lengths) by measurement of the charge deposition on orthogonal, fine-grained (1.5 cm spacing) strips and wires. In this analysis, the central strip chamber information is used for electron/photon transverse shower profile information, and also to separate single photons from multi-photon QCD jet background. The CES chambers provide precise location of an electromagnetic shower, with an rms accuracy of $\sim$ 3.0 mm in $r - z$ and $\sim$ 1.7 mm in $r - \phi$. Figure 4 is a schematic drawing of a central calorimeter wedge. Figure 5 shows the orientation of the cathode strips and anode wires in the CES.

The central hadronic calorimeter [26] (CHA) consists of steel absorber interspersed with acrylic scintillator, totalling 4.5 absorption lengths. The CHA calorimeter has an energy resolution of $\delta E/E = 75\%/\sqrt{E} \oplus 3\%$ for isolated pions.

The plug electromagnetic calorimeter [27] (PEM) is divided into quadrants. It is constructed from lead absorber panels interspersed with gas proportional chambers with cathode pad readout (18-21 radiation lengths in depth, corresponding to 0.6-0.7 absorption lengths). The PEM has an energy resolution of $\delta E/E = 28\%/\sqrt{E} \oplus 2\%$ (E in GeV) and a tower size of $0.09 \times 5°$ in $\eta \times \phi$. Shower positions are determined from θ and ϕ pad information, with a spatial resolution of 2 mm $\times$ 2 mm.

The forward electromagnetic calorimeter [28] (FEM) is also constructed from lead absorber panels interspersed with gas proportional wire chambers and cathode pad readout (25 radiation lengths in depth, corresponding to 0.8 absorption lengths). The FEM has an energy resolution of $\delta E/E = 25\%/\sqrt{E} \oplus 2\%$ (E in GeV) and a tower size of $0.1 \times 5°$ in $\eta \times \phi$. Shower positions are determined from θ and ϕ pad information, with a spatial resolution of $1 - 4$ mm depending on the shower location in the calorimeter.

The plug [29] (PHA) and forward [30] (FHA) hadronic calorimeters are constructed from steel absorbers interspersed with gas proportional chambers as the active medium. The PHA is 5.7 absorption lengths thick and has an energy resolution of $\delta E/E = 90\%/\sqrt{E} \oplus 4\%$ for isolated pions. The FHA is 7.7 absorption lengths thick and has an energy resolution of $\delta E/E = 130\%/\sqrt{E} \oplus 4\%$ for isolated pions.

3.4 Muon Detectors

The central muon chambers [31] (CMU) consist of drift chamber modules located behind approximately 5 hadronic absorption lengths of lead and steel in the central calorimeters at a radius of 3.5 m. Four layers of drift cells in a muon chamber provide three-dimensional reconstruction of tracks from drift-time information in the transverse ($r - \phi$) direction and charge division information in the longitudinal ($r - z$) direction. A drift resolution of 250 μm and charge division resolution of 1.2 mm are determined from cosmic ray studies. Each CMU wedge on either side of $\eta = 0$ covers the region $0.026 < |\eta| < 0.63$ and 15° in ϕ.

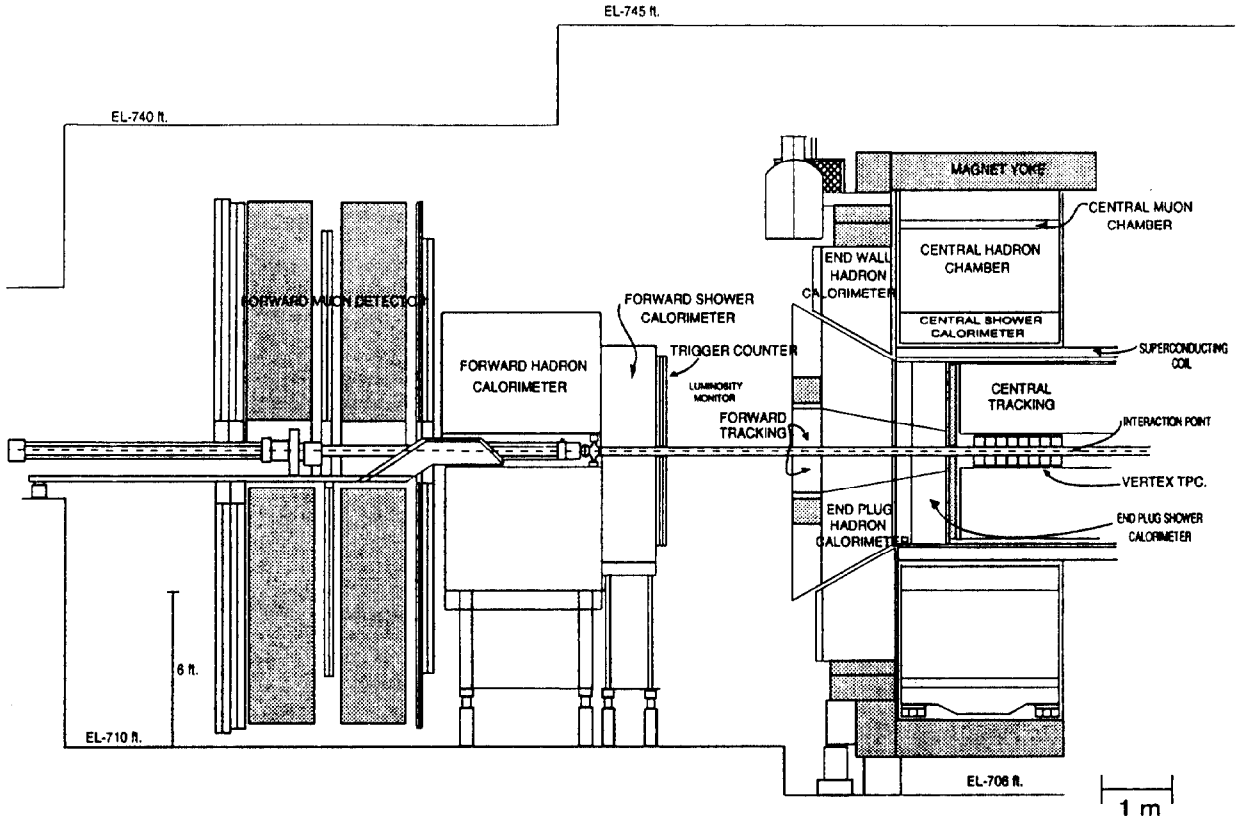

Figure 3: Cutaway view of the forward half of the CDF detector.

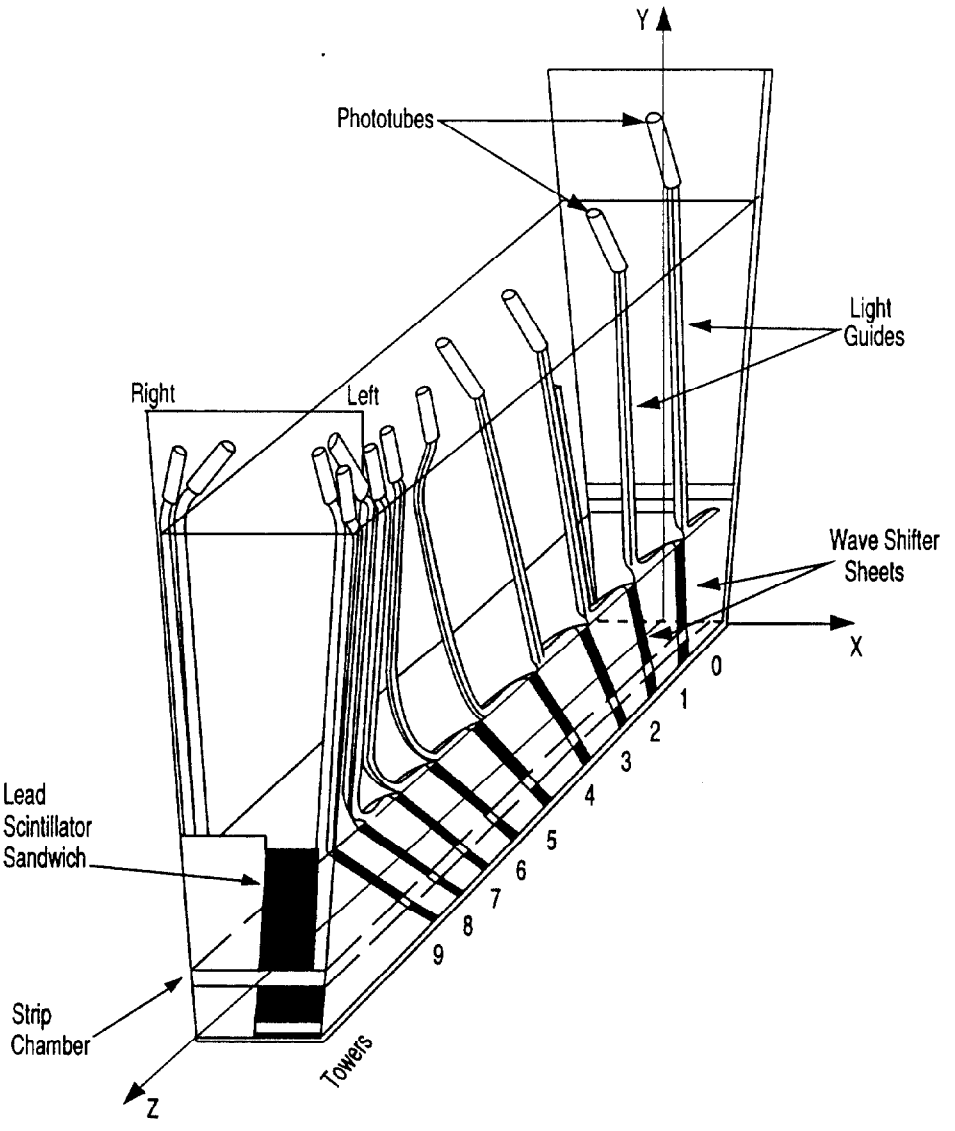

Figure 4: Three-dimensional view of a central calorimeter wedge.

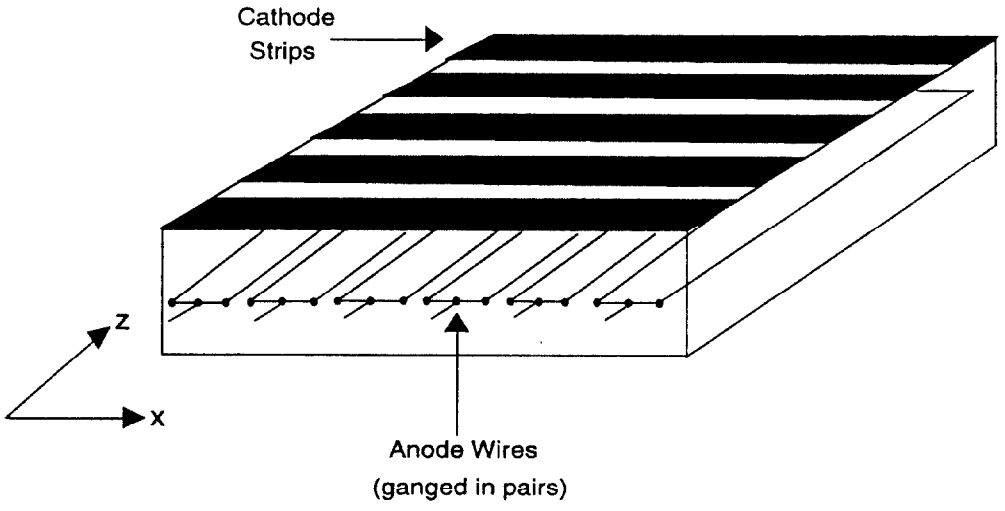

Figure 5: Three-dimensional view of the CES chamber strip and wire orientation. The $\hat{z}-$axis is along the proton beam direction, the local $\hat{x}-$axis is in the azimuthal $\hat{\phi}-$direction.

3.5 Triggering

The $\bar{p}$-p interaction rate at the Tevatron collider is 10^5 times higher than the capability of the CDF data acquisition system. In order to reduce the trigger rate to a level that can be written to magnetic tape, a four-level trigger system is used [32]. A description of the triggers relevant to the collection of inclusive W and Z data samples follows.

The lowest-level triggering scheme (level-0) selects inelastic (minimum bias) $\bar{p}$-p collisions by requiring an in-time coincidence of the BBC planes on either side of the interaction region. This trigger decision is made available in time to inhibit data taking during the next beam crossing, 3.5 μs later.

The level-1 trigger decision is made within the 7.0 μs allowed by level-0. If the event fails in level-1, the front end electronics are reset in time for the second crossing after the initial level-0 decision.

The level-1 calorimeter trigger system [32] computes transverse energy flow in both the electromagnetic and hadronic compartments of the calorimeter. Trigger towers have a width of $0.2 \times 15°$ in $\eta \times \phi$, mapping the detector into two 42×24 ($\eta \times \phi$) arrays, one for electromagnetic, the other for hadronic transverse energy deposition. For central electron W/Z candidates, all events are required to have at least 6.0 GeV in a single trigger tower (two physical towers) of the central electromagnetic calorimeter.

The level-1 central muon trigger [33] uses hits from the central muon TDC's to identify high-P_T track "stubs" in the muon chambers. This trigger imposes a cut on the time difference $|t_4 - t_2|$ or $|t_3 - t_1|$ between two radially-aligned wires in a muon tower, where t_i is the drift time to the i^{th} wire in a muon tower. This requirement restricts the maximum allowed angle of a track with respect to an infinite momentum track emanating from the $\bar{p}$-p vertex, and thus enables a P_T cut on the track. Multiple scattering in the calorimeter upstream of the muon chambers smears the trigger threshold in track P_T. The central muon W/Z data samples used in this analysis have been obtained with a P_T threshold of 3.0 GeV/c. Using cosmic rays, the level-1 muon trigger efficiency is measured to be greater than 90% and independent of P_T for tracks with transverse momentum greater than 10.0 GeV/c.

In level-2, two-dimensional tracking information from the central fast tracker [34] (CFT), a hardware track processor, is combined with level-1 electron and muon information to form level-2 electron and muon triggers. Fast timing information from the CTC is used to detect high transverse momentum tracks in the central region. The track finder analyzes prompt hits from the axial sense wires of the CTC to identify tracks by comparing hits in the CTC to predetermined hit patterns for the range of transverse momenta allowed by the CFT trigger threshold. The track processor covers the P_T range from 2.5 to 15.0 GeV/c with a momentum resolution of $\delta P_T/P_T = 3.5\%$ (P_T in GeV/c). The list of two-dimensional tracks found by the track processor is used in the CDF level-2 trigger system.

The level-2 central electron trigger combines calorimeter and tracking infomation. A hardware cluster finder searches the electromagnetic and hadronic tower arrays, forming clusters around seed towers. The level-2 electron trigger requires (a) a cluster transverse electromagnetic energy (EM E_T) greater than 12.0 GeV (assuming the event vertex to be at $Z = 0$), (b) a ratio of the total cluster E_T to EM E_T less than 1.125, and (c) a CFT track associated with the cluster with transverse momentum $P_T > 6.0$ GeV/c. The efficiency of the level-2 electron trigger for W electrons is 98%.

The level-2 central muon trigger [35] matches the list of two-dimensional CFT tracks to stubs

found by the level-1 muon trigger using look-up tables (which include multiple scattering effects). The level-2 muon trigger requires CFT tracks with $P_T > 6.0$ GeV/c. The efficiency of the level-2 muon trigger for muons with transverse momentum $P_T > 15.0$ GeV/c was 97.0%, independent of the track density in the event.

A level-3 trigger system [36] consists of a "farm" of 60 Motorola 68020 processors. The event data, read out from the entire detector after a level-2 trigger accept, is used by level-3. Because of constraints on the execution time per event, level-3 trigger algorithms use streamlined versions of the complete offline CDF event reconstruction code. The level-3 central electron filter requires that the level-2 central electron cluster have $EM\ E_T > 12.0$ GeV and a two-dimensional track with $P_T > 6.0$ GeV/c as reconstructed by level-3 software. The level-3 central muon filter requires that a two-dimensional track with $P_T > 9.0$ GeV/c match a level-1 central muon trigger stub within a 5.0° window in ϕ, as reconstructed by level-3 software. The efficiency of the level-3 central electron and muon triggers above 15.0 GeV is 100%.

The overall (level-1,2,3) trigger efficiencies for (fiducial) central electrons (muons) associated with the inclusive W/Z data samples is $97.3 \pm 0.5\%$ ($91.0 \pm 0.2\%$).

3.6 Data Collection

The data samples used in this analysis were collected over a 12-month period, during which the peak machine luminosity increased to over 2×10^{30} cm^{-2} s^{-1}. The overall trigger rate was limited to $1-2$ Hz by the speed at which data could be transferred to tape. A typical event record contained ~ 120 kbytes of information.

4 THE ELECTRON AND MUON $W + \gamma$ AND $Z + \gamma$ DATA SAMPLES

4.1 Introduction

The inclusive electron and muon data sets used for the $W\gamma$ and $Z\gamma$ analysis were used for the previous W and Z absolute production cross section $\times$ decay branching ratio measurements [6] and the electron and muon W/Z cross section ratios [7]. In the 1988-89 Tevatron collider run, the integrated luminosities of high$-P_T$ electron and muon data were $\int \mathcal{L}_e dt = 4.05 \pm 0.28$ pb^{-1} and $\int \mathcal{L}_\mu dt = 3.54 \pm 0.24$ pb^{-1}, respectively. The uncertainty in each of these integrated luminosities is 6.8%, primarily from the uncertainty in the total inelastic $\bar{p}$-p cross section as observed by the Beam-Beam Counters, $\sigma_{BBC} = 46.8 \pm 3.2$ mb [7].

4.2 Inclusive Electron W and Z Event Selection

The inclusive electron W and Z samples are extracted from a common central electron sample having the following requirements:

- The event vertex be within $|z_{vtx}| < 60.0$ cm of nominal $z = 0.0$ position.
- The electron cluster have $|\eta_e| < 1.1$, and be within the good fiducial region of the CEM calorimeter, as determined from CES shower centroid information.
- A transverse energy of the central EM cluster of $E_T^{\text{cluster}} > 20.0$ GeV.

- Isolation $I \equiv (E_T^{\rm cone} - E_T^{\rm cluster})/E_T^{\rm cluster} < 0.1$, in an angular cone of size $\Delta R = \sqrt{\Delta\eta^2 + \Delta\phi^2} = 0.4$ centered on the EM cluster (location defined from CES shower centroid information). $E_T^{\rm cone}$ is the sum of the transverse energy in the cone.

- A hadron-to-EM energy ratio for the central EM cluster of $Had/EM < 0.055 + 0.00045 * E$, where E is the total energy of the EM cluster in GeV. An energy-independent efficiency for this cut is obtained using this functional form.

- A CES strip $\chi^2_{\rm strip} < 15.0$, which is a chi-squared comparison of a fit of the leading CES cluster profile in the strip view to test-beam electron shower profiles.

- Lateral shower-shape chi-squared variable $L_{\rm shr} < 0.2$, which is a chi-squared comparison of the observed CEM lateral shower profile to test-beam electron CEM lateral shower profile data.

- A single, reconstructed three-dimensional track associated with the EM cluster with $E/P < 1.5$ which matches the CES shower position to within $|\Delta z| < 3.0$ cm and $|\Delta r - \phi| < 1.5$ cm.

A total of 5012 events pass these requirements.

Electron W candidates are obtained from the common central electron sample by additionally requiring $\not\!\!E_T > 20$ GeV. The W candidates must not be simultaneously consistent with being an electron Z candidate, as defined below. A total of 2664 events pass the electron W requirements.

Electron Z candidates are obtained from the common central electron sample by additionally requiring a second electromagnetic cluster located in a good fiducial region of either the central, plug or forward calorimeters, passing the following selection criteria:

- A transverse energy of the second EM cluster of $E_T^{\rm cluster} > 10$ GeV.

- Isolation $I < 0.1$, in an angular cone of size $\Delta R = 0.4$ centered on the EM cluster.

- A hadron-to-EM energy ratio for the second EM cluster of $Had/EM < 0.10$.

- In the central region, a second EM cluster is required to have a single, three-dimensional track associated with it, and have $E/P < 2.0$.

- In the plug region, a second EM cluster is required to have a lateral shower chi-squared variable defined using a 3×3 matrix of PEM anode pad information of $\chi^2_{3\times3} < 20.0$, which is a chi-squared comparison of the observed lateral shower profile to test-beam lateral shower data. The second EM cluster is also required to have a VTPC hit fraction > 0.5, defined as the fraction of observed to expected hits within a road defined by the event vertex and the centroid of the PEM cluster.

- A dielectron pair invariant mass between $70 < M_{ee} < 110$ GeV/c^2.

A total of 243 events pass the electron Z requirements.

4.3 Inclusive Muon W and Z Event Selection

The inclusive muon W and Z samples are extracted from a common central muon sample having the following requirements:

- The event vertex be within $|z_{\rm vtx}| < 60.0$ cm of nominal $z = 0.0$ position.
- A reconstructed central muon with transverse momentum, $P_T \geq 20.0$ GeV/c, and in a good fiducial region of the central muon system.
- A match of the extrapolated CTC track to the reconstructed muon "stub" in the muon chambers to better than 2 cm in the $r - \phi$ plane.
- A minimum ionizing signature of less than 2.0 GeV (6.0 GeV) of EM (hadronic) energy deposited in the calorimeter towers traversed by the muon.
- Isolation $I \equiv (E_T^{\rm cone} - E_T^{\mu})/P_T^{\mu} < 0.1$, where $E_T^{\rm cone}$ is the sum of the transverse energy observed in the calorimeter within a cone of $\Delta R = 0.4$ centered on the muon track, E_T^{μ} is the transverse energy deposited in the calorimeter towers traversed by the muon and P_T^{μ} is the transverse momentum of the muon track.
- Cosmic ray muons were removed from the sample by using central tracking chamber information to veto events with muon tracks which were inconsistent with coming from the event vertex.

A total of 2011 events pass these requirements.

Muon W candidates are obtained from the common central muon sample by additionally requiring missing transverse energy, $\not\!\!E_T > 20$ GeV. The muon W candidates must not be simultaneously consistent with being a muon Z candidate, as defined below. A total of 1436 events pass the central muon W requirements.

Muon Z candidates are obtained from the common central muon sample by additionally requiring a second minimum ionizing track passing the following selection criteria:

- $P_T \geq 20.0$ GeV/c and $|\eta_{\mu}| < 1.0$.
- Opposite charge sign to the first muon.
- A dimuon pair invariant mass between $65 < M_{\mu\mu} < 115$ GeV/c^2.
- If the second track is within the fiducial acceptance of the central muon system, we additionally require that it have a reconstructed muon "stub" in the muon chamber.

A total of 106 events pass the muon Z requirements.

4.4 Electron and Muon $W\gamma$ and $Z\gamma$ Event Selection

All data sets used in this analysis have been processed with a modified $EM-$clustering algorithm to ensure high efficiency for finding photons down to $E_T^{\gamma} = 3.0$ GeV. Position-dependent response map [37] and energy scale corrections are applied after clustering. A common set of photon identification cuts are then applied to each of the four inclusive W/Z data samples to obtain the electron and muon $W\gamma$ and $Z\gamma$ sub-datasets [8]. A central fiducial photon candidate is defined as follows:

- A cluster of electromagnetic energy deposited in 1-3 contiguous towers in a wedge of the CEM calorimeter with $E_T \geq 5.0$ GeV, after position response and CEM energy scale corrections, with a seed calorimeter tower energy of $E_T \geq 1.0$ GeV.

- A candidate CEM cluster is required to be in a good fiducial region of the central calorimeter, as defined by the position determined from CES shower centroid information.

- An angular separation between the W/Z decay lepton(s) and the photon of $\Delta R_{\ell\gamma} = \sqrt{\Delta\eta^2 + \Delta\phi^2} > 0.7$. This cut is designed to suppress the contribution from radiative W/Z decay. $\Delta R_{\ell\gamma} = 0.7$ corresponds to an opening angle of $\Delta\phi \simeq 40°$ in the $r - \phi$ plane.

- A calorimeter isolation "$ET4$" cut, requiring that the excess transverse energy deposited in a cone of $\Delta R = 0.4$ centered on the CEM cluster, but not including the EM cluster energy, must be $ET4 < 2.0$ GeV.

- A tracking isolation "$\Sigma PT4$" cut, requiring that the summed transverse momentum due to charged tracks within a cone of $\Delta R = 0.4$ centered on the CEM cluster must be less than $\Sigma PT4 < 2.0$ GeV. The tracks participating in the sum must originate within $\Delta z < 10$ cm of the event vertex, and be reconstructed in three dimensions.

- An "$N3D = 0$" cut, requiring no charged tracks pointing at the CEM cluster, originating from *any* vertex. The tracks must be reconstructed in three dimensions.

- A hadron-to-EM energy ratio for the central EM cluster of $Had/EM < 0.055 + 0.00045 * E$, where E is the total energy of the EM cluster in GeV.

- A lateral shower-shape for the CEM cluster of $L_{shr} < 0.5$.

- The CES strip and wire chi-squares for the electron shower profiles of the leading cluster in each of these views, must be $\chi^2_{strip} < 20.0$ and $\chi^2_{wire} < 20.0$.

- A "no 2^{nd} CES" cut, requiring that no additional CES strip/wire clusters with $E_{CES\ 2^{nd}} > 1.0$ GeV be present within the calorimeter towers associated with the CEM cluster. This cut is made to further suppress π^0 and multi-photon QCD jet backgrounds.

For electron and muon $W\gamma$ candidates, a cut removing events with additional high-P_T tracks is made to suppress background from misidentified $Z + \gamma$ events, where one of the Z decay leptons is not detected. This background is discussed in greater detail in Section 5.4.1. A transverse mass cut of $M_T^W > 40$ GeV/c^2 is also made in the $W\gamma$ data samples to suppress the high-$P_T^{W\gamma}$ component of the $(W \rightarrow \tau\ \bar{\nu}_\tau) + \gamma$, $\tau \rightarrow \ell\ \bar{\nu}_\ell\ \nu_\tau$ background. The W transverse mass is defined as $M_T^W \equiv \sqrt{2P_T^\ell P_T^{\bar{\nu}\ell}\,(1 - \cos\Delta\phi_{\ell\bar{\nu}_\ell})}$, where $\Delta\phi_{\ell\bar{\nu}_\ell}$ $(\ell = e,\ \mu)$ is the opening angle between the W decay lepton and neutrino in the $r - \phi$ plane. This background is discussed further in Section 5.4.2.

A total of 8 (5) electron (muon) $W\gamma$ candidate events and 2 (2) electron (muon) $Z\gamma$ candidate events pass the photon identification requirements. The progression of photon cuts for the electron $W\gamma$ channel is shown in Figs. 6a - 6h and summarized in Table 1 for each of the four channels. This Table also summarizes the progression of photon cuts as applied to a non-signal QCD jet background data sample, as discussed in detail in Section 5.3. The salient kinematic properties

of these events for all four channels are summarized in Tables 2-5. Figures 7 - 10 show some of the kinematic properties of electron/muon $W\gamma$ and $Z\gamma$ candidate event samples, overlaid with SM Monte Carlo signal predictions and background expectations for each channel (discussed in greater detail in Section 5 below). The cluster transverse mass (also known as the minimum invariant mass) of the $W + \gamma$ system is defined as:

$$M_{CT}^{W\gamma} \equiv \left\{ \left[\left(M_{\ell\gamma}^2 + |\vec{\mathbf{P}}_T^{\gamma} + \vec{\mathbf{P}}_T^{\ell}|^2 \right)^{\frac{1}{2}} + |\vec{\mathbf{P}}_T^{\nu_\ell}| \right]^2 - |\vec{\mathbf{P}}_T^{\gamma} + \vec{\mathbf{P}}_T^{\ell} + \vec{\mathbf{P}}_T^{\nu_\ell}|^2 \right\}^{\frac{1}{2}} \quad (25)$$

where $M_{\ell\gamma}$ is the invariant mass of the lepton-photon system.

Table 1: Summary of electron and muon $W\gamma$, $Z\gamma$ candidates and Jet-20 QCD background passing successive photon cuts. The entries in the first row of the first four columns are the number of inclusive W/Z events; the entries in the other rows of the first four columns are the number of W/Z events with fiducial CEM clusters surviving the application of successive photon cuts. In the last column, the entry in the first row is the number of central, non-leading jets passing the jet selection criteria. The other entries in this column are the number of fiducial CEM clusters surviving the application of successive photon cuts. See text for further details.

	$W_e\gamma$	$W_\mu\gamma$	$Z_e\gamma$	$Z_\mu\gamma$	Jet-20^{QCD}_{bkgd}
Inclusive W/Z or Jet-20 Data Samples	2664	1436	243	106	11726
Pass FidCEM, $E_T^{\gamma}>5.0$ GeV, $\Delta R_{\ell\gamma}>0.7$ Cuts	107	54	6	7	266
Pass $ET4 < 2.0$ GeV Cut	28	18	6	3	107
Pass $\Sigma PT4 < 2.0$ GeV Cut	16	14	2	2	64
Pass $N3D = 0$ Cut	13	13	2	2	57
Pass Had/EM Cut	13	13	2	2	55
Pass $L_{shr} < 0.5$ Cut	13	10	2	2	42
Pass $\chi^2_{strip} + \chi^2_{wire}$ Cut	13	8	2	2	32
Pass no 2^{nd} $CES > 1$ GeV Cut	9	7	2	2	20
Pass no 2^{nd} Isolated Track Cut ($W\gamma$ only)	8	5	–	–	–

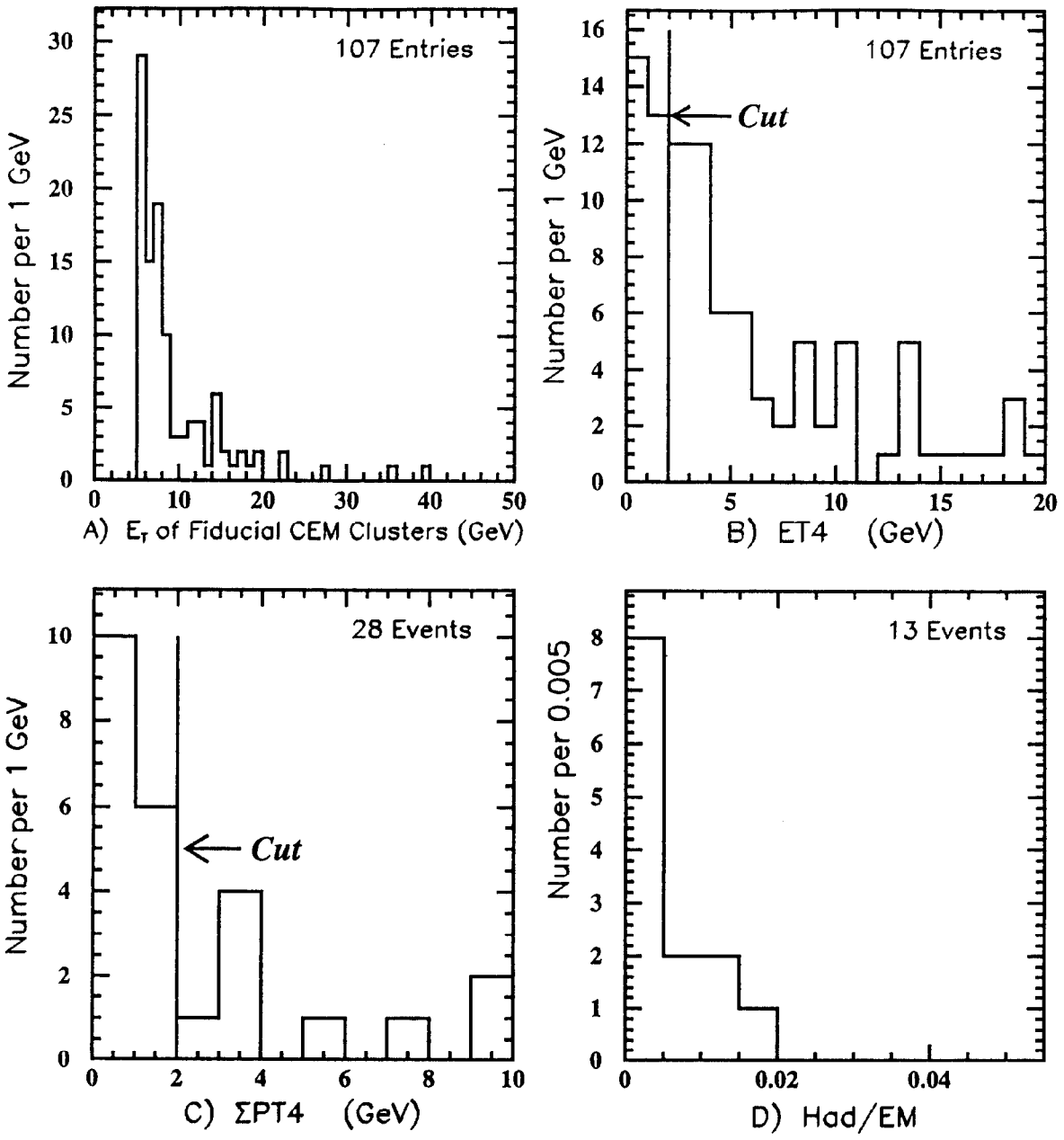

Figure 6: Photon variables as a function of photon cuts, for the electron $W\gamma$ data sample. (A) E_T distribution of fiducial CEM clusters passing the $E_T^\gamma > 5.0$ GeV cut and the $\Delta R_{\ell\gamma} > 0.7$ angular separation cut. (B) The calorimeter isolation distribution before the $ET4 < 2.0$ GeV cut is applied. (C) The tracking isolation distribution before the $\Sigma PT4 < 2.0$ GeV/c cut is applied. (D) The Had/EM distribution before the Had/EM cut is applied.

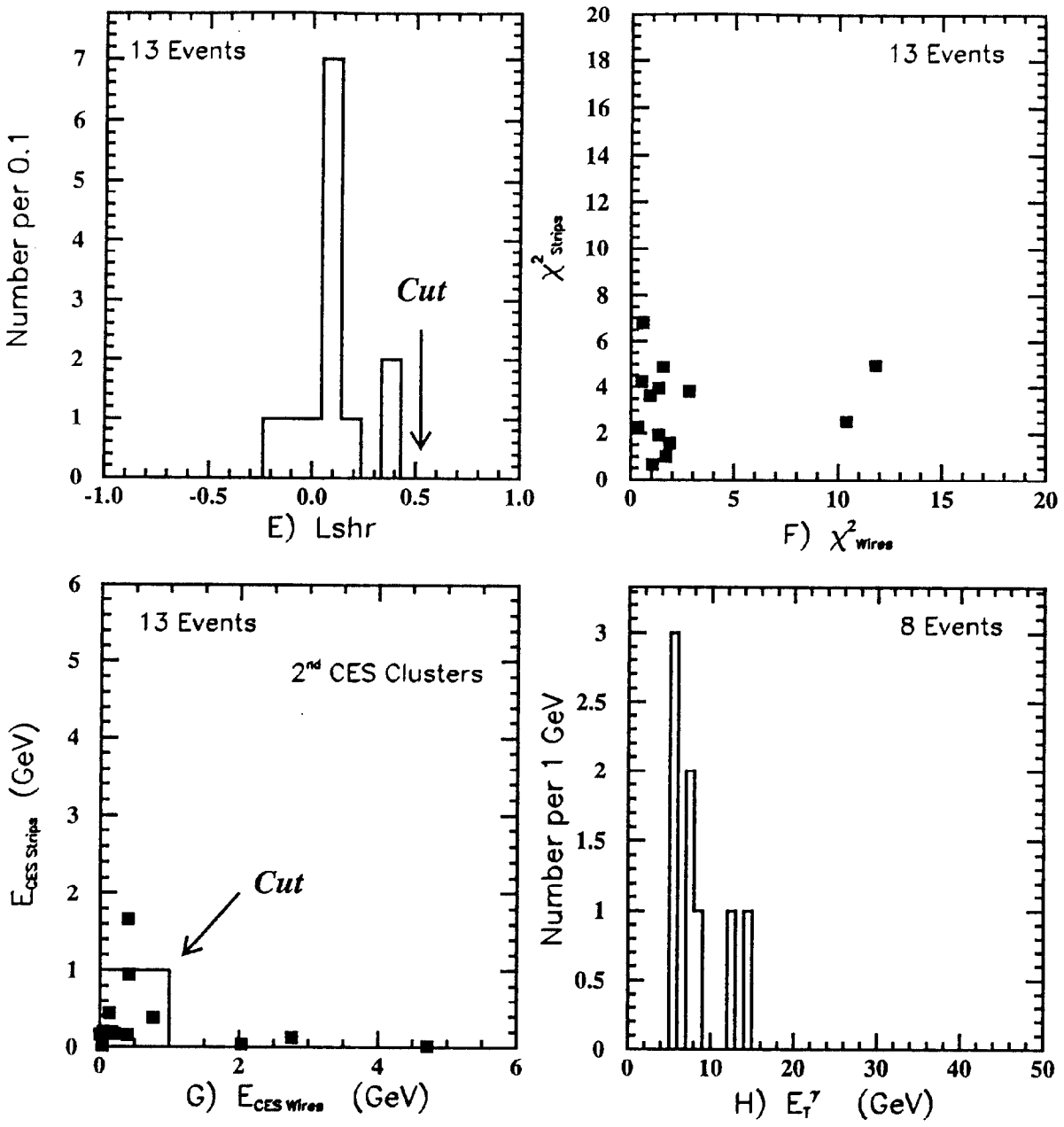

Figure 6: Photon variables as a function of photon cuts, for the electron $W\gamma$ data sample (continued). (E) The L_{shr} distribution before the $L_{shr} < 0.5$ cut is applied. (F) A scatterplot of CES χ^2_{strips} *vs.* χ^2_{wires} before the $\chi^2_{strips} < 20.0$ and $\chi^2_{wires} < 20.0$ cut is applied. (G) A scatterplot of CES E_{strips} *vs.* E_{wires} before the no 2^{nd} CES cluster $E > 1.0$ GeV cut is applied. (H) The E_T^γ distribution after all photon cuts have been applied, including the no 2^{nd} high$-P_T$ track cut for suppression of background from misidentified electron $Z + \gamma$.

Table 2: Kinematic Properties of Electron $W\gamma$ Candidates.

	Run # Event #	E_T^γ (GeV)	Q_W (e)	M_T^W (GeV/c^2)	M_{CT}^W (GeV/c^2)	$\Delta R_{e\gamma}$
1	16801 – 6582	5.17	−1	68.3	80.5	1.28
2	16807 – 4706	8.65	+1	63.8	74.0	0.84
3	17467 – 15981	14.43	−1	59.2	79.1	0.80
4	17529 – 442	5.04	−1	60.8	68.5	2.01
5	17886 – 1796	5.04	−1	83.2	88.5	2.53
6	18720 – 20145	12.29	+1	68.8	96.4	0.76
7	19430 – 20694	7.44	−1	78.4	86.3	0.87
8	19882 – 38400	7.04	+1	85.6	86.7	1.10

Table 3: Kinematic Properties of Muon $W\gamma$ Candidates.

	Run # Event #	E_T^γ (GeV)	Q_W (e)	M_T^W (GeV/c^2)	M_{CT}^W (GeV/c^2)	$\Delta R_{\mu\gamma}$
1	18435 – 606	7.02	−1	50.5	60.5	0.93
2	19177 – 8534	14.71	−1	76.2	94.0	1.44
3	19391 – 43073	20.01	+1	45.0	63.4	1.06
4	19629 – 39980	5.22	+1	79.6	85.4	3.15
5	19932 – 53074	23.58	−1	70.3	106.4	2.22

Table 4: Kinematic Properties of Electron $Z\gamma$ Candidates.

	Run # Event #	E_T^γ (GeV)	$M_{e^+e^-}$ (GeV/c^2)	$M_{Z\gamma}$ (GeV/c^2)	$\Delta R_{e\gamma}$
1	17025 – 5219	13.47	91.0	104.6	1.50
2	18170 – 14254	5.44	82.0	88.2	0.88

Table 5: Kinematic Properties of Muon $Z\gamma$ Candidates.

	Run # Event #	E_T^γ (GeV)	$M_{\mu^+\mu^-}$ (GeV/c^2)	$M_{Z\gamma}$ (GeV/c^2)	$\Delta R_{\mu\gamma}$
1	20361 – 6869	6.40	78.5	84.8	0.71
2	20389 – 23545	7.12	84.0	91.3	1.27

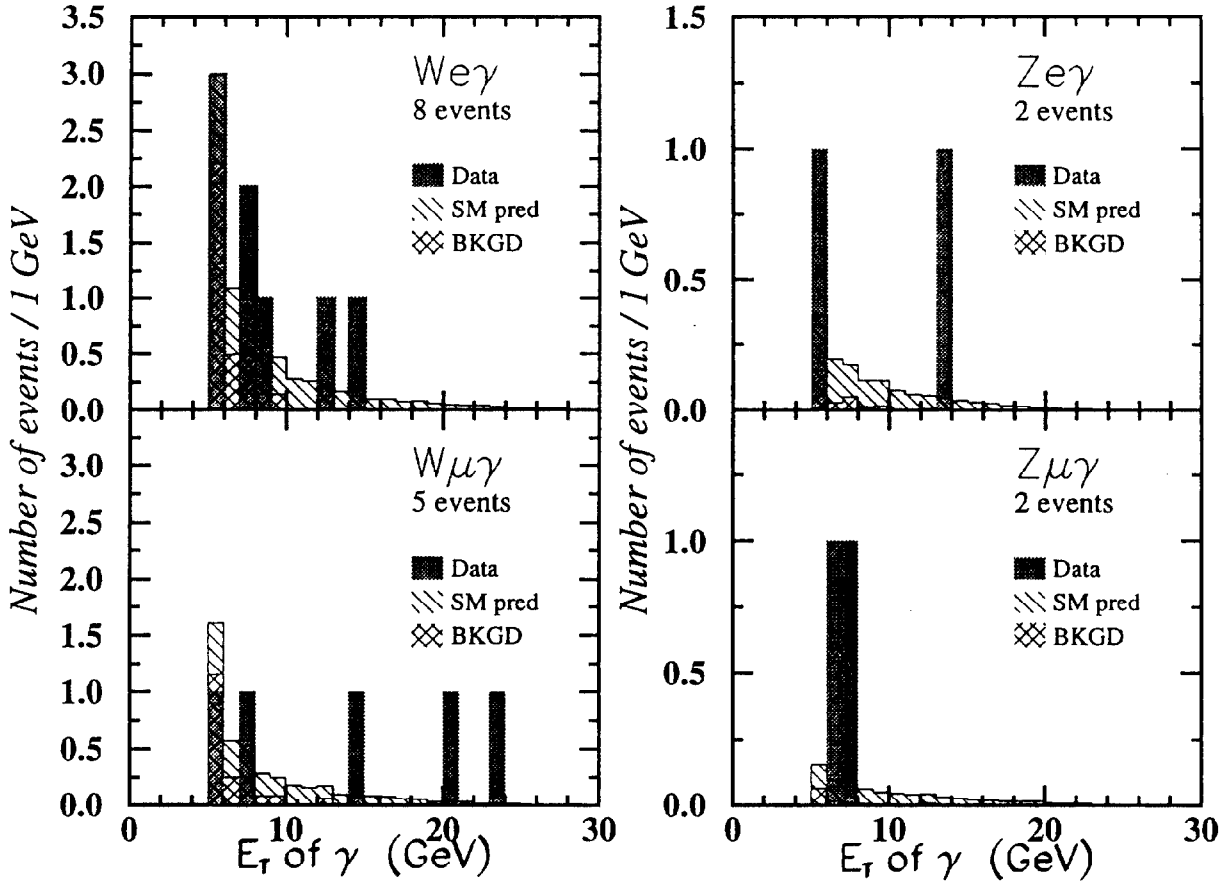

Figure 7: The photon transverse energy (E_T^γ) distributions for each of the four data samples. In each of these figures, for each data sample, the shaded histograms are the event data; the diagonally-hatched histograms are the Standard Model (SM) Monte Carlo predictions for the signal and the cross-hatched histograms are the background predictions. The prediction for the SM signal has been added to the background prediction for each channel.

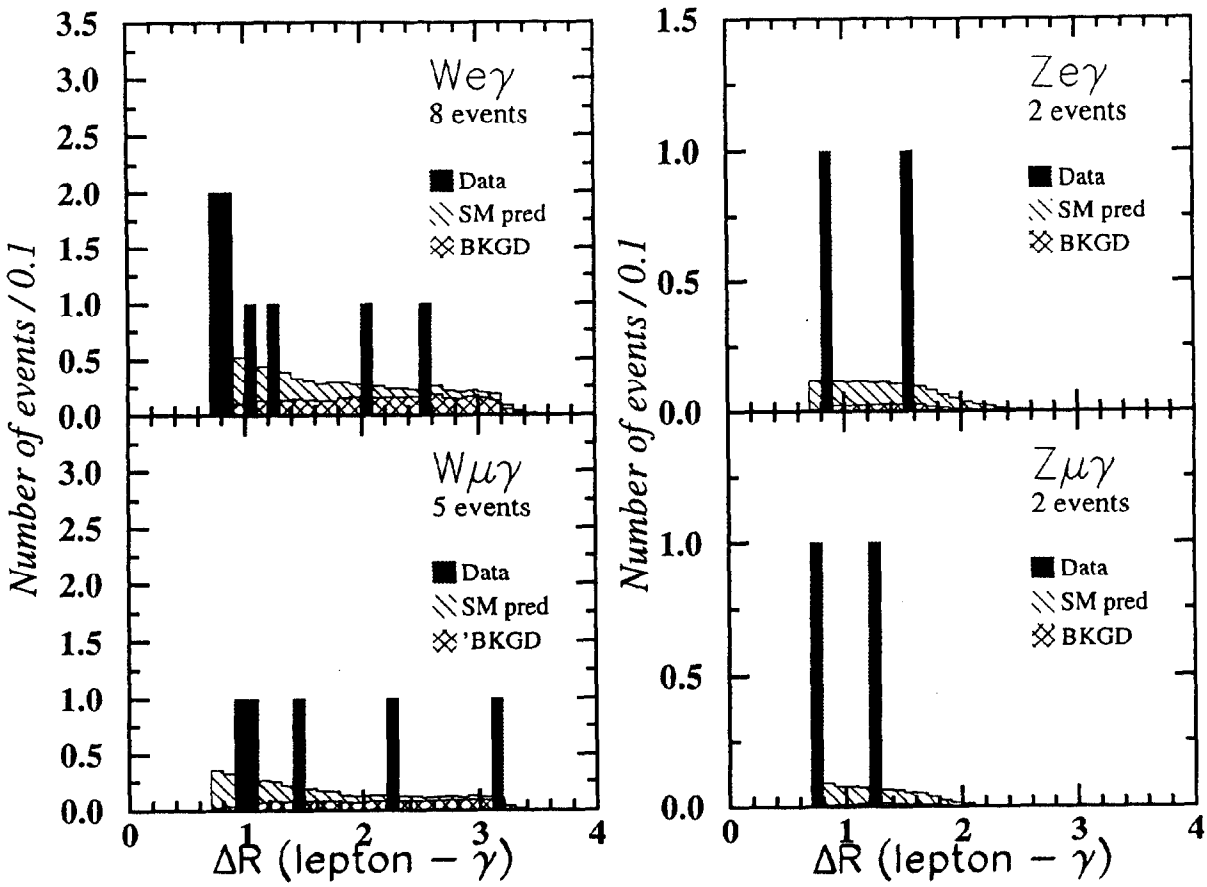

Figure 8: The lepton-photon angular separation ($\Delta R_{\ell\gamma}$) distributions for each of the four data samples. In each of these figures, for each data sample, the shaded histograms are the event data; the diagonally-hatched histograms are the Standard Model (SM) Monte Carlo predictions for the signal and the cross-hatched histograms are the background predictions. The prediction for the SM signal has been added to the background prediction for each channel.

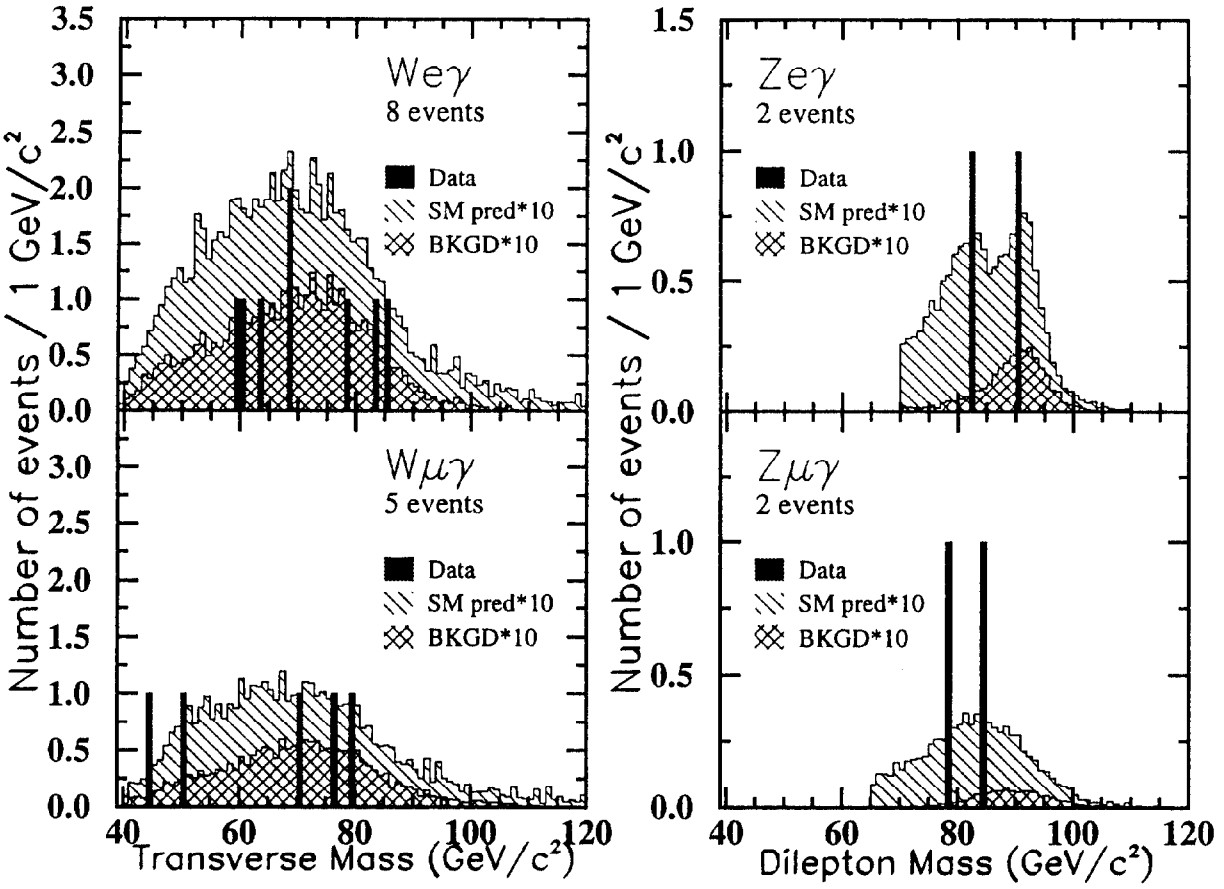

Figure 9: The W boson transverse mass (M_T^W) distributions and Z boson invariant mass ($M_{\ell^+\ell^-}$) distributions for the electron/muon $W\gamma$ and $Z\gamma$ data samples. The two-component structure in the electron channel $Z+\gamma$ prediction is due to radiative Z decay and $Z+\gamma$ contributions. For the muon channel, the momentum resolution obscures this effect. In each of these figures, for each data sample, the shaded histograms are the event data; the diagonally-hatched histograms are the Standard Model (SM) Monte Carlo predictions for the signal and the cross-hatched histograms are the background predictions. The prediction for the SM signal has been added to the background prediction for each channel.

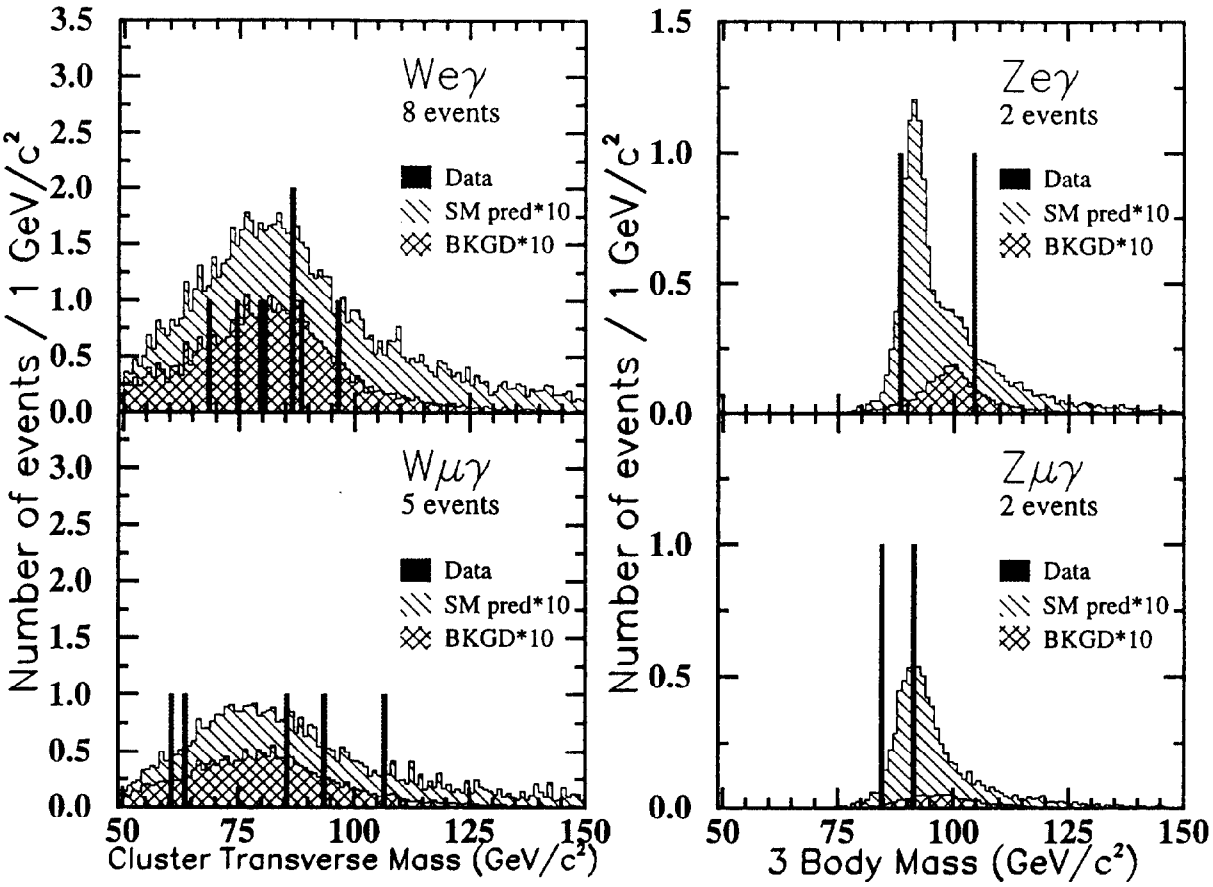

Figure 10: The $W\gamma$ cluster transverse mass (M_{CT}^{W}) distributions and $Z\gamma$ invariant mass ($M_{\ell^+\ell^-\gamma}$) distributions for the electron/muon $W\gamma$ and $Z\gamma$ data samples. In each of these figures, for each data sample, the shaded histograms are the event data; the diagonally-hatched histograms are the Standard Model (SM) Monte Carlo predictions for the signal and the cross-hatched histograms are the background predictions. The prediction for the SM signal has been added to the background prediction for each channel.

5 DETERMINATION OF $\sigma \cdot B(W+\gamma)$ AND $\sigma \cdot B(Z+\gamma)$ IN THE ELECTRON AND MUON CHANNELS

5.1 General Methodology

We compare our results with theoretical expectations using experimental and predicted cross sections $\times$ branching ratios. The $W+\gamma$ and $Z+\gamma$ cross sections $\times$ branching ratios are generically given by:

$$\sigma \cdot B(V_\ell+\gamma) \;=\; \frac{\mathcal{N}_{sig}(V_\ell+\gamma)}{\int \mathcal{L}_\ell dt \cdot \left(A^\ell_{V\gamma} \cdot \epsilon^\ell_{V\gamma}\right)} \;=\; \frac{\mathcal{N}_{obs}(V_\ell+\gamma) - \Sigma\mathcal{N}_{bkg}(V_\ell+\gamma)}{\int \mathcal{L}_\ell dt \cdot \left(A^\ell_{V\gamma} \cdot \epsilon^\ell_{V\gamma}\right)} \tag{26}$$

This comparison can also be made using the experimental *vs.* predicted number of signal events, since

$$\mathcal{N}_{sig}(V_\ell+\gamma) \;=\; \mathcal{N}_{obs}(V_\ell+\gamma) - \Sigma\mathcal{N}_{bkg}(V_\ell+\gamma) \;=\; \sigma \cdot B(V_\ell+\gamma) \cdot \int \mathcal{L}_\ell dt \cdot \left(A^\ell_{V\gamma} \cdot \epsilon^\ell_{V\gamma}\right) \tag{27}$$

where $V = W$ or Z; $\mathcal{N}_{sig}(V_\ell+\gamma) = \mathcal{N}_{obs}(V_\ell+\gamma) - \Sigma\mathcal{N}_{bkg}(V_\ell+\gamma)$ is the number of signal $W\gamma$ or $Z\gamma$ events in a particular leptonic decay channel ($\ell = e$ or μ) and $\mathcal{N}_{obs}(V_\ell+\gamma)$ is the number of observed $W\gamma$ or $Z\gamma$ events in a particular decay channel. The quantity $\Sigma\mathcal{N}_{bkg}(V_\ell+\gamma)$ is the sum of the number of background events expected in each of the data samples originating from various processes capable of mimicking the signal, as defined by our event selection criteria. The integrated luminosity factor is $\int \mathcal{L}_\ell dt$. The product term $\left(A^\ell_{V\gamma} \cdot \epsilon^\ell_{V\gamma}\right)$ is the overall acceptance $\times$ efficiency factor for selecting $W\gamma$ and $Z\gamma$ events, and is a product of a number of acceptances $\times$ efficiency factors. The explicit forms of the product term $\left(A^\ell_{V\gamma} \cdot \epsilon^\ell_{V\gamma}\right)$ for each of the electron/muon $W\gamma/Z\gamma$ decay channels are discussed in detail in Appendix B. These expressions are similar to those used for earlier determinations of the inclusive W/Z cross section $\times$ branching ratio measurements and the W/Z cross section ratio measurements [6, 7], with appropriate modifications to account for the presence of the additional photon in $W\gamma/Z\gamma$ events.

The kinematic and geometrical acceptances for electron and muon $W\gamma$ and $Z\gamma$ events were obtained from detailed Monte Carlo simulations of these processes. The electron, muon and photon efficiencies were determined from $\bar{p}$-p, test-beam and cosmic-ray data samples, and were also cross-checked with Monte Carlo simulations. The numerical values for each of these individual acceptance and efficiency terms for SM electron/muon $W\gamma/Z\gamma$ decay channels are summarized in Tables given in Appendix B. The numerical values associated with the overall acceptance $\times$ efficiency product terms for each of the SM electron/muon $W\gamma/Z\gamma$ decay channels are summarized in Table 6. In general, the W (Z) acceptance in $W\gamma$ ($Z\gamma$) events tends to be less than that associated with inclusive W (Z) production, due to the fact that in radiative W (Z) decays, the emission of a hard photon in the final-state bremsstrahlung process results in a reduction of the W (Z) decay lepton P_T acceptances, respectively.

The Baur $W\gamma$ and $Z\gamma$ Monte Carlo event generators [11, 17] simulate Born-level production and decay kinematics for each of the electron/muon $W\gamma$ and $Z\gamma$ decay channels. These programs generate weighted events using the helicity-amplitude formalism, coherently adding together the contributions of the Feynman graphs of Figs. 1 and 2, respectively. The kinematic phase space is done using the VEGAS adaptive multi-dimensional integration code [38]. The $W\gamma$ and $Z\gamma$ MC

Table 6: Overall Acceptances × Efficiency Factors for Electron and Muon $W\gamma/Z\gamma$.

Acceptance × Efficiency Factor	Electron	Muon
$A^{\ell}_{W\gamma} \cdot \epsilon^{\ell}_{W\gamma}$	$5.0 \pm 0.2\%$	$3.0 \pm 0.2\%$
$A^{\ell}_{Z\gamma} \cdot \epsilon^{\ell}_{Z\gamma}$	$6.0 \pm 0.3\%$	$3.4 \pm 0.2\%$

programs were modified to use the CERN PDFLIB structure functions [39], and include all parton-parton luminosities and (for $W\gamma$) Cabibbo-Kobayashi-Maskawa quark-mixing matrix elements [40]. We also incorporated tau-lepton decays and P_T-boosting of the $V+\gamma$ ($V = W, Z$) system, according to the measured W, Z P_T-distributions into these event generator programs (discussed below in Section 5.8.1). The results presented in this analysis use HMRS-B structure functions [41], which were the "nominal" structure functions used in the determination of the CDF electron and muon W and Z cross sections [6] and W/Z cross section ratios [7]. The cross section output from the $W\gamma/Z\gamma$ MC event generators, $\sigma \cdot B(W/Z+\gamma)_{gen}$ includes a "$K-$factor" of $\left[1+\frac{8\pi}{9}\alpha_s(M_V^2)\right] \simeq 1.35$, to approximate higher-order QCD processes such as $q+\bar{q} \rightarrow g+V+\gamma$ and $q+g \rightarrow q+V+\gamma$ [42]. We have compared, where possible, the Standard Model results associated with the $W\gamma$ and $Z\gamma$ Monte Carlo event generators with several other $W\gamma$ and $Z\gamma$ Monte Carlo event generators which do not simulate final-state bremsstrahlung, such as VVJET [42], ISAJET [43], PAPAGENO [44], PYTHIA [45] and with the CDF radiative W and Z decay Monte Carlo event generator, WZRAD [46]. The cross section results are in good agreement between the various MC event generators, for various regimes of comparison. We have also studied the systematic uncertainties associated with the $W\gamma$ and $Z\gamma$ MC results, varying the shape of the $P_T(V_\ell+\gamma)$ distribution, using several different structure function (SF) choices and studying the Q^2-scale dependence of the calculation (discussed in detail in Sections 5.8.1 - 5.8.5 below).

For a specific choice of anomalous parameters, large samples ($> 500K$) of $W\gamma$ and $Z\gamma$ Monte Carlo events were generated with loose kinematic and geometrical cuts for leptons and photons. A minimum photon transverse energy requirement of $E_T^{\gamma} > 1.0$ GeV and a minimum lepton-photon angular separation requirement of $\Delta R_{\ell\gamma} > 0.3$ were made. Loose kinematic cuts were deliberately chosen well below cut thresholds at the event generation stage in order to avoid potential acceptance biases due to finite detector resolution and geometrical acceptance effects.

The four-vector information associated with the final-state particles generated in each $W\gamma/Z\gamma$ Monte Carlo event was then input to a "fast" Monte Carlo simulation of the CDF detector, which simulated the details of the response of the CDF detector to electrons, muons, photons and $\not\!\!E_T$ via parametrization methods. The purposes of the "fast" $W\gamma/Z\gamma$ Monte Carlo detector simulation programs were to (a) determine all kinematic and geometric acceptance factors, (b) obtain predicted cross sections $\sigma \cdot B(V_\ell+\gamma)_{cuts}$ for events passing all of the $W\gamma/Z\gamma$ event selection cuts, and (c) obtain predictions for the number of electron and muon $W\gamma/Z\gamma$ events, including all relevant electron, muon and photon efficiencies. Typically $\sim 50K$ Monte Carlo events passed all event selection cuts after "fast" Monte Carlo detector simulation. The methodology for obtaining the Monte Carlo predicted $\mathcal{N}_{sig}(V_\ell+\gamma)$ and $\sigma \cdot B(V_\ell+\gamma)_{cuts}$ from $\sigma \cdot B(V_\ell+\gamma)_{gen}$ for $V = W$, Z and $\ell = e$, μ is discussed in detail in Appendix C.

The results of the "fast" Monte Carlo detector simulation were cross-checked with more detailed

Monte Carlo simulations which included the QCD evolution and fragmentation of the underlying event using the ISAJET [43] Monte Carlo event generator and another, independent and detailed CDF detector simulation Monte Carlo program known as QFL.

5.1.1 W/Z Electron and Muon Efficiency Determination

Since we use *precisely* the same event selection cuts for the inclusive W and Z data samples as those used in the determination of the inclusive electron and muon W and Z $\sigma \cdot B$ cross sections [6] and the W/Z cross section ratios [7], the electron and muon efficiencies as determined in these analyses are applicable to the present electron and muon $W\gamma$ and $Z\gamma$ analyses. The individual electron and muon efficiencies for the $W\gamma$ and $Z\gamma$ data samples are discussed further in Appendix B and summarized in Tables 30 and 31, as are the overall electron and muon efficiencies for the $W\gamma$ and $Z\gamma$ data samples as summarized in Tables 32 and 33.

5.1.2 Photon Efficiency Determination

The overall efficiency for central photons, ϵ^{γ}_{cem}, was obtained from the determination of the individual efficiencies associated with each of the above-described CEM photon cuts [8]:

$$\epsilon^{\gamma}_{cem} = \epsilon^{\gamma}_{ET4} \cdot \epsilon^{\gamma}_{\Sigma PT4} \cdot \epsilon^{\gamma}_{N3D} \cdot \epsilon^{\gamma}_{Had/EM} \cdot \epsilon^{\gamma}_{Lshr} \cdot \epsilon^{\gamma}_{\chi^2_{stp}+\chi^2_{wir}} \cdot \epsilon^{\gamma}_{no\ 2^{nd}\ CES} \cdot \mathcal{P}^{\gamma}_{\overline{conv}} \cdot \mathcal{S}^{cem}_{e\to\gamma} \qquad (28)$$

The efficiencies of the calorimeter isolation $ET4 < 2.0$ GeV cut, the tracking isolation $\Sigma PT4 < 2.0$ GeV cut and the $N3D = 0$ cut were determined by examining the efficiency for applying these cuts in randomly-oriented cones of size $\Delta R = 0.4$ in the inclusive electron and muon W/Z data samples, where the cone axis was required to be more than $\Delta R > 0.7$ from the W/Z decay lepton(s) and to be within good fiducial regions of the central calorimeter, $|\eta| < 1.1$.

The photon efficiencies related to energy sharing and CES shower profile cuts were determined from $5 - 50$ GeV CEM electron test-beam data. Cross-checks on the determination of individual CEM photon efficiencies were obtained from Baur/ISAJET/QFL $W\gamma$ and $Z\gamma$ MC simulations and QFL photon *vs.* electron MC simulations. The efficiencies associated with these studies are summarized in Tables $7 - 8$. The photon efficiencies obtained from random cone studies in the electron and muon inclusive W/Z data samples are in good agreement with one another. The $ET4$, $(ET4 \cdot \Sigma PT4)$ and $(ET4 \cdot \Sigma PT4 \cdot N3D)$ photon efficiencies as determined from Baur/ISAJET/QFL $W\gamma$ and $Z\gamma$ Monte Carlo simulations are systematically slightly higher than those determined from random cone studies using the inclusive W/Z data samples, due to the fact that the underlying event in the ISAJET MC simulation carries slightly less transverse energy and total charged track P_T than that associated with the inclusive W/Z data samples.

We also carried out random cone studies using minimum bias event data and an inclusive jet data sample (see Section 5.3 below) in order to bracket the *extrema* of the systematic uncertainties associated with the efficiencies for the calorimeter isolation $ET4 < 2.0$ GeV cut, the tracking isolation $\Sigma PT4 < 2.0$ GeV cut and the $N3D = 0$ cut. The transverse energy flow in minimum bias events is on average slightly less than that for inclusive W/Z events, resulting in somewhat higher values for these efficiencies. Two random cone studies were done using the inclusive jet data sample. The first study (Jet-20a) required random cones to be more than $\Delta R > 1.1$ away from *all* central jets in the event. The second study (Jet-20b) required random cones to be more than $\Delta R > 1.1$ from the two leading (highest E_T) jets in the central region of the event. In this latter

study, random cones were therefore allowed to overlap the non-leading (lower E_T) jets in the central region of the detector, resulting in somewhat lower efficiencies for these three cuts. The last three rows of Table 7 summarize these results.

The efficiencies for the Had/EM, L_{shr}, $\chi^2_{stp} + \chi^2_{wir}$ and the no 2^{nd} CES cuts as determined from 5 – 50 GeV electron test beam data are in good agreement with efficiency results obtained from Baur/ISAJET/QFL $W\gamma$ and $Z\gamma$ Monte Carlo simulations, and with QFL single electron and single photon MC simulations.

Table 9 summarizes the individual CEM photon efficiencies, the photon survival probability factor, the correction factor for photon *vs.* electron EM shower development, and the overall CEM photon efficiency (the product of all individual efficiency factors) for the common photon selection cuts associated with the electron and muon $W\gamma$ and $Z\gamma$ data samples. The statistical and systematic uncertainties associated with each quantity are also given in this table. The $ET4$, $\Sigma PT4$ and $N3D$ photon efficiencies for the common photon selection were obtained from weighted averages of the four individual e/μ $W + \gamma$ and $Z + \gamma$ random cone results summarized in Table 7. The photon efficiencies for the Had/EM, L_{shr}, $\chi^2_{stp} + \chi^2_{wir}$ and the no 2^{nd} CES cluster cuts for the common photon selection were obtained from weighted averages of the electron test beam results summarized in Table 8.

From CEM energy scale studies associated with the CDF measurement of the W and Z boson masses [47, 48], the photon survival probability factor $\mathcal{P}^{\gamma}_{\overline{conv}}$ is known from the average amount of material associated with the inner central detector, $< \Delta T >= 4.6 \pm 0.3\%$ of a radiation length, χ^e_o (corresponding to $3.6 \pm 0.2\%$ of a conversion length, χ^{γ}_o). The Baur/ISAJET/QFL $W\gamma$ and $Z\gamma$ Monte Carlo simulations provide a cross-check on $\mathcal{P}^{\gamma}_{\overline{conv}}$ by determining the fraction of $W\gamma/Z\gamma$ MC events where the photon, had it not converted to an e^+e^- pair, would have passed all photon cuts. The rate of pair conversions determined from Baur/ISAJET/QFL $W\gamma/Z\gamma$ MC events was $4.5 \pm 1.2\%$, in good agreement with the calculation. The difference between the two methods is used to define the systematic uncertainty associated with $\mathcal{P}^{\gamma}_{\overline{conv}}$. Another cross-check on $\mathcal{P}^{\gamma}_{\overline{conv}}$ was to explicitly search for isolated $\gamma \rightarrow e^+e^-$ conversion pairs with $|\eta_{\gamma \rightarrow e^+e^-}| < 1.1$ in each of the four data samples. From the observed numbers of events in each of our four data samples, no candidate $W + (\gamma \rightarrow e^+e^-)$ or $Z + (\gamma \rightarrow e^+e^-)$ are expected, and none were found.

The photon *vs.* electron shower development correction factor $\mathcal{S}^{cem}_{e \rightarrow \gamma}$ was determined by comparing QFL photon *vs.* electron MC simulations, and is defined as the ratio of QFL photon to electron efficiency product factors given in the last two rows of Table 8.

The overall fiducial CEM photon *selection* efficiency is

$$\epsilon^{\gamma}_{cem\ sel} = 84.7 \pm 1.4\ (stat) \pm 1.8\ (syst)\%$$

The overall fiducial CEM photon efficiency, including the photon survival probability, $\mathcal{P}^{\gamma}_{\overline{conv}}$ and $e \rightarrow \gamma$ EM shower development correction factor, $\mathcal{S}^{cem}_{e \rightarrow \gamma}$ is

$$\epsilon^{\gamma}_{cem} = 82.0 \pm 1.5\ (stat) \pm 2.1\ (syst)\%$$

Table 7: CEM Photon Efficiency Determination – Isolation Variables. The statistical uncertainty associated with each quantity is given.

Data Sample	ϵ^{γ}_{ET4}	$\epsilon^{\gamma}_{ET4} \cdot \epsilon^{\gamma}_{\Sigma PT4}$	$\epsilon^{\gamma}_{ET4} \cdot \epsilon^{\gamma}_{\Sigma PT4} \cdot \epsilon^{\gamma}_{N3D}$
W_e Random Cones	$95.5 \pm 0.5\%$	$93.4 \pm 0.6\%$	$89.2 \pm 0.7\%$
W_μ Random Cones	$95.9 \pm 0.4\%$	$93.1 \pm 0.6\%$	$88.6 \pm 0.7\%$
Z_e Random Cones	$95.8 \pm 0.6\%$	$93.6 \pm 0.7\%$	$89.1 \pm 0.9\%$
Z_μ Random Cones	$94.5 \pm 1.2\%$	$91.1 \pm 1.4\%$	$87.3 \pm 1.6\%$
QFL e $W\gamma$ MC	$98.9 \pm 0.6\%$	$96.4 \pm 1.0\%$	$90.2 \pm 1.5\%$
QFL μ $W\gamma$ MC	$99.3 \pm 0.7\%$	$96.6 \pm 1.2\%$	$93.3 \pm 1.6\%$
QFL e $Z\gamma$ MC	$97.9 \pm 1.2\%$	$97.0 \pm 1.3\%$	$91.9 \pm 2.0\%$
QFL μ $Z\gamma$ MC	$98.3 \pm 0.7\%$	$94.8 \pm 1.1\%$	$91.9 \pm 1.4\%$
MinBias Random Cones	$98.6 \pm 0.2\%$	$97.7 \pm 0.2\%$	$92.8 \pm 0.2\%$
Jet-20a Random Cones	$99.1 \pm 0.1\%$	$97.6 \pm 0.1\%$	$92.7 \pm 0.2\%$
Jet-20b Random Cones	$92.7 \pm 0.2\%$	$89.3 \pm 0.3\%$	$84.2 \pm 0.3\%$

Table 8: CEM Photon Efficiency Determination – *EM* Shower Variables. The statistical uncertainty associated with each quantity is given.

Data Sample	$\epsilon^{\gamma}_{Had/EM}$	ϵ^{γ}_{Lshr}	$\epsilon^{\gamma}_{\chi^2_{strp}+\chi^2_{wir}}$	$\epsilon^{\gamma}_{no\ 2^{nd}\ CES}$
5 GeV e Test Beam	$98.9 \pm 0.2\%$	$99.9 \pm 0.1\%$	$97.3 \pm 0.3\%$	$98.0 \pm 0.1\%$
10 GeV e Test Beam	$99.6 \pm 0.1\%$	$98.8 \pm 0.4\%$	$96.2 \pm 0.4\%$	$97.9 \pm 0.1\%$
18 GeV e Test Beam	$99.1 \pm 0.9\%$	$100.0\ ^{+0.0}_{-1.7}\%$	$98.2 \pm 1.8\%$	$98.2 \pm 1.6\%$
30 GeV e Test Beam	$98.9 \pm 0.9\%$	$100.0\ ^{+0.0}_{-1.1}\%$	$99.2 \pm 0.7\%$	$98.2 \pm 1.0\%$
50 GeV e Test Beam	$98.0 \pm 0.3\%$	$99.9 \pm 0.1\%$	$99.2 \pm 0.2\%$	$97.6 \pm 0.2\%$
QFL e $W\gamma$ MC	$99.3 \pm 0.6\%$	$99.7 \pm 0.3\%$	$98.4 \pm 0.5\%$	$94.6 \pm 1.2\%$
QFL μ $W\gamma$ MC	$99.7 \pm 0.3\%$	$100.0\ ^{+0.0}_{-0.4}\%$	$97.5 \pm 1.1\%$	$95.0 \pm 1.6\%$
QFL e $Z\gamma$ MC	$99.2 \pm 0.8\%$	$100.0\ ^{+0.0}_{-0.5}\%$	$95.4 \pm 1.6\%$	$95.0 \pm 2.4\%$
QFL μ $Z\gamma$ MC	$99.4 \pm 0.5\%$	$100.0\ ^{+0.0}_{-0.2}\%$	$97.7 \pm 0.8\%$	$95.2 \pm 1.2\%$
QFL γ MC $5-15$ GeV	$99.7 \pm 0.1\%$	$99.8 \pm 0.1\%$	$97.4 \pm 0.3\%$	$96.8 \pm 0.3\%$
QFL e MC $5-15$ GeV	$99.9 \pm 0.1\%$	$99.9 \pm 0.1\%$	$97.9 \pm 0.2\%$	$95.8 \pm 0.3\%$

Table 9: Overall CEM Photon Efficiency Determination. The statistical and sytematic uncertainties associated with each quantity are given.

ϵ^{γ}_{ET4}	$95.7 \pm 0.3 \pm 0.5\%$	Calorimeter Isolation
$\epsilon^{\gamma}_{\Sigma PT4}$	$97.4 \pm .0.4 \pm 0.8\%$	Tracking Isolation
ϵ^{γ}_{N3D}	$95.3 \pm 0.5 \pm 0.7\%$	No track @ EM Cluster
$\epsilon^{\gamma}_{Had/EM}$	$99.2 \pm 0.1 \pm 0.8\%$	Had/EM Cut
ϵ^{γ}_{Lshr}	$99.9 \pm 0.1 \pm 0.3\%$	Lateral Shower Cut
$\epsilon^{\gamma}_{\chi^2_{stp}+\chi^2_{wir}}$	$98.4 \pm 0.1 \pm 0.9\%$	CES strip/wire χ^2 Cut
$\epsilon^{\gamma}_{no\ 2^{nd}\ CES}$	$97.9 \pm 0.7 \pm 1.0\%$	No 2^{nd} CES Clusters
$\mathcal{P}^{\gamma}_{conv}$	$96.5 \pm 0.2 \pm 1.0\%$	Photon Survival
$\mathcal{S}^{cem}_{e\to\gamma}$	$100.3 \pm 0.6 \pm 1.0\%$	e *vs.* γ Shower Development
ϵ^{γ}_{cem}	$82.0 \pm 1.5 \pm 2.1\%$	Overall Photon Efficiency

5.2 Theory Predictions for Electron and Muon $W\gamma$ and $Z\gamma$ Signal

The Standard Model predictions for the expected number of electron and muon $W/Z+\gamma$ events are summarized in Table 10 for integrated luminosities of $\int \mathcal{L}_e dt = 4.05 \pm 0.28$ pb^{-1} for electrons and $\int \mathcal{L}_\mu dt = 3.54 \pm 0.24$ pb^{-1} for muons, using the Baur $W\gamma/Z\gamma$ + "fast" MC simulation programs and also the Baur/ISAJET/QFL $W\gamma/Z\gamma$ MC simulation programs. There is good agreement between the two basic MC simulation methods. For the $Z\gamma$ cases, we also explicitly show the Baur + fast MC prediction for Drell-Yan (DY) + $Z\gamma$. The Drell-Yan contribution can be seen to be quite small. We explicitly correct for it via the f^{ℓ}_{DY} factors, as shown in equations 76 and 77 and as summarized in Tables 30 and 31 of Appendix B.

Table 10: Predicted number of Standard Model signal events for electron and muon $W\gamma$ & $Z\gamma$. The statistical uncertainty associated with each quantity is given.

	Electron	Muon
Baur Fast $W\gamma$ MC	4.56 ± 0.38	2.40 ± 0.22
Baur QFL $W\gamma$ MC	4.38 ± 0.57	2.41 ± 0.32
Baur Fast $Z\gamma$ MC	1.35 ± 0.11	0.66 ± 0.06
Baur Fast $Z + DY\gamma$ MC	1.40 ± 0.11	0.69 ± 0.06
Baur QFL $Z\gamma$ MC	1.37 ± 0.18	0.68 ± 0.11

5.3 Determination of QCD Jet Background in the $W\gamma$ and $Z\gamma$ Data Samples

The largest photon background in the $W\gamma$ and $Z\gamma$ signal samples is due to QCD processes, where a central jet in inclusive W/Z+Jet events fragments in such a way as to mimic a photon, as defined by our photon cuts. Initial/final-state radiation is considered part of the $W\gamma/Z\gamma$ signal,

since the Feynman diagrams for initial state radiation, as shown in Figs. 1 and 2 are included in the theory calculation for the $W\gamma/Z\gamma$ signal; the "$K-$factor" of 1.35 included in the $W\gamma/Z\gamma$ MC event generators approximates the contributions from final-state radiation diagrams associated with higher-order QCD processes such as $q + g \rightarrow q + W/Z + \gamma$.

The primary method for the determination of the level of QCD jet background in each of the $W\gamma$ and $Z\gamma$ data samples used an independent, non-signal control data sample to determine the QCD jet misidentification probability, $\mathcal{P}_{Jet\rightarrow\text{"}\gamma\text{"}}^{Control\ Sample}(E_T)$ as a function of jet E_T for central jets to fragment in such a way as to mimic a photon. We then convoluted this probability distribution with the E_T-distribution of central jets associated with each of the inclusive electron/muon W and Z data samples. This method of determining the amount of QCD jet background tacitly assumes that the QCD jet misidentification probability distributions are the same in both the non-signal control data sample and the $\ell = e$ or μ inclusive W/Z data samples over the photon E_T range of interest, *i.e.* that

$$\mathcal{P}_{Jet\rightarrow\text{"}\gamma\text{"}}^{Control\ Sample}(E_T) \;=\; \mathcal{P}_{Jet\rightarrow\text{"}\gamma\text{"}}^{W_\ell/Z_\ell}(E_T) \tag{29}$$

Detailed tests of this relation are discussed in Appendix D which explicitly demonstrate the validity of this relation, well within statistical uncertainties.

Note that by using the *inclusive* electron and muon $W/Z+$Jets data samples, the *inclusive* QCD jet background for each of the four channels will automatically be taken into account. For example, the inclusive electron/muon $W+$ QCD jet background for the electron/muon $W\gamma$ data samples consists of a contribution from (a) "direct" electron/muon $W+$Jet background, with *additional* QCD jet background contributions from (b) misidentified electron/muon $Z+$Jet events, where one of the Z decay leptons is not detected, but satisifies the $W\gamma$ event selection criteria and (c) from $(W \rightarrow \tau\ \bar{\nu}_\tau)+$Jet events, where $\tau \rightarrow \ell\ \bar{\nu}_\ell\ \nu_\tau$ and $\ell = e/\mu$, again satisfying the $W\gamma$ event selection criteria.

The QCD jet misidentification probability distribution was obtained using a 4.2 pb^{-1} sample of inclusive jet data (primarily di-jets) taken concurrently with the inclusive W/Z data during the run. The trigger requirement for this particular jet data sample (known as the Jet-20 data sample) was a localized cluster of energy deposited in the calorimeter with transverse energy $E_T > 20.0$ GeV, prescaled to accept 1 out of every 300 events [49]. The jet clustering cone size used in this data sample was $\Delta R_{clust}^{Jet} = \sqrt{\Delta\eta^2 + \Delta\phi^2} = 0.7$. In the off-line analysis of this jet data sample, jet energy corrections were applied to the data to correct for non-linear calorimeter response effects, calorimeter energy scale corrections, energy corrections to account for losses in un-instrumented regions of the calorimeter, *etc.*

The QCD jet misidentification probability in the low$-E_T$ region, $E_T > 5.0$ GeV was determined from use of fiducial CEM clusters and non-leading central jets. Due to trigger bias associated with the calorimeter energy response at trigger threshold, it was not possible to use the leading, highest-E_T jets associated with events in the Jet-20 data sample for these purposes.

Events in the Jet-20 data sample with non-leading jets were selected by requiring the two leading jets, one in the central calorimeter ($|\eta_{J1}| < 1.1$), the other in the central or plug calorimeter ($|\eta_{J2}| < 2.4$), to have (corrected) $E_T^J > 15$ GeV and $M_{JJ} > 40$ GeV. The physics motivation for this choice of leading jet selection was to obtain a sample of events which had approximately the same $\sqrt{\hat{s}}$ as that for the inclusive electron and muon W/Z data samples. The non-leading central jets ($|\eta_J| < 1.1$) in these events were required to be above a (corrected) $E_T^J > 5.0$ GeV and more than $\Delta R > 1.4$ away from either of the two leading jets. A total of 11726 non-leading central jets passed these cuts.

Jet-20 events with fiducial CEM clusters were required to pass the same leading jet event selection requirements as for events with non-leading central jets. A total of 431 central EM clusters with $E_T > 5.0$ GeV and $\Delta R > 1.4$ away from either of the two leading jets were obtained from the Jet-20 data sample. Of these, a total of 266 were *fiducial* CEM clusters; a total of 64 events passed the $ET4 < 2.0$ GeV and $\Sigma PT4 < 2.0$ GeV requirements. A total of 20 Jet-20 events passed the entirety of the photon cuts used for selecting the electron/muon $W\gamma/Z\gamma$ data samples. The progression of Jet-20 CEM clusters surviving the application of successive photon cuts is summarized in the last column of Table 1.

The angular separation requirement of $\Delta R > 1.4$ was imposed for both non-leading central jets and fiducial CEM clusters with respect to leading jets due to the fact that jets with angular separation less than this amount will overlap with each other, biasing the number of non-leading jets because of the $R^{Jet}_{clust} = 0.7$ cone size used for jet clustering. This same angular separation requirement was therefore applied to the selection of fiducial CEM clusters in the Jet-20 data sample. A variation of the angular separation requirement $\Delta R > 1.4$ by $\delta(\Delta R) = \pm 0.4$ had $< 10\%$ impact on the overall determination of the level of QCD jet background in each of the four data samples.

Using the fiducial CEM clusters and non-leading central jets selected from the Jet-20 data sample as described above, the QCD jet misidentification probability for a given E_T-bin is defined as the ratio of the number of fiducial CEM clusters passing all $W\gamma/Z\gamma$ photon cuts to the number of non-leading central jets. For the i^{th} E_T-bin, this ratio is:

$$\mathcal{P}^{J20}_{i\ Jet\rightarrow"\gamma"} = \left[\frac{\Delta\mathcal{N}^{Fid\ CEM\ J20}_i}{\Delta\mathcal{N}^{Extra\ Jet\ J20}_i}\right] \tag{30}$$

The determination of the inclusive QCD jet background in each of the four inclusive $V_\ell = W_\ell/Z_\ell$ data samples, for $E^J_T > 5.0$ GeV was obtained by using equations (29) and (30). Since

$$\mathcal{P}^{V_\ell}_{Jet\rightarrow"\gamma"}(E_T) = \left[\frac{\Delta\mathcal{N}^{Fid\ CEM\ V_\ell}_{i\ \gamma\ Bkgnd}}{\Delta\mathcal{N}^{Extra\ Jet\ V_\ell}_i}\right] \tag{31}$$

then

$$\begin{aligned}\mathcal{N}^{Fid\ CEM\ V_\ell}_{\gamma\ Bkgnd} &= \sum_i \Delta\mathcal{N}^{Fid\ CEM\ V_\ell}_{i\ \gamma\ Bkgnd} \\ &= \sum_i \Delta\mathcal{N}^{Extra\ Jet\ V_\ell}_i \cdot \left[\frac{\Delta\mathcal{N}^{Fid\ CEM\ J20}_i}{\Delta\mathcal{N}^{Extra\ Jet\ J20}_i}\right]\end{aligned} \tag{32}$$

The total number of central jets in the inclusive W/Z event samples with $E^J_T > 5$ GeV was 2041 (1099) for e (μ) $W-$data and 175 (69) for e (μ) $Z-$data, respectively.

Figure 11 summarizes the method as used for determining the inclusive QCD jet background for the electron $W\gamma$ sample. A comparison of central jet E_T spectra for each of the four data samples is shown in Fig. 12. There is excellent agreement between the shapes of the jet E_T spectra in the electron *vs.* muon W (and Z) data samples. The inclusive QCD jet background as a function of E_T for each of the four data samples are shown in Figs. 13a-13d. Note that the QCD jet background is sharply peaked at threshold in the E^γ_T distribution in each of the four data samples. The first column of Table 11 summarizes the inclusive QCD jet background for each of the four

inclusive W/Z data samples via this "standard" method. We have also investigated the systematic uncertainties associated with the QCD jet background determination due to binning effects and the use of uncorrected jet energies instead of corrected jet energies for the non-leading central jets in the Jet-20 and inclusive W/Z data samples. The second column of Table 11 summarizes the QCD jet backgrounds determined using only one E_T-bin ($E_T > 5.0$ GeV) and corrected jet energies; the third column of this table summarizes the QCD jet background determined using the "standard" method but with uncorrected jet energies; the fourth column of this table summarizes the QCD jet background determined by using only one E_T-bin and uncorrected jet energies. The level of agreement between the four methods used in determining the QCD jet background for each of the four $W\gamma/Z\gamma$ channels is well within statistical uncertainties. The first column of Table 11 is taken as the primary definition of the inclusive QCD jet background for each of the four data samples.

Table 11: Predicted number of inclusive QCD jet background events for electron and muon $W\gamma$ & $Z\gamma$. The statistical uncertainty associated with each quantity is given.

Channel	Standard Method Corrected Jets	Summed Method Corrected Jets	Standard Method Uncorrected Jets	Summed Method Uncorrected Jets
$e\ W\gamma$:	3.57 ± 0.81	3.48 ± 0.87	2.92 ± 0.67	3.42 ± 0.85
$\mu\ W\gamma$:	1.87 ± 0.42	1.87 ± 0.46	1.48 ± 0.34	1.86 ± 0.46
$e\ Z\gamma$:	0.30 ± 0.07	0.30 ± 0.07	0.28 ± 0.07	0.30 ± 0.07
$\mu\ Z\gamma$:	0.11 ± 0.03	0.12 ± 0.03	0.07 ± 0.02	0.12 ± 0.03

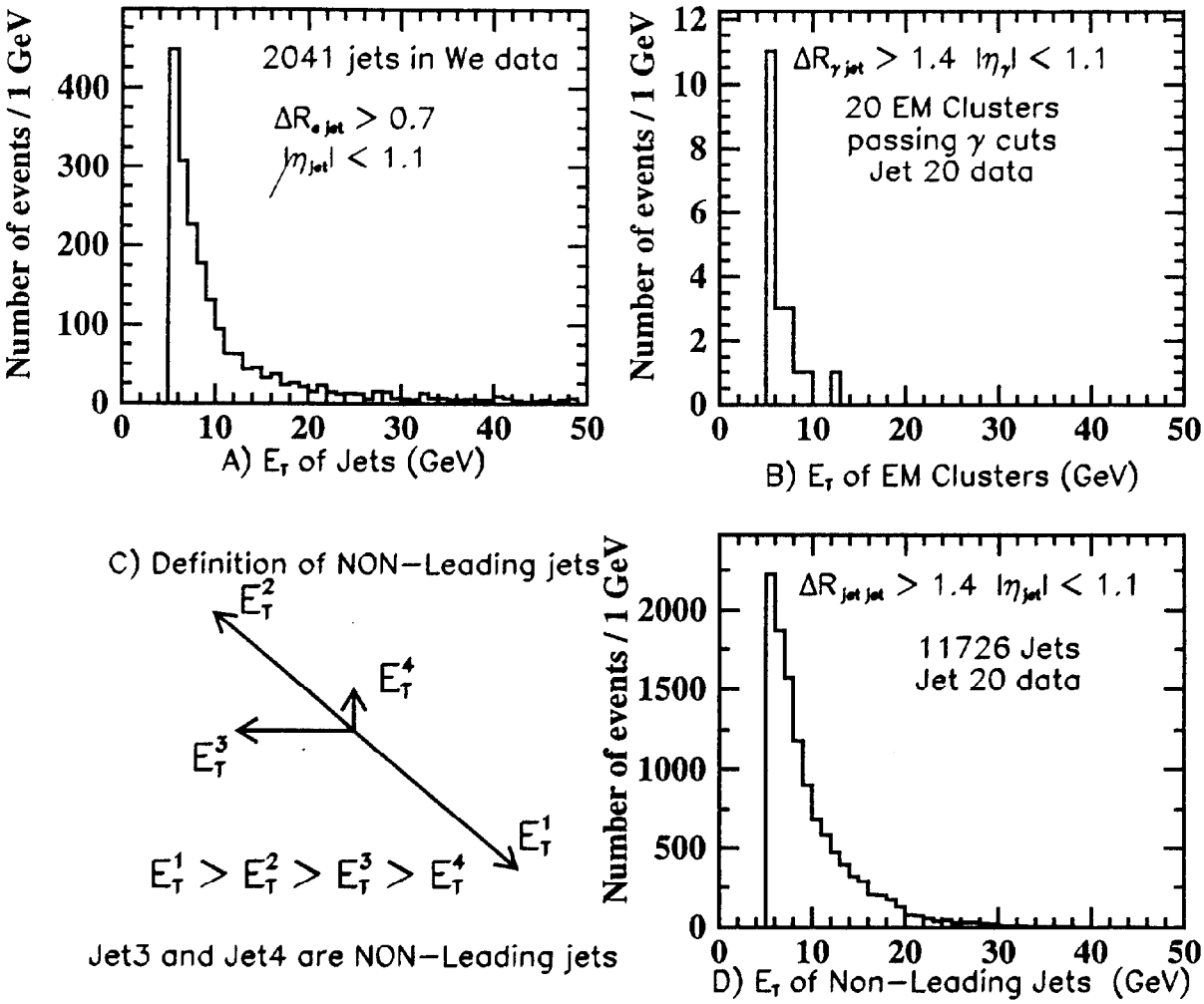

Figure 11: Inclusive QCD jet background determination for the electron $W\gamma$ data sample. (A) The transverse energy (E_T^J) distribution of jets in the inclusive electron W data sample. (B) The transverse energy (E_T^γ) distribution of central fiducial EM clusters passing all photon cuts in the Jet-20 inclusive jet data sample. (C) Schematic vector-representation of leading/non-leading jets in the Jet-20 inclusive jet data sample. (D) The transverse energy (E_T^J) distribution of non-leading jets in the Jet-20 inclusive jet data sample.

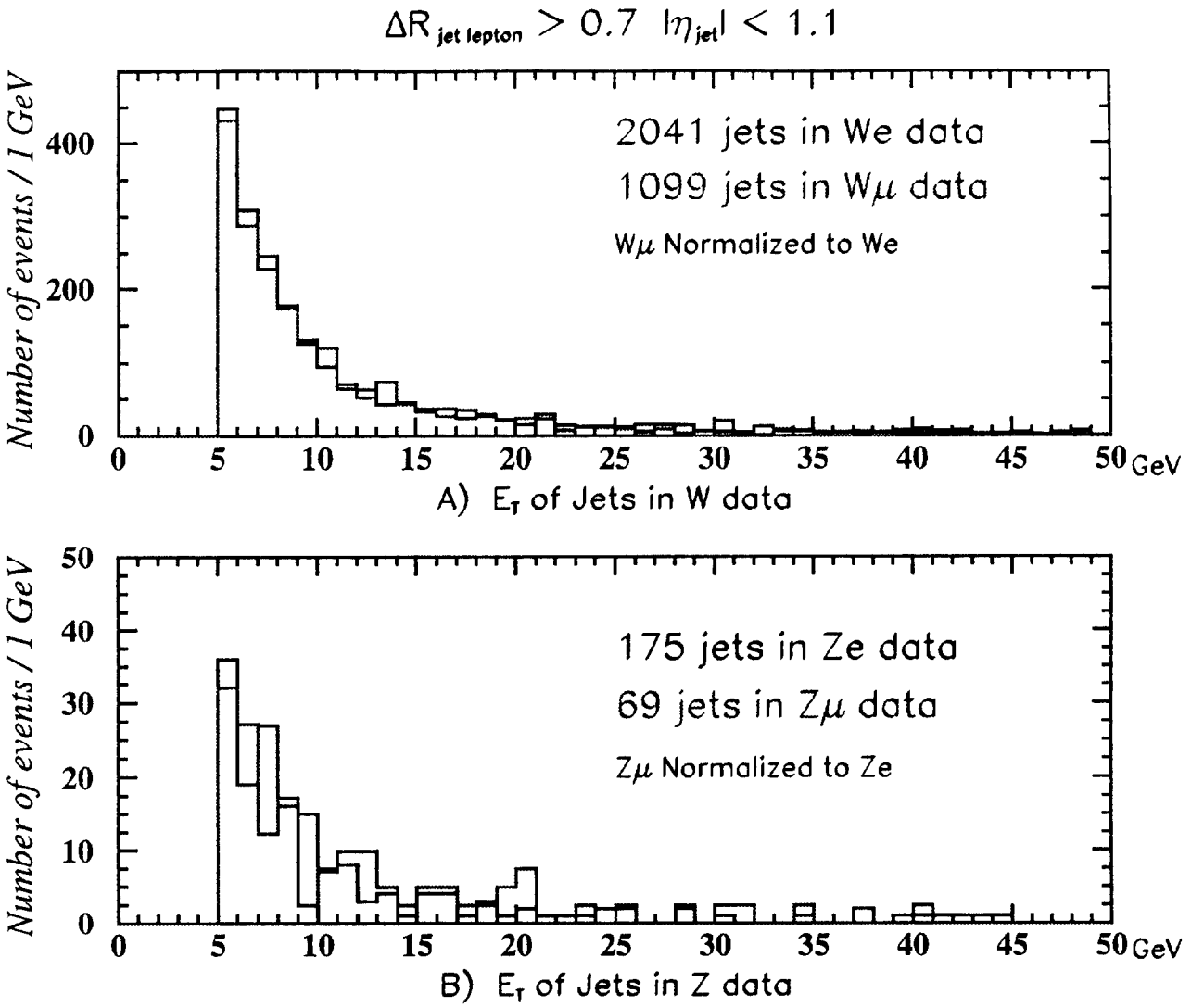

Figure 12: Central jet E_T^J–spectra for inclusive W/Z data sets. (A) Comparison of central jets in inclusive electron (dark histogram) *vs.* muon (light histogram) W data samples. The muon data has been normalized to the electron data for these purposes. (B) Comparison of central jets in inclusive electron (dark histogram) *vs.* muon (light histogram) Z data samples. The muon data has been normalized to the electron data for these purposes.

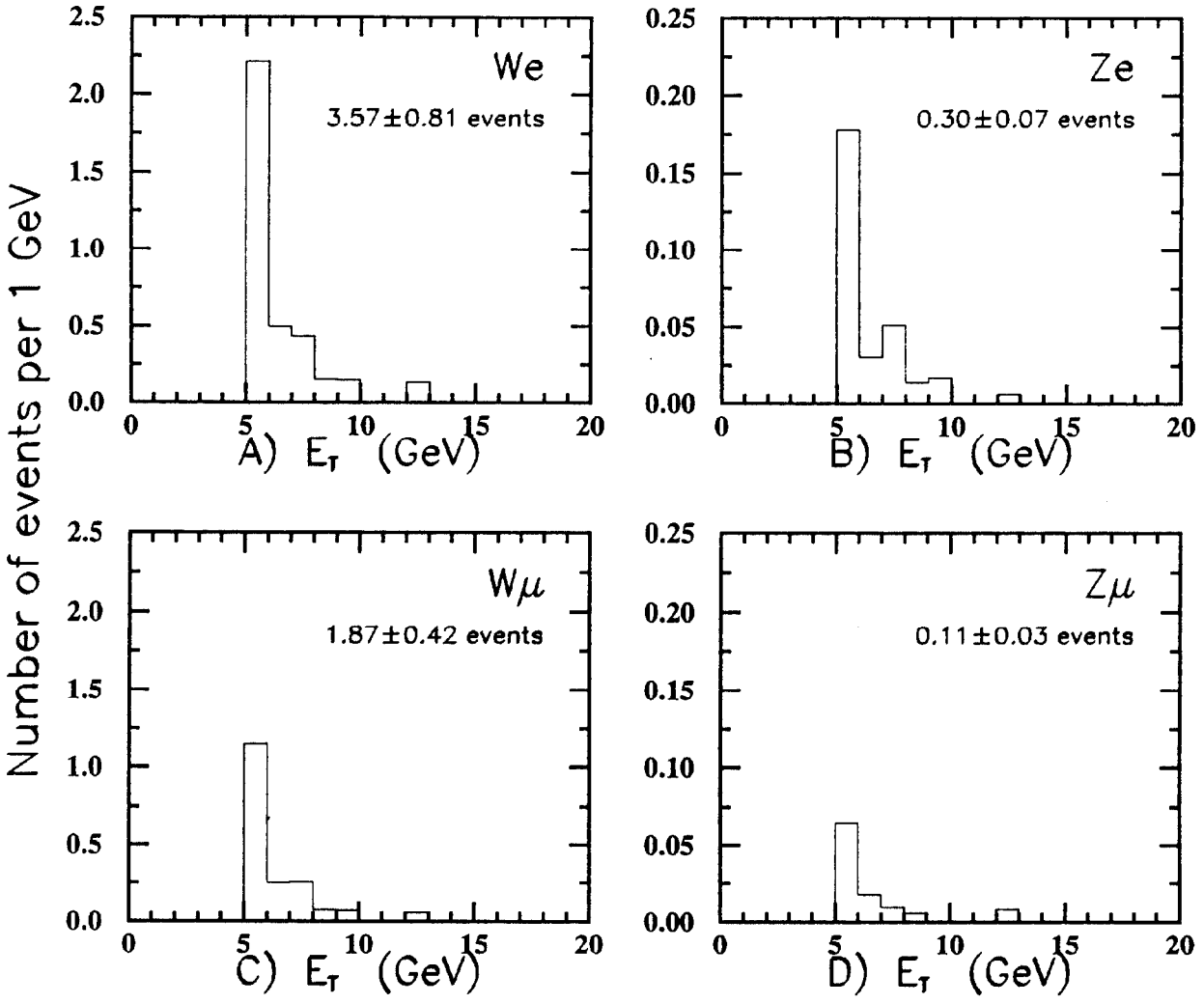

Figure 13: Inclusive QCD background E_T−distributions for the $W\gamma$ and $Z\gamma$ data samples. (A)-(D) Inclusive QCD background as a function of E_T for the electron, muon $W\gamma$ data samples and electron, muon $Z\gamma$ data samples, respectively.

A cross-check on the determination of the level of "direct" (as opposed to inclusive) QCD jet background in each of the electron and muon $W\gamma$ and $Z\gamma$ data samples was obtained from simulations of inclusive W/Z+Jets using the VECBOS[50] $W/Z+n$Jets (n=0-4) Monte Carlo event generator, the HERWIG [51] Monte Carlo to generate both the underlying event and to fragment the jets recoiling against the W/Z bosons, and finally the QFL Monte Carlo for CDF detector simulation. Monte Carlo VECBOS/HERWIG/QFL W/Z + 0, 1 and 2−jet data samples using a jet parton P_T^{min} cut of 8 GeV in VECBOS were passed through the same set of above-described $W\gamma/Z\gamma$ event selection cuts to obtain properly normalized, luminosity-weighted predictions for the level of "direct" QCD jet background in the each of the four $W\gamma$ and $Z\gamma$ data samples. Note that the HERWIG Monte Carlo generates additional, low−P_T jets in the fragmentation process. Note also that for a parton P_T^{min} = 6 GeV cutoff, an increase of $30 \pm 45\%$ in the VECBOS/HERWIG/QFL prediction for the "direct" QCD background was obtained relative to the event yield prediction obtained using the parton P_T^{min} = 8 GeV cutoff.

The determination of the additional QCD jet background contributions (b) and (c) mentioned above are small in comparison to the "direct" contribution to the inclusive QCD jet background and are discussed in detail in Section 5.4.

The inclusive and "direct" QCD backgrounds obtained via these methods are summarized in Table 12 for each of the four data sets. The uncertainties quoted in this table are statistical only; the systematic uncertainties associated with the QCD backgrounds are discussed below in Section 5.5.

Table 12: Predicted number of QCD jet background events for electron and muon $W\gamma$ & $Z\gamma$. The statistical uncertainty associated with each quantity is given.

QCD Background	Electron	Muon
$W\gamma$: Inclusive $W + Jets$ Data	3.57 ± 0.81	1.87 ± 0.42
$W\gamma$: VECBOS $W + nJets$ MC	2.60 ± 0.65	1.68 ± 0.51
$W\gamma$: $Z + Jet \rightarrow$ "W" + "γ"	0.02 ± 0.01	0.04 ± 0.01
$W\gamma$: $W^{\tau\rightarrow\ell} + Jet \rightarrow W^{\tau\rightarrow\ell}$ + "γ"	0.07 ± 0.02	0.03 ± 0.01
$W\gamma$: VECBOS + $(Z + Jet)$ + $(W^{\tau\rightarrow\ell} + Jet)$	2.69 ± 0.65	1.75 ± 0.51
$Z\gamma$: Inclusive $Z + Jets$ Data	0.30 ± 0.07	0.11 ± 0.03
$Z\gamma$: VECBOS $Z + nJets$ MC	0.20 ± 0.09	0.12 ± 0.06

5.4 Additional Backgrounds in the $W\gamma$ and $Z\gamma$ Data Samples

5.4.1 $Z\gamma$ Backgrounds in the $W\gamma$ Data Samples

The $Z\gamma$ and inclusive Z+Jet processes (where a QCD jet is misidentified as a photon) can contribute to background in the $W\gamma$ data samples if one of the Z decay leptons is not detected. For electron $Z\gamma$ events, this can occur only if one of the decay electrons passes through a non-fiducial region (e.g. a crack) in the EM calorimeters. Muon $Z\gamma$ events can be misidentified as a $W\gamma$ candidate if one of the Z decay muons is outside of the central region ($|\eta_\mu| > 1$). The $Z\gamma$ background in the $W\gamma$ data samples was determined using the Baur $Z\gamma$ event generator and "fast" Monte Carlo

detector simulation and was cross-checked using the Baur/ISAJET/QFL $Z\gamma$ Monte Carlo. The Z+Jet background in the electron and muon $W\gamma$ data samples was determined from the "direct" QCD Z+Jet background in the electron and muon $Z\gamma$ data samples and the ratio of acceptance $\times$ efficiency product terms for the two situations:

$$\mathcal{N}_{bkg}^{ZW_{QCD}} = \mathcal{N}_{bkg}^{Z_{QCD}} \cdot \left[\frac{A^{\ell}_{ZW\text{``}\gamma\text{''}} \cdot \epsilon^{\ell}_{ZW\text{``}\gamma\text{''}}}{A^{\ell}_{Z\text{``}\gamma\text{''}} \cdot \epsilon^{\ell}_{Z\text{``}\gamma\text{''}}} \right] \tag{33}$$

The determination of these backgrounds is discussed further in Appendix E. With no further cuts imposed, 0.55 ± 0.05 $Z\gamma$ and 0.11 ± 0.02 Z+Jet background events are expected in the electron $W\gamma$ data sample; 0.90 ± 0.09 $Z\gamma$ and 0.14 ± 0.02 Z+Jet background events are expected in the muon $W\gamma$ data sample.

Contamination from $Z\gamma$ and Z+Jet backgrounds in the $W\gamma$ data samples can be additionally suppressed by making a cut on additional high-P_T tracks. If events in the $W\gamma$ data samples have an additional, *isolated* three-dimensional track with $P_T > 10$ GeV/c with opposite charge sign to the W decay lepton and have a pair-mass of $70 < M_{ee} < 110$ GeV/c^2 for electrons ($40 < M_{\mu\mu} < 140$ GeV/c^2 for muons), the event is rejected as a background $Z\gamma$ candidate. We do not consider high-P_T tracks within $\Delta R < 0.7$ of a *hadronic* jet (EM fraction < 0.85) since we are *not* vetoing $W\gamma$+Jet events in this analysis. For muons, the 2^{nd} track is additionally required to have a minimum-ionizing calorimeter signature. From studies using Baur/ISAJET/QFL $W\gamma$ and $Z\gamma$ MC simulated data for electrons and muons, no $W\gamma$ signal events are lost by these 2^{nd} track cuts. After making such cuts, a residual of 0.14 ± 0.01 $Z\gamma$ and 0.02 ± 0.01 Z+Jet background events are predicted in the electron $W\gamma$ data sample; 0.45 ± 0.07 $Z\gamma$ and 0.04 ± 0.02 Z+Jet background events are predicted in the muon $W\gamma$ data sample. Note that the Z+Jet background is *already* included in the inclusive QCD background determination for the electron and muon $W\gamma$ data samples. Note also that by application of the cut on no additional isolated high-P_T tracks, one (two) $Z\gamma$ candidates were found in, and rejected from, the electron (muon) $W\gamma$ data samples, respectively.

5.4.2 Tau Lepton Backgrounds in the $W\gamma$ and $Z\gamma$ Data Samples

The processes $(W \rightarrow \tau\bar{\nu}_\tau) + \gamma$ and $(W \rightarrow \tau\bar{\nu}_\tau) + Jet$, where a QCD jet is misidentified as a photon can also contribute to the background in the electron and muon $W\gamma$ data samples when the τ decays to an electron or muon, respectively. The corresponding processes $(Z \rightarrow \tau^+\tau^-) + \gamma$ and $(Z \rightarrow \tau^+\tau^-) + Jet$ can also contribute to the background in the electron and muon $Z\gamma$ data samples. However, because of the additional tau branching ratio factor, $B(\tau \rightarrow \ell\,\bar{\nu}_\ell\,\nu_\tau) \simeq 17.8\%$ [52] and the three-body nature of the tau decay (softening the final-state lepton P_T and $\not\!\!E_T$ spectrum), these background contributions to $W\gamma$ and $Z\gamma$ are suppressed. For $Z\gamma$, tau backgrounds are suppressed by the *square* of these two factors.

The tau $W\gamma$ and $Z\gamma$ backgrounds were determined with the use of the Baur $W\gamma/Z\gamma$ and "fast" Monte Carlo detector simulation programs, using the same methodology as for the electron/muon $W\gamma$ and $Z\gamma$ signals. The tau backgrounds were obtained using the appropriately modified version of equation (90) for each channel, including tau branching ratio factors.

The tau decay contribution to the $W\gamma$ background in the electron and muon channels was found to be small, 0.09 ± 0.01 and 0.05 ± 0.01 events, respectively. The tau decay contribution to the W+Jet background in the electron and muon $W\gamma$ data samples was also found to be small, 0.07 ± 0.01 and 0.03 ± 0.01 events, respectively. This background is also *already* included in the

inclusive QCD background determination for the electron and muon $W\gamma$ data samples. The tau decay contribution to the $Z\gamma$ background in the electron and muon channels was found to be extremely small ($<<$ 0.1 events), and hence is neglected. The tau decay contribution to the $Z\gamma$ background in the electron and muon $W\gamma$ data sets was calculated via similar methods as those used for determining the "direct" electron and muon $Z\gamma$ backgrounds. This non-QCD background contribution to the electron and muon $W\gamma$ data samples was found to be extremely small ($<<$ 0.1 events), and is neglected. The tau decay contribution to the inclusive Z+Jet background in the electron and muon $W\gamma$ data sets was calculated via similar methods as those used for determining the *direct* electron and muon Z+Jet backgrounds. These background contributions were also found to be extremely small ($<<$ 0.1 events), and are also neglected. The determination of the QCD-related tau backgrounds is discussed further in Appendix E.

5.5 Summary of Backgrounds in the $W\gamma$ and $Z\gamma$ Data Samples

The inclusive QCD jet backgrounds in each of the four data samples are summarized in Table 12. The non-QCD $Z + \gamma$ and τ backgrounds in the electron and muon $W\gamma$ data samples are summarized in Table 13. The observed number of events, the total background, the experimental number of signal events and the SM-predicted number of signal events in each of the four data samples is summarized in Table 14. The first uncertainty associated with the entries in this table is the statistical uncertainty; the second is the systematic uncertainty associated with the total background for that channel.

The systematic uncertainty on the inclusive QCD jet background for each of the four channels is conservatively defined as the quadrature sum of: (a) the *maximum* difference between the four different methods used in determining the inclusive QCD jet backgrounds, as summarized in Table 11, and (b) the *difference* between the inclusive QCD jet background and the sum of (1) the "direct" QCD jet background as determined by the VECBOS/HERWIG/QFL $W/Z + n-$jets MC simulations plus (2) the "indirect" QCD jet background contributions, which for $W\gamma$ are due to Z+Jet and tau W+Jet processes. The "indirect" QCD jet background contribution for $Z\gamma$ originating from tau Z+Jet is negligible.

Note that the relative level of QCD background in the $Z\gamma$ data samples ($\sim 10 \pm 5\%$) is substantially less than that for the $W\gamma$ data samples ($\sim 45 \pm 10\%$). The Monte Carlo determination of the QCD backgrounds in the $W\gamma$ and $Z\gamma$ data samples, which are in good agreement with the results obtained from the inclusive QCD background determination, also indicate substantially less background in the $Z\gamma$ data samples than for the $W\gamma$ data samples. There are two main reasons for this difference. First, the ratio of inclusive W/Z boson cross sections $\times$ branching ratios is $\mathcal{R}(W/Z)_\ell \sim 11$. For W and Z events produced with accompanying central jets with $E_T^J > 5$ GeV, the ratio of $\mathcal{R}(W + \text{Jet}/Z + \text{Jet})_\ell$ is expected to be comparable [53]. An implicit assumption in our inclusive background determination for each of the four data samples is that the QCD jet fragmentation probability is the same for W+Jet and Z+Jet events. Thus, the *intrinsic* ratio of $\mathcal{R}(W + \text{"}\gamma\text{"}/Z + \text{"}\gamma\text{"})_\ell$ is also expected to be comparable to the inclusive W/Z cross section ratio. The ratio $\mathcal{R}(W + \text{"}\gamma\text{"}/Z + \text{"}\gamma\text{"})_\ell$ after photon cuts are applied will be larger than this, because the $\Delta R_{\ell\gamma} > 0.7$ cut is applied to *both* decay leptons for $Z\gamma$, whereas this cut is applied to the single decay lepton for $W\gamma$. Second, the SM prediction for the ratio of the $W\gamma/Z\gamma$ cross sections (passing our photon cuts) is $\mathcal{R}(W\gamma/Z\gamma)_\ell \sim 4$ (the ratio $\mathcal{R}(W\gamma/W)$ is significantly less than $\mathcal{R}(Z\gamma/Z)$ for our choice of photon cuts). We discuss these ratios further in Section 6, below.

Although the number of observed events in each of the four channels is limited, we emphasize here their statistical significance in terms of a true signal for the observation of the $W+\gamma$ and $Z+\gamma$ processes. From the information summarized in Table 14, the probability of 3.8 ± 1.4, 2.4 ± 0.6 and 6.2 ± 1.6 background events in the e, μ and $e+\mu$ combined $W+\gamma$ candidate samples fluctuating to 8, 5 and 13 or more events is 7.5%, 10.6% and 2.5%, respectively. The probability of 0.3 ± 0.1, 0.1 ± 0.1 and 0.4 ± 0.1 background events in the e, μ and $e+\mu$ combined $Z+\gamma$ candidate samples fluctuating to 2, 2 and 4 or more events is 3.9%, 0.6% and 0.1%, respectively. Note also that these backgrounds are most significant in the $5 < E_T^\gamma < 6$ GeV region.

Table 13: Predicted number of non-QCD background events for electron and muon $W\gamma$. The statistical uncertainty associated with each quantity is given.

Background Process	Electron	Muon
$Z+\gamma \rightarrow$ "W" $+\gamma$	0.14 ± 0.01	0.45 ± 0.07
$W^{\tau \rightarrow \ell}+\gamma$	0.09 ± 0.01	0.05 ± 0.01

Table 14: Summary of $W\gamma$ and $Z\gamma$ results. The observed number of events $\mathcal{N}_{obs}$, predicted number of total background events $\Sigma\mathcal{N}_{bkgnd}$, number of signal events $\mathcal{N}_{signal} = \mathcal{N}_{obs} - \Sigma\mathcal{N}_{bkgnd}$ and predicted number of SM signal events, $\mathcal{N}_{pred}^{SM}$ for each channel are given. The statistical and systematic uncertainties associated with $\Sigma\mathcal{N}_{bkgnd}$ and $\mathcal{N}_{signal}$ are given for each channel. The statistical uncertainty associated with $\mathcal{N}_{pred}^{SM}$ is given for each channel.

Channel	$\mathcal{N}_{obs}$	$\Sigma\mathcal{N}_{bkgnd}$	$\mathcal{N}_{signal}$	$\mathcal{N}_{pred}^{SM}$
e $W\gamma$	8	$3.8 \pm 0.8 \pm 1.1$	$4.2 \pm 2.9 \pm 1.1$	4.6 ± 0.4
μ $W\gamma$	5	$2.4 \pm 0.4 \pm 0.4$	$2.6 \pm 2.3 \pm 0.4$	2.4 ± 0.2
$e+\mu$ $W\gamma$	13	$6.2 \pm 1.2 \pm 1.2$	$6.8 \pm 3.8 \pm 1.2$	7.0 ± 0.6
e $Z\gamma$	2	$0.3 \pm 0.1 \pm 0.1$	$1.7 \pm 1.4 \pm 0.1$	1.3 ± 0.1
μ $Z\gamma$	2	$0.1 \pm 0.1 \pm 0.1$	$1.9 \pm 1.4 \pm 0.1$	0.7 ± 0.1
$e+\mu$ $Z\gamma$	4	$0.4 \pm 0.1 \pm 0.1$	$3.6 \pm 2.0 \pm 0.1$	2.0 ± 0.2

5.6 Electron and Muon Channel $\mathcal{N}_{sig}(W+\gamma)$, $\mathcal{N}_{sig}(Z+\gamma)$, $\sigma \cdot B(W+\gamma)$ and $\sigma \cdot B(Z+\gamma)$ Results

The experimental results for the number of signal events and the production cross sections $\times$ decay branching ratios for $W\gamma$ and $Z\gamma$ in the electron/muon channels were determined using equations 26 - 27 (72 - 73) and 74 - 77 (from Appendix B). Monte Carlo methods were used to determine the statistical, systematic and overall uncertainties associated with $\mathcal{N}_{sig}(V_\ell + \gamma)$ and $\sigma \cdot B(V_\ell + \gamma)$. We simulated 10^6 CDF experiments, Poisson-fluctuating the number of observed events for each simulated experiment for each channel, and using Gaussian fluctuations for the integrated luminosities, overall acceptance and efficiency terms. The statistical and systematic

uncertainties associated with the individual backgrounds for each channel were Gaussian-fluctuated and subtracted from the observed number of events on an "experiment-by-experiment" basis. We obtained the experimental $\mathcal{N}_{sig}(V_\ell + \gamma)$ and cross section $\sigma \cdot B(V_\ell + \gamma)_{expt}$ from finely-binned histograms (incremented once per "experiment") as shown in Figures 14 and 15 for $W\gamma$ and $Z\gamma$, respectively. The mean and $\pm 1\sigma$ uncertainties for $\mathcal{N}_{sig}$ and $\sigma \cdot B$ were determined, as well as the 68% and 95% CL upper limits to $\mathcal{N}_{sig}$ and $\sigma \cdot B$, using the method of a bounded physical region [54]. The number of signal events and cross section $\times$ branching ratio results for each of the four channels are summarized in Tables 15 and 16 for $W\gamma$ and $Z\gamma$, respectively. The first uncertainty is statistical only; the second uncertainty is the systematic uncertainty associated with the integrated luminosity, acceptances and efficiencies; the third uncertainty is the systematic uncertainty associated with the QCD jet background determination. These results were cross-checked with analytic calculations of $\mathcal{N}_{sig}(V_\ell + \gamma)$ and $\sigma \cdot B(V_\ell + \gamma)$ and their associated $\pm 1\sigma$ statistical, systematic and overall uncertainties. The results obtained from the analytic calculations are in extremely good agreement with that obtained via the Monte Carlo method for each of the four channels.

The $\sigma \cdot B(W_\ell + \gamma)$ results obtained for the electron and muon $W\gamma$ channels are in excellent agreement with each other and with the SM prediction. Similarly, the $\sigma \cdot B(Z_\ell + \gamma)$ results obtained for the electron and muon $Z\gamma$ channels are also in good agreement with each other and with the SM prediction, within statistical uncertainties.

5.7 Combining Electron and Muon Cross Sections

To combine the individual $\ell = e$ and μ $\sigma \cdot B(V_\ell + \gamma)$ production cross sections $\times$ decay branching ratios, one makes the assumption that the electron and muon channels are measuring the same physical process (i.e. that lepton universality holds: $\sigma \cdot B = \sigma \cdot B_e = \sigma \cdot B_\mu$). The combined $e + \mu$ production cross section $\times$ decay branching ratio for $V + \gamma$ is therefore given by:

$$\sigma \cdot B(V + \gamma)_{e+\mu} = \frac{\mathcal{N}^e_{signal} + \mathcal{N}^\mu_{signal}}{\int \mathcal{L}_e dt \cdot \left(A^e_{V\gamma} \cdot \epsilon^e_{V\gamma}\right) + \int \mathcal{L}_\mu dt \cdot \left(A^\mu_{V\gamma} \cdot \epsilon^\mu_{V\gamma}\right)} \tag{34}$$

The same Monte Carlo $\sigma \cdot B(V_\ell + \gamma)$ programs used to calculate the individual e and μ results also calculated the combined $e + \mu$ result for $W\gamma$ and $Z\gamma$. We have cross-checked this method of combining cross sections with test distributions and also with analytic methods. All results agree extremely well with each other for these comparative tests, including $\pm 1\sigma$ statistical and systematic uncertainties.

Figures 14 and 15 show the electron, muon and $e + \mu$ combined $W\gamma$ and $Z\gamma$ $\mathcal{N}_{sig}$ and $\sigma \cdot B$ probability distributions, respectively. These probability distributions are nearly Gaussian, but with a small high-side tail, due mainly to small-number Poisson statistics. The narrowing of the $\sigma \cdot B$ probability distribution for the $e + \mu$ combined cross sections is readily apparent. Tables 15 and 16 summarize the number of signal events and cross sections for the electron, muon and combined $e + \mu$ $W\gamma$ and $Z\gamma$ results.

Table 15: Summary of $\mathcal{N}_{signal}(W+\gamma)$ and $\sigma \cdot B(W+\gamma)$ results. For $\mathcal{N}_{signal}(W_\ell+\gamma)_{expt}$ and $\sigma \cdot B(W_\ell+\gamma)_{expt}$, the $\pm 1\sigma$ uncertainties are given. The first uncertainty is the overall statistical uncertainty ($stat$); the second is the overall systematic uncertainty ($syst_1$) associated with integrated luminosity, acceptances and efficiencies; the third is the overall systematic uncertainty ($syst_2$) associated with the background for each channel. The fourth uncertainty is the combined ($stat + syst_1 + syst_2$) uncertainty. The statistical and luminosity-dependent uncertainty for $\mathcal{N}_{signal}(W_\ell+\gamma)^{SM}_{pred}$ is given. The statistical uncertainty for $\sigma \cdot B(W_\ell+\gamma)^{SM}_{pred}$ is given. The 68% and 95% CL upper limits on $\mathcal{N}_{signal}(W+\gamma)_{expt}$ and $\sigma \cdot B(W_\ell+\gamma)_{expt}$ are also given for the individual electron, muon and $e+\mu$ combined results. See text for further details.

$W\gamma$ Channel	$\mathcal{N}_{signal}(W_\ell\gamma)_{expt}$	$\mathcal{N}_{signal}(W_\ell\gamma)^{SM}_{pred}$	$\sigma \cdot B(W_\ell\gamma)_{expt}$ (pb)	$\sigma \cdot B(W_\ell\gamma)^{SM}_{pred}$ (pb)
e	$4.2^{+2.9}_{-2.9}\ ^{+0.0}_{-0.0}\ ^{+1.1}_{-1.1} = 4.2^{+3.2}_{-3.2}$ < 5.8 (68% CL) < 9.7 (95% CL)	4.6 ± 0.4	$20.6^{+14.4}_{-14.5}\ ^{+1.9}_{-1.6}\ ^{+5.5}_{-5.5} = 20.6^{+15.7}_{-15.5}$ < 28.8 (68% CL) < 48.8 (95% CL)	22.4 ± 0.1
μ	$2.6^{+2.3}_{-2.3}\ ^{+0.0}_{-0.0}\ ^{+0.4}_{-0.4} = 2.6^{+2.3}_{-2.3}$ < 3.9 (68% CL) < 6.9 (95% CL)	2.4 ± 0.2	$24.6^{+21.2}_{-21.1}\ ^{+2.5}_{-2.0}\ ^{+4.4}_{-4.3} = 24.6^{+22.1}_{-21.6}$ < 36.6 (68% CL) < 65.5 (95% CL)	22.4 ± 0.1
$e+\mu$	$6.8^{+3.8}_{-3.8}\ ^{+0.0}_{-0.0}\ ^{+1.2}_{-1.2} = 6.8^{+3.9}_{-3.9}$ < 8.7 (68% CL) < 13.6 (95% CL)	7.0 ± 0.6	$22.0^{+12.0}_{-11.9}\ ^{+2.0}_{-1.6}\ ^{+4.0}_{-3.9} = 22.0^{+12.9}_{-12.6}$ < 28.2 (68% CL) < 44.5 (95% CL)	22.4 ± 0.1

Table 16: Summary of $\mathcal{N}_{signal}(Z+\gamma)$ and $\sigma \cdot B(Z+\gamma)$ results. For $\mathcal{N}_{signal}(Z_\ell+\gamma)_{expt}$ and $\sigma \cdot B(Z_\ell+\gamma)_{expt}$, the $\pm 1\sigma$ uncertainties are given. The first uncertainty is the overall statistical uncertainty ($stat$); the second is the overall systematic uncertainty ($syst_1$) associated with integrated luminosity, acceptances and efficiencies; the third is the overall systematic uncertainty ($syst_2$) associated with the background for each channel. The fourth uncertainty is the combined ($stat + syst_1 + syst_2$) uncertainty. The statistical and luminosity-dependent uncertainty for $\mathcal{N}_{signal}(Z_\ell+\gamma)^{SM}_{pred}$ is given. The statistical uncertainty for $\sigma \cdot B(Z_\ell+\gamma)^{SM}_{pred}$ is given. The 68% and 95% CL upper limits on $\mathcal{N}_{signal}(Z+\gamma)_{expt}$ and $\sigma \cdot B(Z_\ell+\gamma)_{expt}$ are also given for the individual electron, muon and $e+\mu$ combined results. See text for further details.

$Z\gamma$ Channel	$\mathcal{N}_{signal}(Z_\ell\gamma)_{expt}$	$\mathcal{N}_{signal}(Z_\ell\gamma)^{SM}_{pred}$	$\sigma \cdot B(Z_\ell\gamma)_{expt}$ (pb)	$\sigma \cdot B(Z_\ell\gamma)^{SM}_{pred}$ (pb)
e	$1.7^{+1.4}_{-1.4}\ ^{+0.0}_{-0.0}\ ^{+0.1}_{-0.1} = 1.7^{+1.4}_{-1.4}$ < 2.4 (68% CL) < 4.4 (95% CL)	1.3 ± 0.1	$7.0^{+5.8}_{-5.7}\ ^{+0.7}_{-0.5}\ ^{+0.4}_{-0.4} = 7.0^{+5.9}_{-5.7}$ < 9.9 (68% CL) < 18.3 (95% CL)	5.5 ± 0.1
μ	$1.9^{+1.4}_{-1.4}\ ^{+0.0}_{-0.0}\ ^{+0.1}_{-0.1} = 1.9^{+1.4}_{-1.4}$ < 2.5 (68% CL) < 4.5 (95% CL)	0.7 ± 0.1	$15.8^{+11.8}_{-11.8}\ ^{+1.7}_{-1.4}\ ^{+0.3}_{-0.4} = 15.8^{+12.0}_{-11.8}$ < 21.3 (68% CL) < 38.8 (95% CL)	5.5 ± 0.1
$e+\mu$	$3.6^{+2.0}_{-2.0}\ ^{+0.0}_{-0.0}\ ^{+0.1}_{-0.1} = 3.6^{+2.0}_{-2.0}$ < 4.4 (68% CL) < 7.2 (95% CL)	2.0 ± 0.2	$9.9^{+5.5}_{-5.4}\ ^{+0.9}_{-0.7}\ ^{+0.3}_{-0.3} = 9.9^{+5.7}_{-5.4}$ < 12.4 (68% CL) < 20.1 (95% CL)	5.5 ± 0.1

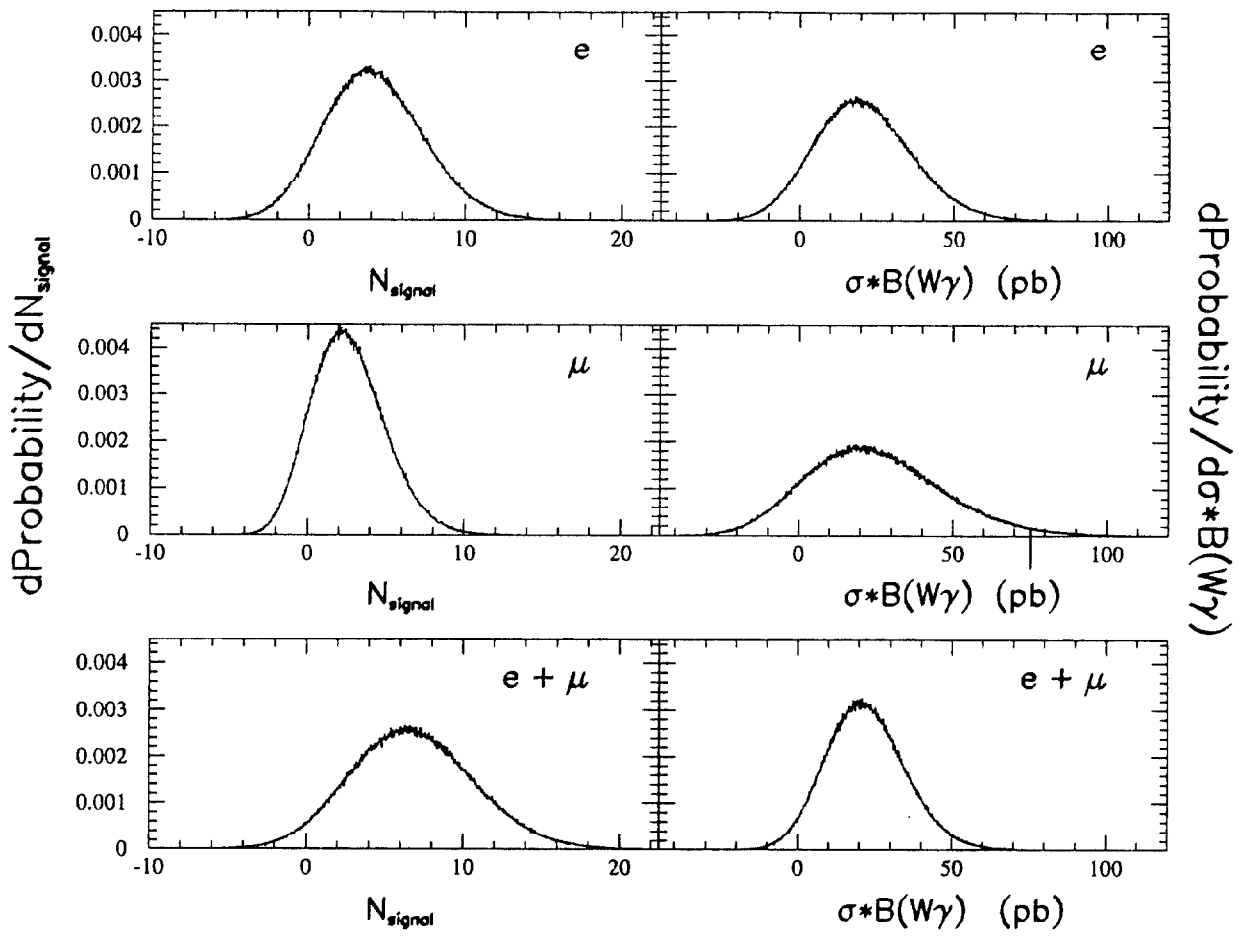

Figure 14: Electron, muon and combined $e + \mu$ $\mathcal{N}_{signal}(W + \gamma)$ and $\sigma \cdot B(W + \gamma)$ probability distributions.

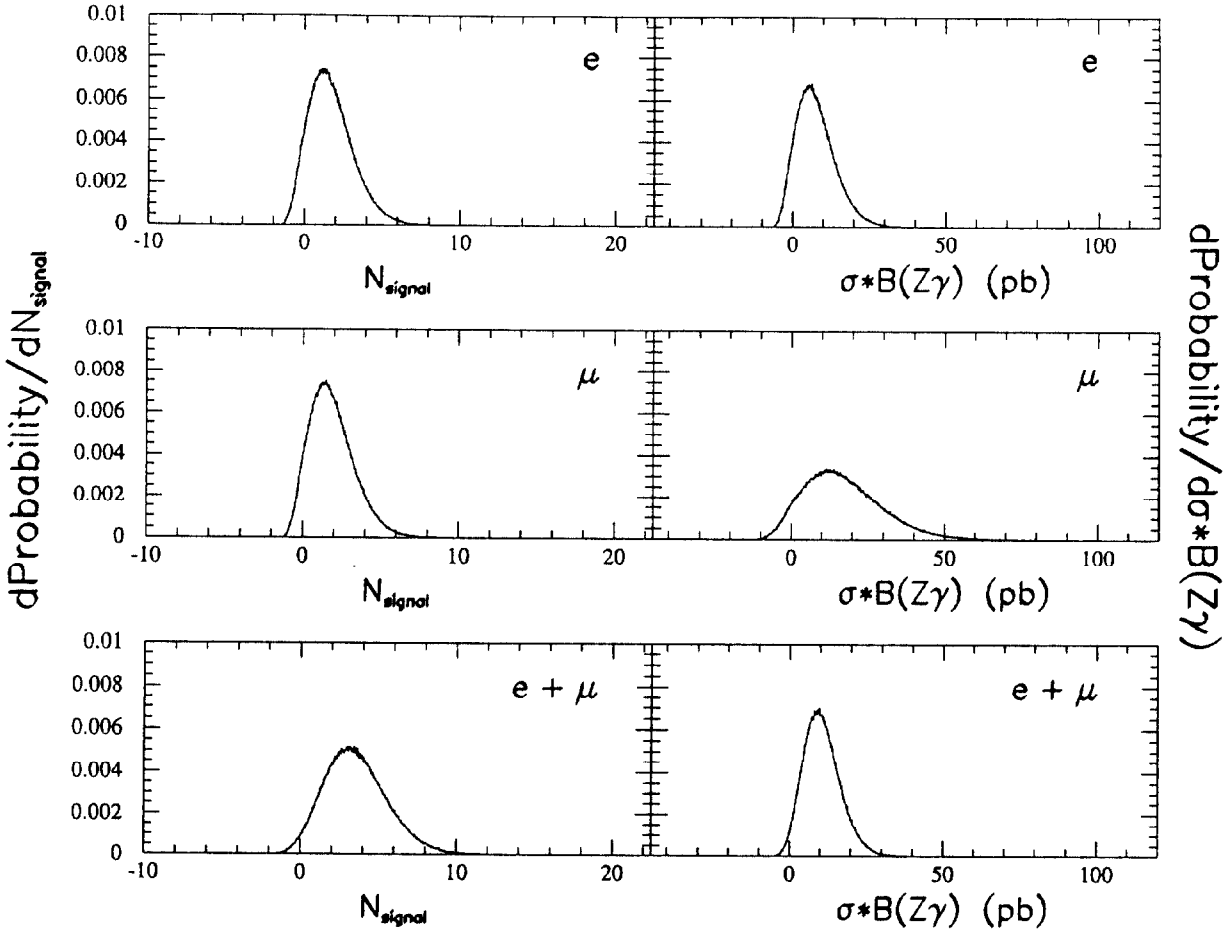

Figure 15: Electron, muon and combined $e + \mu$ $\mathcal{N}_{signal}(Z + \gamma)$ and $\sigma \cdot B(Z + \gamma)$ probability distributions.

5.8 Additional Systematic Uncertainties on $\mathcal{N}_{sig}(W+\gamma)$, $\mathcal{N}_{sig}(Z+\gamma)$, $\sigma \cdot B(W+\gamma)$ and $\sigma \cdot B(Z+\gamma)$

For each of the four channels, we studied the systematic effects of varying the diboson $P_T(V_\ell+\gamma)$ distribution, structure function (SF) choice and the Q^2-scale dependence for the nominal SF (HMRS-B) choice on the Monte Carlo predictions for $\mathcal{N}_{sig}(V_\ell+\gamma)_{MC}$, $\sigma \cdot B(V_\ell+\gamma)_{MC}$ and the determination of $\sigma \cdot B(V_\ell+\gamma)_{expt}$. The systematic effects of varying the CEM energy scale and CEM energy resolution were also investigated. The importance of each of these contributions to the overall uncertainty associated with the individual (and combined) cross sections, relative to the statistical uncertainty associated with each measurement is small.

5.8.1 Systematic Uncertainties due to $P_T(W/Z+\gamma)$

Since there are as yet no experimental measurements of the diboson $P_T(W/Z+\gamma)$ spectrum, and no theoretical predictions for these distributions in the low $P_T(W/Z+\gamma)$ region (below ~ 10 GeV/c), we approximated these distributions in the Monte Carlo simulation programs by using the measured CDF $P_T(W/Z)$ distributions [55], which is reasonable for the photon E_T^γ range we are sensitive to in this analysis. The measured $d\sigma/dP_T(W/Z)$ distributions for inclusive W/Z production are in good agreement with theoretical predictions [56]. The shapes of the $P_T(W/Z+\gamma)$ distributions are expected to be similar to $P_T(W/Z)$ for the $W\gamma/Z\gamma$ event selection cuts used in this analysis. We studied the systematic effects of varying the shape of the assumed $P_T(V_\ell+\gamma)$ distribution on the W/Z/photon acceptances, MC predicted cross sections, MC expected number of events and the experimental cross section results.

For each of the four channels, using the nominal structure function choice, the MC diboson $P_T(V_\ell+\gamma)$ distributions were varied within the $\pm 1\sigma$ limits allowed by the fit to the shape of the $d\sigma/dP_T(W/Z)$ distributions. The method involved using the fast MC detector simulation programs to determine kinematic/geometrical acceptances, $\mathcal{N}_{sig}(V_\ell+\gamma)$ and $\sigma \cdot B(V_\ell+\gamma)_{cuts}$, requiring the MC events to pass all event selection cuts, and including the efficiencies of these cuts in the fast MC detector simulation. The acceptance results for each $P_T(V_\ell+\gamma)$ choice, as obtained from the fast Monte Carlo detector simulation were then input to the experimental determination of the $\sigma \cdot B(V_\ell+\gamma)_{expt}$ for each of the four decay channels.

Several $P_T(V_\ell+\gamma)$ distributions for each decay channel were investigated to obtain acceptance factors used in the determination of both MC and experimental $\sigma \cdot B(V_\ell+\gamma)$ results, associated with: (1) a "soft" (-1σ) P_T boost, (2) a "nominal" P_T boost and (3) a "hard" $(+1\sigma)$ P_T boost. The systematic uncertainties for the combined $e+\mu$ results were obtained via the same method as used for combining the "nominal" $e+\mu$ cross sections.

5.8.2 Systematic Uncertainties due to Structure Function Q^2 Scale Dependence

The systematic uncertainties associated with the momentum scale (Q^2-scale) dependence for the nominal structure function choice (HMRS-B) were studied by varying the Q^2-scale between the limits of $\frac{1}{4}M^2_{V+\gamma} < Q^2 < 4M^2_{V+\gamma}$, for each of the four decay channels. Small correlations between Q^2-scale dependence and the shape of the diboson $P_T(V_\ell+\gamma)$ distribution due to four-momentum conservation in the $V_\ell+\gamma$ production process are neglected.

5.8.3 Systematic Uncertainties due to Structure Function Choice

Five different choices of structure functions, DFLM-260 [57], MRS-B [58], HMRS-B [41], MRS-S0 [59] and MT-B1 [60] were used in order to determine the systematic uncertainties associated with the structure function choice for each of the four decay channels. The $W\gamma$ and $Z\gamma$ Monte Carlo events generated with each structure function choice were passed through the fast MC detector simulation programs to obtain predictions for kinematic/geometrical acceptances, $\mathcal{N}_{sig}(V_\ell+\gamma)$ and $\sigma \cdot B(V_\ell+\gamma)_{cuts}$.

5.8.4 Systematic Uncertainties due to CEM Energy Scale and Energy Resolution

We have calibrated the CEM energy scale over the energy range $5 < E_T < 40$ GeV with E/P studies using inclusive electrons in the low-energy range and electrons from W decay in the high energy range. The CEM energy scale in the 5 GeV region is accurate to within $\sim$ 1.0% and in the 40 GeV region, accurate to within $\pm 0.24\%$ [47]. This level of uncertainty has a negligible impact on the observed and predicted number of $W\gamma/Z\gamma$ events, and the MC predicted and experimental cross sections.

Similarly, the effect of $\pm 1\sigma$ variations of the stochastic and constant terms associated with the CEM calorimeter energy resolution,

$$\delta E/E \;=\; (13.5 \pm 1.5)\%/\sqrt{E_T} \;\; \oplus \;\; (\;\; 2.0 \pm 0.3)\% \quad (E,\; E_T \text{ in GeV}) \tag{35}$$

also have negligible impact on the MC predicted and/or observed number of $W\gamma/Z\gamma$ events and the predicted and/or experimental cross sections for $E_T^\gamma > 5.0$ GeV.

5.8.5 Summary of Additional Systematic Uncertainties on $\mathcal{N}_{sig}(V_\ell+\gamma)$ and $\sigma \cdot B(V_\ell+\gamma)$

The systematic uncertainties associated with varying the diboson $P_T(V_\ell+\gamma)$ distributions, the Q^2-scale dependence and SF choices for the Monte Carlo and the experimental results are correlated with each other, since the acceptance factors as determined from the fast Monte Carlo detector simulations are also used in determining the experimental $\sigma \cdot B(V_\ell+\gamma)$ cross sections. Note that the experimental determination of the number of signal events is not correlated in this manner to the predicted number of Monte Carlo signal events. The MC and experimental $\sigma \cdot B(V_\ell+\gamma)$ cross section results for each of the four decay channels, in isolation of each other, must include the respective contributions to the overall uncertainty from these three systematic uncertainties, due to their (common) impact on the acceptance factors. These effects must also be included for the predicted number of MC signal events. In Table 17 we summarize the (quadrature) combined systematic uncertainties associated with varying the diboson $P_T(V_\ell+\gamma)$ distribution, the Q^2-scale dependence and SF choices.

Table 17: Summary of additional systematic uncertainties associated with $\mathcal{N}_{signal}(V+\gamma)$ and $\sigma \cdot B(V+\gamma)$. The $+1\sigma$ and -1σ quadrature sum of the *fractional* systematic uncertainties associated with variations of the $P_T(V+\gamma)$ distribution, Q^2-scale dependence and structure function choice for the Monte Carlo $\mathcal{N}_{signal}(V+\gamma)$ and $\sigma \cdot B(V+\gamma)$ predictions (only), the experimental $\sigma \cdot B(V+\gamma)$ results (only), and the correlated Monte Carlo − experiment $\sigma \cdot B(V+\gamma)$ difference are given.

Channel	$\Delta\mathcal{N}_{signal}(V\gamma)_{MC}$ (%)	$\Delta\sigma \cdot B(V\gamma)_{MC}$ (%)	$\Delta\sigma \cdot B(V\gamma)_{Expt}$ (%)	$\Delta\sigma \cdot B(V\gamma)_{MC-Expt}$ (%)
e $W\gamma$	$^{+8.9}_{-3.7}$	$^{+19.9}_{-5.8}$	$^{+7.3}_{-4.9}$	$^{+13.6}_{-2.4}$
μ $W\gamma$	$^{+11.3}_{-6.6}$	$^{+13.4}_{-3.7}$	$^{+8.9}_{-3.2}$	$^{+10.0}_{-5.3}$
$e+\mu$ $W\gamma$	$^{+10.3}_{-4.0}$	$^{+15.0}_{-4.1}$	$^{+7.7}_{-4.1}$	$^{+10.5}_{-5.5}$
e $Z\gamma$	$^{+11.1}_{-4.5}$	$^{+7.1}_{-2.9}$	$^{+4.3}_{-8.6}$	$^{+8.6}_{-5.7}$
μ $Z\gamma$	$^{+7.8}_{-2.3}$	$^{+4.4}_{-1.3}$	$^{+3.8}_{-3.2}$	$^{+4.4}_{-2.5}$
$e+\mu$ $Z\gamma$	$^{+7.9}_{-3.5}$	$^{+7.1}_{-2.0}$	$^{+5.1}_{-4.0}$	$^{+5.1}_{-3.0}$

5.9 Summary of $W\gamma$ and $Z\gamma$ Cross Section Results

We summarize here the results for the individual e, μ and combined $e+\mu$ $W\gamma$ and $Z\gamma$ cross sections and their SM predictions, explicitly taking into account the systematic uncertainties associated with the $P_T(V_\ell+\gamma)$ distribution, structure function Q^2-scale dependence and structure function choice. The experimental cross section results are in good agreement with the Standard Model predictions.

$$\begin{aligned}
\sigma \cdot B(W\gamma)_e &= 20.6^{+15.8}_{-15.5}\ (stat+syst)\ \text{pb} \\
\sigma \cdot B(W\gamma)_\mu &= 24.6^{+22.1}_{-21.6}\ (stat+syst)\ \text{pb} \\
\sigma \cdot B(W\gamma)_{e+\mu} &= 22.0^{+13.0}_{-12.6}\ (stat+syst)\ \text{pb} \\
\sigma \cdot B(W\gamma)_{SM} &= 22.4^{+\ 3.3}_{-\ 0.9}\ (stat+syst)\ \text{pb}
\end{aligned}$$

$$\begin{aligned}
\sigma \cdot B(Z\gamma)_e &= 7.0^{+\ 5.9}_{-\ 5.7}\ (stat+syst)\ \text{pb} \\
\sigma \cdot B(Z\gamma)_\mu &= 15.8^{+12.0}_{-11.8}\ (stat+syst)\ \text{pb} \\
\sigma \cdot B(Z\gamma)_{e+\mu} &= 9.9^{+\ 5.7}_{-\ 5.5}\ (stat+syst)\ \text{pb} \\
\sigma \cdot B(Z\gamma)_{SM} &= 5.5^{+\ 0.5}_{-\ 0.2}\ (stat+syst)\ \text{pb}
\end{aligned}$$

6 $W\gamma$ AND $Z\gamma$ CROSS SECTION RATIOS

A more illuminating comparison of our cross section measurements with the Standard Model is provided by forming the following cross section ratios:

$$
\begin{aligned}
(1) \quad & \mathcal{R}(W\gamma/W)_\ell \equiv \sigma \cdot B(W_\ell + \gamma) \;/\; \sigma \cdot B(W_\ell) \\
(2) \quad & \mathcal{R}(Z\gamma/Z)_\ell \equiv \sigma \cdot B(Z_\ell + \gamma) \;/\; \sigma \cdot B(Z_\ell) \\
(3) \quad & \mathcal{R}(W\gamma/Z\gamma)_\ell \equiv \sigma \cdot B(W_\ell + \gamma) \;/\; \sigma \cdot B(Z_\ell + \gamma) \\
(4) \quad & \mathcal{R}(W/Z)_\ell \equiv \sigma \cdot B(W_\ell) \;/\; \sigma \cdot B(Z_\ell)
\end{aligned}
$$

CDF has already published results for the e, μ and $e+\mu$ combined cross section ratio (4) from the 1988-89 collider run [7]. By taking ratios of these cross sections, as in the case of the $\mathcal{R}(W/Z)_\ell$ cross section ratio, many common experimental (and theoretical) uncertainties cancel [61]. These four cross section ratios are shown below in Figs. 16a - 16d and summarized in Table 18. The first and third cross section ratios, $\mathcal{R}(W\gamma/W)_\ell$ and $\mathcal{R}(W\gamma/Z\gamma)_\ell$, in the context of the SM are sensitive to the destructive interference between the $u-$, $t-$ and $s-$channel Feynman amplitudes for the $W\gamma$ process [53].

The SM prediction for $\mathcal{R}(W\gamma/W)_\ell$ (for our choice of photon cuts) is 1.1%, whereas if these events were due solely to radiative W decay [62], this ratio would instead be 0.6%. The experimental results are statistically compatible with either hypothesis, although they favor the SM $W\gamma$ prediction by approximately 0.5σ.

The second cross section ratio, $\mathcal{R}(Z\gamma/Z)_\ell$ is shown in Fig. 16b, along with its SM prediction of 2.8%. If these events were due solely to radiative Z decay, this ratio would be 1.9%.

The third cross section ratio, that of $\mathcal{R}(W\gamma/Z\gamma)_\ell$ is predicted to be 4.0 in the SM. If the photons observed in W events were due solely to final-state bremsstrahlung, this ratio is expected to be 2.5 instead, whereas if the photons observed in Z events were due solely to final-state bremsstrahlung, this ratio is expected to be 5.4. If the photons observed in both W and Z events were both due solely to final-state bremsstrahlung, this ratio is instead expected to be 3.3. The data for this cross section ratio weakly favor this latter number, simply due to the higher-than-expected $Z+\gamma$ cross section result(s). Due to the limited statistics, the e, μ and $e+\mu$ $\mathcal{R}(W\gamma/Z\gamma)$ cross section ratios are also quite compatible with the SM prediction.

The fourth cross section ratio is the inclusive W/Z cross section ratio, $\mathcal{R}(W/Z)_\ell$ which is predicted to be 10.7. These cross section ratio results are in good agreement with Standard Model expectations.

Table 18: W and Z cross section ratios. The combined ($stat$ + $syst$) uncertainty associated with each quantity is given.

Cross Section Ratio	$\mathcal{R}_{expt}$	$\mathcal{R}_{pred}^{SM}$	$\mathcal{R}_{pred}^{rad}$	
$\mathcal{R}(W\gamma/W)_e$	$0.9^{+0.7}_{-0.7}\%$			
$\mathcal{R}(W\gamma/W)_\mu$	$1.1^{+1.0}_{-1.0}\%$	$1.07 \pm 0.02\%$	$0.61 \pm 0.01\%$	
$\mathcal{R}(W\gamma/W)_{e+\mu}$	$1.0^{+0.6}_{-0.6}\%$			
$\mathcal{R}(Z\gamma/Z)_e$	$3.3^{+2.8}_{-2.8}\%$			
$\mathcal{R}(Z\gamma/Z)_\mu$	$7.0^{+5.3}_{-5.3}\%$	$2.83 \pm 0.03\%$	$1.93 \pm 0.02\%$	
$\mathcal{R}(Z\gamma/Z)_{e+\mu}$	$4.6^{+2.6}_{-2.6}\%$			
$\mathcal{R}(W\gamma/Z\gamma)_e$	$3.0^{+2.8}_{-3.0}$		2.47 ± 0.04	(rad $W/Z\gamma$)
$\mathcal{R}(W\gamma/Z\gamma)_\mu$	$1.6^{+1.9}_{-1.6}$	4.05 ± 0.07	5.41 ± 0.10	($W\gamma$/rad Z)
$\mathcal{R}(W\gamma/Z\gamma)_{e+\mu}$	$2.2^{+2.3}_{-1.5}$		3.30 ± 0.06	(rad W/rad Z)
$\mathcal{R}(W/Z)_e$	$10.2^{+0.9}_{-0.9}$			
$\mathcal{R}(W/Z)_\mu$	$9.8^{+1.2}_{-1.2}$	10.69 ± 0.22		
$\mathcal{R}(W/Z)_{e+\mu}$	$10.0^{+0.7}_{-0.7}$			

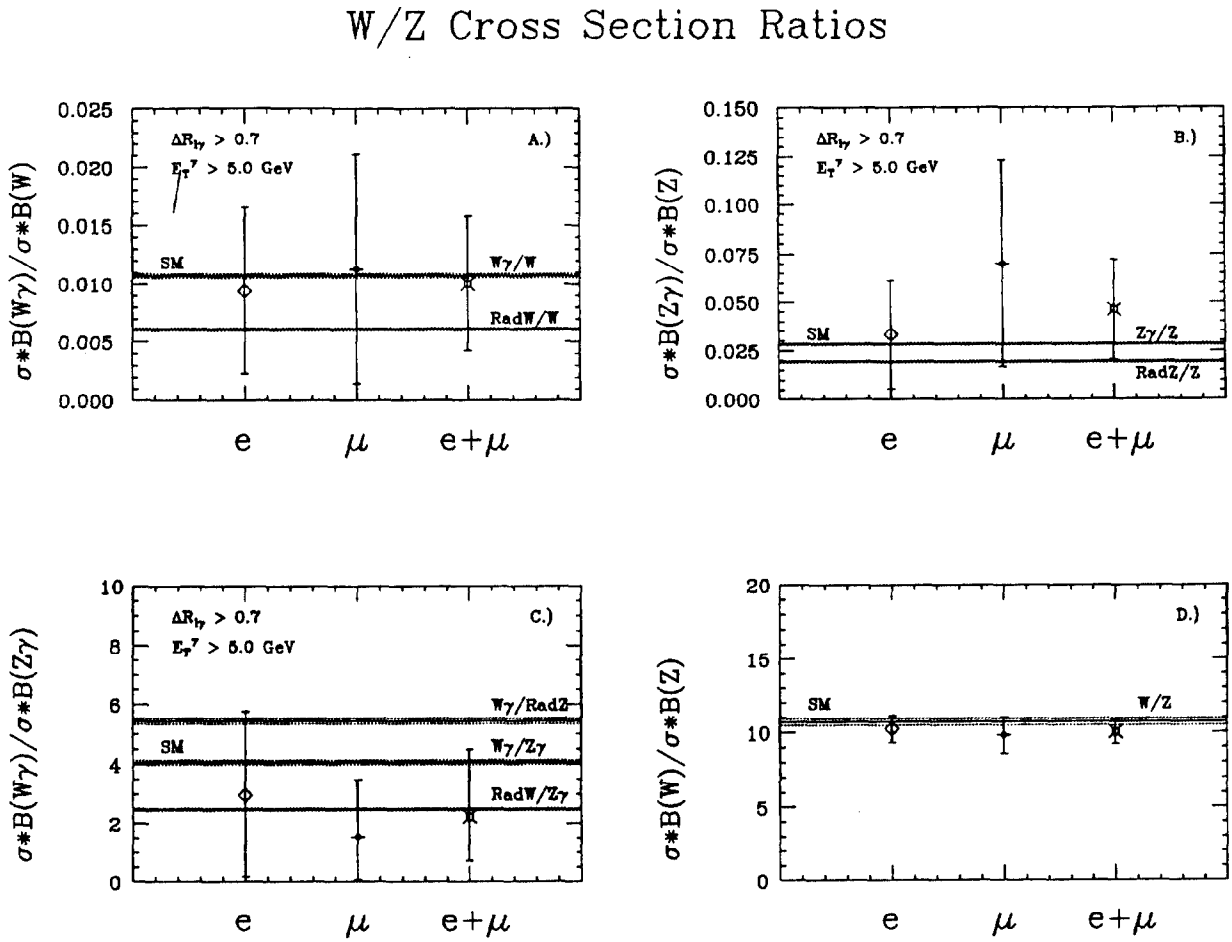

Figure 16: W/Z cross section ratios. (A) The individual electron, muon and combined $e+\mu$ cross section ratios $\mathcal{R}(W\gamma/W)_\ell = \sigma \cdot B(W\gamma)/\sigma \cdot B(W)$. The Standard Model $W\gamma/W$ and radiative W/W (only) cross section ratio predictions and their $\pm 1\sigma$ theoretical uncertainties are indicated by the upper and lower horizontal lines, respectively. (B) The individual electron, muon and combined $e+\mu$ cross section ratios $\mathcal{R}(Z\gamma/Z)_\ell = \sigma \cdot B(Z\gamma)/\sigma \cdot B(Z)$. The Standard Model $Z\gamma/Z$ and radiative Z/Z (only) cross section ratio predictions and their $\pm 1\sigma$ theoretical uncertainties are indicated by the upper and lower horizontal lines, respectively. (C) The individual electron, muon and combined $e+\mu$ cross section ratios $\mathcal{R}(W\gamma/Z\gamma)_\ell = \sigma \cdot B(W\gamma)/\sigma \cdot B(Z\gamma)$. The $W\gamma$/radiative Z (only), Standard Model $W\gamma/Z\gamma$ and radiative $W/Z\gamma$ (only) cross section ratio predictions and their $\pm 1\sigma$ theoretical uncertainties are indicated by the upper, middle and lower horizontal lines, respectively. (D) The individual electron, muon and combined $e+\mu$ cross section ratios $\mathcal{R}(W/Z)_\ell = \sigma \cdot B(W)/\sigma \cdot B(Z)$. The Standard Model inclusive W/Z cross section ratio prediction and its $\pm 1\sigma$ theoretical uncertainty is indicated by the horizontal line.

7 DIRECT LIMITS ON $WW\gamma$, $ZZ\gamma$ and $Z\gamma\gamma$ ANOMALOUS COUPLINGS

7.1 General Methodology

If the W and Z bosons are composite objects, large values of $WW\gamma$, $ZZ\gamma$ or $Z\gamma\gamma$ anomalous couplings ($>> \alpha$) may be realized in nature. Depending on the nature and magnitude of these non-standard couplings, an excess of isolated, high-E_T photons accompanying the production of W and Z bosons is expected, relative to SM $W\gamma$ and $Z\gamma$ predictions. The angular distribution for hard photons associated with anomalous couplings is more central than for the SM $W\gamma$ and $Z\gamma$ couplings [11, 17]. Table 19 summarizes the number of electron and muon $W\gamma$ events predicted by the Baur + fast $W\gamma$ Monte Carlo program for several sample choices of the $\Delta\kappa$ and λ parameters. Figures 17 and 18, respectively show the predicted central photon E_T^γ and $\Delta R_{\ell\gamma}$ distributions for these same choices of anomalous parameters. For $Z\gamma$, the behavior is very similar for non-SM values of $ZZ\gamma/Z\gamma\gamma$ anomalous couplings. The experimental sensitivity to possible $WW\gamma$ ($ZZ\gamma/Z\gamma\gamma$) anomalous couplings for $W\gamma$ ($Z\gamma$) is determined by the *absence* of an excess of such events, or, equivalently, obtained by setting an upper limit to an experimental cross section.

Table 19: Sample MC predictions for the number of electron and muon $W\gamma$ events. The statistical uncertainty associated with each quantity is given.

Anomalous Coupling	$E_T^\gamma > 5$ GeV	$5 < E_T^\gamma \leq 15$ GeV	$E_T^\gamma > 15$ GeV
$e\,W\gamma$: $\Delta\kappa = 0,\ \lambda = 0$ (SM)	4.6 ± 0.4	3.7 ± 0.3	0.9 ± 0.1
$e\,W\gamma$: $\Delta\kappa = 7,\ \lambda = 0$	11.0 ± 1.0	4.6 ± 0.4	6.4 ± 0.6
$e\,W\gamma$: $\Delta\kappa = 0,\ \lambda = 3$	12.6 ± 1.2	3.9 ± 0.4	8.7 ± 0.8
$e\,W\gamma$: $\Delta\kappa = 5,\ \lambda = 5$	39.5 ± 3.6	5.5 ± 0.5	34.0 ± 3.2
$\mu\,W\gamma$: $\Delta\kappa = 0,\ \lambda = 0$ (SM)	2.4 ± 0.2	1.9 ± 0.2	0.5 ± 0.1
$\mu\,W\gamma$: $\Delta\kappa = 7,\ \lambda = 0$	6.0 ± 0.6	2.5 ± 0.2	3.5 ± 0.3
$\mu\,W\gamma$: $\Delta\kappa = 0,\ \lambda = 3$	7.3 ± 0.7	2.3 ± 0.2	5.0 ± 0.5
$\mu\,W\gamma$: $\Delta\kappa = 5,\ \lambda = 5$	22.6 ± 2.2	3.1 ± 0.3	19.5 ± 1.9

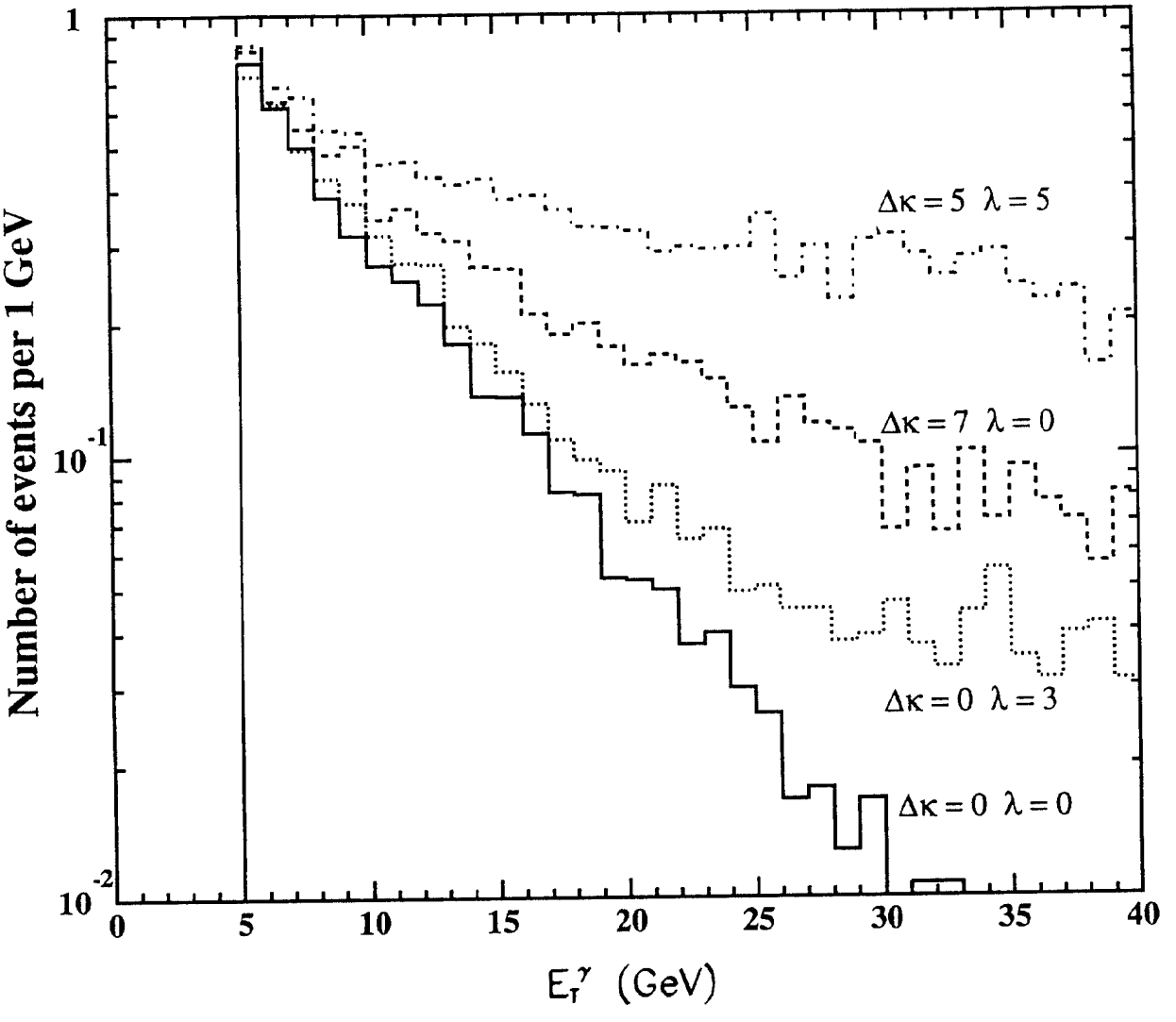

Figure 17: Monte Carlo E_T^γ predictions for various $\mathcal{CP}$–conserving $WW\gamma$ anomalous couplings. The Standard Model prediction is $\Delta\kappa = 0$, $\lambda = 0$.

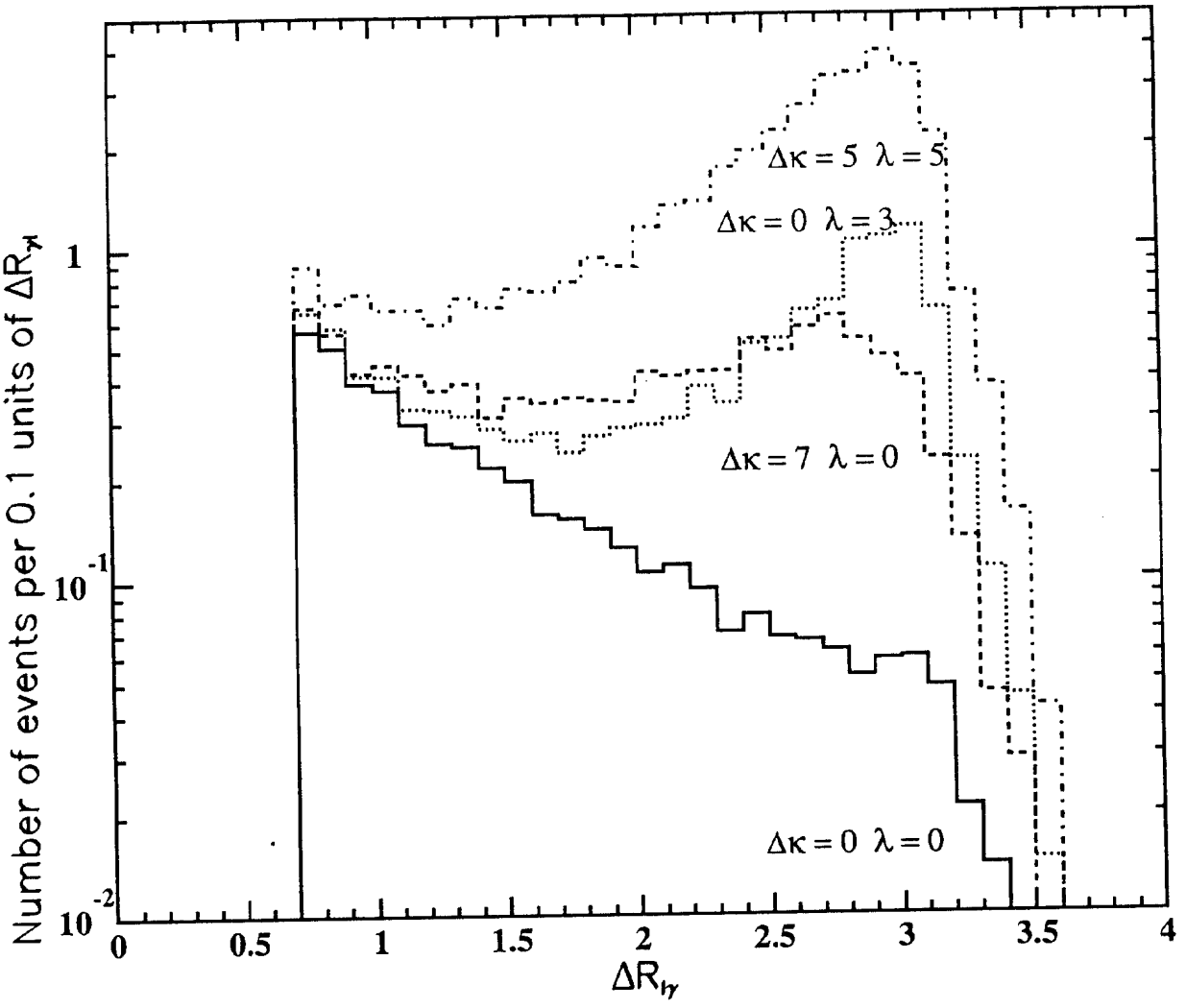

Figure 18: Monte Carlo $\Delta R_{\ell\gamma}$ predictions for various $\mathcal{CP}$–conserving $WW\gamma$ anomalous couplings. The Standard Model prediction is $\Delta\kappa = 0$, $\lambda = 0$.

Operationally, we determined the experimental 68% and 95% CL limits on $WW\gamma$, $ZZ\gamma$ and $Z\gamma\gamma$ anomalous couplings by using the Baur $W\gamma$ and $Z\gamma$ Monte Carlo event generator programs to step through a matrix of (x, y) *pairs* of anomalous parameter values. In general, since there are *four* independent anomalous coupling parameters (x, y, u, v) for $WW\gamma$, $ZZ\gamma$ and $Z\gamma\gamma$ anomalous couplings, we restricted our analysis to obtain limits on $\mathcal{CP}-$conserving anomalous couplings, assuming the $\mathcal{CP}-$violating anomalous couplings to be zero, and to obtain limits on $\mathcal{CP}-$violating anomalous couplings, assuming the $\mathcal{CP}-$conserving anomalous couplings to be zero. For the $Z+\gamma$ case, we additionally restricted our analysis to obtain limits on $ZZ\gamma$ anomalous couplings, assuming the $Z\gamma\gamma$ anomalous couplings to be zero, and *vice-versa*. Note that the $W+\gamma$ $(Z+\gamma)$ experimental results in fact impose simultaneous constraints on *all* $WW\gamma$ ($ZZ\gamma$ and $Z\gamma\gamma$) anomalous couplings, respectively. However, a fully-generalized analysis of this nature is beyond the scope of this paper.

The Monte Carlo $W\gamma$ $(Z\gamma)$ four-vector data for each pair of anomalous coupling parameters was analyzed with the use of the fast $W\gamma$ $(Z\gamma)$ Monte Carlo detector simulation programs. We recorded all kinematic/geometrical acceptances, the MC $\sigma \cdot B(V_\ell+\gamma)_{gen,cuts}$ cross sections and the predicted number of MC e or μ events passing all cuts for each $W\gamma$ $(Z\gamma)$ decay channel, for each point in the (x, y) anomalous couplings plane. This included recording *all* statistical uncertainties associated with these variables. For $W\gamma$, the Baur MC was run with non-zero values of anomalous parameters with a form factor scale $\Lambda_W = 10$ TeV and form factor power $n = 2$ (see equation 6). The $W\gamma$ cross section results are negligbly different if a form factor scale $\Lambda_W = 1$ TeV is chosen, since the parton SF luminosities for very large Bjorken-x ($x \geq 0.5$) contribute negligibly to the overall $W\gamma$ cross section at our center-of-mass energy. Only for $\Lambda_W \leq 500$ GeV is the $W\gamma$ cross section influenced in a significant way. For $Z\gamma$, the anomalous contributions to the helicity amplitudes rise much faster with energy than those in the $W\gamma$ case. This results in a much greater sensitivity to the form factor scale Λ_Z. We therefore used three sets of form factor scales: $\Lambda_Z = 250$, 500 and 750 GeV with $n = 3$ $(n = 4)$ for $h^V_{30,10}$ $(h^V_{40,20})$, respectively (see equation 14). In this manner the three-dimensional $\mathcal{N}_{sig}(V_\ell+\gamma)$ and $\sigma \cdot B(V_\ell+\gamma)$ surfaces as a function of (x, y) anomalous couplings pairs were determined.

Each set of the matrix of MC $\mathcal{N}_{sig}(V_\ell + \gamma)$ (x, y) or (u, v) data points was then fit using MINUIT [63] to obtain a three-dimensional analytic description of the $\mathcal{N}_{sig}(V_\ell + \gamma)$ surface in the (x, y) or (u, v) anomalous couplings plane. The most general form for this surface, for four independent anomalous coupling parameters (x, y, u, v) is given by:

$$z(x, y, u, v) = z_{SM} + ax + bx^2 + cy + dy^2 + ex \cdot y + \beta u^2 + \delta v^2 + \epsilon u \cdot v \qquad (36)$$

where (x, y) represent $\mathcal{CP}-$conserving anomalous couplings and (u, v) represent $\mathcal{CP}-$violating anomalous couplings. No higher-order terms in (x, y, u, v) are needed, since the overall invariant amplitude $\mathcal{M}_{V\gamma}$ containing the anomalous contributions to the $V+\gamma$ process is *linear* in the anomalous coupling parameters. The terms in equation 36 that are linear in (x, y) arise from interference of the $\mathcal{CP}-$conserving anomalous coupling contribution in the overall invariant amplitude with the Standard Model contribution. Note that no such interference occurs between the $\mathcal{CP}-$violating anomalous coupling terms and the Standard Model term, nor is there any interference between $\mathcal{CP}-$conserving and $\mathcal{CP}-$violating anomalous coupling terms [11, 17]. The terms proportional to xy (uv) arise from interference between the two independent $\mathcal{CP}-$conserving ($\mathcal{CP}-$violating) anomalous contributions, x and y (u and v) respectively. Note that for the two-dimensional case of (x, y) anomalous couplings, or for the two-dimensional case of (u, v) anomalous couplings, the above expression describes the surface of an elliptic paraboloid.

For the $\mathcal{CP}$−conserving ($\mathcal{CP}$−violating) case there are six (four) free parameters associated with describing this surface, and therefore a minumum of six (four) discrete results for $\mathcal{N}_{sig}(V_\ell+\gamma)$ or $\sigma \cdot B(V_\ell + \gamma)$ are required. Operationally, at least nine such data points were used to over-determine each surface, using non-zero anomalous coupling parameter values in the neighborhood of anticipated 95% CL limits. The MINUIT fits to each data set returned the fitted values of the parameters z_{SM}, $a - e$ (or z_{SM}, $\beta - \epsilon$) and their uncertainties. In general the χ^2/N_{dof} of each of the fits are extremely good. Two examples of the fitted values of these coefficients are (a) the $\mathcal{N}_{sig}(W+\gamma)_{e+\mu}$ surface for $\mathcal{CP}$−conserving anomalous couplings:

$$\mathcal{N}_{sig}^{WV\gamma}(\Delta\kappa,\lambda) = 6.95 - 0.07\Delta\kappa + 0.20(\Delta\kappa)^2 + 0.09\lambda + 1.42\lambda^2 + 0.63(\Delta\kappa\cdot\lambda) \qquad (37)$$

and (b) the $\mathcal{N}_{sig}(Z+\gamma)_{e+\mu}$ surface for $\mathcal{CP}$−conserving anomalous couplings, for $\Lambda_Z = 500$ GeV:

$$\mathcal{N}_{sig}^{Z\gamma}(h_{30}^Z, h_{40}^Z) = 2.01 + 1.61\times 10^{-5}\ h_{30}^Z + 0.12(h_{30}^Z)^2 + 0.01h_{40}^Z + 1.76(h_{40}^Z)^2 - 0.77(h_{30}^Z\cdot h_{40}^Z) \quad (38)$$

The determination of the 68% and 95% CL limits on $WW\gamma$, $ZZ\gamma$, $Z\gamma\gamma$ anomalous couplings was accomplished by comparing the Monte Carlo prediction, $\mathcal{N}_{sig}(V_\ell+\gamma)_{MC}$ with the experimental result, $\mathcal{N}_{sig}(V_\ell+\gamma)_{expt}$ for each case. For the each of the four individual and combined $e+\mu$ channels, the analytic expression obtained from the MINUIT fit of the $\mathcal{N}_{sig}(V_\ell+\gamma)_{MC}$ surface is shifted relative to its nominal central value by $-\Delta\mathcal{N}_{sig}(V_\ell+\gamma)_{MC}$, as given by the relevant entry in the first column of Table 17. The intersection of the *plane* containing the 68% or 95% upper CL limit on the experimental $\mathcal{N}_{sig}(V_\ell+\gamma)_{expt}$ with the -1σ shifted MC $\mathcal{N}_{sig}(V_\ell+\gamma)_{MC}$ surface determines the limit contours for the anomalous coupling parameters for each case.

7.2 Direct Limits on $WW\gamma$ Anomalous Couplings

The 68% and 95% CL limits on $WW\gamma$ anomalous couplings for the electron, muon and $e+\mu$ combined $W\gamma$ results are summarized in Tables 20 - 22. Figures 19a - 19f show the projections of the predicted $\mathcal{N}_{sig}(W+\gamma)_{MC}$ surface on the $\Delta\kappa$ and λ axes for the $\mathcal{CP}$−conserving $WW\gamma$ anomalous couplings for the electron, muon and $e+\mu$ combined result. (The corresponding curves for the $\mathcal{CP}$−violating $WW\gamma$ anomalous couplings $\tilde{\kappa}$, $\tilde{\lambda}$ are very similar.) The solid curve indicates the central value of the prediction, the upper and lower dotted curves indicate the overall $\pm1\sigma$ (stat+syst) uncertainties on the Monte Carlo prediction. The central value of the electron, muon and $e+\mu$ combined $\mathcal{N}_{sig}(W+\gamma)_{expt}$ result is shown as a solid horizontal line in each figure. The $\pm1\sigma$ (stat+syst) uncertainties are shown as dotted horizontal lines. The 95% CL upper limit to $\mathcal{N}_{sig}(W+\gamma)_{expt}$ is indicated as a solid horizontal line in each figure.

The experimental limits on the λ, $\tilde{\lambda}$ parameters are more stringent than those for $\Delta\kappa$, $\tilde{\kappa}$ because the anomalous contributions to the $W\gamma$ helicity amplitudes grow like $\sqrt{\hat{s}}/M_W$ for $\Delta\kappa$, $\tilde{\kappa}$ and $(\sqrt{\hat{s}}/M_W)^2$ for λ, $\tilde{\lambda}$.

The 68% and 95% CL contours for $\mathcal{CP}$−conserving and $\mathcal{CP}$−violating $WW\gamma$ anomalous couplings for the individual electron, muon and $e+\mu$ combined results are shown in Figs. 20a − 20f. For the $\mathcal{CP}$−conserving $WW\gamma$ anomalous couplings, note that there exist possible non-SM values of $\Delta\kappa$ and λ where the magnetic dipole moment, μ_W and the electric quadrupole moment, Q_W^e of the W boson vanish separately:

$$\begin{aligned} &\text{The } Q_W^e \text{ axis, where } \mu_W = 0: \quad \lambda = -(\Delta\kappa+2) \\ &\text{The } \mu_W \text{ axis, where } Q_W^e = 0: \quad \lambda = (\Delta\kappa+1) \end{aligned}$$

and one point, $(\Delta\kappa,\ \lambda) = (-\frac{3}{2},\ -\frac{1}{2})$ where both quantities vanish simultaneously. This point is contained within the experimental 68% CL limit contour. Similarly, for the $\mathcal{CP}-$violating $WW\gamma$ anomalous couplings, note that there exist possible non-SM values of $\tilde{\kappa}$ and $\tilde{\lambda}$ where the electric dipole moment, d_W and the magnetic quadrupole moment, Q_W^m of the W boson vanish separately:

$$\begin{aligned} \text{The } Q_W^m \text{ axis, where } d_W &= 0: \quad \tilde{\lambda} = -\tilde{\kappa} \\ \text{The } d_W \text{ axis, where } Q_W^m &= 0: \quad \tilde{\lambda} = \tilde{\kappa} \end{aligned}$$

and one point, $(\tilde{\kappa},\ \tilde{\lambda}) = (0,\ 0)$ where both quantities vanish simultaneously. This point is contained within the experimental 68% CL limit contour. Note also the relative orientation of the contour limits in the $\Delta\kappa - \lambda$ ($\tilde{\kappa} - \tilde{\lambda}$) plane with respect to the $\Delta\kappa$ and λ axes ($\tilde{\kappa}$ and $\tilde{\lambda}$ axes), indicating the magnitude of the interference effects present between these pairs anomalous parameters at our center-of-mass energy, $\sqrt{s} = 1.8$ TeV. The contour limits on $WW\gamma$ anomalous couplings are more (less) stringent when constructive (destructive) interference occurs between pairs of anomalous couplings.

Table 20: Electron channel limits on $WW\gamma$ anomalous couplings. The $\pm 1\sigma$, 68% and 95% CL limits on $\Delta\kappa$, λ, $\tilde{\kappa}$ and $\tilde{\lambda}$ are given. For each entry in the Table, all other $WW\gamma$ anomalous couplings are assumed to be at their SM values. For the $\pm 1\sigma$ limits, the first uncertainty is the overall statistical uncertainty (*stat*); the second is the overall systematic uncertainty (*syst*); the third uncertainty is the combined (*stat* + *syst*) uncertainty. See text for further details.

$\mathcal{CP}-$Conserving Couplings	$\mathcal{CP}-$Violating Couplings
$\Delta\kappa = 0.0^{+4.6}_{-4.2} \pm 1.2 = 0.0^{+4.8}_{-4.4}$	$\tilde{\kappa} = 0.0^{+4.4}_{-4.4} \pm 1.2 = 0.0^{+4.6}_{-4.6}$
$-3.5 < \Delta\kappa < +3.9$ (68% CL)	$-3.7 < \tilde{\kappa} < +3.7$ (68% CL)
$-6.5 < \Delta\kappa < +6.9$ (95% CL)	$-6.7 < \tilde{\kappa} < +6.7$ (95% CL)
$\lambda = 0.0^{+1.7}_{-1.7} \pm 0.5 = 0.0^{+1.7}_{-1.8}$	$\tilde{\lambda} = 0.0^{+1.7}_{-1.7} \pm 0.5 = 0.0^{+1.7}_{-1.7}$
$-1.4 < \lambda < +1.4$ (68% CL)	$-1.4 < \tilde{\lambda} < +1.4$ (68% CL)
$-2.6 < \lambda < +2.6$ (95% CL)	$-2.6 < \tilde{\lambda} < +2.6$ (95% CL)

Table 21: Muon channel limits on $WW\gamma$ anomalous couplings. The $\pm 1\sigma$, 68% and 95% CL limits on $\Delta\kappa$, λ, $\tilde{\kappa}$ and $\tilde{\lambda}$ are given. For each entry in the Table, all other $WW\gamma$ anomalous couplings are assumed to be at their SM values. For the $\pm 1\sigma$ limits, the first uncertainty is the overall statistical uncertainty (*stat*); the second is the overall systematic uncertainty (*syst*); the third uncertainty is the combined (*stat* + *syst*) uncertainty. See text for further details.

$\mathcal{CP}$−Conserving Couplings	$\mathcal{CP}$−Violating Couplings
$\Delta\kappa = 0.0^{+6.1}_{-5.9} \pm 0.9 = 0.0^{+6.2}_{-6.0}$	$\tilde{\kappa} = 0.0^{+6.0}_{-6.0} \pm 0.9 = 0.0^{+6.1}_{-6.1}$
$-5.2 < \Delta\kappa < +5.4$ (68% CL)	$-5.3 < \tilde{\kappa} < +5.3$ (68% CL)
$-8.6 < \Delta\kappa < +8.8$ (95% CL)	$-8.7 < \tilde{\kappa} < +8.7$ (95% CL)
$\lambda = 0.0^{+2.2}_{-2.3} \pm 0.4 = 0.0^{+2.2}_{-2.3}$	$\tilde{\lambda} = 0.0^{+2.3}_{-2.3} \pm 0.4 = 0.0^{+2.3}_{-2.3}$
$-2.0 < \lambda < +1.9$ (68% CL)	$-2.0 < \tilde{\lambda} < +2.0$ (68% CL)
$-3.3 < \lambda < +3.2$ (95% CL)	$-3.2 < \tilde{\lambda} < +3.2$ (95% CL)

Table 22: $e + \mu$ combined limits on $WW\gamma$ anomalous couplings. The $\pm 1\sigma$, 68% and 95% CL limits on $\Delta\kappa$, λ, $\tilde{\kappa}$ and $\tilde{\lambda}$ are given. For each entry in the Table, all other $WW\gamma$ anomalous couplings are assumed to be at their SM values. For the $\pm 1\sigma$ limits, the first uncertainty is the overall statistical uncertainty (*stat*); the second is the overall systematic uncertainty (*syst*); the third uncertainty is the combined (*stat* + *syst*) uncertainty. See text for further details.

$\mathcal{CP}$−Conserving Couplings	$\mathcal{CP}$−Violating Couplings
$\Delta\kappa = 0.0^{+4.4}_{-4.0} \pm 1.0 = 0.0^{+4.5}_{-4.1}$	$\tilde{\kappa} = 0.0^{+4.2}_{-4.2} \pm 1.0 = 0.0^{+4.3}_{-4.3}$
$-3.4 < \Delta\kappa < +3.7$ (68% CL)	$-3.5 < \tilde{\kappa} < +3.5$ (68% CL)
$-6.0 < \Delta\kappa < +6.4$ (95% CL)	$-6.2 < \tilde{\kappa} < +6.2$ (95% CL)
$\lambda = 0.0^{+1.6}_{-1.6} \pm 0.4 = 0.0^{+1.6}_{-1.7}$	$\tilde{\lambda} = 0.0^{+1.6}_{-1.6} \pm 0.4 = 0.0^{+1.6}_{-1.6}$
$-1.4 < \lambda < +1.3$ (68% CL)	$-1.3 < \tilde{\lambda} < +1.3$ (68% CL)
$-2.4 < \lambda < +2.3$ (95% CL)	$-2.4 < \tilde{\lambda} < +2.4$ (95% CL)

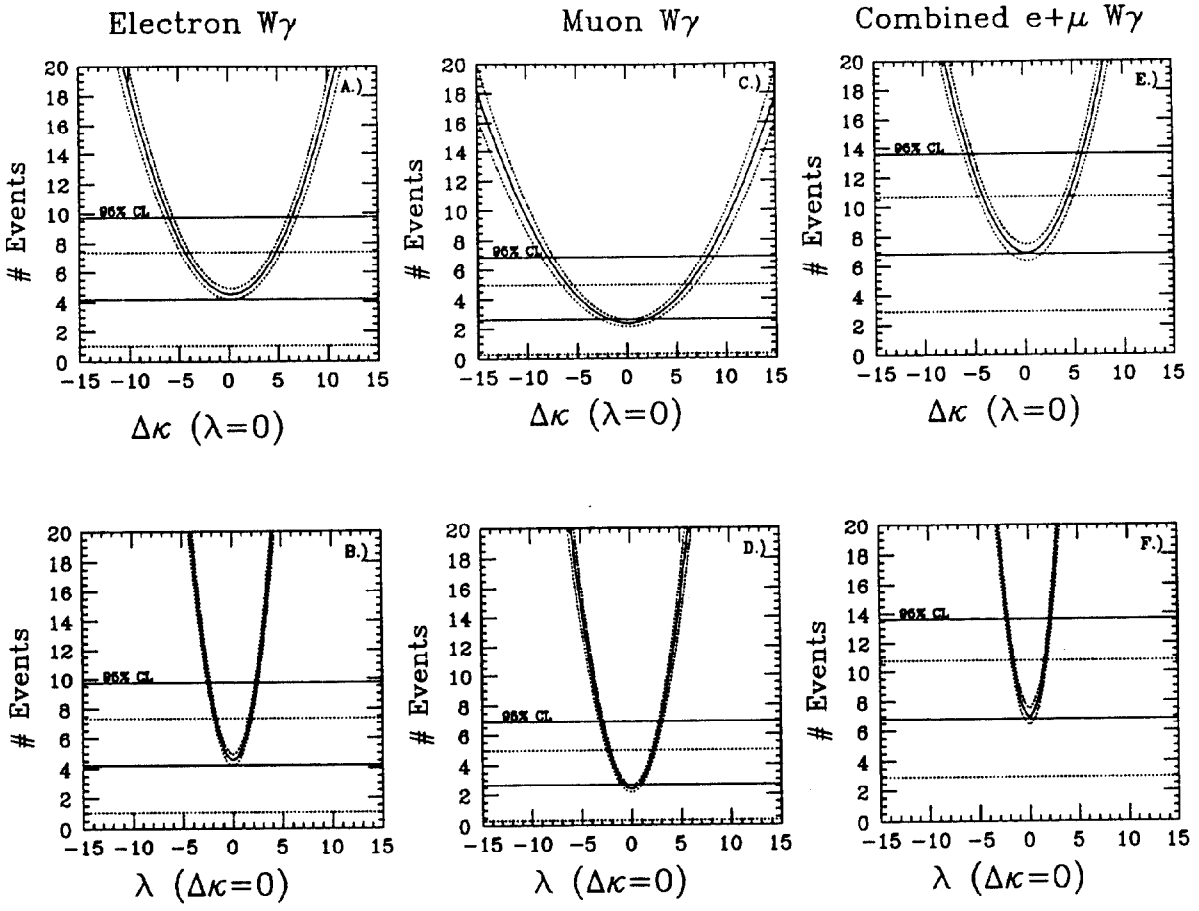

Figure 19: Direct limits on $\mathcal{CP}$−conserving $WW\gamma$ anomalous couplings. (A) $\mathcal{N}_{sig}(W+\gamma)$ as a function of $\Delta\kappa$ for electron $W\gamma$. (B) $\mathcal{N}_{sig}(W+\gamma)$ as a function of λ for electron $W\gamma$. (C) $\mathcal{N}_{sig}(W+\gamma)$ as a function of $\Delta\kappa$ for muon $W\gamma$. (D) $\mathcal{N}_{sig}(W+\gamma)$ as a function of λ for muon $W\gamma$. (E) $\mathcal{N}_{sig}(W+\gamma)$ as a function of $\Delta\kappa$ for $e+\mu$ $W\gamma$. (F) $\mathcal{N}_{sig}(W+\gamma)$ as a function of λ for $e+\mu$ $W\gamma$. Shown in each of these figures, are the central value (solid horizontal line) and its associated $\pm 1\sigma$ $(stat + syst)$ uncertainty (dotted horizontal lines) for the measured $\mathcal{N}_{sig}(W+\gamma)$ and the 95% CL upper limits on the measured $\mathcal{N}_{sig}(W+\gamma)$ (solid horizontal lines). The solid curve in each figure is the central value of the theoretical prediction for $\mathcal{N}_{sig}(W+\gamma)$ as a function of the $\mathcal{CP}$−conserving $WW\gamma$ anomalous couplings $\Delta\kappa$, λ. The dotted curves are the $\pm 1\sigma$ overall systematic uncertainties on the theoretical prediction. Only one $WW\gamma$ anomalous coupling is assumed to be non-zero at a time. The corresponding curves for $\mathcal{CP}$−violating $WW\gamma$ anomalous couplings are very similar. See text for further details.

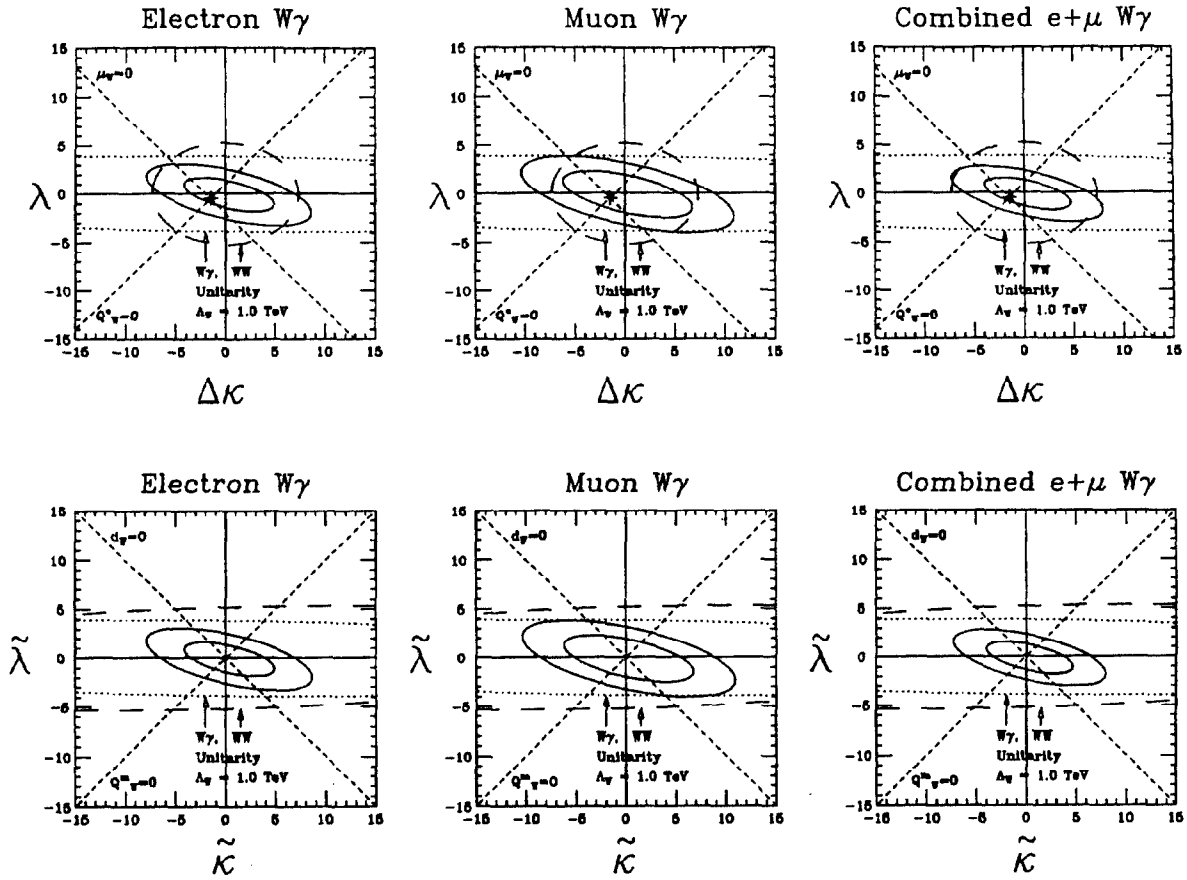

Figure 20: Contour limits on $\mathcal{CP}-$conserving and $\mathcal{CP}-$violating $WW\gamma$ anomalous coupling pairs. The solid ellipses show the 68% and 95% CL contour limits for the electron, muon and combined $e+\mu$ results for $\mathcal{CP}-$conserving and $\mathcal{CP}-$violating $WW\gamma$ anomalous coupling pairs. The orientation of these contours relative to the anomalous coupling axes is due to interference effects between these parameters in the overall invariant amplitude $\mathcal{M}_{W\gamma}$ for the $W+\gamma$ process. The SM prediction for each plot occurs at $(0,0)$. For the $\mathcal{CP}-$conserving couplings, the global minimum of the anomalous coupling surface is displaced slightly from the SM prediction due to interference effects between the SM and these anomalous coupling contributions to the overall invariant amplitude for $W\gamma$ production in $\sqrt{s} = 1.8$ TeV $\bar{\text{p}}$-p collisions. No such displacement occurs for $\mathcal{CP}-$violating $WW\gamma$ anomalous couplings. For the $\mathcal{CP}-$conserving couplings, the μ_W/μ_W^o ($Q_W^e = 0$) and Q_W^e/Q_W^{eo} ($\mu_W = 0$) axes are indicated by (orthogonal) dashed lines, intersecting at the point $(\Delta\kappa,\ \lambda) = (-3/2,\ -1/2)$. For the $\mathcal{CP}-$violating couplings, the d_W/d_W^o ($Q_W^m = 0$) and Q_W^m/Q_W^{mo} ($d_W = 0$) axes are indicated by (orthogonal) dashed lines, intersecting at the point $(\tilde{\kappa},\ \tilde{\lambda}) = (0,\ 0)$. The $W\gamma$ and W^+W^- unitarity limits are indicated by dotted and dashed curves, respectively for a form factor scale $\Lambda_W = 1$ TeV. See text for further details.

7.2.1 Unitarity Constraints for $W\gamma$ – Form Factor Scale Λ_W Sensitivity

Partial wave unitarity places restrictions on the reduced amplitudes, $A^W_{\lambda_W\lambda_\gamma}$ for arbitrary values of $WW\gamma$ anomalous couplings. There are in fact two such unitarity restrictions, one associated with $W+\gamma$ production and another associated with W^+W^- production, for both $\mathcal{CP}-$conserving and $\mathcal{CP}-$violating $WW\gamma$ anomalous couplings. Both physics processes impose unitarity constraints, because both processes occur *e.g.* in high-energy $\bar{\text{p}}$-p collisions [64].

The unitarity restriction for $\mathcal{CP}-$conserving $WW\gamma$ anomalous couplings for $W+\gamma$ production is [10, 12]:

$$\sum_{\lambda_W\lambda_\gamma}\left|A^W_{\lambda_W\lambda_\gamma}\right|^2 < \frac{3\sin^2\theta_W}{\alpha^2(\hat{s})\left(1-\frac{M_W^2}{\hat{s}}\right)} \tag{39}$$

where λ_W, λ_γ are the final-state W boson and photon helicities, respectively. For the assumed generalized dipole form factor and form factor power ($n=2$), unitarity is violated in the $W+\gamma$ process if

$$\frac{(\frac{\hat{s}}{M_W^2}-1)}{(1+\frac{\hat{s}}{\Lambda_W^2})^4}\left[(\Delta\kappa+\lambda)^2+\left(\frac{\hat{s}}{M_W^2}\right)\left(\Delta\kappa\left(\frac{M_W^2}{\hat{s}}\right)+\lambda\right)^2\right] \geq \frac{6\sin^2\theta_W}{\alpha^2(\hat{s})} \tag{40}$$

over the $\sqrt{\hat{s}}$ range $M_W < \sqrt{\hat{s}} < 1.8$ TeV.

The unitarity restriction for $\mathcal{CP}-$conserving $WW\gamma$ anomalous couplings for W^+W^- production is [10, 12]:

$$\sum_{\lambda_{W^+}\lambda_{W^-}}\left|A^W_{\lambda_{W^+}\lambda_{W^-}}\right|^2 < \frac{3\,(3-6\sin^2\theta_W+8\sin^4\theta_W)}{5\alpha^2(\hat{s})\left(1-\frac{4M_W^2}{\hat{s}}\right)^{\frac{3}{2}}} \tag{41}$$

where λ_{W^+}, λ_{W^-} are the final-state W^+, W^- boson helicities, respectively. For the assumed dipole form factor, unitarity is violated in the W^+W^- process if

$$\frac{(1-\frac{4M_W^2}{\hat{s}})^{\frac{3}{2}}}{(1+\frac{\hat{s}}{\Lambda_W^2})^4}\left[\left(\frac{\hat{s}}{M_W^2}\right)(\Delta\kappa+\lambda)^2+\frac{1}{2}\left(\frac{\hat{s}}{M_W^2}\right)^2\lambda^2+\frac{1}{4}\left(\frac{\hat{s}}{M_W^2}\right)^2\Delta\kappa^2\right] \geq \frac{3\,(3-6\sin^2\theta_W+8\sin^4\theta_W)}{5\alpha^2(\hat{s})} \tag{42}$$

over the $\sqrt{\hat{s}}$ range $2M_W < \sqrt{\hat{s}} < 1.8$ TeV.

If only one anomalous $WW\gamma$ coupling is assumed to be non-zero at a time, then for $\Lambda_W >> M_W$ and the assumed dipole form factor ($n=2$), the unitarity limits are:

$$\begin{aligned} W\gamma: \quad & |\Delta\kappa| < \tfrac{37.1\ \text{TeV}}{\Lambda_W} \qquad |\lambda| < \tfrac{3.9\ \text{TeV}^2}{\Lambda_W^2} \\ W^+W^-: \quad & |\Delta\kappa| < \tfrac{7.3\ \text{TeV}^2}{\Lambda_W^2} \qquad |\lambda| < \tfrac{5.3\ \text{TeV}^2}{\Lambda_W^2} \end{aligned}$$

For $W+\gamma$ production, the unitarity restriction for $\mathcal{CP}-$violating $WW\gamma$ anomalous couplings is of the same form as that for $\mathcal{CP}-$conserving $WW\gamma$ anomalous couplings [10, 12]:

$$\sum_{\lambda_W\lambda_\gamma}\left|A^W_{\lambda_W\lambda_\gamma}\right|^2 < \frac{3\sin^2\theta_W}{\alpha^2(\hat{s})\left(1-\frac{M_W^2}{\hat{s}}\right)} \tag{43}$$

For the assumed dipole form factor, unitarity is violated in the $W+\gamma$ process if

$$\frac{(\frac{\hat{s}}{M_W^2}-1)}{(1+\frac{\hat{s}}{\Lambda_W^2})^4}\left[\left(\tilde{\kappa}+\tilde{\lambda}\right)^2+\left(\frac{\hat{s}}{M_W^2}\right)\left(\tilde{\kappa}\left(\frac{M_W^2}{\hat{s}}\right)+\tilde{\lambda}\right)^2\right] \geq \frac{6\sin^2\theta_W}{\alpha^2(\hat{s})} \tag{44}$$

over the $\sqrt{\hat{s}}$ range $M_W < \sqrt{\hat{s}} < 1.8$ TeV. For W^+W^- production, the unitarity restriction for $\mathcal{CP}-$violating $WW\gamma$ anomalous couplings is [10, 12]:

$$\sum_{\lambda_{W^+}\lambda_{W^-}}\left|A^W_{\lambda_{W^+}\lambda_{W^-}}\right|^2 < \frac{3\,(3-6\sin^2\theta_W+8\sin^4\theta_W)}{5\alpha^2(\hat{s})\left(1-\frac{4M_W^2}{\hat{s}}\right)^{\frac{3}{2}}} \tag{45}$$

For the assumed dipole form factor, unitarity is violated in the W^+W^- process if

$$\frac{(1-\frac{4M_W^2}{\hat{s}})^{\frac{1}{2}}}{(1+\frac{\hat{s}}{\Lambda_W^2})^4}\left[\left(\frac{\hat{s}}{M_W^2}\right)\left(\tilde{\kappa}-\tilde{\lambda}\right)^2+2\left\{\tilde{\kappa}+\left(1-\frac{1}{2}\frac{\hat{s}}{M_W^2}\right)\tilde{\lambda}\right\}^2\right] \geq \frac{3\,(3-6\sin^2\theta_W+8\sin^4\theta_W)}{5\alpha^2(\hat{s})} \tag{46}$$

over the $\sqrt{\hat{s}}$ range $2M_W < \sqrt{\hat{s}} < 1.8$ TeV.

If only one anomalous $WW\gamma$ coupling is assumed to be non-zero at a time, then for $\Lambda_W >> M_W$ and the assumed dipole form factor ($n=2$), the unitarity limits are:

$$\begin{aligned} W\gamma: \quad & |\tilde{\kappa}| < \tfrac{37.1\ \text{TeV}}{\Lambda_W} \qquad |\tilde{\lambda}| < \tfrac{3.9\ \text{TeV}^2}{\Lambda_W^2} \\ W^+W^-: \quad & |\tilde{\kappa}| < \tfrac{35.0\ \text{TeV}}{\Lambda_W} \qquad |\tilde{\lambda}| < \tfrac{5.3\ \text{TeV}^2}{\Lambda_W^2} \end{aligned}$$

In Figs. 20a – 20f, the contours for the $W\gamma$ (W^+W^-) unitarity limits on $WW\gamma$ anomalous couplings are indicated by dotted (dashed) curves, respectively, for a form factor scale $\Lambda_W = 1.0$ TeV. For this value of Λ_W, the region exterior to these curves is excluded by unitarity. If the scale Λ_W is decreased (increased), the area enclosed by the unitarity curves is increased (decreased). The enclosed area of the unitarity curves doubles (halves) if values of $\Lambda_W = 0.8\,(1.5)$ TeV are chosen, respectively. For the $e+\mu$ combined results, our 95% CL contours are entirely contained within both $W\gamma$ and W^+W^- unitarity contours for $\Lambda_W \simeq 970$ GeV.

The $W\gamma$ and W^+W^- unitarity limits as a function of Λ_W for $\mathcal{CP}-$conserving and $\mathcal{CP}-$violating $WW\gamma$ anomalous couplings are shown in Figs. 21 and 22, respectively. The region above the unitarity curve in each figure is excluded. Superimposed on these plots are the combined $e+\mu$ 68% and 95% CL limits on each of the anomalous couplings as indicated by the dotted and solid curves, respectively. The region above the experimental curves is excluded. In the small Λ_W region the experimental results are more stringent than the unitarity constraint, whereas in the large Λ_W region the converse is true. Note that our experimental results are essentially independent of the form factor scale for Λ_W above a few hundred GeV. Note also that the experimental limits on anomalous couplings must *simultaneously* obey both $W\gamma$ unitarity *and* W^+W^- unitarity constraints, since both processes are operative in $\sqrt{s} = 1.8$ TeV $\bar{\text{p}}$-p collisions. In each of these figures, the value of Λ_W where the experimental curves cross the unitarity curve is the limit of experimental sensitivity to that particular anomalous coupling and Λ_W-scale. For form factor scales

$$\begin{aligned} \Lambda_W^{\Delta\kappa} &\geq 1.0\ \text{TeV} \qquad \Lambda_W^{\lambda} \geq 1.2\ \text{TeV} \\ \Lambda_W^{\tilde{\kappa}} &\geq 5.0\ \text{TeV} \qquad \Lambda_W^{\tilde{\lambda}} \geq 1.2\ \text{TeV} \end{aligned}$$

the unitarity limit is more stringent than our $e + \mu$ combined 95% CL limits on $WW\gamma$ anomalous couplings, assuming only one such coupling to be non-zero at a time. These form factor scales correspond to distance scale sensitivities $L_W = \hbar c/\Lambda_W$ for probing possible internal structure of the W boson of order:

$$L_W^{\Delta\kappa} \leq 2.0 \times 10^{-4} \text{ fm} = .0.08\ \lambda\!\!\!^{-}_W \qquad L_W^{\lambda} \leq 1.6 \times 10^{-4} \text{ fm} = 0.07\ \lambda\!\!\!^{-}_W$$

$$L_W^{\tilde{\kappa}} \leq 0.4 \times 10^{-4} \text{ fm} = 0.02\ \lambda\!\!\!^{-}_W \qquad L_W^{\tilde{\lambda}} \leq 1.6 \times 10^{-4} \text{ fm} = 0.07\ \lambda\!\!\!^{-}_W$$

where $\lambda\!\!\!^{-}_W = \hbar/M_W c$ is the reduced Compton wavelength of the W boson.

The unitarity bounds and the Λ_W scale sensitivity have some model-dependence associated with the choice of the form factor power n used in the generalized form factor. For example, we have chosen $n = 2$ for the form factor power in this analysis, motivated by the well-known behavior of the nucleon form factors. If instead, a value of $n = 1$ is chosen for the form factor power, the unitarity bounds on $WW\gamma$ anomalous couplings are made a factor of ~ 4 times more stringent; the corresponding Λ_W–scale sensitivity is reduced by a factor of ~ 2 [10]. The experimental limits are not significantly changed for $n = 1$.

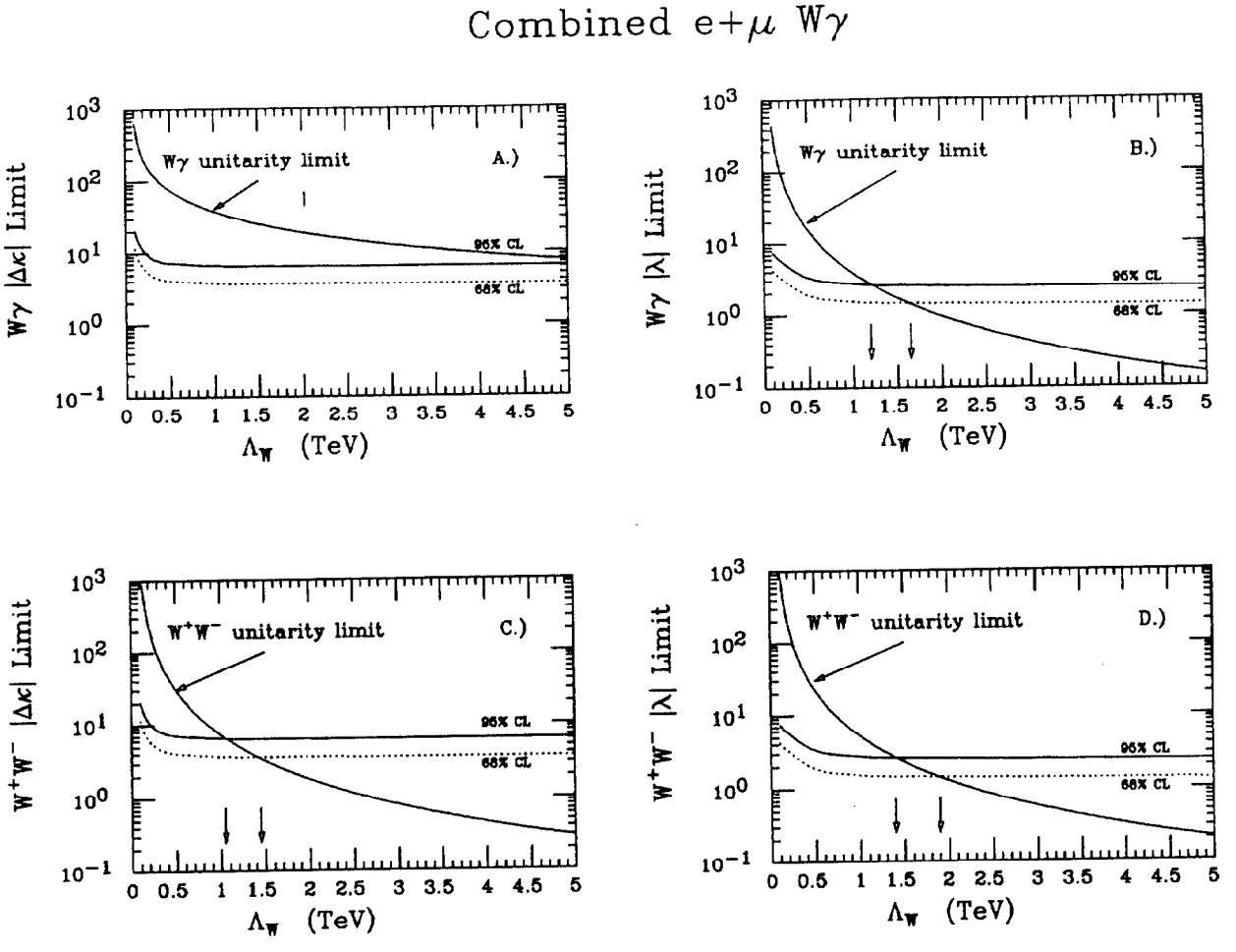

Figure 21: Unitarity limits as a function of Λ_W for $\mathcal{CP}$–conserving $WW\gamma$ anomalous couplings. (A) $|\Delta\kappa|$ unitarity limit as a function of form factor scale Λ_W. (B) $|\lambda|$ unitarity limit as a function of form factor scale Λ_W. (C) $|\Delta\kappa|$ unitarity limit as a function of form factor scale Λ_W. (D) $|\lambda|$ unitarity limit as a function of form factor scale Λ_W. Only one $WW\gamma$ anomalous coupling is assumed to be non-zero at a time. Also shown in each figure are the experimental $e + \mu$ combined 68% and 95% CL limits (dotted and solid curves, respectively) on $|\Delta\kappa|$ (or $|\lambda|$) as a function of form factor scale Λ_W. The downward-pointing arrows indicate the value of Λ_W associated with the intersection of the experimental limits with the unitarity curve in each figure. See text for further details.

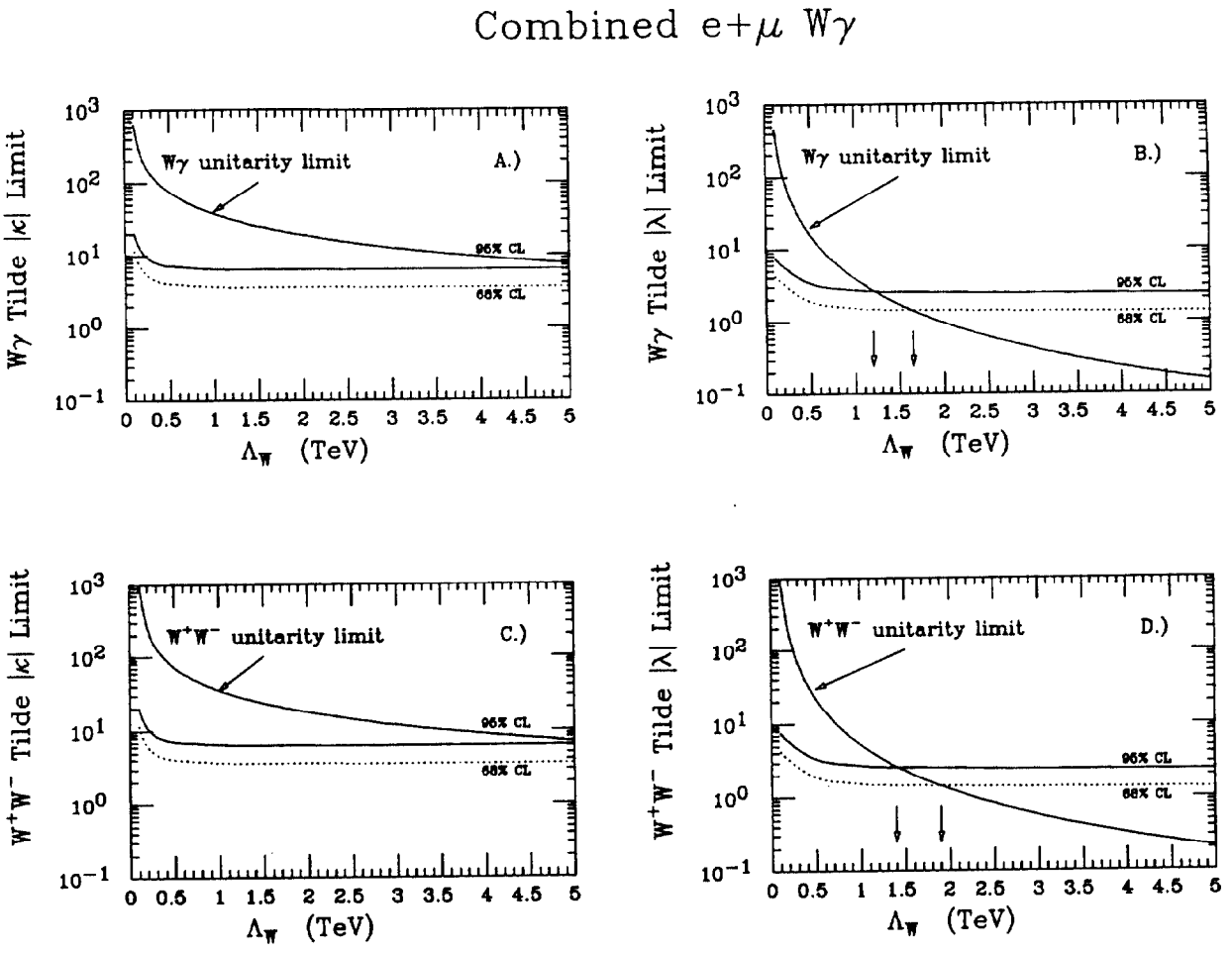

Figure 22: Unitarity limits as a function of Λ_W for $\mathcal{CP}-$violating $WW\gamma$ anomalous couplings. (A) $|\tilde{\kappa}|$ unitarity limit as a function of form factor scale Λ_W. (B) $|\tilde{\lambda}|$ unitarity limit as a function of form factor scale Λ_W. (C) $|\tilde{\kappa}|$ unitarity limit as a function of form factor scale Λ_W. (D) $|\tilde{\lambda}|$ unitarity limit as a function of form factor scale Λ_W. Only one $WW\gamma$ anomalous coupling is assumed to be non-zero at a time. Also shown in each figure are the experimental $e+\mu$ combined 68% and 95% CL limits (dotted and solid curves, respectively) on $|\tilde{\kappa}|$ (or $|\tilde{\lambda}|$) as a function of form factor scale Λ_W. The downward-pointing arrows indicate the value of Λ_W associated with the intersection of the experimental limits with the unitarity curve in each figure. See text for further details.

7.2.2 Direct Limits on the W Boson Higher-Order Electromagnetic Moments and Mean-Squared Charge Radius

Experimental limits on $WW\gamma$ anomalous couplings also place bounds on the higher-order electromagnetic moments of the W boson and the W boson mean-squared charge radius. These quantities are related to the anomalous coupling parameters, in the static limit (and with $\hbar = c = 1$) by:

$$\mu_W = \frac{e}{2M_W}(2 + \Delta\kappa + \lambda) \quad (47)$$

$$Q_W^e = -\frac{e}{M_W^2}(1 + \Delta\kappa - \lambda) \quad (48)$$

$$d_W = \frac{e}{2M_W}(\tilde{\kappa} + \tilde{\lambda}) \quad (49)$$

$$Q_W^m = -\frac{e}{M_W^2}(\tilde{\kappa} - \tilde{\lambda}) \quad (50)$$

$$<R_W^2> = \frac{1}{M_W^2}(1 + \Delta\kappa + \lambda) \quad (51)$$

Recall that the Standard Model tree-level values of the $WW\gamma$ anomalous couplings are: $\Delta\kappa = 1 - \kappa = \lambda = \tilde{\kappa} = \tilde{\lambda} = 0$. It is illuminating to calculate the numerical values associated with the following classical parameters:

$$\mu_W^o = \frac{e\hbar}{2M_W} = 3.691 \pm 0.012 \times 10^{-16} \text{ MeV/T}$$

$$Q_W^{eo} = -e\lambda\!\!\!^{-2}_W = -6.063 \pm 0.041 \times 10^{-6}\ e - \text{fm}^2$$

$$d_W^o = \tfrac{1}{2}e\lambda\!\!\!^{-}_W = 1.231 \pm 0.004 \times 10^{-3}\ e - \text{fm}$$

$$Q_W^{mo} = -\frac{e\hbar^2}{M_W^2 c} = -1.818 \pm 0.012 \times 10^{-18} \text{ MeV–fm/T}$$

$$<R_W^{o2}> = \lambda\!\!\!^{-2}_W = 6.063 \pm 0.041 \times 10^{-6} \text{ fm}^2$$

$$\lambda\!\!\!^{-}_W = \frac{\hbar}{M_W c} = 2.462 \pm 0.008 \times 10^{-3} \text{ fm}$$

Note that the uncertainties associated with these classical quantities for the W boson are due primarily to the uncertainty on the W boson mass, $M_W = 80.14 \pm 0.27$ GeV/c^2 (the combined CDF+UA2 result) [47, 65].

We define the following dimensionless (scaled) classical quantities for the W boson:

$$g_W - 2 \equiv \frac{\mu_W}{\mu_W^o} - 2 = \Delta\kappa + \lambda \quad (52)$$

$$q_W^e - 1 \equiv \frac{Q_W^e}{Q_W^{eo}} - 1 = \Delta\kappa - \lambda \quad (53)$$

$$\delta_W \equiv \frac{d_W}{d_W^o} = \tilde{\kappa} + \tilde{\lambda} \quad (54)$$

$$q_W^m \equiv \frac{Q_W^m}{Q_W^{mo}} = \tilde{\kappa} - \tilde{\lambda} \quad (55)$$

$$r_W^2 - 1 \equiv \frac{<R_W^2>}{<R_W^{o2}>} - 1 = \Delta\kappa + \lambda \quad (56)$$

The individual electron, muon and the combined $e + \mu$ limits on the W boson electromagnetic moments and mean-squared charge radius, are summarized in Tables 23 - 25. Figures 23a – 23f show the 68% and 95% CL limit contours for the $\mathcal{CP}$–conserving and $\mathcal{CP}$–violating higher-order

electromagnetic moments of the W boson. The corresponding $W+\gamma$ (W^+W^-) unitarity limits on these quantities are also shown on these figures, for a form factor scale of $\Lambda_W = 1.0$ TeV, as indicated by the dotted (dashed) curves, respectively.

Table 23: Electron channel limits on higher-order W boson EM moments. The $\pm 1\sigma$, 68% and 95% CL limits on $g_W - 2$, $q^e_W - 1$, δ_W, q^m_W and $r^2_W - 1$ are given. For each entry in the Table, all other W boson EM moments are assumed to be at their SM values. For the $\pm 1\sigma$ limits, the first uncertainty is the overall statistical uncertainty (*stat*); the second is the overall systematic uncertainty (*syst*); the third uncertainty is the combined (*stat* + *syst*) uncertainty. See text for further details.

$\mathcal{CP}$–Conserving Couplings	$\mathcal{CP}$–Violating Couplings
$g_W - 2 = 0.0^{+2.7}_{-2.7} \pm 0.7 = 0.0^{+2.8}_{-2.8}$	$\delta_W = 0.0^{+2.7}_{-2.7} \pm 0.7 = 0.0^{+2.8}_{-2.8}$
$-2.2 < g_W - 2 < +2.2$ (68% CL)	$-2.2 < \delta_W < +2.2$ (68% CL)
$-4.1 < g_W - 2 < +4.1$ (95% CL)	$-4.1 < \delta_W < +4.1$ (95% CL)
$q^e_W - 1 = 0.0^{+4.2}_{-3.9} \pm 1.0 = 0.0^{+4.4}_{-4.1}$	$q^m_W - 1 = 0.0^{+4.1}_{-4.1} \pm 1.0 = 0.0^{+4.2}_{-4.2}$
$-3.3 < q^e_W - 1 < +3.5$ (68% CL)	$-3.4 < q^m_W < +3.4$ (68% CL)
$-6.0 < q^e_W - 1 < +6.3$ (95% CL)	$-6.2 < q^m_W < +6.2$ (95% CL)
$r^2_W - 1 = 0.0^{+2.7}_{-2.7} \pm 0.7 = 0.0^{+2.8}_{-2.8}$	
$-2.2 < r^2_W - 1 < +2.2$ (68% CL)	
$-4.1 < r^2_W - 1 < +4.1$ (95% CL)	

Table 24: Muon channel limits on higher-order W boson EM moments. The $\pm 1\sigma$, 68% and 95% CL limits on $g_W - 2$, $q^e_W - 1$, δ_W, q^m_W and $r^2_W - 1$ are given. For each entry in the Table, all other W boson EM moments are assumed to be at their SM values. For the $\pm 1\sigma$ limits, the first uncertainty is the overall statistical uncertainty (*stat*); the second is the overall systematic uncertainty (*syst*); the third uncertainty is the combined (*stat* + *syst*) uncertainty. See text for further details.

$\mathcal{CP}$–Conserving Couplings	$\mathcal{CP}$–Violating Couplings
$g_W - 2 = 0.0^{+3.5}_{-3.6} \pm 0.5 = 0.0^{+3.6}_{-3.6}$	$\delta_W = 0.0^{+3.6}_{-3.6} \pm 0.5 = 0.0^{+3.6}_{-3.6}$
$-3.2 < g_W - 2 < +3.1$ (68% CL)	$-3.1 < \delta_W < +3.1$ (68% CL)
$-5.2 < g_W - 2 < +5.1$ (95% CL)	$-5.1 < \delta_W < +5.1$ (95% CL)
$q^e_W - 1 = 0.0^{+5.5}_{-5.1} \pm 0.7 = 0.0^{+5.5}_{-5.2}$	$q^m_W - 1 = 0.0^{+5.3}_{-5.3} \pm 0.7 = 0.0^{+5.3}_{-5.3}$
$-4.5 < q^e_W - 1 < +4.8$ (68% CL)	$-4.7 < q^m_W < +4.7$ (68% CL)
$-7.5 < q^e_W - 1 < +7.8$ (95% CL)	$-7.6 < q^m_W < +7.6$ (95% CL)
$r^2_W - 1 = 0.0^{+3.5}_{-3.6} \pm 0.5 = 0.0^{+3.6}_{-3.6}$	
$-3.2 < r^2_W - 1 < +3.1$ (68% CL)	
$-5.2 < r^2_W - 1 < +5.1$ (95% CL)	

Table 25: $e+\mu$ combined limits on higher-order W boson EM moments. The $\pm 1\sigma$, 68% and 95% CL limits on $g_W - 2$, $q_W^e - 1$, δ_W, q_W^m and $r_W^2 - 1$ are given. For each entry in the Table, all other W boson EM moments are assumed to be at their SM values. For the $\pm 1\sigma$ limits, the first uncertainty is the overall statistical uncertainty ($stat$); the second is the overall systematic uncertainty ($syst$); the third uncertainty is the combined ($stat + syst$) uncertainty. See text for further details.

$\mathcal{CP}$–Conserving Couplings	$\mathcal{CP}$–Violating Couplings
$g_W - 2 = 0.0 \,^{+2.5}_{-2.5} \pm 0.6 = 0.0 \,^{+2.6}_{-2.6}$	$\delta_W = 0.0 \,^{+2.5}_{-2.5} \pm 0.6 = 0.0 \,^{+2.6}_{-2.6}$
$-2.1 < g_W - 2 < +2.1$ (68% CL)	$-2.1 < \delta_W < +2.1$ (68% CL)
$-3.7 < g_W - 2 < +3.7$ (95% CL)	$-3.7 < \delta_W < +3.7$ (95% CL)
$q_W^e - 1 = 0.0 \,^{+4.0}_{-3.7} \pm 0.9 = 0.0 \,^{+4.1}_{-3.8}$	$q_W^m - 1 = 0.0 \,^{+3.8}_{-3.8} \pm 0.9 = 0.0 \,^{+3.9}_{-3.9}$
$-3.0 < q_W^e - 1 < +3.4$ (68% CL)	$-3.2 < q_W^m < +3.2$ (68% CL)
$-5.5 < q_W^e - 1 < +5.8$ (95% CL)	$-5.6 < q_W^m < +5.6$ (95% CL)
$r_W^2 - 1 = 0.0 \,^{+2.5}_{-2.5} \pm 0.5 = 0.0 \,^{+2.6}_{-2.6}$	
$-2.1 < r_W^2 - 1 < +2.1$ (68% CL)	
$-3.7 < r_W^2 - 1 < +3.7$ (95% CL)	

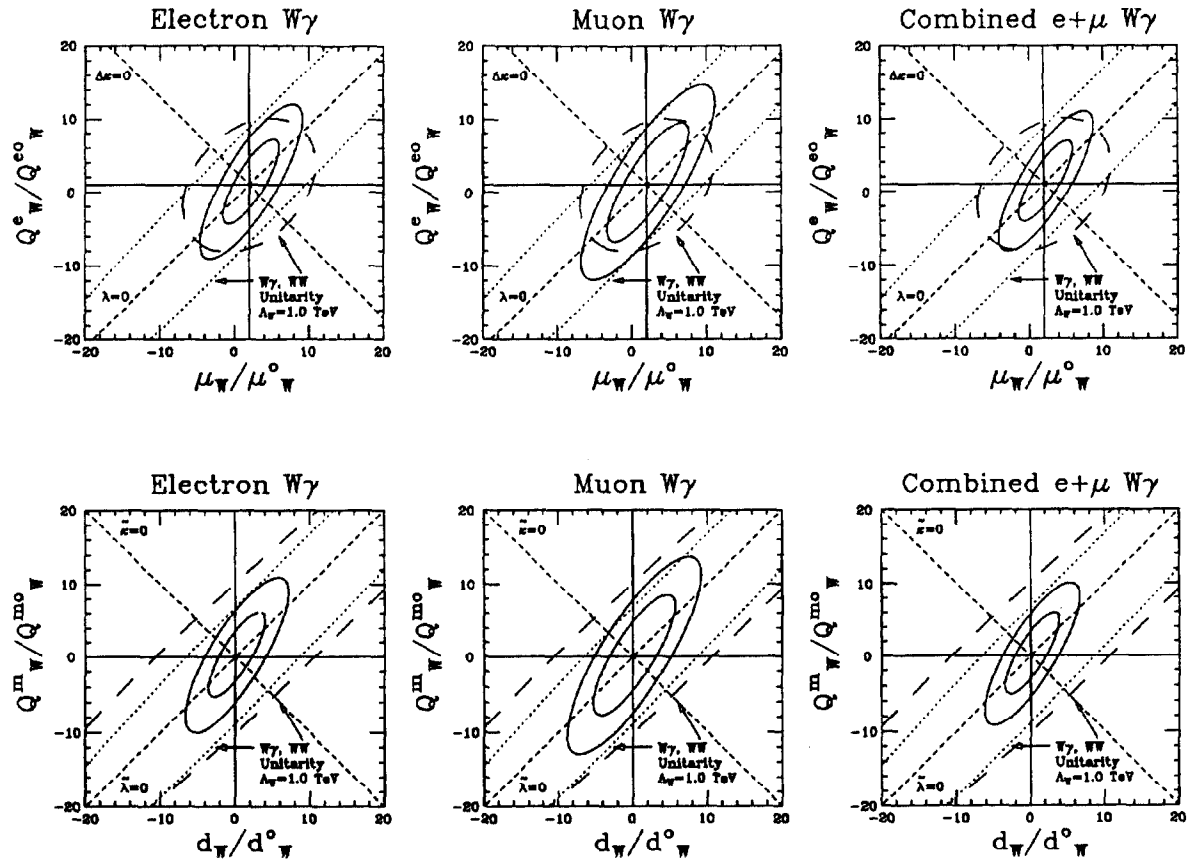

Figure 23: Contour limits on $\mathcal{CP}-$conserving and $\mathcal{CP}-$violating W boson higher-order EM moments. The solid ellipses show the 68% and 95% CL contour limits for the electron, muon and combined $e+\mu$ results for $\mathcal{CP}-$conserving and $\mathcal{CP}-$violating W boson higher-order EM moments. For the $\mathcal{CP}-$conserving moments, the tree-level SM prediction is $\mu_W/\mu_W^\circ = 2$ and $Q_W^e/Q_W^{e\circ} = 1$. The $\Delta\kappa$ ($\lambda = 0$) and λ ($\Delta\kappa = 0$) axes are indicated by (orthogonal) dashed lines, intersecting at the point $(\mu_W/\mu_W^\circ,\ Q_W^e/Q_W^{e\circ}) = (2,\ 1)$. For the $\mathcal{CP}-$violating moments, the tree-level SM prediction is $d_W/d_W^\circ = 0$ and $Q_W^m/Q_W^{m\circ} = 0$. The $\tilde{\kappa}$ ($\tilde{\lambda} = 0$) and $\tilde{\lambda}$ ($\tilde{\kappa} = 0$) axes are indicated by (orthogonal) dashed lines, intersecting at the point $(d_W/d_W^\circ,\ Q_W^m/Q_W^{m\circ}) = (0,\ 0)$. The $W\gamma$ and W^+W^- unitarity limits are indicated by dotted and dashed curves, respectively for a form factor scale $\Lambda_W = 1$ TeV. See text for further details.

7.2.3 Comparison with Existing Limits on $WW\gamma$ Anomalous Couplings

Indirect limits on $WW\gamma$ anomalous couplings can be obtained from precision low-energy experiments. For $\mathcal{CP}-$conserving $WW\gamma$ anomalous couplings $\Delta\kappa$ and λ, the most stringent low-energy constraint on these parameters has been extracted from the precision measurement of the muon $g_\mu - 2$ anomaly [66, 67, 68]. However, these low-energy bounds on $\Delta\kappa$ and λ are quite model-dependent [69] and are also sensitive to the cutoff used to regulate divergences and to the regularization scheme used in the loop calculation [70].

More stringent indirect bounds on $\Delta\kappa$ and λ have been derived from the photon propagator as measured at PETRA [72] and the W/Z mass ratio [67, 73]. However these bounds are also controversial because loop corrections are ill-defined in these cases. For example, for the W/Z mass ratio the limits on $\Delta\kappa$ and λ are expressed in terms of deviations of the $\rho-$parameter, $\rho = M_W^2/M_Z^2\cos^2\theta_W$ from its tree-level SM value of $\rho = 1$. However, the $\rho-$parameter is also sensitive to SM electroweak radiative corrections (e.g. M_{top}, M_{Higgs}) and loop corrections due to other possible deviations from the (minimal) SM, such as heavy W' and/or Z' bosons.

No rigorous bounds on $WW\gamma$ anomalous couplings can be obtained from high-precision measurements in the $Z-$resonance region from LEP-I e^+e^- data if correlations between different contributions to the anomalous couplings are fully taken into account, as there exist ambiguities and model-dependencies in the results [74, 75, 76]. Assuming there are no significant cancellations among various one-loop contributions, present data on the S, T and U parameters [77] (or equivalently the ϵ_1, ϵ_2 and ϵ_3 parameters [78]), imply constraints on the $\Delta\kappa$ and λ parameters of order $|\Delta\kappa|$, $|\lambda| \leq 0.5 - 1.5$ at the 90% CL [76, 79].

The UA2 Collaboration has recently published direct limits on $\Delta\kappa$ and λ from an analysis of 13 pb^{-1} of $\bar{p}\,p \to e^\pm\nu\gamma$ electron data [80]. A total of 16 $W\gamma$ candidate events were found, passing central photon selection requirements of $E_T^\gamma > 4.5$ GeV and lepton-photon angular separation $\Delta\theta_{e\gamma}^{open} > 15°$, with an expected background of 6.8 ± 1.0 events, leading to a $W\gamma$ signal of $9.2 \pm 4.0(stat) \pm 1.0(syst)$ events. The UA2 Collaboration analyzed their data by comparing the number of signal events to the number of predicted events. A second method, comparing the observed E_T^γ spectrum to MC expectations was also used. For the latter method, the UA2 experiment obtained limits on $\Delta\kappa$ and λ, assuming only one $WW\gamma$ anomalous coupling to be non-zero at a time, of

$$\Delta\kappa = 0.0^{+2.6}_{-2.2}\ \ (stat + syst) \qquad \lambda = 0.0^{+1.7}_{-1.8}\ \ (stat + syst)$$

The corresponding 95% CL limits on these quantities are:

$$-4.5 < \Delta\kappa < +4.9 \qquad -3.6 < \lambda < +3.5$$

Note that the correlations between $\Delta\kappa$ and λ are much stronger for $\sqrt{s} = 630$ GeV than at the Tevatron. As a consequence of these interference effects, the orientation of the UA2 68% (95%) CL limit contours in the $\Delta\kappa - \lambda$ plane are rotated significantly more with respect to the $\Delta\kappa - \lambda$ axes than our corresponding 68% (95%) CL limit contours (see Fig. 24). Note further that the *area* contained within our $e + \mu$ combined 68% (95%) contours in the $\Delta\kappa - \lambda$ plane is approximately 50% of that contained within the corresponding UA2 68% (95%) contours, which were obtained using their E_T^γ method. The area contained within these contours is in fact the most appropriate measure for comparison of $\Delta\kappa - \lambda$ limits between the two experiments.

For $\mathcal{CP}/\mathcal{T}-$violating $WW\gamma$ anomalous couplings, $\tilde{\kappa}$ and $\tilde{\lambda}$, the most stringent low-energy constraint on these parameters has been extracted from the experimental upper limit on the electric

dipole moment (EDM) of the neutron, $d_n < 1.2 \times 10^{-12}\, e - \text{fm}$ (95% CL) [81]. The upper limit on the neutron EDM places indirect limits on $|\tilde{\kappa}|$, $|\tilde{\lambda}| < \mathcal{O}(10^{-3})$ [70, 71] unless extreme cancellation between these two parameters occurs [10]. These limits are also model-dependent, sensitive to the cutoff used to regulate divergences and are also dependent on the regularization scheme used in the loop calculation [70].

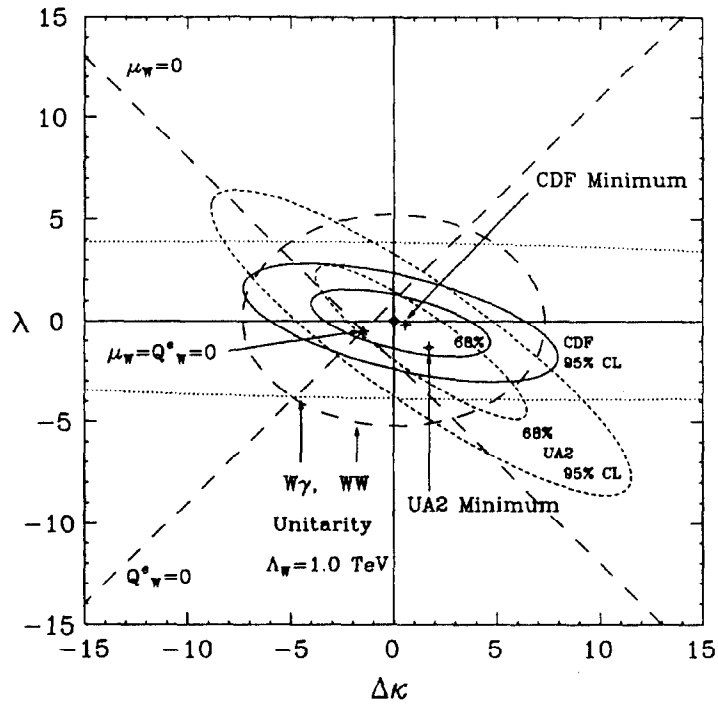

Figure 24: CDF and UA2 contour limits on $\mathcal{CP}$−conserving $WW\gamma$ anomalous couplings. The solid ellipses show the CDF combined $e + \mu$ 68% and 95% CL limits in the $\Delta\kappa - \lambda$ plane $\Delta\kappa - \lambda$ plane ($\sqrt{s}$ = 1.8 TeV). The dashed ellipses show the UA2 68% and 95% CL limits in the $\Delta\kappa - \lambda$ plane ($\sqrt{s}$ = 630 GeV). The difference in the orientation of the CDF and UA2 contours is due to energy-dependent interference effects between these parameters in the overall invariant amplitude $\mathcal{M}_{W\gamma}$ for the $W + \gamma$ process. The SM prediction is $\Delta\kappa = \lambda = 0$. The CDF and UA2 global minima for the $WW\gamma$ anomalous coupling $\mathcal{N}_{sig}(W + \gamma)$ surfaces are displaced from the SM prediction, due to energy-dependent interference effects between the SM and these anomalous coupling contributions to the overall invariant amplitude. The μ_W/μ_W° ($Q_W^e = 0$) and $Q_W^e/Q_W^{e\circ}$ ($\mu_W = 0$) axes are indicated in this figure by (orthogonal) dashed lines. The $W\gamma$ and W^+W^- unitarity limits are indicated by dotted and dashed curves, respectively for a form factor scale $\Lambda_W = 1$ TeV. See text for further details.

7.3 Direct Limits on Anomalous $ZZ\gamma$ and $Z\gamma\gamma$ Couplings

From the absence of an excess of high E_T^γ photons in electron and muon $Z\gamma$ events, we obtain direct limits on $ZZ\gamma$ and $Z\gamma\gamma$ anomalous couplings using the same methods as those used for obtaining direct limits on $WW\gamma$ anomalous couplings. As the phase space associated with exploring all possible combinations of $ZZ\gamma$ and $Z\gamma\gamma$ anomalous couplings is quite large, we limit our study to the consideration of pairs of non-zero $ZZ\gamma$ and/or $Z\gamma\gamma$ anomalous couplings. Specifically, we consider here only the following four possible cases:

$$\begin{aligned}
&(1)\ ZZ\gamma: \quad \text{only } h_{30}^Z \text{ and } h_{40}^Z \text{ non-zero}\\
&(2)\ ZZ\gamma: \quad \text{only } h_{10}^Z \text{ and } h_{20}^Z \text{ non-zero}\\
&(3)\ Z\gamma\gamma: \quad \text{only } h_{30}^\gamma \text{ and } h_{40}^\gamma \text{ non-zero}\\
&(4)\ Z\gamma\gamma: \quad \text{only } h_{10}^\gamma \text{ and } h_{20}^\gamma \text{ non-zero}
\end{aligned}$$

These choices are motivated by the fact that there are no interference effects between $\mathcal{CP}-$conserving anomalous couplings ($h_{30,40}^V$) and $\mathcal{CP}-$violating anomalous couplings ($h_{10,20}^V$) for $V = Z, \gamma$. Furthermore, the $ZZ\gamma$ anomalous couplings interfere only weakly with $Z\gamma\gamma$ anomalous couplings [17].

Because of the nature of the $ZZ\gamma$ and $Z\gamma\gamma$ vertex functions, the experimental limits we obtain for the $\mathcal{CP}-$conserving $ZZ\gamma$ anomalous couplings (case 1) will be nearly identical (to within $\sim 1\%$) of the limits we obtain for the $\mathcal{CP}-$violating $ZZ\gamma$ anomalous couplings (case 2). Similarly, the experimental limits we obtain for the case 3 will be nearly identical (to within $\sim 1\%$) of the limits we obtain for case 4. Finally, the limits on $Z\gamma\gamma$ anomalous couplings (cases 3 and 4) are $\sim 5\%$ higher than those for $ZZ\gamma$ (cases 1 and 2).

For the $Z+\gamma$ process, the dependence on the form factor scale Λ_Z is much greater than that for the $W+\gamma$ process. We compare our experimental measurements of $\mathcal{N}_{sig}(Z+\gamma)$ with $Z+\gamma$ Monte Carlo predictions for three different values of $\Lambda_Z = 250$, 500, and 750 GeV.

The 68% and 95% CL limits on $ZZ\gamma$ and $Z\gamma\gamma$ anomalous couplings for the electron, muon and $e+\mu$ combined results are summarized in Tables 26 - 28. Figures 25a - 25f show the projections of the predicted $\mathcal{N}_{sig}(Z+\gamma)_{MC}$ surface on the h_{30}^Z and h_{40}^Z axes for the $\mathcal{CP}-$conserving $ZZ\gamma$ anomalous couplings, for the electron, muon and $e+\mu$ combined results, and for $\Lambda_Z = 250$, 500, and 750 GeV. (The corresponding curves for the $\mathcal{CP}-$violating $ZZ\gamma$ anomalous couplings h_{10}^Z and h_{20}^Z are very similar, as well as the MC prediction for $Z\gamma\gamma$ anomalous couplings). The solid curve indicates the central value of the prediction, the upper and lower dotted curves indicate the overall $\pm 1\sigma$ (stat+syst) uncertainties on the Monte Carlo prediction. The central value of the electron, muon and $e+\mu$ combined $\mathcal{N}_{sig}(Z+\gamma)_{expt}$ result is shown as a solid horizontal line in each figure; the $\pm 1\sigma$ (stat+syst) uncertainties are shown as dotted horizontal lines. The 95% CL upper limit to $\mathcal{N}_{sig}(Z+\gamma)_{expt}$ is indicated as a solid horizontal line in each figure. The $ZZ\gamma$ unitarity constraints in each figure are discussed in Section 7.3.1 below.

The experimental limits on the $h_{40,20}^V$ parameters are more stringent than those for $h_{30,10}^V$ ($V = Z, \gamma$) because the anomalous contributions to the $Z\gamma$ helicity amplitudes grow like $(\sqrt{\hat{s}}/M_Z)^3$ for $h_{30,10}^V$ and $(\sqrt{\hat{s}}/M_Z)^5$ for $h_{40,20}^V$.

The 68% and 95% CL contours for $ZZ\gamma$ anomalous couplings for the combined $e+\mu$ $Z\gamma$ results are shown in Figs. 26a - 26c for $\Lambda_Z = 250$, 500 and 750 GeV, respectively. The corresponding contours for $Z\gamma\gamma$ anomalous couplings for the combined $e+\mu$ $Z\gamma$ results are shown in Figs. 26d

- 26f, respectively. The unitarity constraints in each figure are discussed in Section 7.3.1 below. Note also the relative orientation of the contour limits in the $h_{30}^V - h_{40}^V$ ($h_{10}^V - h_{20}^V$) plane with respect to the h_{i0}^V axes indicating the degree of interference effects present between these pairs anomalous parameters at our center-of-mass energy. The contour limits on $ZZ\gamma/Z\gamma\gamma$ anomalous couplings are more (less) stringent when constructive (destructive) interference occurs between pairs of anomalous couplings.

Table 26: Electron channel limits on $ZZ\gamma$ and $Z\gamma\gamma$ anomalous couplings. The $\pm 1\sigma$, 68% and 95% CL limits on the $ZZ\gamma$ and $Z\gamma\gamma$ $C\mathcal{P}-$conserving anomalous coupling parameters h_{30}^V and h_{40}^V ($V = Z, \gamma$) are given, for $\Lambda_Z = 250$, 500, and 750 GeV. These limits are also valid to within 1% for the $C\mathcal{P}-$violating parameters h_{10}^V and h_{20}^V by replacing $h_{30}^V \to h_{10}^V$ and $h_{40}^V \to h_{20}^V$. For each entry in the Table, all other $ZZ\gamma$ and $Z\gamma\gamma$ anomalous couplings are assumed to be at their SM values. For the $\pm 1\sigma$ limits, the first uncertainty is the overall statistical uncertainty (*stat*); the second is the overall systematic uncertainty (*syst*); the third uncertainty is the combined (*stat* + *syst*) uncertainty. Entries in the table which exceed the unitarity limit are indicated with a †. See text for further details.

	$ZZ\gamma$ Anomalous Couplings	$Z\gamma\gamma$ Anomalous Couplings
$\Lambda_Z = 250$ GeV	$h_{30}^Z = 0.0^{+18.7}_{-18.9} \pm 0.4 = 0.0^{+18.7}_{-18.9}$ $-15.9 < h_{30}^Z < +15.7$ (68% CL) $-26.3 < h_{30}^Z < +26.1$ (95% CL)	$h_{30}^\gamma = 0.0^{+19.7}_{-19.9} \pm 0.5 = 0.0^{+19.7}_{-19.9}$ $-16.7 < h_{30}^\gamma < +16.5$ (68% CL) $-27.6 < h_{30}^\gamma < +27.5$ (95% CL)
$\Lambda_Z = 250$ GeV	$h_{40}^Z = 0.0^{+15.9}_{-15.8} \pm 0.4 = 0.0^{+15.9}_{-15.8}$ $-13.3 < h_{40}^Z < +13.3$ (68% CL) $-22.0 < h_{40}^Z < +22.1$ (95% CL)	$h_{40}^\gamma = 0.0^{+16.7}_{-16.5} \pm 0.4 = 0.0^{+16.7}_{-16.5}$ $-13.9 < h_{40}^\gamma < +14.0$ (68% CL) $-23.1 < h_{40}^\gamma < +23.2$ (95% CL)
$\Lambda_Z = 500$ GeV	$h_{30}^Z = 0.0^{+4.9}_{-4.9} \pm 0.1 = 0.0^{+4.9}_{-4.9}$ $-4.1 < h_{30}^Z < +4.1$ (68% CL) $-6.8 < h_{30}^Z < +6.8$ (95% CL)	$h_{30}^\gamma = 0.0^{+5.2}_{-5.2} \pm 0.1 = 0.0^{+5.2}_{-5.2}$ $-4.3 < h_{30}^\gamma < +4.3$ (68% CL) $-7.2 < h_{30}^\gamma < +7.2$ (95% CL)
$\Lambda_Z = 500$ GeV	$h_{40}^Z = 0.0^{+1.3}_{-1.3} \pm 0.1 = 0.0^{+1.3}_{-1.3}$ $-1.1 < h_{40}^Z < +1.1^\dagger$ (68% CL) $-1.8 < h_{40}^Z < +1.8^\dagger$ (95% CL)	$h_{40}^\gamma = 0.0^{+1.3}_{-1.3} \pm 0.1 = 0.0^{+1.3}_{-1.3}$ $-1.1 < h_{40}^\gamma < +1.1^\dagger$ (68% CL) $-1.9 < h_{40}^\gamma < +1.9^\dagger$ (95% CL)
$\Lambda_Z = 750$ GeV	$h_{30}^Z = 0.0^{+2.9}_{-2.9} \pm 0.1 = 0.0^{+2.9}_{-2.9}$ $-2.4 < h_{30}^Z < +2.4$ (68% CL) $-4.0 < h_{30}^Z < +4.0^\dagger$ (95% CL)	$h_{30}^\gamma = 0.0^{+3.0}_{-3.0} \pm 0.1 = 0.0^{+3.0}_{-3.0}$ $-2.5 < h_{30}^\gamma < +2.5$ (68% CL) $-4.2 < h_{30}^\gamma < +4.2^\dagger$ (95% CL)
$\Lambda_Z = 750$ GeV	$h_{40}^Z = 0.0^{+0.4}_{-0.4} \pm 0.1 = 0.0^{+0.4}_{-0.4}$ $-0.4 < h_{40}^Z < +0.4^\dagger$ (68% CL) $-0.6 < h_{40}^Z < +0.6^\dagger$ (95% CL)	$h_{40}^\gamma = 0.0^{+0.4}_{-0.4} \pm 0.1 = 0.0^{+0.4}_{-0.4}$ $-0.4 < h_{40}^\gamma < +0.4^\dagger$ (68% CL) $-0.6 < h_{40}^\gamma < +0.6^\dagger$ (95% CL)

Table 27: Muon channel limits on $ZZ\gamma$ and $Z\gamma\gamma$ anomalous couplings. The $\pm 1\sigma$, 68% and 95% CL limits on the $ZZ\gamma$ and $Z\gamma\gamma$ $C\mathcal{P}$–conserving anomalous coupling parameters h_{30}^V and h_{40}^V ($V = Z, \gamma$) are given, for Λ_Z = 250, 500, and 750 GeV. These limits are also valid to within 1% for the $C\mathcal{P}$–violating parameters h_{10}^V and h_{20}^V by replacing $h_{30}^V \to h_{10}^V$ and $h_{40}^V \to h_{20}^V$. For each entry in the Table, all other $ZZ\gamma$ and $Z\gamma\gamma$ anomalous couplings are assumed to be at their SM values. For the $\pm 1\sigma$ limits, the first uncertainty is the overall statistical uncertainty (*stat*); the second is the overall systematic uncertainty (*syst*); the third uncertainty is the combined (*stat* + *syst*) uncertainty. Entries in the table which exceed the unitarity limit are indicated with a †. See text for further details.

	$ZZ\gamma$ Anomalous Couplings	$Z\gamma\gamma$ Anomalous Couplings
Λ_Z = 250 GeV	$h_{30}^Z = 0.0^{+31.6}_{-31.6} \pm 0.6 = 0.0^{+31.6}_{-31.6}$ $-28.5 < h_{30}^Z < +28.5$ (68% CL) $-40.8 < h_{30}^Z < +40.8$ (95% CL)	$h_{30}^\gamma = 0.0^{+33.1}_{-33.3} \pm 0.6 = 0.0^{+33.1}_{-33.3}$ $-29.9 < h_{30}^\gamma < +29.9$ (68% CL) $-42.9 < h_{30}^\gamma < +42.9$ (95% CL)
Λ_Z = 250 GeV	$h_{40}^Z = 0.0^{+26.4}_{-26.2} \pm 0.5 = 0.0^{+26.4}_{-26.2}$ $-23.6 < h_{40}^Z < +23.8$ (68% CL) $-33.9 < h_{40}^Z < +34.1$ (95% CL)	$h_{40}^\gamma = 0.0^{+27.7}_{-27.5} \pm 0.5 = 0.0^{+27.7}_{-27.5}$ $-24.8 < h_{40}^\gamma < +25.0$ (68% CL) $-35.6 < h_{40}^\gamma < +35.8$ (95% CL)
Λ_Z = 500 GeV	$h_{30}^Z = 0.0^{+7.9}_{-7.9} \pm 0.2 = 0.0^{+7.9}_{-7.9}$ $-7.1 < h_{30}^Z < +7.1$ (68% CL) $-10.2 < h_{30}^Z < +10.2^\dagger$ (95% CL)	$h_{30}^\gamma = 0.0^{+8.3}_{-8.3} \pm 0.2 = 0.0^{+8.3}_{-8.3}$ $-7.4 < h_{30}^\gamma < +7.4$ (68% CL) $-10.7 < h_{30}^\gamma < +10.7^\dagger$ (95% CL)
Λ_Z = 500 GeV	$h_{40}^Z = 0.0^{+2.0}_{-2.0} \pm 0.1 = 0.0^{+2.0}_{-2.0}$ $-1.8 < h_{40}^Z < +1.8^\dagger$ (68% CL) $-2.5 < h_{40}^Z < +2.5^\dagger$ (95% CL)	$h_{40}^\gamma = 0.0^{+2.1}_{-2.1} \pm 0.1 = 0.0^{+2.1}_{-2.1}$ $-1.8 < h_{40}^\gamma < +1.8^\dagger$ (68% CL) $-2.6 < h_{40}^\gamma < +2.6^\dagger$ (95% CL)
Λ_Z = 750 GeV	$h_{30}^Z = 0.0^{+4.4}_{-4.5} \pm 0.1 = 0.0^{+4.4}_{-4.5}$ $-4.0 < h_{30}^Z < +4.0^\dagger$ (68% CL) $-5.7 < h_{30}^Z < +5.7^\dagger$ (95% CL)	$h_{30}^\gamma = 0.0^{+4.7}_{-4.7} \pm 0.1 = 0.0^{+4.7}_{-4.7}$ $-4.2 < h_{30}^\gamma < +4.2^\dagger$ (68% CL) $-6.0 < h_{30}^\gamma < +6.0^\dagger$ (95% CL)
Λ_Z = 750 GeV	$h_{40}^Z = 0.0^{+0.6}_{-0.6} \pm 0.1 = 0.0^{+0.6}_{-0.6}$ $-0.6 < h_{40}^Z < +0.6^\dagger$ (68% CL) $-0.8 < h_{40}^Z < +0.8^\dagger$ (95% CL)	$h_{40}^\gamma = 0.0^{+0.7}_{-0.7} \pm 0.1 = 0.0^{+0.7}_{-0.7}$ $-0.6 < h_{40}^\gamma < +0.6^\dagger$ (68% CL) $-0.8 < h_{40}^\gamma < +0.8^\dagger$ (95% CL)

Table 28: $e + \mu$ combined limits on $ZZ\gamma$ and $Z\gamma\gamma$ anomalous couplings. The $\pm 1\sigma$, 68% and 95% CL limits on the $ZZ\gamma$ and $Z\gamma\gamma$ $C\mathcal{P}-$conserving anomalous coupling parameters h_{30}^V and h_{40}^V ($V = Z, \gamma$) are given, for $\Lambda_Z = 250$, 500, and 750 GeV. These limits are also valid to within 1% for the $C\mathcal{P}-$violating parameters h_{10}^V and h_{20}^V by replacing $h_{30}^V \to h_{10}^V$ and $h_{40}^V \to h_{20}^V$. For each entry in the Table, all other $ZZ\gamma$ and $Z\gamma\gamma$ anomalous couplings are assumed to be at their SM values. For the $\pm 1\sigma$ limits, the first uncertainty is the overall statistical uncertainty (*stat*); the second is the overall systematic uncertainty (*syst*); the third uncertainty is the combined (*stat* + *syst*) uncertainty. Entries in the table which exceed the unitarity limit are indicated with a †. See text for further details.

	$ZZ\gamma$ Anomalous Couplings	$Z\gamma\gamma$ Anomalous Couplings
$\Lambda_Z = 250$ GeV	$h_{30}^Z = 0.0^{+21.6}_{-21.8} \pm 0.4 = 0.0^{+21.6}_{-21.8}$ $-19.3 < h_{30}^Z < +19.2$ (68% CL) $-27.6 < h_{30}^Z < +27.5$ (95% CL)	$h_{30}^\gamma = 0.0^{+22.7}_{-22.9} \pm 0.4 = 0.0^{+22.7}_{-22.9}$ $-20.3 < h_{30}^\gamma < +20.2$ (68% CL) $-29.0 < h_{30}^\gamma < +29.0$ (95% CL)
$\Lambda_Z = 250$ GeV	$h_{40}^Z = 0.0^{+18.3}_{-18.1} \pm 0.5 = 0.0^{+18.3}_{-18.1}$ $-16.1 < h_{40}^Z < +16.2$ (68% CL) $-23.0 < h_{40}^Z < +23.2$ (95% CL)	$h_{40}^\gamma = 0.0^{+19.2}_{-19.0} \pm 0.5 = 0.0^{+19.2}_{-19.0}$ $-16.9 < h_{40}^\gamma < +17.0$ (68% CL) $-24.2 < h_{40}^\gamma < +24.4$ (95% CL)
$\Lambda_Z = 500$ GeV	$h_{30}^Z = 0.0^{+5.6}_{-5.6} \pm 0.1 = 0.0^{+5.6}_{-5.6}$ $-4.9 < h_{30}^Z < +4.9$ (68% CL) $-7.1 < h_{30}^Z < +7.1$ (95% CL)	$h_{30}^\gamma = 0.0^{+5.8}_{-5.8} \pm 0.1 = 0.0^{+5.8}_{-5.8}$ $-5.2 < h_{30}^\gamma < +5.2$ (68% CL) $-7.4 < h_{30}^\gamma < +7.4$ (95% CL)
$\Lambda_Z = 500$ GeV	$h_{40}^Z = 0.0^{+1.4}_{-1.4} \pm 0.1 = 0.0^{+1.4}_{-1.4}$ $-1.3 < h_{40}^Z < +1.3^\dagger$ (68% CL) $-1.8 < h_{40}^Z < +1.8^\dagger$ (95% CL)	$h_{40}^\gamma = 0.0^{+1.5}_{-1.5} \pm 0.1 = 0.0^{+1.5}_{-1.5}$ $-1.3 < h_{40}^\gamma < +1.3^\dagger$ (68% CL) $-1.9 < h_{40}^\gamma < +1.9^\dagger$ (95% CL)
$\Lambda_Z = 750$ GeV	$h_{30}^Z = 0.0^{+3.2}_{-3.2} \pm 0.1 = 0.0^{+3.2}_{-3.2}$ $-2.8 < h_{30}^Z < +2.8^\dagger$ (68% CL) $-4.1 < h_{30}^Z < +4.1^\dagger$ (95% CL)	$h_{30}^\gamma = 0.0^{+3.4}_{-3.4} \pm 0.1 = 0.0^{+3.4}_{-3.4}$ $-3.0 < h_{30}^\gamma < +3.0^\dagger$ (68% CL) $-4.3 < h_{30}^\gamma < +4.3^\dagger$ (95% CL)
$\Lambda_Z = 750$ GeV	$h_{40}^Z = 0.0^{+0.5}_{-0.5} \pm 0.1 = 0.0^{+0.5}_{-0.5}$ $-0.4 < h_{40}^Z < +0.4^\dagger$ (68% CL) $-0.6 < h_{40}^Z < +0.6^\dagger$ (95% CL)	$h_{40}^\gamma = 0.0^{+0.5}_{-0.5} \pm 0.1 = 0.0^{+0.5}_{-0.5}$ $-0.4 < h_{40}^\gamma < +0.4^\dagger$ (68% CL) $-0.6 < h_{40}^\gamma < +0.6^\dagger$ (95% CL)

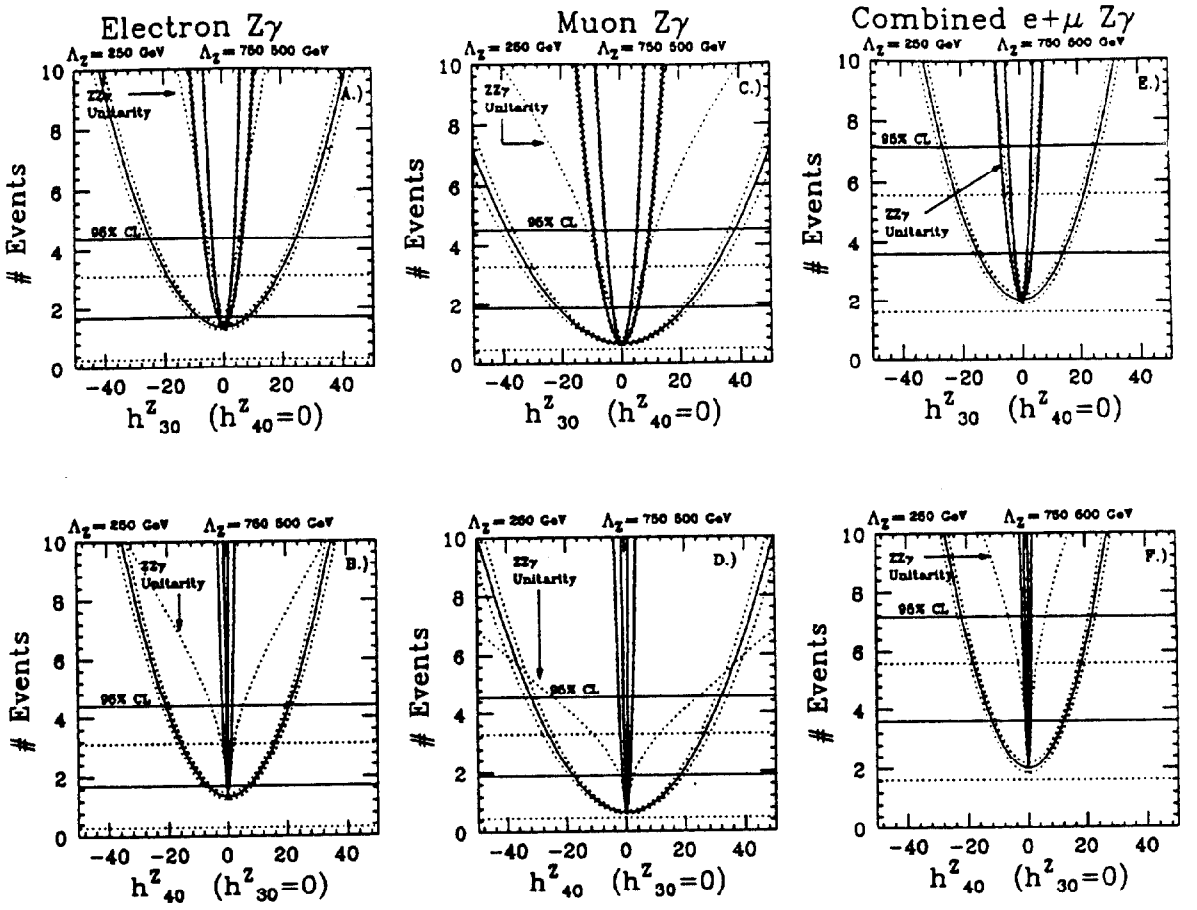

Figure 25: Direct limits on $ZZ\gamma$ and $Z\gamma\gamma$ anomalous couplings. (A) $\mathcal{N}_{sig}(Z+\gamma)$ as a function of h_{30}^Z for electron $Z\gamma$. (B) $\mathcal{N}_{sig}(Z+\gamma)$ as a function of h_{30}^Z for electron $Z\gamma$. (C) $\mathcal{N}_{sig}(Z+\gamma)$ as a function of h_{30}^Z for muon $Z\gamma$. (D) $\mathcal{N}_{sig}(Z+\gamma)$ as a function of h_{30}^Z for muon $Z\gamma$. (E) $\mathcal{N}_{sig}(Z+\gamma)$ as a function of h_{30}^Z for $e+\mu$ $Z\gamma$. (F) $\mathcal{N}_{sig}(Z+\gamma)$ as a function of h_{30}^Z for $e+\mu$ $Z\gamma$. Shown in each of these figures, are the central value (solid horizontal line) and its associated $\pm 1\sigma$ $(stat+syst)$ uncertainty (dotted horizontal lines) for the measured $\mathcal{N}_{sig}(Z+\gamma)$ and the 95% CL upper limits on the measured $\mathcal{N}_{sig}(Z+\gamma)$ (solid horizontal lines). The central values for three theoretical predictions for $\mathcal{N}_{sig}(Z+\gamma)$ for form factor scales Λ_Z = 250, 500, and 750 GeV as a function of h_{30}^Z or h_{40}^Z is shown as solid curve. The dotted curves are the $\pm 1\sigma$ overall systematic uncertainties on the theoretical prediction. Only one $ZZ\gamma$ anomalous coupling is assumed to be non-zero at a time. The unitarity limit for the relevant anomalous $ZZ\gamma$ coupling is also shown in each figure as a dotted curve. The region above each of these curves is excluded by unitarity. For $ZZ\gamma$ anomalous couplings, the individual electron, muon and combined $e+\mu$ limits on the $\mathcal{CP}-$conserving h_{30}^Z (h_{40}^Z) parameters are also valid for the $\mathcal{CP}-$violating h_{10}^Z (h_{20}^Z) parameters, respectively. The limits on $Z\gamma\gamma$ anomalous couplings are related to the limits on $ZZ\gamma$ anomalous couplings by $h_{i0}^\gamma \simeq 1.05 h_{i0}^Z$, for $i = 1-4$. The unitarity bound for $Z\gamma\gamma$ anomalous couplings is a factor of $\sim 20\%$ less stringent than the unitarity bound for $ZZ\gamma$ anomalous couplings. See text for further details.

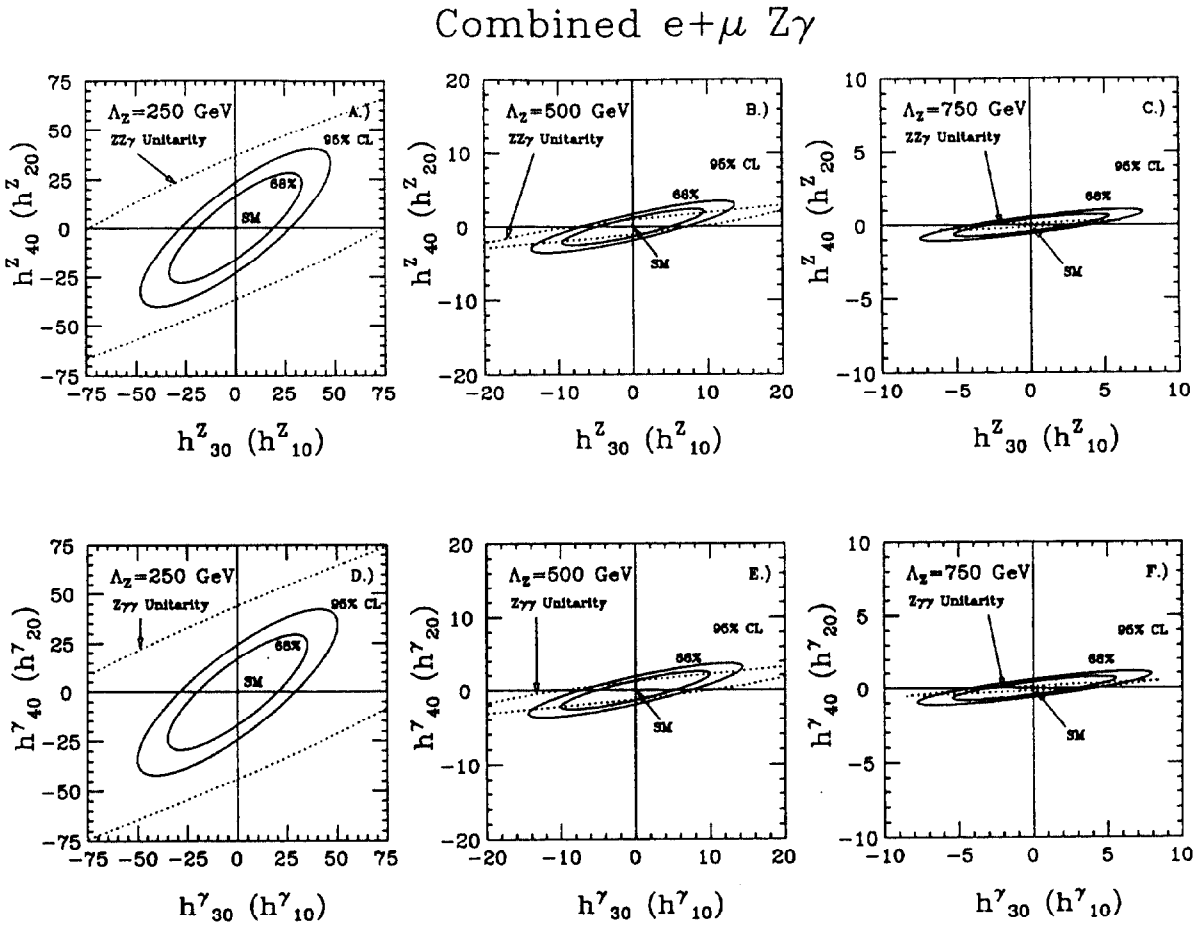

Figure 26: Contour limits on $ZZ\gamma$ and $Z\gamma\gamma$ anomalous coupling pairs. In Figs. (A)-(C), the solid ellipses show the combined $e + \mu$ 68% and 95% CL limits for $\mathcal{CP}-$conserving (and $\mathcal{CP}-$violating) $ZZ\gamma$ anomalous couplings for Λ_Z = 250, 500 and 750 GeV, respectively. In Figs. (D)-(F), the solid ellipses show the combined $e + \mu$ 68% and 95% CL limits for $\mathcal{CP}-$conserving (and $\mathcal{CP}-$violating) $Z\gamma\gamma$ anomalous couplings for Λ_Z = 250, 500 and 750 GeV, respectively. The orientation of the contours relative to the h_{i0}^V axes is due to interference effects between these parameters in the overall invariant amplitude $\mathcal{M}_{Z\gamma}$ for the $Z + \gamma$ process. The SM prediction is $h_{i0}^V = 0$, for $i = 1 - 4$. For the $\mathcal{CP}-$conserving couplings, the global minimum of the anomalous coupling surface is displaced slightly from the SM prediction due to interference effects between the SM and these anomalous coupling contributions to the overall invariant amplitude for $Z\gamma$ production in $\sqrt{s}$ = 1.8 TeV $\bar{p}$-p collisions. No such displacement occurs for $\mathcal{CP}-$violating $ZZ\gamma$ or $Z\gamma\gamma$ anomalous couplings. The $ZZ\gamma$ and $Z\gamma\gamma$ unitarity limits for the relevant form factor scale Λ_Z are indicated by dotted curves in Figs. (A)-(C) and Figs. (D)-(F) respectively. See text for further details.

7.3.1 Unitarity Constraints for $Z\gamma$ – Form Factor Scale Λ_Z Sensitivity

Partial wave unitarity places restrictions on the reduced amplitudes, $A^Z_{\lambda_Z\lambda_\gamma}$ for arbitrary values of h^Z_{i0} $(i = 1-4)$ for $ZZ\gamma$ anomalous couplings [82, 17]:

$$\sum_{\lambda_Z\lambda_\gamma} \left|A^Z_{\lambda_Z\lambda_\gamma}\right|^2 < \frac{24\sin^2\theta_W\ \cos^2\theta_W}{5\ \alpha^2(\hat{s})\left(1-\frac{M_Z^2}{\hat{s}}\right)^3} \tag{57}$$

where λ_Z, λ_γ are the final-state Z boson and photon helicities, respectively. For the assumed generalized dipole form factor and form factor powers ($n = 3$ for h^Z_{30} and $n = 4$ for h^Z_{40}), unitarity is violated for h^Z_{30} and h^Z_{40} $ZZ\gamma$ anomalous couplings if

$$\frac{(\frac{\hat{s}}{M_Z^2}-1)^3}{(1+\frac{\hat{s}}{\Lambda_Z^2})^6}\left[\left(h^Z_{30}-\frac{1}{2}h^Z_{40}\frac{(\frac{\hat{s}}{M_Z^2}-1)}{(1+\frac{\hat{s}}{\Lambda_Z^2})}\right)^2+(h^Z_{30})^2\frac{M_Z^2}{\hat{s}}\right] \geq \frac{48\sin^2\theta_W\ \cos^2\theta_W}{5\alpha^2(\hat{s})} \tag{58}$$

over the $\sqrt{\hat{s}}$ range $M_Z < \sqrt{\hat{s}} < 1.8$ TeV. A similar unitarity relation holds for h^Z_{10} and h^Z_{20} $ZZ\gamma$ anomalous couplings, replacing $h^Z_{30} \to h^Z_{10}$ and $h^Z_{40} \to h^Z_{20}$ [82, 17].

Partial wave unitarity also places restrictions on the reduced amplitudes for arbitrary values of h^γ_{i0} $(i = 1-4)$ for $Z\gamma\gamma$ anomalous couplings [82, 17]:

$$\sum_{\lambda_Z\lambda_\gamma} \left|A^\gamma_{\lambda_Z\lambda_\gamma}\right|^2 < \frac{3\,(3-6\sin^2\theta_W+8\sin^4\theta_W)}{5\ \alpha^2(\hat{s})\left(1-\frac{M_Z^2}{\hat{s}}\right)^3} \tag{59}$$

where λ_Z, λ_γ are the final-state Z boson and photon helicities, respectively. For the assumed form factor, unitarity is violated for h^γ_{30} and h^γ_{40} $Z\gamma\gamma$ anomalous couplings if

$$\frac{(\frac{\hat{s}}{M_Z^2}-1)^3}{(1+\frac{\hat{s}}{\Lambda_Z^2})^6}\left[\left(h^\gamma_{30}-\frac{1}{2}h^\gamma_{40}\frac{(\frac{\hat{s}}{M_Z^2}-1)}{(1+\frac{\hat{s}}{\Lambda_Z^2})}\right)^2+(h^\gamma_{30})^2\frac{M_Z^2}{\hat{s}}\right] \geq \frac{6\,(3-6\sin^2\theta_W+8\sin^4\theta_W)}{5\alpha^2(\hat{s})} \tag{60}$$

over the $\sqrt{\hat{s}}$ range $M_Z < \sqrt{\hat{s}} < 1.8$ TeV. A similar unitarity relation holds for h^γ_{10} and h^γ_{20} $Z\gamma\gamma$ anomalous couplings, replacing $h^\gamma_{30} \to h^\gamma_{10}$ and $h^\gamma_{40} \to h^\gamma_{20}$ [82, 17].

If only one $ZZ\gamma$ anomalous coupling is assumed to be non-zero at a time, then for $\Lambda_Z >> M_Z$ and for the assumed form factor, the unitarity limits are:

$$|h^Z_{10}|,\ |h^Z_{30}| < \frac{1.00\ \text{TeV}^3}{\Lambda_Z^3} \quad (n=3)$$
$$|h^Z_{20}|,\ |h^Z_{40}| < \frac{0.030\ \text{TeV}^5}{\Lambda_Z^5} \quad (n=4)$$

For $Z\gamma\gamma$ anomalous couplings, the corresponding unitarity limits are:

$$|h^\gamma_{10}|,\ |h^\gamma_{30}| < \frac{1.20\ \text{TeV}^3}{\Lambda_Z^3} \quad (n=3)$$
$$|h^\gamma_{20}|,\ |h^\gamma_{40}| < \frac{0.036\ \text{TeV}^5}{\Lambda_Z^5} \quad (n=4)$$

In each of Figs. 25a - 25f, the $ZZ\gamma$ unitarity constraint on $\mathcal{N}_{sig}(Z+\gamma)$ *vs.* h_{30}^Z and h_{40}^Z is shown as a dotted curve. The region above the $ZZ\gamma$ unitarity curves is excluded. Note that the value of Λ_Z increases as the h_{i0}^Z decrease. The limiting case of the Standard Model is obtained when $\Lambda_Z \to \infty$ and $h_{i0}^Z \to 0$. In each figure, the region which is simultaneously above the $ZZ\gamma$ unitarity curve and below the experimental 68% or 95% CL upper limits on $\mathcal{N}_{sig}(Z+\gamma)_{expt}$ is the region where unitarity imposes a more stringent constraint on $ZZ\gamma$ anomalous couplings than our experimental results. For $Z\gamma\gamma$ anomalous couplings, note that the unitarity constraint is $\sim 20\%$ less stringent than that for $ZZ\gamma$ anomalous couplings, while the expected number of $Z+\gamma$ events from $Z\gamma\gamma$ anomalous couplings is $\sim 10\%$ lower than that from $ZZ\gamma$ anomalous couplings. In Tables 26 - 28, we explicitly flag the h_{i0}^V limits which violate unitarity at the Λ_Z scale given in each of the tables with a "†" symbol.

In Figs. 26a - 26c, the contours for $ZZ\gamma$ unitarity limits are indicated by dotted curves. Similarly, in Figs. 26d - 26f the contours for $Z\gamma\gamma$ unitarity limits are also indicated by dotted curves. The region enclosed by each of these contours is allowed by unitarity considerations. It can be seen that for $\Lambda_Z = 250$ GeV, the combined $e+\mu$ limits are entirely within the region allowed by unitarity, whereas for $\Lambda_Z = 500$ GeV, the unitarity bound is more stringent than our experimental contour limits in a significant portion of the $h_{30}^V - h_{40}^V$ ($h_{10}^V - h_{20}^V$) plane. For $\Lambda_Z = 750$ GeV, the unitarity bound is more stringent than nearly all of the experimental contour limits.

In Figs. 27a - 27d the unitarity limits as a function of Λ_Z for $ZZ\gamma$ and $Z\gamma\gamma$ anomalous couplings are shown. The region above the unitarity curves is excluded. Superimposed on these curves are the combined $e+\mu$ experimental limits on $ZZ\gamma$ and $Z\gamma\gamma$ anomalous couplings as a function of Λ_Z. The region above the experimental curves is excluded. In the small Λ_Z region the experimental results are more stringent than the unitarity constraint, whereas in the large Λ_Z region, the converse is true. Note that our experimental limits on $ZZ\gamma$ and $Z\gamma\gamma$ anomalous couplings have significant dependence on the form factor scale Λ_Z. In each of these figures, the value of Λ_Z where the experimental curves cross the unitarity curve is the limit of experimental sensitivity to that particular anomalous coupling and Λ_Z–scale. Our $e+\mu$ combined 95% CL limits on $ZZ\gamma/Z\gamma\gamma$ anomalous couplings *and* form factor scale Λ_Z, assuming only one such coupling to be non-zero at a time, are:

$$-6.3 < h_{30,10}^Z < 6.3 \quad \text{for} \quad \Lambda_Z^{h_{30,10}^Z} = 550 \text{ GeV}$$

$$-7.2 < h_{40,20}^Z < 7.2 \quad \text{for} \quad \Lambda_Z^{h_{40,20}^Z} = 320 \text{ GeV}$$

$$-5.8 < h_{30,10}^\gamma < 5.8 \quad \text{for} \quad \Lambda_Z^{h_{30,10}^\gamma} = 600 \text{ GeV}$$

$$-4.3 < h_{40,20}^\gamma < 4.3 \quad \text{for} \quad \Lambda_Z^{h_{40,20}^\gamma} = 390 \text{ GeV}$$

For form factor scales

$$\Lambda_Z^{h_{30,10}^Z} \geq 550 \text{ GeV}$$

$$\Lambda_Z^{h_{40,20}^Z} \geq 320 \text{ GeV}$$

$$\Lambda_Z^{h_{30,10}^\gamma} \geq 600 \text{ GeV}$$

$$\Lambda_Z^{h_{40,20}^\gamma} \geq 390 \text{ GeV}$$

the unitarity limit is more stringent than our $e+\mu$ combined 95% CL limits on $ZZ\gamma/Z\gamma\gamma$ anomalous

couplings. These form factor scales correspond to distance scale sensitivities $L_Z = \hbar c/\Lambda_Z$ for probing possible internal structure of the Z boson of order:

$$
\begin{aligned}
L_Z^{h^Z_{30,10}} &\leq 3.6 \times 10^{-4} \text{ fm} = 0.17\, \lambda\!\!\!^{-}_Z \\
L_Z^{h^Z_{40,20}} &\leq 6.2 \times 10^{-4} \text{ fm} = 0.28\, \lambda\!\!\!^{-}_Z \\
L_Z^{h^\gamma_{30,10}} &\leq 3.3 \times 10^{-4} \text{ fm} = 0.15\, \lambda\!\!\!^{-}_Z \\
L_Z^{h^\gamma_{40,20}} &\leq 5.1 \times 10^{-4} \text{ fm} = 0.23\, \lambda\!\!\!^{-}_Z
\end{aligned}
$$

where $\lambda\!\!\!^{-}_Z = \hbar/M_Z c$ is the reduced Compton wavelength of the Z boson.

Here again we point out that the unitarity bounds and the Λ_Z sensitivity have some model-dependence associated with the choice of the form factor powers n used in the generalized form factor. Our choice of $n = 3$ for $h^V_{1,3}$ and $n = 4$ for $h^V_{2,4}$ was motivated mainly by the requirement that unitarity be preserved at high energies ($\sqrt{\hat{s}} >> \Lambda_Z >> M_Z$) and that terms proportional to $h^V_{2,4}$ have the same high-energy behavior as those proportional to $h^V_{1,3}$. For a different choice of form factor powers, e.g. $n = 2$ for $h^V_{1,3}$ ($n = 3$ for $h^V_{2,4}$), the unitarity bounds on the $h^V_{10,30}$ ($h^V_{20,40}$) anomalous couplings are made more stringent by factors of ~ 2.6 (~ 2.9), respectively. The corresponding sensitivity to Λ_Z is reduced by factors of at most ~ 1.4 (~ 1.2) respectively, partially offset by the fact that the predicted rate of $Z\gamma$ production is also slightly enhanced for the choice of form factor powers of $n = 2$ for $h^V_{1,3}$ ($n = 3$ for $h^V_{2,4}$) compared to the choice of $n = 3$ for $h^V_{1,3}$ ($n = 4$ for $h^V_{2,4}$).

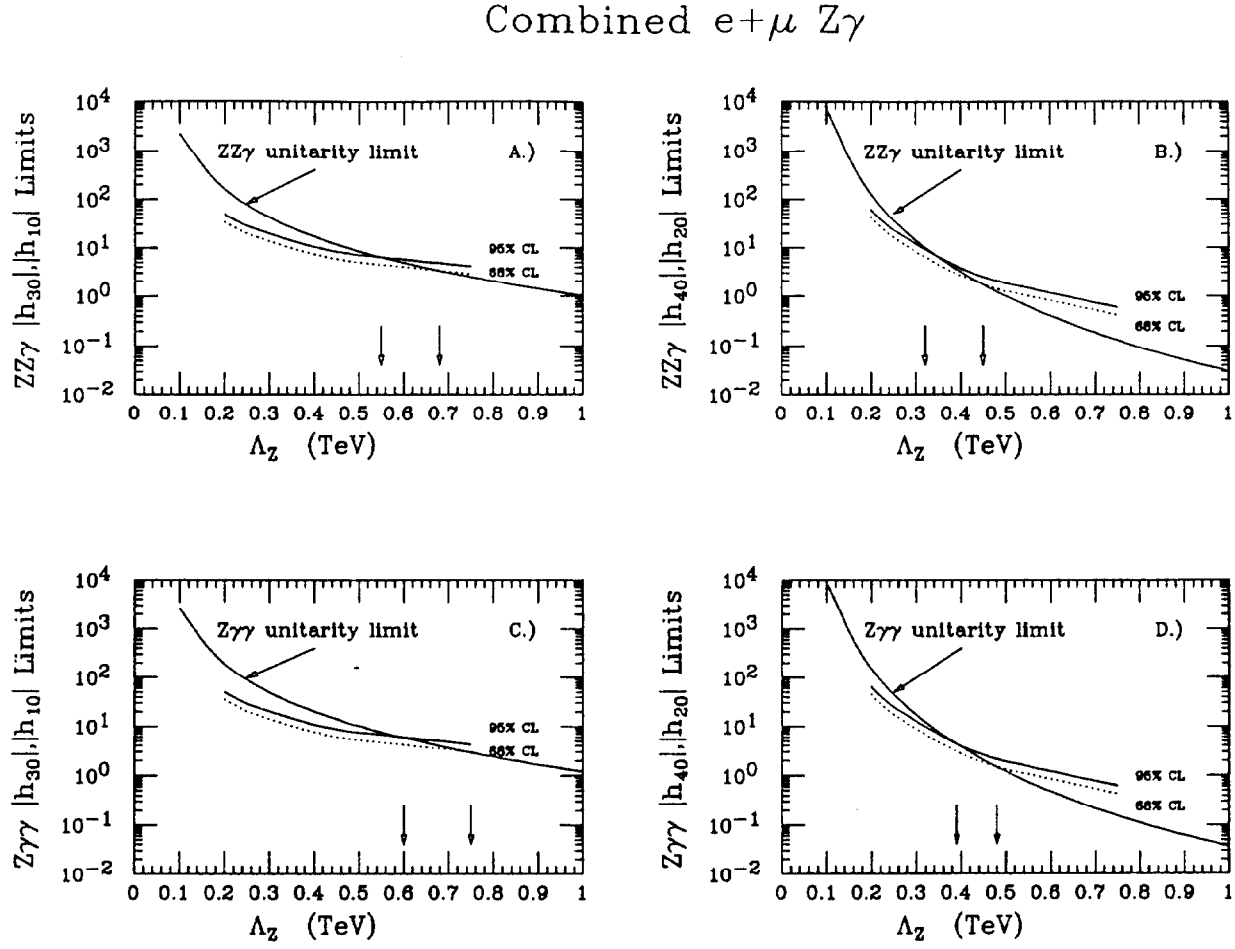

Figure 27: Unitarity limits as a function of Λ_Z for $ZZ\gamma$ and $Z\gamma\gamma$ anomalous couplings. (A) $|h_{30}^Z|$, $|h_{10}^Z|$ unitarity limits as a function of form factor scale Λ_Z. (B) $|h_{40}^Z|$, $|h_{20}^Z|$ unitarity limits as a function of form factor scale Λ_Z. (C) $|h_{30}^\gamma|$, $|h_{10}^\gamma|$ unitarity limits as a function of form factor scale Λ_Z. (D) $|h_{40}^\gamma|$, $|h_{20}^\gamma|$ unitarity limits as a function of form factor scale Λ_Z. Only one $ZZ\gamma$ or $Z\gamma\gamma$ anomalous coupling is assumed to be non-zero at a time. Also shown in each figure are the combined $e + \mu$ 68% and 95% CL limits (dotted and solid curves, respectively) on these anomalous couplings as a function of form factor scale Λ_Z. The downward-pointing arrows indicate the value of Λ_Z associated with the intersection of the experimental limit with the unitarity curve in each figure. See text for further details.

7.3.2 Direct Limits on $ZZ\gamma$ Transition Moments

Direct experimental limits on the $ZZ\gamma$ anomalous couplings also place bounds on the transition moments of the Z boson, since these quantities are related to each other in the static limit (photon energy, $k \to 0$) by:

$$d_{Z_T} = -\frac{e}{M_Z}\frac{1}{\sqrt{2}}\frac{k^2}{M_Z^2}\left(h_{30}^Z - h_{40}^Z\right) \quad (61)$$

$$Q_{Z_T}^m = \frac{e}{M_Z^2}\sqrt{10}\left(2h_{30}^Z\right) \quad (62)$$

$$\mu_{Z_T} = -\frac{e}{M_Z}\frac{1}{\sqrt{2}}\frac{k^2}{M_Z^2}\left(h_{10}^Z - h_{20}^Z\right) \quad (63)$$

$$Q_{Z_T}^e = \frac{e}{M_Z^2}\sqrt{10}\left(2h_{10}^Z\right) \quad (64)$$

In the SM (at the tree level) all $ZZ\gamma$ couplings vanish: $h_{i0}^Z = 0$ for $(i = 1 - 4)$, thus all SM transition moments also vanish, at the tree level. We define the following classical parameters for the Z boson, in analogy with those for the W, and calculate their numerical values:

$$\begin{aligned}
d_{Z_T}^\circ &= -\tfrac{1}{2}e\lambda\!\!\!^{-}_Z &&= -1.0820 \pm 0.0001 \times 10^{-3} \;\; e - \text{fm} \\
Q_{Z_T}^{m\circ} &= \tfrac{e\hbar^2}{M_Z^2 c} &&= 1.4038 \pm 0.0002 \times 10^{-18} \;\; \text{MeV–fm/T} \\
\mu_{Z_T}^\circ &= -\tfrac{e\hbar}{2M_Z} &&= -3.2437 \pm 0.0003 \times 10^{-16} \;\; \text{MeV/T} \\
Q_{Z_T}^{e\circ} &= e\lambda\!\!\!^{-2}_Z &&= 4.6828 \pm 0.0007 \times 10^{-6} \;\; e - \text{fm}^2 \\
\lambda\!\!\!^{-}_Z &= \tfrac{\hbar}{M_Z c} &&= 2.1640 \pm 0.0002 \times 10^{-3} \;\; \text{fm}
\end{aligned}$$

We also define the following dimensionless classical quantities for the Z boson:

$$\delta_{Z_T} \equiv \frac{d_{Z_T}}{d_{Z_T}^\circ} = \sqrt{2}\left(\frac{k^2}{M_Z^2}\right)\left(h_{30}^Z - h_{40}^Z\right) \quad (65)$$

$$q_{Z_T}^m \equiv \frac{Q_{Z_T}^m}{Q_{Z_T}^{m\circ}} = \sqrt{10}\left(2h_{30}^Z\right) \quad (66)$$

$$g_{Z_T} \equiv \frac{\mu_{Z_T}}{\mu_{Z_T}^\circ} = \sqrt{2}\left(\frac{k^2}{M_Z^2}\right)\left(h_{10}^Z - h_{20}^Z\right) \quad (67)$$

$$q_{Z_T}^e \equiv \frac{Q_{Z_T}^e}{Q_{Z_T}^{e\circ}} = \sqrt{10}\left(2h_{10}^Z\right) \quad (68)$$

Setting direct experimental limits on δ_{Z_T} and g_{Z_T} as defined above is problematic because the $Z + \gamma$ photon energy spectrum is continuous, and sharply peaked at the experimental cutoff in E_T^γ. The factor (k^2/M_Z^2) in the definition of these transition moments is rather ill-defined, experimentally. Hence, we define the following variables for these two quantities:

$$\delta_{Z_T}^* \equiv \delta_{Z_T}\left[\frac{M_Z^2}{k^2}\right] = \sqrt{2}\left(h_{30}^Z - h_{40}^Z\right) \quad (69)$$

$$g_{Z_T}^* \equiv g_{Z_T}\left[\frac{M_Z^2}{k^2}\right] = \sqrt{2}\left(h_{10}^Z - h_{20}^Z\right) \quad (70)$$

Table 29 summarizes the limits on $ZZ\gamma$ transition moments for the $e+\mu$ combined result. Figures 28a - 28c show the 68% and 95% CL contours in the $\delta^*_{Z_T} - q^m_{Z_T}$ plane (or equivalently, the $g^*_{Z_T} - q^e_{Z_T}$ plane) for the combined $e+\mu$ results, for Λ_Z = 250, 500 and 750 GeV, respectively. The corresponding unitarity curves for the $ZZ\gamma$ transition moments are also shown in each figure as dotted contours.

In Figs. 29a - 29b the unitarity limits as a function of Λ_Z for the $ZZ\gamma$ transition moments are shown. The region above the unitarity curves is excluded. Superimposed on these curves are the combined $e+\mu$ experimental limits on the $ZZ\gamma$ transition moments as a function of Λ_Z. The region above the experimental curves is excluded. Here again, note that our experimental limits on the $ZZ\gamma$ transition moments have significant dependence on the form factor scale Λ_Z. In each of these figures, the value of Λ_Z where the experimental curves cross the unitarity curve is the limit of experimental sensitivity to that particular transition moment and Λ_Z−scale. Our $e+\mu$ combined 95% CL limits on $ZZ\gamma$ transition moments *and* form factor scale Λ_Z, assuming only one such transition moment to be non-zero at a time, are:

$$
\begin{aligned}
-14.1 < \delta^*_{Z_T} < 14.1 \quad &\text{for} \quad \Lambda_Z^{\delta^*_{Z_T}} = 320 \text{ GeV} \\
-123.4 < q^m_{Z_T} < 123.4 \quad &\text{for} \quad \Lambda_Z^{q^m_{Z_T}} = 300 \text{ GeV} \\
-14.1 < g^*_{Z_T} < 14.1 \quad &\text{for} \quad \Lambda_Z^{g^*_{Z_T}} = 320 \text{ GeV} \\
-123.4 < q^e_{Z_T} < 123.4 \quad &\text{for} \quad \Lambda_Z^{q^e_{Z_T}} = 300 \text{ GeV}
\end{aligned}
$$

For form factor scales

$$
\begin{aligned}
\Lambda_Z^{\delta^*_{Z_T}} &\geq 320 \text{ GeV} \\
\Lambda_Z^{q^m_{Z_T}} &\geq 300 \text{ GeV} \\
\Lambda_Z^{g^*_{Z_T}} &\geq 320 \text{ GeV} \\
\Lambda_Z^{q^e_{Z_T}} &\geq 300 \text{ GeV}
\end{aligned}
$$

the unitarity limit is more stringent than our $e+\mu$ combined 95% CL limits on $ZZ\gamma$ transition moments, assuming only one such coupling to be non-zero at a time. These form factor scales correspond to distance scale sensitivities $L_Z = \hbar c/\Lambda_Z$ for probing possible internal structure of the Z boson of order:

$$
\begin{aligned}
L_Z^{\delta^*_{Z_T}} &\leq 6.2 \times 10^{-4} \text{ fm} = 0.28 \, \lambda\!\!\!^{-}_Z \\
L_Z^{q^m_{Z_T}} &\leq 6.6 \times 10^{-4} \text{ fm} = 0.30 \, \lambda\!\!\!^{-}_Z \\
L_Z^{g^*_{Z_T}} &\leq 6.2 \times 10^{-4} \text{ fm} = 0.28 \, \lambda\!\!\!^{-}_Z \\
L_Z^{q^e_{Z_T}} &\leq 6.6 \times 10^{-4} \text{ fm} = 0.30 \, \lambda\!\!\!^{-}_Z
\end{aligned}
$$

The result obtained from limits on the $\delta^*_{Z_T}$ transition moment is the same as that obtained from limits on the h^Z_{40} anomalous coupling, due to the fact that the unitarity curve for the $\delta^*_{Z_T}$ transition moment is obtained for $q^m_{Z_T} = 0$, which requires $h^Z_{30} = 0$. The unitarity curve for $\delta^*_{Z_T}$ is therefore due entirely to non-zero h^Z_{40}. Similar comments apply for the limits on the $g^*_{Z_T}$ transition moment

and h_{20}^Z anomalous coupling, where $q^e_{Z_T} = 0$, which requires $h_{10}^Z = 0$. (see equations 69, 70, 66 and 68). The unitarity curve for the $q^m_{Z_T}$ transition moment is obtained for $\delta^*_{Z_T} = 0$, which requires $h_{30}^Z = h_{40}^Z$. Therefore this unitarity curve is due to non-zero $h_{30}^Z = h_{40}^Z$, simultaneously involving both h_{30}^Z and h_{40}^Z. Note that the unitarity limit on h_{40}^Z for $h_{30}^Z = 0$ with $\Lambda_Z > 200$ GeV is considerably more stringent than that for h_{30}^Z for $h_{40}^Z = 0$ (see Figs 27a – 27b). This is again due to the fact that the anomalous contributions to the $Z\gamma$ helicity amplitudes grow like $(\sqrt{\hat{s}}/M_Z)^3$ for $h^V_{30,10}$ and $(\sqrt{\hat{s}}/M_Z)^5$ for $h^V_{40,20}$. The unitarity constraint on non-zero $h_{30}^Z = h_{40}^Z$ is more stringent than that for h_{40}^Z with $h_{30}^Z = 0$. Similar comments apply for the limits on the $q^e_{Z_T}$ transition moment where $g^*_{Z_T} = 0$, which requires $h_{10}^Z = h_{20}^Z$. Therefore this unitarity curve is due to non-zero $h_{10}^Z = h_{20}^Z$, simultaneously involving both h_{10}^Z and h_{20}^Z.

Table 29: $e+\mu$ combined limits on $ZZ\gamma$ transition moments. The $\pm 1\sigma$, 68% and 95% CL limits on the $ZZ\gamma$ transition moments $\delta^*_{Z_T}$, $q^m_{Z_T}$, $g^*_{Z_T}$ and $q^e_{Z_T}$ are given for $\Lambda_Z = 250$, 500, and 750 GeV. For each entry in the Table, all other $ZZ\gamma$ transition moments are assumed to be at their SM values. For the $\pm 1\sigma$ limits, the first uncertainty is the overall statistical uncertainty (*stat*); the second is the overall systematic uncertainty (*syst*); the third uncertainty is the combined (*stat* + *syst*) uncertainty. Entries in the table which exceed the unitarity limit are indicated with a †. See text for further details.

	$\mathcal{CP}$–Conserving Couplings	$\mathcal{CP}$–Violating Couplings
$\Lambda_Z = 250$ GeV	$\delta^*_{Z_T} = 0.0\ ^{+25.6}_{-25.6} \pm 0.4 = 0.0\ ^{+25.6}_{-25.6}$ $-22.9 < \delta^*_{Z_T} < +22.7$ (68% CL) $-32.8 < \delta^*_{Z_T} < +32.6$ (95% CL)	$g^*_{Z_T} = 0.0\ ^{+25.7}_{-25.7} \pm 0.4 = 0.0\ ^{+25.7}_{-25.7}$ $-22.8 < g^*_{Z_T} < +22.8$ (68% CL) $-32.7 < g^*_{Z_T} < +32.7$ (95% CL)
$\Lambda_Z = 250$ GeV	$q^m_{Z_T} = 0.0^{+200.1}_{-198.8} \pm 4.2 = 0.0^{+200.2}_{-198.9}$ $-176.4 < q^m_{Z_T} < +177.7$ (68% CL) $-253.0 < q^m_{Z_T} < +254.4$ (95% CL)	$q^e_{Z_T} = 0.0^{+199.0}_{-199.0} \pm 4.2 = 0.0^{+199.0}_{-199.0}$ $-176.6 < q^e_{Z_T} < +176.6$ (68% CL) $-253.0 < q^e_{Z_T} < +253.0$ (95% CL)
$\Lambda_Z = 500$ GeV	$\delta^*_{Z_T} = 0.0\ ^{+2.0}_{-2.0} \pm 0.1 = 0.0\ ^{+2.0}_{-2.0}$ $-1.8 < \delta^*_{Z_T} < +1.8$ (68% CL) $-2.6 < \delta^*_{Z_T} < +2.6$ (95% CL)	$g^*_{Z_T} = 0.0\ ^{+2.0}_{-2.0} \pm 0.1 = 0.0\ ^{+2.0}_{-2.0}$ $-1.8 < g^*_{Z_T} < +1.8$ (68% CL) $-2.6 < g^*_{Z_T} < +2.6$ (95% CL)
$\Lambda_Z = 500$ GeV	$q^m_{Z_T} = 0.0\ ^{+11.3}_{-11.4} \pm 0.2 = 0.0\ ^{+11.3}_{-11.4}$ $-10.1 < q^m_{Z_T} < +10.1^\dagger$ (68% CL) $-14.5 < q^m_{Z_T} < +14.4^\dagger$ (95% CL)	$q^e_{Z_T} = 0.0\ ^{+11.4}_{-11.4} \pm 0.2 = 0.0\ ^{+11.4}_{-11.4}$ $-10.1 < q^e_{Z_T} < +10.1^\dagger$ (68% CL) $-14.4 < q^e_{Z_T} < +14.4^\dagger$ (95% CL)
$\Lambda_Z = 750$ GeV	$\delta^*_{Z_T} = 0.0\ ^{+0.7}_{-0.7} \pm 0.1 = 0.0\ ^{+0.7}_{-0.7}$ $-0.6 < \delta^*_{Z_T} < +0.6^\dagger$ (68% CL) $-0.8 < \delta^*_{Z_T} < +0.8^\dagger$ (95% CL)	$g^*_{Z_T} = 0.0\ ^{+0.7}_{-0.7} \pm 0.1 = 0.0\ ^{+0.7}_{-0.7}$ $-0.6 < g^*_{Z_T} < +0.6^\dagger$ (68% CL) $-0.8 < g^*_{Z_T} < +0.8^\dagger$ (95% CL)
$\Lambda_Z = 750$ GeV	$q^m_{Z_T} = 0.0\ ^{+3.3}_{-3.3} \pm 0.1 = 0.0\ ^{+3.3}_{-3.3}$ $-2.9 < q^m_{Z_T} < +3.0^\dagger$ (68% CL) $-4.2 < q^m_{Z_T} < +4.2^\dagger$ (95% CL)	$q^e_{Z_T} = 0.0\ ^{+3.3}_{-3.3} \pm 0.1 = 0.0\ ^{+3.3}_{-3.3}$ $-2.9 < q^e_{Z_T} < +2.9^\dagger$ (68% CL) $-4.2 < q^e_{Z_T} < +4.2^\dagger$ (95% CL)

Combined e+μ Zγ

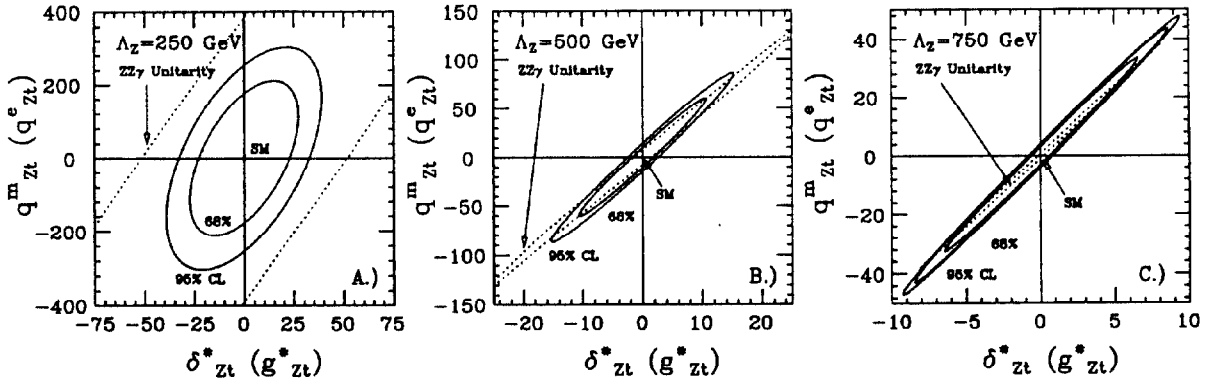

Figure 28: Contour limits on $\mathcal{CP}-$conserving and $\mathcal{CP}-$violating Z boson transition moments. In Figs. (A)-(C), the solid ellipses show the combined $e+\mu$ 68% and 95% CL limits in the $\delta^*_{Z_T} - q^m_{Z_T}$ ($g^*_{Z_T} - q^e_{Z_T}$) plane for $ZZ\gamma$ anomalous couplings with Λ_Z = 250, 500 and 750 GeV, respectively. The orientation of the contours relative to the axes is due to interference effects between these parameters in the overall invariant amplitude $\mathcal{M}_{Z\gamma}$ for the $Z+\gamma$ process. All transition moments vanish at the tree level in the SM. The $ZZ\gamma$ unitarity limits for the relevant form factor scale Λ_Z are indicated by dotted curves in Figs. (A)-(C), respectively. See text for further details.

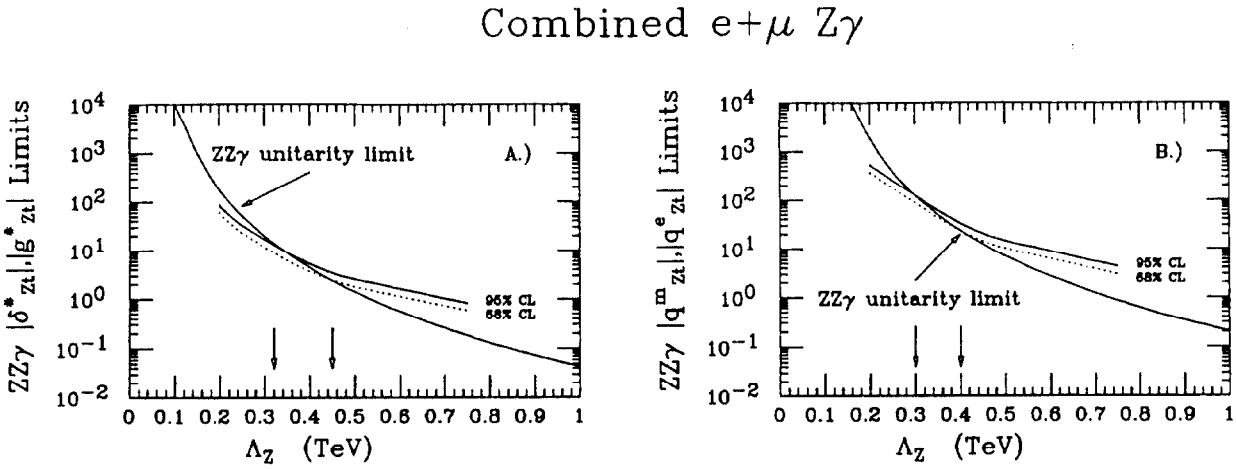

Figure 29: Unitarity limits as a function of Λ_Z for $ZZ\gamma$ transition moments. (A) $|\delta^*_{Z_T}|$, $|g^*_{Z_T}|$ unitarity limits as a function of form factor scale Λ_Z. (B) $|q^m_{Z_T}|$, $|q^e_{Z_T}|$ unitarity limits as a function of form factor scale Λ_Z. Only one $ZZ\gamma$ transition moment is assumed to be non-zero at a time. Also shown in each figure are the combined $e + \mu$ 68% and 95% CL limits (dotted and solid curves, respectively) on these transition moments as a function of Λ_Z. The downward-pointing arrows indicate the value of Λ_Z associated with the intersection of the experimental limits with the unitarity curve in each figure. See text for further details.

7.3.3 Comparison with Existing Limits on $ZZ\gamma/Z\gamma\gamma$ Anomalous Couplings

Low-energy, indirect bounds on $ZZ\gamma$ and $Z\gamma\gamma$ anomalous couplings due to non-SM loop contributions to the muon $g_\mu - 2$ anomaly have also been considered [68]. Only $Z\gamma\gamma$ couplings are found to give a non-zero contribution. These bounds are again sensitive to the cutoff used to regulate divergences and are also dependent on the regularization scheme used in the loop calculation.

The $L3$ Collaboration has recently obtained an experimental limit on the h_3^Z form factor from a measurement of the cross section for the process $e^+e^- \to Z^0 \to \nu\bar{\nu}\gamma$ [83]. From the absence of an excess of such events in the Z resonance region from 11.2 pb^{-1} data, for $E_\gamma > \frac{1}{2}E_{beam}$ they obtain a limit on the h_3^Z form factor (for $h_4^Z = 0$) of:

$$\left|h_3^Z(P^2 = M_Z^2,\ q_1^2 < M_Z^2,\ q_2^2 = 0)\right| < 1.6 \ \ (95\%\ CL) \tag{71}$$

Translating this result into limits on the h_{30}^Z parameter, using equation (14) with a generalized form-factor power of $n = 3$, the L3 result is $|h_{30}^Z| < 2.3,\ 1.8,\ 1.7$ $(95\%\ CL)$, for $\Lambda_Z = 250,\ 500,\ 750$ GeV, respectively. The L3 h_{30}^Z results are well within the $|h_{30}^Z|$ unitarity limit for the assumed values of Λ_Z. Unitarity is violated for $\Lambda_Z > 840$ GeV.

The L3 $Z \to \nu\bar{\nu}\gamma$ results are sensitive only to $ZZ\gamma$ anomalous couplings, and place no constraints on $Z\gamma\gamma$ anomalous couplings. The direct experimental limits on $Z\gamma\gamma$ anomalous couplings obtained by CDF are therefore unique in this regard.

In principle, the experimental upper limit on the neutron EDM could also place significant constraints on *e.g.* $\mathcal{CP}/\mathcal{T}-$violating $Z\gamma\gamma$ anomalous couplings. However, this is currently still an open issue as the necessary theoretical calculations have yet to be carried out.

8 CONCLUSIONS

We have measured the production cross section $\times$ decay branching ratio for $W + \gamma$ and $Z + \gamma$ in the electron and muon channels using the inclusive W and Z data samples from the CDF 1988-89 Tevatron collider run, with 4.05 ± 0.28 pb^{-1} (3.54 ± 0.24 pb^{-1}) of electron (muon) data. For central photons with $E_T^\gamma > 5.0$ GeV and $\Delta R_{\ell\gamma} > 0.7$, we observe 8 (5) electron (muon) $W\gamma$ candidates and 2 (2) electron (muon) $Z\gamma$ candidates. From these events, we extract $\sigma \cdot B(W\gamma)$ and $\sigma \cdot B(Z\gamma)$ for the electron, muon and $e + \mu$ combined samples, and compare to Standard Model predictions:

$$\begin{aligned}
\sigma \cdot B(W\gamma)_e &= 20.6^{+15.8}_{-15.5}\ \ (stat + syst)\ \text{pb} \\
\sigma \cdot B(W\gamma)_\mu &= 24.6^{+22.1}_{-21.6}\ \ (stat + syst)\ \text{pb} \\
\sigma \cdot B(W\gamma)_{e+\mu} &= 22.0^{+13.0}_{-12.6}\ \ (stat + syst)\ \text{pb} \\
\sigma \cdot B(W\gamma)_{SM} &= 22.4^{+\ 3.3}_{-\ 0.9}\ \ (stat + syst)\ \text{pb}
\end{aligned}$$

$$\begin{aligned}
\sigma \cdot B(Z\gamma)_e &= 7.0^{+\ 5.9}_{-\ 5.7}\ \ (stat + syst)\ \text{pb} \\
\sigma \cdot B(Z\gamma)_\mu &= 15.8^{+12.0}_{-11.8}\ \ (stat + syst)\ \text{pb} \\
\sigma \cdot B(Z\gamma)_{e+\mu} &= 9.9^{+\ 5.7}_{-\ 5.5}\ \ (stat + syst)\ \text{pb} \\
\sigma \cdot B(Z\gamma)_{SM} &= 5.5^{+\ 0.5}_{-\ 0.2}\ \ (stat + syst)\ \text{pb}
\end{aligned}$$

We have also obtained three new results on cross section ratios. When combined with the previous CDF measurements of the inclusive W/Z cross section ratio, they provide more stringent tests of the Standard Model and are also sensitive to anomalous couplings of the W and Z bosons. For the combined $e+\mu$ data samples, we find:

$$\begin{aligned}
\mathcal{R}(W\gamma/W)_{e+\mu} &= 1.0^{+0.6}_{-0.6}\% \quad (stat+syst) \\
\mathcal{R}(Z\gamma/Z)_{e+\mu} &= 4.6^{+2.6}_{-2.5}\% \quad (stat+syst) \\
\mathcal{R}(W\gamma/Z\gamma)_{e+\mu} &= 2.2^{+2.3}_{-1.5} \quad (stat+syst) \\
\mathcal{R}(W/Z)_{e+\mu} &= 10.0^{+0.7}_{-0.7} \quad (stat+syst)
\end{aligned}$$

$$\begin{aligned}
\mathcal{R}(W\gamma/W)_{SM} &= 1.07 \pm 0.02\% \\
\mathcal{R}(Z\gamma/Z)_{SM} &= 2.83 \pm 0.03\% \\
\mathcal{R}(W\gamma/Z\gamma)_{SM} &= 4.05 \pm 0.07 \\
\mathcal{R}(W/Z)_{SM} &= 10.69 \pm 0.22
\end{aligned}$$

We have also obtained direct limits on $WW\gamma$, $ZZ\gamma$ and $Z\gamma\gamma$ anomalous couplings, providing constraints on possible internal (composite) structure for these particles. From the combined $e+\mu$ result for $W+\gamma$, we obtain direct limits on $\mathcal{CP}-$conserving and $\mathcal{CP}-$violating $WW\gamma$ anomalous couplings, assuming only one such coupling to deviate from its SM value at a time, of:

$$\begin{aligned}
\Delta\kappa &= 0.0^{+4.5}_{-4.1} \quad (stat+syst) \\
\lambda &= 0.0^{+1.6}_{-1.7} \quad (stat+syst) \\
\tilde{\kappa} &= 0.0^{+4.3}_{-4.3} \quad (stat+syst) \\
\tilde{\lambda} &= 0.0^{+1.6}_{-1.6} \quad (stat+syst)
\end{aligned}$$

The 95% CL limits on these quantities are:

$$\begin{aligned}
-6.0 &< \Delta\kappa < +6.4 \\
-2.4 &< \lambda < +2.3 \\
-6.2 &< \tilde{\kappa} < +6.2 \\
-2.4 &< \tilde{\lambda} < +2.4
\end{aligned}$$

These experimental results are essentially independent of the form factor scale for Λ_W above a few hundred GeV.

For form factor (compositeness) scales of

$$\begin{aligned}
\Lambda_W^{\Delta\kappa} &\geq 1.0 \text{ TeV} \\
\Lambda_W^{\lambda} &\geq 1.2 \text{ TeV} \\
\Lambda_W^{\tilde{\kappa}} &\geq 5.0 \text{ TeV} \\
\Lambda_W^{\tilde{\lambda}} &\geq 1.2 \text{ TeV}
\end{aligned}$$

the unitarity limit is more stringent than our $e+\mu$ combined 95% CL limits on $WW\gamma$ anomalous couplings, assuming only one such coupling to be non-zero at a time. These form factor scales correspond to distance scale sensitivities for probing possible internal structure of the W boson of order:

$$\begin{aligned} L_W^{\Delta\kappa} &\leq 2.0\times10^{-4}\text{ fm} = 0.08\,\lambda\!\!\!^{-}_W \\ L_W^{\lambda} &\leq 1.6\times10^{-4}\text{ fm} = 0.07\,\lambda\!\!\!^{-}_W \\ L_W^{\tilde{\kappa}} &\leq 0.4\times10^{-4}\text{ fm} = 0.02\,\lambda\!\!\!^{-}_W \\ L_W^{\tilde{\lambda}} &\leq 1.6\times10^{-4}\text{ fm} = 0.07\,\lambda\!\!\!^{-}_W \end{aligned}$$

The $WW\gamma$ anomalous couplings are related (in the static limit) to the W boson higher-order EM moments and mean-squared charge radius. We obtain direct limits on the W boson higher-order electromagnetic moments, again assuming only one such moment to deviate from its SM value at a time, of:

$$\begin{aligned} g_W - 2 &= 0.0^{+2.6}_{-2.6}\ (stat+syst) \\ q_W^e - 1 &= 0.0^{+4.1}_{-3.8}\ (stat+syst) \\ \delta_W &= 0.0^{+2.6}_{-2.6}\ (stat+syst) \\ q_W^m &= 0.0^{+3.9}_{-3.9}\ (stat+syst) \\ r_W^2 - 1 &= 0.0^{+2.6}_{-2.6}\ (stat+syst) \end{aligned}$$

The 95% CL limits on these quantities are:

$$\begin{aligned} -3.7 < g_W - 2 &< +3.7 \\ -5.5 < q_W^e - 1 &< +5.8 \\ -3.7 < \delta_W &< +3.7 \\ -5.6 < q_W^m &< +5.6 \\ -3.7 < r_W^2 - 1 &< +3.7 \end{aligned}$$

We have also obtained direct limits on $\mathcal{CP}-$conserving and $\mathcal{CP}-$violating $ZZ\gamma$ and $Z\gamma\gamma$ anomalous couplings for three different choices of form factor scale $\Lambda_Z = 250$, 500, and 750 GeV for the electron, muon and $e+\mu$ combined data samples. Our experimental limits on $ZZ\gamma$ and $Z\gamma\gamma$ anomalous couplings have significant dependence on the form factor scale Λ_Z. Our $e+\mu$ combined 95% CL limits on $ZZ\gamma$ and $Z\gamma\gamma$ anomalous couplings *and* form factor (compositeness) scale Λ_Z, assuming only one such coupling to be non-zero at a time, are:

$$\begin{aligned} -6.3 < h_{30,10}^Z < 6.3 \quad &\text{for} \quad \Lambda_Z^{h_{30,10}^Z} = 550\text{ GeV} \\ -7.2 < h_{40,20}^Z < 7.2 \quad &\text{for} \quad \Lambda_Z^{h_{40,20}^Z} = 320\text{ GeV} \\ -5.8 < h_{30,10}^\gamma < 5.8 \quad &\text{for} \quad \Lambda_Z^{h_{30,10}^\gamma} = 600\text{ GeV} \\ -4.3 < h_{40,20}^\gamma < 4.3 \quad &\text{for} \quad \Lambda_Z^{h_{40,20}^\gamma} = 390\text{ GeV} \end{aligned}$$

For form factor scales

$$\begin{aligned}
\Lambda_Z^{h_{30,10}^Z} &\geq 550 \text{ GeV} \\
\Lambda_Z^{h_{40,20}^Z} &\geq 320 \text{ GeV} \\
\Lambda_Z^{h_{30,10}^\gamma} &\geq 600 \text{ GeV} \\
\Lambda_Z^{h_{40,20}^\gamma} &\geq 390 \text{ GeV}
\end{aligned}$$

the unitarity limit is more stringent than our $e+\mu$ combined 95% CL limits on $ZZ\gamma/Z\gamma\gamma$ anomalous couplings. These form factor scales correspond to distance scale sensitivities for probing possible internal structure of the Z boson of order:

$$\begin{aligned}
L_Z^{h_{30,10}^Z} &\leq 3.6 \times 10^{-4} \text{ fm} = 0.17\, \lambda\!\!\!^{-}_Z \\
L_Z^{h_{40,20}^Z} &\leq 6.2 \times 10^{-4} \text{ fm} = 0.28\, \lambda\!\!\!^{-}_Z \\
L_Z^{h_{30,10}^\gamma} &\leq 3.3 \times 10^{-4} \text{ fm} = 0.15\, \lambda\!\!\!^{-}_Z \\
L_Z^{h_{40,20}^\gamma} &\leq 5.1 \times 10^{-4} \text{ fm} = 0.23\, \lambda\!\!\!^{-}_Z
\end{aligned}$$

In the static limit, our direct experimental limits on $ZZ\gamma$ anomalous couplings for Λ_Z = 250, 500, and 750 GeV also place bounds on the $ZZ\gamma$ transition moments of the Z boson. Our $e+\mu$ combined 95% CL limits on $ZZ\gamma$ transition moments *and* form factor scale Λ_Z, assuming only one such transition moment to be non-zero at a time, are:

$$\begin{aligned}
-14.1 < \delta^*_{Z_T} < 14.1 \quad &\text{for} \quad \Lambda_Z^{\delta^*_{Z_T}} = 320 \text{ GeV} \\
-123.4 < q^m_{Z_T} < 123.4 \quad &\text{for} \quad \Lambda_Z^{q^m_{Z_T}} = 300 \text{ GeV} \\
-14.1 < g^*_{Z_T} < 14.1 \quad &\text{for} \quad \Lambda_Z^{g^*_{Z_T}} = 320 \text{ GeV} \\
-123.4 < q^e_{Z_T} < 123.4 \quad &\text{for} \quad \Lambda_Z^{q^e_{Z_T}} = 300 \text{ GeV}
\end{aligned}$$

The experimental results presented in this paper are in good agreement with Standard Model predictions. We look forward to continuing this program with data from future Tevatron collider runs.

ACKNOWLEDGEMENTS

We are extremely grateful to Ulrich Baur for his enormous help and the extensive use of his Monte Carlo programs. We deeply appreciate the many stimulating discussions we have had with him during the course of this analysis. We also wish to thank Fawzi Boudjema for his help on the $ZZ\gamma$ transition moments. We thank the Fermilab Accelerator Division, the Computer Division and the technical staffs of CDF and the collaborating institutions for their effort in the construction and operation of the Tevatron, the Antiproton Source, and this experiment. This work was supported by the Department of Energy, the National Science foundation, Instituto Nazionale di Fisica Nucleare, the Ministry of Science, Culture and Education of Japan, and the A.P. Sloan Foundation.

A THE $W+\gamma$ ANGULAR DISTRIBUTION

The $W+\gamma$ production and decay kinematics in high-energy $\bar{p}$-p collisions is very rich in structure. At large photon scattering angles, θ^* in the $W\gamma$ center of mass, where θ^* is defined as the angle between the photon and the incoming quark in the $W\gamma$ rest frame, the $u-$ and $t-$channel diagrams interfere destructively with the $s-$channel diagram. This results in a radiation amplitude zero [84] in the $W^{\pm}\gamma$ differential cross section $d\sigma/d\cos\theta^*$ at $\cos\theta^* = \mp\frac{1}{3}$. However, the radiation zero is expected to be at least partially filled in due to effects such as higher-order QCD corrections [85], the finite decay width of the W boson, background processes, event mis-reconstruction associated with the two-fold ambiguity of the longitudinal component of the neutrino momentum, structure function effects (*e.g.* $\bar{d}_p u_{\bar{p}} \rightarrow W^+\gamma$ sea-sea interactions) and possible non-gauge theory values of $WW\gamma$ anomalous couplings [84]. For large-statistics samples, measurement of the *depth* of the dip in the differential cross section at $\cos\theta^* = \mp\frac{1}{3}$ and the *shape* of the $cos\theta^*$ distribution provides a sensitive measurement of the values of these anomalous parameters.

Another method for observing the radiation zero, which does not require reconstruction of the $W\gamma$ center-of-mass system and hence is not subject to smearing effects due to event mis-reconstruction is to study the photon−lepton pseudorapidity correlations in $W^{\pm}\gamma$ production [86]. The SM predicts a "valley" or a "channel" in the three-dimensional surface associated with the $d^2\sigma/d\eta_\gamma d\eta_{\ell^\pm}$ distribution (where pseudorapidity $\eta = -\ln(\tan\theta/2)$, and θ is the usual lab-frame polar angle), corresponding to a pronounced "dip" in the $\Delta\eta_{\gamma\ell^\pm} = \eta_\gamma - \eta_{\ell^\pm}$ distribution at $\Delta\eta_{\gamma\ell^\pm} \sim \mp\ 0.35$ for $W^{\pm}\gamma$ production. The "channel" in the $d^2\sigma/d\eta_\gamma d\eta_{\ell^\pm}$ distribution and the corresponding "dip" in the $\Delta\eta_{\gamma\ell^\pm}$ distribution are remnants of the SM radiation amplitude zero in the $\cos\theta^*$ angular distribution and as such are also potentially sensitive to $WW\gamma$ anomalous couplings.

The use of these distributions for setting limits on $WW\gamma$ anomalous couplings is not yet feasible with the small-statistics $W\gamma$ data samples presently available. However, the measurement of the $W\gamma$ production cross section $\times$ decay branching ratio, or equivalently the integral number of isolated photons above a minimum photon E_T^γ cut and a lepton-photon angular separation cut is also sensitive to $WW\gamma$ anomalous couplings, and is the underlying method used in this analysis.

As more integrated luminosity is acquired in the future, with large-statistics $W+\gamma$ data samples it will become possible to study the detailed *shapes* of the photon E_T distribution, the photon-lepton angular separation distribution $\Delta R_{\gamma\ell}$, the photon-lepton pseudorapidity correlation η_γ *vs.* η_{ℓ^+}, and the cluster transverse mass distribution, $M_{CT}^{W\gamma}$ $(\sim \sqrt{\hat{s}})$. These kinematic distributions all contain information on the $W+\gamma$ process which are sensitive to the destructive interference present in the SM production of $W+\gamma$, and which are also sensitive to possible $WW\gamma$ anomalous couplings. The most stringent experimental limits on such couplings will be obtained by simultaneous use of *all* relevant kinematic information.

B METHODOLOGY FOR THE DETERMINATION OF $\sigma \cdot B(W+\gamma)$ AND $\sigma \cdot B(Z+\gamma)$ IN THE ELECTRON AND MUON CHANNELS

The $W+\gamma$ and $Z+\gamma$ cross sections $\times$ branching ratios are generically given by:

$$\sigma \cdot B(V_\ell+\gamma) \;=\; \frac{\mathcal{N}_{sig}(V_\ell+\gamma)}{\int \mathcal{L}_\ell dt \cdot \left(A^\ell_{V\gamma} \cdot \epsilon^\ell_{V\gamma}\right)} \;=\; \frac{\mathcal{N}_{obs}(V_\ell+\gamma) - \Sigma\mathcal{N}_{bkg}(V_\ell+\gamma)}{\int \mathcal{L}_\ell dt \cdot \left(A^\ell_{V\gamma} \cdot \epsilon^\ell_{V\gamma}\right)} \tag{72}$$

or, conversely the number of $W+\gamma$ and $Z+\gamma$ signal events is generically given by:

$$\mathcal{N}_{sig}(V_\ell+\gamma) \;=\; \mathcal{N}_{obs}(V_\ell+\gamma) - \Sigma\mathcal{N}_{bkg}(V_\ell+\gamma) \;=\; \sigma \cdot B(V_\ell+\gamma) \cdot \int \mathcal{L}_\ell dt \cdot \left(A^\ell_{V\gamma} \cdot \epsilon^\ell_{V\gamma}\right) \tag{73}$$

where $V = W$ or Z; $\mathcal{N}_{sig}(V_\ell+\gamma) = \mathcal{N}_{obs}(V_\ell+\gamma) - \Sigma\mathcal{N}_{bkg}(V_\ell+\gamma)$ is the number of signal $W\gamma$ or $Z\gamma$ events in a particular leptonic decay channel ($\ell = e$ or μ); $\mathcal{N}_{obs}(V_\ell+\gamma)$ is the number of observed $W\gamma$ or $Z\gamma$ events in a particular decay channel; $\Sigma\mathcal{N}_{bkg}(V_\ell+\gamma)$ is the number of (summed) background events expected in each of the data samples. The integrated luminosity factor is $\int \mathcal{L}_\ell dt$. The product term $\left(A^\ell_{V\gamma} \cdot \epsilon^\ell_{V\gamma}\right)$ is the overall acceptance $\times$ efficiency factor for selecting $W\gamma$ and $Z\gamma$ events, and is a product of a number of acceptances $\times$ efficiency factors. The explicit forms of the product term $\left(A^\ell_{V\gamma} \cdot \epsilon^\ell_{V\gamma}\right)$ for each of the electron/muon $W\gamma/Z\gamma$ decay channels are given below.

For $W\gamma$ in the electron channel:

$$A^e_{W\gamma} \cdot \epsilon^e_{W\gamma} = \epsilon_{zvx} \cdot A^e_{M^T_W} \cdot \left(A^e_W \cdot T^e \cdot \epsilon^e_{cent_T}\right) \cdot \left(f^{\gamma e}_{Wcem} \cdot A^{\gamma e}_{Wcem} \cdot \epsilon^\gamma_{cem}\right) \tag{74}$$

For $W\gamma$ in the muon channel:

$$A^\mu_{W\gamma} \cdot \epsilon^\mu_{W\gamma} = \epsilon_{zvx} \cdot A^\mu_{M^T_W} \cdot \left(A^\mu_W \cdot T^\mu \cdot \epsilon^\mu_{cent_T} \cdot \epsilon^\mu_{Wcos}\right) \cdot \left(f^{\gamma\mu}_{Wcem} \cdot A^{\gamma\mu}_{Wcem} \cdot \epsilon^\gamma_{cem}\right) \tag{75}$$

For $Z\gamma$ in the electron channel:

$$\begin{aligned}
A^e_{Z\gamma} \cdot \epsilon^e_{Z\gamma} \;=\; & \frac{1}{f^e_{DY}} \cdot \epsilon_{zvx} \cdot A^e_{M_Z} \cdot \left(A^e_Z \cdot T^e \cdot \epsilon^e_{cent_T}\right) \\
& \times \Big[\left\{ f^e_{Zcc} \cdot \left(2\epsilon^e_{cent_L} - T^e \cdot \epsilon^e_{cent_T}\right) \right\} \cdot \left(f^{\gamma e}_{Zcc} \cdot A^{\gamma e}_{Zcc} \cdot \epsilon^\gamma_{cem}\right) \\
& + \left(f^e_{Zcp} \cdot \epsilon^e_{plug}\right) \cdot \left(f^{\gamma e}_{Zcp} \cdot A^{\gamma e}_{Zcp} \cdot \epsilon^\gamma_{cem}\right) \\
& + \left(f^e_{Zcf} \cdot \epsilon^e_{fwrd}\right) \cdot \left(f^{\gamma e}_{Zcf} \cdot A^{\gamma e}_{Zcf} \cdot \epsilon^\gamma_{cem}\right) \Big] \\
= \; & \frac{1}{f^e_{DY}} \cdot \epsilon_{zvx} \cdot A^e_{M_Z} \cdot \left(T^e \cdot \epsilon^e_{cent_T}\right) \\
& \times \Big[\left\{ A^e_{Zcc} \cdot \left(2\epsilon^e_{cent_L} - T^e \cdot \epsilon^e_{cent_T}\right) \right\} \cdot \left(f^{\gamma e}_{Zcc} \cdot A^{\gamma e}_{Zcc} \cdot \epsilon^\gamma_{cem}\right) \\
& + \left(A^e_{Zcp} \cdot \epsilon^e_{plug}\right) \cdot \left(f^{\gamma e}_{Zcp} \cdot A^{\gamma e}_{Zcp} \cdot \epsilon^\gamma_{cem}\right) \\
& + \left(A^e_{Zcf} \cdot \epsilon^e_{fwrd}\right) \cdot \left(f^{\gamma e}_{Zcf} \cdot A^{\gamma e}_{Zcf} \cdot \epsilon^\gamma_{cem}\right) \Big]
\end{aligned} \tag{76}$$

For $Z\gamma$ in the muon channel:

$$
\begin{aligned}
A^{\mu}_{Z\gamma}\cdot\epsilon^{\mu}_{Z\gamma} &= \frac{1}{f^{\mu}_{DY}}\cdot\epsilon_{zvx}\cdot A^{\mu}_{M_Z}\cdot\left(A^{\mu}_{Z}\cdot T^{\mu}\cdot\epsilon^{\mu}_{cent_T}\cdot\epsilon^{\mu}_{Zcos}\right)\\
&\quad\times\Big[\left\{f^{\mu}_{Zcc}\cdot(2-T^{\mu})\cdot\left(2\epsilon^{\mu}_{cent_{L_1}}-\epsilon^{\mu}_{cent_T}\right)\right\}\cdot\left(f^{\gamma_\mu}_{Zcc}\cdot A^{\gamma_\mu}_{Zcc}\cdot\epsilon^{\gamma}_{cem}\right)\\
&\quad+\left(f^{\mu}_{Zc\bar{c}}\cdot\epsilon^{\mu}_{cent_{L_2}}\right)\cdot\left(f^{\gamma_\mu}_{Zc\bar{c}}\cdot A^{\gamma_\mu}_{Zc\bar{c}}\cdot\epsilon^{\gamma}_{cem}\right)\Big]\\
&= \frac{1}{f^{\mu}_{DY}}\cdot\epsilon_{zvx}\cdot A^{\mu}_{M_Z}\cdot\left(T^{\mu}\cdot\epsilon^{\mu}_{cent_T}\cdot\epsilon^{\mu}_{Zcos}\right)\\
&\quad\times\Big[\left\{A^{\mu}_{Zcc}\cdot(2-T^{\mu})\cdot\left(2\epsilon^{\mu}_{cent_{L_1}}-\epsilon^{\mu}_{cent_T}\right)\right\}\cdot\left(f^{\gamma_\mu}_{Zcc}\cdot A^{\gamma_\mu}_{Zcc}\cdot\epsilon^{\gamma}_{cem}\right)\\
&\quad+\left(A^{\mu}_{Zc\bar{c}}\cdot\epsilon^{\mu}_{cent_{L_2}}\right)\cdot\left(f^{\gamma_\mu}_{Zc\bar{c}}\cdot A^{\gamma_\mu}_{Zc\bar{c}}\cdot\epsilon^{\gamma}_{cem}\right)\Big] \qquad (77)
\end{aligned}
$$

The factor ϵ_{zvx} is the efficiency of the $|z_{\rm vtx}| < 60$ cm cut, common to all four data samples. For $\ell = e$ or μ $Z\gamma$ events, f^{ℓ}_{DY} (< 1) is a small correction factor which explicitly takes into account the removal of the Drell-Yan $DY + \gamma$ contribution to events in the $Z + \gamma$ data within the $Z \rightarrow \ell^+\ell^-$ mass window, and also corrects for the loss of $Z + \gamma$ events outside the $Z \rightarrow \ell^+\ell^-$ mass window.

The factor $A^{\ell}_{M^T_W}$ is the acceptance of the transverse mass $M^T_W > 40$ GeV/c^2 cut for $W\gamma$ events passing all other cuts; $A^{\ell}_{M_Z}$ is the acceptance of the Z mass-window cut for $Z\gamma$ events passing all other cuts.

The acceptance factor $A^{e}_{W} = A^{e}_{W\ E_T}\cdot A^{e}_{W fid\ cem}\cdot A^{\bar{\nu}_e}_{W\ \not\!\!E_T}$ is the overall kinematic $\times$ geometrical acceptance for $W \rightarrow e\ \bar{\nu}_e$ in electron $W\gamma$ events, where $A^{e}_{W\ E_T}$ is the kinematical acceptance for central fiducial electrons passing the $E^{e}_T > 20$ GeV cut, $A^{e}_{W fid\ cem}$ is the geometrical acceptance for fiducial central electrons and $A^{\bar{\nu}_e}_{W\ \not\!\!E_T}$ is the kinematic acceptance for the $\not\!\!E_T > 20$ GeV cut.

Similarly, $A^{\mu}_{W} = A^{\mu}_{W\ P_T}\cdot A^{\mu}_{W fid\ cmu}\cdot A^{\bar{\nu}_\mu}_{W\ \not\!\!E_T}$ is the overall kinematic $\times$ geometrical acceptance for $W \rightarrow \mu\ \bar{\nu}_\mu$ in muon $W\gamma$ events, where $A^{\mu}_{W\ P_T}$ is the kinematical acceptance for central fiducial muons passing the $P^{\mu}_T > 20$ GeV cut, $A^{\mu}_{W fid\ cmu}$ is the geometrical acceptance for fiducial central muons and $A^{\bar{\nu}_\mu}_{W\ \not\!\!E_T}$ is the kinematic acceptance for the $\not\!\!E_T > 20$ GeV cut.

The overall kinematic $\times$ geometrical acceptance factor for electron Z decays is $A^{e}_{Z} = A^{e}_{Zcc} + A^{e}_{Zcp} + A^{e}_{Zcf}$, where the factors A^{e}_{Zcc}, A^{e}_{Zcp} and A^{e}_{Zcf} are the overall kinematical $\times$ geometrical acceptances for the topological classes of central-central, central-plug and central-forward fiducial-fiducial dielectrons from Z decay, respectively. The overall kinematic $\times$ geometrical acceptance factors for the three topological classes are products of individual kinematic $\times$ geometrical acceptance factors:

$$A^{e}_{Zcx} = \left(A^{e_1}_{Zc\ E_T}\cdot A^{e_1}_{Zc\ fid\ cem}\right)\cdot\left(A^{e_2}_{Zx\ E_T}\cdot A^{e_2}_{Zx\ fid}\right) \qquad (78)$$

where cx = cc, cp or cf, and $A^{e_1}_{Zc\ E_T}$ is the kinematic acceptance for the commonly-selected "tight" electron passing the $E^{e}_T > 20$ GeV cut and $A^{e_1}_{Zc\ fid\ cem}$ is the geometrical fiducial acceptance associated with the central EM calorimeter. The factor $A^{e_2}_{Zx\ E_T}$ is the kinematic acceptance for the "loose" electron passing the $E^{e}_T > 10$ GeV cut and $A^{e_2}_{Zx\ fid}$ is the geometrical acceptance associated with the fiducial acceptance of the central, plug or forward EM calorimeters, for $x = c$, p, or f, respectively. The corresponding acceptance fractions f^{e}_{Zcc} , f^{e}_{Zcp} and f^{e}_{Zcf} are given by $f^{e}_{Zcc} = A^{e}_{Zcc}/A^{e}_{Z}$, $f^{e}_{Zcp} = A^{e}_{Zcp}/A^{e}_{Z}$ and $f^{e}_{Zcf} = A^{e}_{Zcf}/A^{e}_{Z}$, respectively.

The overall kinematic × geometrical acceptance factor for muon Z decays is $A^{\mu}_{Z} = A^{\mu}_{Zcc} + A^{\mu}_{Zc\bar{c}}$, where the factors A^{μ}_{Zcc}, $A^{\mu}_{Zc\bar{c}}$ are the overall kinematical × geometrical acceptances for the topological classes of central-central fiducial-fiducial and fiducial-nonfiducial dimuons from Z decay, respectively. The overall kinematic × geometrical acceptance factors for the two topological classes are products of individual kinematic × geometrical acceptance factors:

$$A^{\mu}_{Zcx} = \left(A^{\mu_1}_{Zc\ P_T} \cdot A^{\mu_1}_{Zc\ fid\ cmu}\right) \cdot \left(A^{\mu_2}_{Zx\ P_T} \cdot A^{\mu_2}_{Zx\ fid}\right) \tag{79}$$

where $cx = cc$ or $c\bar{c}$, and $A^{\mu_1}_{Zc\ P_T}$ is the kinematic acceptance for the commonly-selected "tight" muon passing the $P^{\mu}_{T} > 20$ GeV/c cut and $A^{\mu_1}_{Zc\ fid\ cmu}$ is the geometrical fiducial acceptance associated with the central muon system. The factor $A^{\mu_2}_{Zx\ P_T}$ is the kinematic acceptance for the "loose" muon passing the $P^{\mu}_{T} > 20$ GeV/c cut and $A^{\mu_2}_{Zx\ fid}$ is the geometrical acceptance for either the fiducial acceptance ($x = c$), or the allowed non-fiducial acceptance ($x = \bar{c}$). The corresponding acceptance fractions f^{μ}_{Zcc} and $f^{\mu}_{Zc\bar{c}}$ are given by $f^{\mu}_{Zcc} = A^{\mu}_{Zcc}/A^{\mu}_{Z}$ and $f^{\mu}_{Zc\bar{c}} = A^{\mu}_{Zc\bar{c}}/A^{e}_{Z}$, respectively.

The overall W/Z lepton trigger efficiency for the common "tight" central lepton selection is $T^{\ell} = \epsilon^{\ell}_{L1} \cdot \epsilon^{\ell}_{L2} \cdot \epsilon^{\ell}_{L3}$, where the ϵ^{ℓ}_{Li}, $i = 1 - 3$ are the individual level-1 - level-3 lepton ($\ell = e$ or μ) trigger efficiencies, respectively.

The overall "tight" central fiducial electron selection efficiency, common for both W and Z boson decay is given by:

$$\epsilon^{e}_{cent_T} = \epsilon^{cem}_{iso} \cdot \epsilon^{cem}_{(Had/EM)_T} \cdot \epsilon^{cem}_{\chi^2_{strip}} \cdot \epsilon^{cem}_{Lshr} \cdot \epsilon^{cem}_{(E/P)_T} \cdot \epsilon^{cem}_{trk} \cdot \epsilon^{cem}_{\Delta z} \cdot \epsilon^{cem}_{\Delta x} \tag{80}$$

where the individual efficiencies for the common central electron selection are the isolation $I < 0.1$ cut, ϵ^{cem}_{iso}; the "tight" Had/EM cut, $\epsilon^{cem}_{(Had/EM)_T}$; the CES strip $\chi^2 < 20$ cut, $\epsilon^{cem}_{\chi^2_{strip}}$; the $L_{\rm shr} < 0.2$ cut, ϵ^{cem}_{Lshr}; the "tight" $E/P < 1.5$ cut, $\epsilon^{cem}_{(E/P)_T}$; CTC electron track reconstruction, ϵ^{cem}_{trk} and the CTC-CES $\Delta z < 3.0$ cm and $\Delta r - \phi < 1.5$ cm track match cuts, $\epsilon^{cem}_{\Delta z}$ and $\epsilon^{cem}_{\Delta x}$, respectively.

The overall "loose" central electron selection efficiency for Z boson decay is given by

$$\epsilon^{e}_{cent_L} = \epsilon^{cem}_{iso} \cdot \epsilon^{cem}_{(Had/EM)_L} \cdot \epsilon^{cem}_{(E/P)_L} \tag{81}$$

where the individual common central electron selection efficiencies are the isolation $I < 0.1$ cut, ϵ^{cem}_{iso}; the "loose" Had/EM cut, $\epsilon^{cem}_{(Had/EM)_L}$ and the "loose" $E/P < 2.0$ cut, $\epsilon^{cem}_{(E/P)_L}$.

The overall plug electron selection efficiency for Z boson decay is given by

$$\epsilon^{e}_{plug} = \epsilon^{pem}_{iso} \cdot \epsilon^{pem}_{(Had/EM)} \cdot \epsilon^{pem}_{\chi^2_{3x3}} \cdot \epsilon^{pem}_{vtpc} \tag{82}$$

where the individual common plug electron selection efficiencies are the isolation $I < 0.1$ cut, ϵ^{pem}_{iso}; the Had/EM cut, $\epsilon^{pem}_{(Had/EM)}$; the pad $\chi^2_{3x3} < 20$ cut, $\epsilon^{pem}_{\chi^2_{3x3}}$ and the VTPC hit fraction > 0.5 cut, ϵ^{pem}_{vtpc}.

The overall forward electron selection efficiency for Z boson decay is given by

$$\epsilon^{e}_{fwrd} = \epsilon^{fem}_{iso} \cdot \epsilon^{fem}_{(Had/EM)} \tag{83}$$

where the individual common forward electron selection efficiencies are the isolation $I < 0.1$ cut, ϵ^{fem}_{iso} and the "loose" Had/EM cut, $\epsilon^{fem}_{(Had/EM)_L}$.

The overall "tight" central fiducial muon selection efficiency, common for both W and Z boson decay is given by:

$$\epsilon^{\mu}_{cent_T} = \epsilon^{cmu}_{iso} \cdot \epsilon^{cmu}_{mi} \cdot \epsilon^{cmu}_{stub} \cdot \epsilon^{cmu}_{trk} \cdot \epsilon^{cmu}_{\Delta x} \tag{84}$$

where the individual efficiencies for the common central muon selection are the isolation $I < 0.1$ cut, ϵ^{cmu}_{iso}; the minimum ionizing cut, ϵ^{cmu}_{mi}; the CMU stub-finding efficiency, ϵ^{cmu}_{stub}; the CTC re-tracking efficiency for the $P^{\mu}_T > 20$ GeV/c cut, ϵ^{cmu}_{trk} and the CTC-CMU $\Delta r - \phi < 1.5$ cm track-stub matching cut, $\epsilon^{cem}_{\Delta x}$.

The overall "loose" central fiducial and non-fiducial muon selection efficiencies for Z boson decay are respectively given by:

$$\epsilon^{\mu}_{cent_{L_1}} = \epsilon^{cmu}_{mi} \cdot \epsilon^{cmu}_{stub} \cdot \epsilon^{cmu}_{trk} \tag{85}$$

$$\epsilon^{\mu}_{cent_{L_2}} = \epsilon^{cmu}_{mi} \cdot \epsilon^{cmu}_{trk} \tag{86}$$

The factors $\epsilon^{\mu}_{W,Z\ cos}$ account for a small over-efficiency in the removal of cosmic ray background from the $W\gamma$ and $Z\gamma$ data samples, respectively.

For central photons in $\ell = e$ or μ $W\gamma$ events, the factor $f^{\gamma\ell}_{Wcem}$ is defined as the fraction of all photons that are central ($|\eta_\gamma| < 1.1$), which are produced in $W\gamma$ events where the W decay leptons pass the W selection requirements and the photon has already satisfied the $E^{\gamma}_T > 5.0$ GeV and $\Delta R_{\ell\gamma} > 0.7$ requirements. The photon acceptance factor is

$$\begin{aligned} A^{\gamma\ell}_{Wcem} &= A^{\gamma\ell}_{W\ E^{\gamma}_T} \cdot A^{\gamma\ell}_{W fid\ cem} \cdot A^{\gamma\ell}_{W\ \Delta R_{\ell\gamma}} \\ &= 1.0 \cdot A^{\gamma\ell}_{W fid\ cem} \cdot 1.0 = A^{\gamma\ell}_{W fid\ cem} \end{aligned} \tag{87}$$

We are measuring only that portion of the (total) production cross section $\times$ branching ratio, $\sigma \cdot B(W + \gamma)$ associated with photons above $E^{\gamma}_T > 5.0$ GeV and lepton-photon angular separation $\Delta R_{\ell\gamma} > 0.7$. Therefore, the photon acceptance factor $A^{\gamma\ell}_{Wcem}$ is defined such that the kinematic acceptance factor, $A^{\gamma\ell}_{W\ E^{\gamma}_T} = 1.0$ since by our definition of the $\sigma \cdot B(W + \gamma)$ cross section all central photons with W bosons must intrinsically pass the $E^{\gamma}_T > 5.0$ GeV requirement. The factor $A^{\gamma\ell}_{W fid\ cem}$ is the geometrical acceptance for photons which are in the central region ($|\eta_\gamma| < 1.1$) for $W\gamma$ events with W decay leptons passing the W selection requirements and central photons already satisfying the $E^{\gamma}_T > 5.0$ GeV and $\Delta R_{\ell\gamma} > 0.7$ requirements and passing the CEM fiducial requirements. Similarly, the lepton-photon angular separation acceptance factor for central photons is $A^{\gamma\ell}_{W\ \Delta R_{\ell\gamma}} = 1.0$ since by our definition of the $\sigma \cdot B(W + \gamma)$ cross section all photons must also intrinsically pass the $\Delta R_{\ell\gamma} > 0.7$ angular separation requirement. The product $f^{\gamma\ell}_{Wcem} \cdot A^{\gamma\ell}_{Wcem}$ is therefore the acceptance factor for central fiducial photons from $\ell = e$ or μ $W\gamma$ events that have already satisfied the W selection and $E^{\gamma}_T > 5.0$ GeV and $\Delta R_{\ell\gamma} > 0.7$ requirements.

For central photons in electron $Z\gamma$ events, the factors $f^{\gamma e}_{Zcc}$, $f^{\gamma e}_{Zcp}$ and $f^{\gamma e}_{Zcf}$ are defined as the fraction of all photons that are central ($|\eta_\gamma| < 1.1$), which are produced in electron $Z\gamma$ events where the Z decay electrons pass the Z selection requirements for each class of central-central, central-plug and central-forward fiducial-fiducial Z bosons, respectively, and the photon has already satisfied the $E^{\gamma}_T > 5.0$ GeV and $\Delta R_{e\gamma} > 0.7$ requirements. For central photons in muon $Z\gamma$ events, the factors $f^{\gamma\mu}_{Zcc}$ and $f^{\gamma\mu}_{Zc\bar{c}}$ are similarly defined as the fraction of all photons that are central ($|\eta_\gamma| < 1.1$), which are produced in muon $Z\gamma$ events where the Z decay muons pass the Z selection requirements for both classes of central-central fiducial-fiducial and fiducial-nonfiducial Z bosons, respectively,

and the photon has already satisfied the $E_T^\gamma > 5.0$ GeV and $\Delta R_{e\gamma} > 0.7$ requirements. For electron $Z\gamma$, the factors $A_{Zcc}^{\gamma_e}$, $A_{Zcp}^{\gamma_e}$ and $A_{Zcf}^{\gamma_e}$ represent the individual overall acceptances associated with central photons passing all photon cuts in electron $Z\gamma$ events for central-central, central-plug and central-forward fiducial-fiducial dielectrons from Z decay, respectively. For muon $Z\gamma$, the factors $A_{Zcc}^{\gamma_\mu}$ and $A_{Zc\bar{c}}^{\gamma_\mu}$ represent the individual overall acceptances associated with central photons passing all photon cuts in muon $Z\gamma$ events for central-central, fiducial-fiducial and fiducial-nonfiducial dimuons from Z decay, respectively.

Each of the individual central photon acceptance terms is in turn a product of individual central photon acceptances:

$$\begin{aligned} A_{Zcx}^{\gamma\ell} &= A_{Zcx\ E_T^\gamma}^{\gamma\ell} \cdot A_{Zcx\ fid\ cem}^{\gamma\ell} \cdot A_{Zcx\ \Delta R_{\ell\gamma}}^{\gamma\ell} \\ &= 1.0 \cdot A_{Zcx\ fid\ cem}^{\gamma\ell} \cdot 1.0 \ = \ A_{Zcx\ fid\ cem}^{\gamma\ell} \end{aligned} \tag{88}$$

where $\ell = e$ or μ, and $cx = cc$, cp, or cf for electron $Z\gamma$ and $cx = cc$, or $c\bar{c}$ for muon $Z\gamma$. We are measuring only that portion of the (total) production cross section $\times$ branching ratio, $\sigma \cdot B(Z+\gamma)$ associated with photons above $E_T^\gamma > 5.0$ GeV and lepton-photon angular separation $\Delta R_{\ell\gamma} > 0.7$. Therefore, the photon acceptance factor $A_{Zcx}^{\gamma\ell}$ is such that the kinematic acceptance factor $A_{Zcx\ E_T^\gamma}^{\gamma\ell} = 1.0$ since by our definition of the $\sigma \cdot B(Z+\gamma)$ cross section, all central photons associated with cx Z bosons must intrinsically pass the $E_T^\gamma > 5.0$ GeV requirement. The factor $A_{Zcx\ fid\ cem}^{\gamma\ell}$ is the geometrical acceptance for photons which are in the central ($|\eta_\gamma| < 1.1$) region associated with cx Z bosons from $Z\gamma$ events with Z decay leptons passing the Z selection requirements and central photons already satisfying the $E_T^\gamma > 5.0$ GeV and $\Delta R_{\ell\gamma} > 0.7$ requirements, that pass the CEM fiducial requirements. Similarly, the lepton-photon angular separation acceptance factor for central photons associated with cx Z bosons is $A_{Zcx\ \Delta R_{\ell\gamma}}^{\gamma\ell} = 1.0$ since by our definition of $\sigma \cdot B(Z+\gamma)$, all photons must also intrinsically pass the $\Delta R_{\ell\gamma} > 0.7$ angular separation requirement, which is applied to both of the Z decay leptons. The product $f_{Zcx}^{\gamma\ell} \cdot A_{Zcx}^{\gamma\ell}$ is therefore the acceptance factor for central fiducial photons associated with $\ell = e$ or μ cx $Z\gamma$ events that have already satisfied the Z selection and $E_T^\gamma > 5.0$ GeV and $\Delta R_{\ell\gamma} > 0.7$ requirements.

The central fiducial photon selection efficiency, common to all four $W\gamma$ and $Z\gamma$ data sets, is given by

$$\epsilon_{cem}^\gamma = \epsilon_{ET4}^\gamma \cdot \epsilon_{\Sigma PT4}^\gamma \cdot \epsilon_{N3D}^\gamma \cdot \epsilon_{Had/EM}^\gamma \cdot \epsilon_{Lshr}^\gamma \cdot \epsilon_{\chi^2_{stp}+\chi^2_{wir}}^\gamma \cdot \epsilon_{no\ 2^{nd}\ CES}^\gamma \cdot \mathcal{P}_{\overline{conv}}^\gamma \cdot \mathcal{S}_{e\to\gamma}^{cem} \tag{89}$$

where the individual terms are the central fiducial photon efficiencies for passing the calorimeter isolation $ET4 < 2.0$ GeV cut, followed in sequence by the tracking isolation $\Sigma PT4 < 2.0$ GeV cut, the $N3D = 0$ cut, the Had/EM cut, the $L_{shr} < 0.5$ cut, the CES $\chi^2_{strip} < 20$ and χ^2_{wire} cuts and the no 2^{nd} CES strip or wire clusters with $E_{2^{nd}}^{ces} > 1$ GeV cut. The factor $\mathcal{P}_{\overline{conv}}^\gamma$ is the photon survival probability for a photon to traverse the material of the inner central detector without converting to an e^+e^- pair. The factor $\mathcal{S}_{e\to\gamma}^{cem}$ is a small correction to account for differences in EM shower development for electrons *vs.* photons, since electron test beam data was used to determine some of the individual photon efficiencies.

The numerical values associated with the overall acceptance $\times$ efficiency product terms for each of the electron/muon $W\gamma/Z\gamma$ decay channels are summarized in Table 6 in the main text. The individual electron and muon efficiencies for the $W\gamma$ and $Z\gamma$ data samples are summarized in Tables 30 and 31. The overall electron and muon efficiencies for the $W\gamma$ and $Z\gamma$ data samples are

summarized in Tables 32 and 33. The kinematic × geometrical acceptance factors for the W and Z bosons and for photons associated with Standard Model $W\gamma$ and $Z\gamma$ processes in the electron and muon channels as determined using the Baur $W\gamma/Z\gamma$ and "fast" MC detector simulation programs, for the "nominal" set of HMRS-B structure functions are summarized in Table 34. The photon acceptance fractions $f^{\gamma\ell}$ and acceptance factors $A^{\gamma\ell}$ associated with $\sigma \cdot B(V_\ell + \gamma)_{cuts}$ for $W\gamma$ and $Z\gamma$ are summarized in Tables 35 and 36, respectively.

Table 30: Individual Electron Efficiencies for $W\gamma$ and $Z\gamma$ Data Samples. The statistical uncertainty associated with each quantity is given.

f^e_{DY}	$98.5 \pm 0.5\%$	$70 < M^{ee}_Z < 110$ GeV/c^2
ϵ_{zvx}	$95.4 \pm 0.1\%$	$\lvert z_{\rm vtx}\rvert < 60$ cm
ϵ^{cem}_{iso}	$96.0 \pm 1.0\%$	Isolation $I < 0.1$ Cut
$\epsilon^{cem}_{(Had/EM)_T}$	$99.0 \pm 1.0\%$	Tight Had/EM Cut
$\epsilon^{cem}_{(Had/EM)_L}$	$99.0 \pm 1.0\%$	Loose Had/EM Cut
$\epsilon^{cem}_{\chi^2_{strip}}$	$97.0 \pm 1.0\%$	$\chi^2_{strip} < 15.0$ Cut
ϵ^{cem}_{Lshr}	$97.0 \pm 1.0\%$	$L_{shr} < 0.2$ Cut
$\epsilon^{cem}_{(E/P)_T}$	$93.0 \pm 1.0\%$	Tight E/P < 1.5 Cut
$\epsilon^{cem}_{(E/P)_L}$	$97.0 \pm 1.0\%$	Loose E/P < 2.0 Cut
ϵ^{cem}_{trk}	$100.0^{+0.0}_{-0.1}\%$	CTC Track Reconstruction
$\epsilon^{cem}_{\Delta x}$	$97.0 \pm 1.0\%$	$\Delta x < 1.5$ cm Matching Cut
$\epsilon^{cem}_{\Delta z}$	$98.0 \pm 1.0\%$	$\Delta z < 3.0$ cm Matching Cut
ϵ^{pem}_{iso}	$96.0 \pm 1.0\%$	Isolation $I < 0.1$ Cut
$\epsilon^{pem}_{(Had/EM)}$	$99.0 \pm 1.0\%$	Had/EM Cut
$\epsilon^{pem}_{\chi^2_{3x3}}$	$94.0 \pm 1.0\%$	$\chi^2_{3x3} < 20$ Cut
ϵ^{pem}_{vtpc}	$93.0 \pm 2.0\%$	VTPC hit fraction > 0.5 Cut
ϵ^{fem}_{iso}	$91.0 \pm 1.0\%$	Isolation $I < 0.1$ Cut
$\epsilon^{fem}_{(Had/EM)}$	$100.0^{+0.0}_{-0.1}\%$	Had/EM Cut
ϵ^{e}_{L1}	$99.3 \pm 0.3\%$	Level-1 Central Electron Trigger
ϵ^{e}_{L2}	$98.0 \pm 0.4\%$	Level-2 Central Electron Trigger
ϵ^{e}_{L3}	$100.0^{+0.0}_{-0.1}\%$	Level-3 Central Electron Trigger

Table 31: Individual Muon Efficiencies for $W\gamma$ and $Z\gamma$ Data Samples. The statistical uncertainty associated with each quantity is given.

f^{μ}_{DY}	$97.0 \pm 0.2\%$	$65 < M_Z^{\mu\mu} < 115$ GeV/c^2
ϵ_{zvx}	$95.4 \pm 0.1\%$	$\lvert z_{\rm vtx}\rvert < 60$ cm
ϵ^{cmu}_{iso}	$98.0 \pm 1.0\%$	Muon Isolation Cut ($\Delta R = 0.4$)
ϵ^{cmu}_{mi}	$98.7 \pm {}^{0.3}_{0.4}\%$	Minimum Ionizing Energy Cut
ϵ^{cmu}_{trk}	$98.7 \pm 1.0\%$	CTC Re-Tracking
ϵ^{cmu}_{stub}	$98.6 \pm {}^{1.2}_{3.3}\%$	CMU Stub Finding
$\epsilon^{cmu}_{\Delta x}$	$96.0 \pm 1.0\%$	$\Delta z < 2.0$ cm Track Match
ϵ^{μ}_{Wcos}	$99.7 \pm 0.2\%$	Cosmic Ray Filter
ϵ^{μ}_{Zcos}	$99.7 \pm 0.2\%$	Cosmic Ray Filter
ϵ^{μ}_{L1}	$93.4 \pm 0.4\%$	Level-1 Central Muon Trigger
ϵ^{μ}_{L2}	$97.2 \pm {}^{1.5}_{2.7}\%$	Level-2 Central Muon Trigger
ϵ^{μ}_{L3}	$100.0^{+0.0}_{-2.8}\%$	Level-3 Central Muon Trigger

Table 32: Overall Electron Efficiencies for $W\gamma$ and $Z\gamma$ Data Samples. The statistical uncertainty associated with each quantity is given.

$\int \mathcal{L}_e \cdot dt$	4.05 ± 0.28	Integrated Luminosity (pb^{-1})
T^e	$97.3 \pm 0.5\%$	Central Fiducial Electron Trigger
$\epsilon^{e}_{cent_T}$	$84.0 \pm 3.0\%$	"Tight" Central Fiducial Electron
$\epsilon^{e}_{cent_L}$	$93.0 \pm 3.0\%$	"Loose" Central Fiducial Electron
ϵ^{e}_{plug}	$90.0 \pm 3.0\%$	Plug Fiducial Electron
ϵ^{e}_{fwrd}	$91.0 \pm 3.0\%$	Forward Fiducial Electron

Table 33: Overall Muon Efficiencies for $W\gamma$ and $Z\gamma$ Data Samples. The statistical uncertainty associated with each quantity is given.

$\int \mathcal{L}_\mu \cdot dt$	3.54 ± 0.24	Integrated Luminosity (pb^{-1})
T^{μ}	$91.0 \pm 2.0\%$	Central Fiducial Muon Trigger
$\epsilon^{\mu}_{cent_T}$	$90.4 \pm 3.8\%$	"Tight" Central Fiducial Muon
$\epsilon^{\mu}_{cent_{L_1}}$	$96.0 \pm 3.5\%$	"Loose" Central Fiducial Muon
$\epsilon^{\mu}_{cent_{L_2}}$	$97.4 \pm 1.1\%$	"Loose" Central Non-Fiducial Muon

Table 34: W and Z Acceptances for e and μ $\sigma \cdot B(W/Z+\gamma)_{cuts}$. The statistical uncertainty associated with each quantity is given.

Acceptance	Electron	Muon
A_W^ℓ	$22.4 \pm 0.1\%$	$13.4 \pm 0.1\%$
$A_{M_W^T}^\ell$	$98.3 \pm 0.1\%$	$98.7 \pm 0.1\%$
A_Z^ℓ	$28.9 \pm 0.1\%$	$15.0 \pm 0.1\%$
$A_{M_Z}^\ell$	$83.1 \pm 0.2\%$	$86.9 \pm 0.2\%$
A_{Zcc}^ℓ	$12.9 \pm 0.1\%$	$4.8 \pm 0.1\%$
A_{Zcp}^e or $A_{Zc\bar{c}}^\mu$	$13.3 \pm 0.1\%$	$10.2 \pm 0.1\%$
A_{Zcf}^ℓ	$2.7 \pm 0.1\%$	–
A_{ZW}^ℓ	$2.5 \pm 0.1\%$	$14.3 \pm 0.1\%$

Table 35: Photon Fractions and Acceptances for e and μ $\sigma \cdot B(W+\gamma)_{cuts}$. The statistical uncertainty associated with each quantity is given.

$W\gamma$	Electron	Muon
$f_{Wcem}^{\gamma\ell}$	$47.4 \pm 0.3\%$	$47.4 \pm 0.5\%$
$A_{Wcem}^{\gamma\ell}$	$75.3 \pm 0.2\%$	$75.5 \pm 0.3\%$

Table 36: Photon Fractions and Acceptances for e and μ $\sigma \cdot B(Z+\gamma)_{cuts}$. The statistical uncertainty associated with each quantity is given.

$Z\gamma$	Electron	Muon
$f_{Zcc}^{\gamma\ell}$	$64.5 \pm 0.4\%$	$66.2 \pm 0.7\%$
$f_{Zcp}^{\gamma e}$ or $f_{Zc\bar{c}}^{\gamma\mu}$	$55.7 \pm 0.5\%$	$64.3 \pm 0.5\%$
$f_{Zcf}^{\gamma\ell}$	$39.4 \pm 1.1\%$	–
$A_{Zcc}^{\gamma\ell}$	$76.9 \pm 0.3\%$	$76.9 \pm 0.5\%$
$A_{Zcp}^{\gamma e}$ or $A_{Zc\bar{c}}^{\gamma\mu}$	$76.6 \pm 0.4\%$	$76.1 \pm 0.4\%$
$A_{Zcf}^{\gamma\ell}$	$71.3 \pm 1.4\%$	–

C METHODOLOGY FOR THE DETERMINATION OF $\sigma \cdot B(V_\ell + \gamma)_{cuts}$ FROM MONTE CARLO $\sigma \cdot B(V_\ell + \gamma)_{gen}$

The Monte Carlo $W\gamma/Z\gamma$ production cross sections $\times$ decay branching ratios passing all photon cuts, $\sigma \cdot B(V_\ell + \gamma)_{cuts}$ are determined from the cross section output from the Baur $W\gamma/Z\gamma$ Monte Carlo event generators, $\sigma \cdot B(V_\ell + \gamma)_{gen}$ by using the fact that:

$$\mathcal{N}_{V_\ell+\gamma} = \sigma \cdot B(V_\ell + \gamma)_{cuts} \cdot \int \mathcal{L}_\ell dt \cdot \left(A^\ell_{V\gamma} \cdot \epsilon^\ell_{V\gamma}\right) \tag{90}$$

However:

$$\mathcal{N}_{V_\ell+\gamma} = \sigma \cdot B(V_\ell + \gamma)_{gen} \cdot \int \mathcal{L}_\ell dt \cdot \left(A'^\ell_{V\gamma} \cdot \epsilon^\ell_{V\gamma}\right) \tag{91}$$

The product factor $(A^\ell_{V\gamma} \cdot \epsilon^\ell_{V\gamma})$ is given by equations (74) – (77). The overall kinematic/geometrical acceptance factor $\times$ efficiency for $V_\ell + \gamma$ events ($V = W$ or Z, $\ell = e$ or μ) for the *generated* $V_\ell + \gamma$ events to pass the $E_T^\gamma > 5.0$ GeV and $\Delta R_{\ell\gamma} > 0.7$ cuts is $(A'^\ell_{V\gamma} \cdot \epsilon^\ell_{V\gamma})$. Thus the $(A'^\ell_{V\gamma} \cdot \epsilon^\ell_{V\gamma})$ are the same as equations (74) – (77) except that all of the individual acceptance terms A_i are replaced by A'_i. We thus obtain the general relation:

$$\sigma \cdot B(V_\ell + \gamma)_{cuts} = \sigma \cdot B(V_\ell + \gamma)_{gen} \cdot \left[\frac{A'^\ell_{V\gamma} \cdot \epsilon^\ell_{V\gamma}}{A^\ell_{V\gamma} \cdot \epsilon^\ell_{V\gamma}}\right] \tag{92}$$

The predicted number of electron $W + \gamma$ events can then be obtained by use of either equation (90) or equation (91).

In Table 34 we summarize the Standard Model kinematic $\times$ geometrical acceptance factors associated with $\sigma \cdot B(V_\ell + \gamma)_{cuts}$ for the W and Z bosons from the $W\gamma$ and $Z\gamma$ processes in the electron and muon channels, as determined using the Baur $W\gamma/Z\gamma$ and "fast" MC detector simulation programs, for the "nominal" set of HMRS-B structure functions. The photon acceptance fractions $f^{\gamma\ell}$ and acceptance factors $A^{\gamma\ell}$ associated with $\sigma \cdot B(V_\ell + \gamma)_{cuts}$ for $W\gamma$ and $Z\gamma$ are summarized in Tables 35 and 36, respectively. Table 37 summarizes the kinematic $\times$ geometrical acceptance factors with $\sigma \cdot B(V_\ell + \gamma)_{gen}$ for the e and μ channel W and Z bosons from the $W\gamma$ and $Z\gamma$ processes. The photon acceptance fractions $f'^{\gamma\ell}$ and acceptance factors $A'^{\gamma\ell}$ associated with $\sigma \cdot B(V_\ell + \gamma)_{gen}$ are summarized in Tables 38 and 39, for $W\gamma$ and $Z\gamma$, respectively.

Table 37: W and Z Acceptances for e and μ $\sigma \cdot B(W/Z+\gamma)_{gen}$. The statistical uncertainty associated with each quantity is given.

Acceptance	Electron	Muon
$A_W^{\prime\ell}$	$34.1 \pm 0.1\%$	$20.4 \pm 0.1\%$
$A_{M_W^T}^{\prime\ell}$	$98.4 \pm 0.1\%$	$98.7 \pm 0.1\%$
$A_Z^{\prime\ell}$	$36.6 \pm 0.1\%$	$19.2 \pm 0.1\%$
$A_{M_Z}^{\prime\ell}$	$83.1 \pm 0.2\%$	$86.9 \pm 0.2\%$
$A_{Zcc}^{\prime\ell}$	$16.4 \pm 0.1\%$	$6.1 \pm 0.1\%$
$A_{Zcp}^{\prime e}$ or $A_{Zc\bar{c}}^{\prime\mu}$	$16.9 \pm 0.1\%$	$13.1 \pm 0.1\%$
$A_{Zcf}^{\prime\ell}$	$3.3 \pm 0.1\%$	–
$A_{ZW}^{\prime\ell}$	$3.2 \pm 0.1\%$	$17.5 \pm 0.1\%$

Table 38: Photon Fractions and Acceptances for e and μ $\sigma \cdot B(W+\gamma)_{gen}$. The statistical uncertainty associated with each quantity is given.

$W\gamma$	Electron	Muon
$f_{Wcem}^{\prime\gamma_\ell}$	$47.5 \pm 0.1\%$	$47.4 \pm 0.1\%$
$A_{Wcem}^{\prime\gamma_\ell}$	$13.6 \pm 0.1\%$	$13.7 \pm 0.1\%$

Table 39: Photon Fractions and Acceptances for e and μ $\sigma \cdot B(Z+\gamma)_{gen}$. The statistical uncertainty associated with each quantity is given.

$Z\gamma$	Electron	Muon
$f_{Zcc}^{\prime\gamma_\ell}$	$71.9 \pm 0.2\%$	$75.0 \pm 0.3\%$
$f_{Zcp}^{\prime\gamma_e}$ or $f_{c\bar{c}}^{\prime\gamma_\mu}$	$52.3 \pm 0.2\%$	$72.0 \pm 0.3\%$
$f_{Zcf}^{\prime\gamma_\ell}$	$40.2 \pm 0.2\%$	–
$A_{Zcc}^{\prime\gamma_\ell}$	$19.1 \pm 0.2\%$	$18.9 \pm 0.3\%$
$A_{Zcp}^{\prime\gamma_e}$ or $A_{c\bar{c}}^{\prime\gamma_\mu}$	$20.1 \pm 0.2\%$	$19.3 \pm 0.2\%$
$A_{Zcf}^{\prime\gamma_\ell}$	$13.3 \pm 0.6\%$	–

D TESTS OF THE QCD JET MISIDENTIFICATION PROBABILITY DISTRIBUTION

In order to determine the level of background from QCD W/Z+Jet in $W/Z + \gamma$ data samples, we have used a non-signal control sample of Jet-20 data to obtain the QCD jet misidentification probability distribution $\mathcal{P}_{Jet\rightarrow"\gamma"}^{Control\ Sample}(E_T)$. A total of 20 Jet-20 events passed all photon cuts used for selecting the electron/muon $W\gamma/Z\gamma$ data samples. A total of 11726 non-leading central jets passed our jet selection cuts. Due to the limited statistics in the numerator, this probability distribution calculated with a finite number of discrete bins in E_T, and then bin-by-bin multiplied by the number of central jets in each of the four data samples. This method of determining the amount of QCD jet background in each data sample therefore tacitly assumes that the QCD jet misidentification probability distributions are the same in both the non-signal control sample and the signal data samples:

$$\mathcal{P}_{Jet\rightarrow"\gamma"}^{Control\ Sample}(E_T) \;=\; \mathcal{P}_{Jet\rightarrow"\gamma"}^{W_\ell/Z_\ell}(E_T) \tag{93}$$

The validity of this relation can be tested by explicitly comparing the QCD jet misidentification probability distribution obtained from the Jet-20 data sample with that obtained from the combined $e + \mu$ inclusive W data samples, where for the latter, we *assume* the $W\gamma$ signal to be that of the Standard Model prediction, and subtract it out from the numerator of the combined $e + \mu$ W data samples' QCD jet misidentification probability distribution, such that for the i^{th} E_T−bin, this relation becomes:

$$\left[\frac{\Delta\mathcal{N}_i^{Fid\ CEM\ J20}}{\Delta\mathcal{N}_i^{Extra\ Jet\ J20}}\right] \;=\; \left[\frac{\Delta\mathcal{N}_{i\ \gamma\ Bkgnd}^{Fid\ CEM\ V_\ell}}{\Delta\mathcal{N}_i^{Extra\ Jet\ V_\ell}}\right] \tag{94}$$

These results are summarized in Table 40. The available statistics are limited for each case, even after combining the $e + \mu$ inclusive W data samples. The Jet-20 (combined $e + \mu$ inclusive W) data sample has 20 (13) events passing all cuts, respectively. A SM signal of 7.0 ± 0.6 events is expected for the combined $e + \mu$ $W\gamma$ data. Despite the limited statistics, the agreement between the two probability distributions is reasonably good. If a non-SM $W\gamma$ signal, as allowed by our experimental 95% CL limits on $WW\gamma$ anomalous couplings and within the E_T range $5 < E_T < 15$ GeV is subtracted instead of the SM signal, the fractional change in the combined $e + \mu$ QCD jet misidentification probability distribution over this E_T range is $\sim \pm 25\%$, well within statistical uncertainties. (See Section 7, especially Table 19 and Fig. 17.)

We have also carried out this same comparison, but relaxing the photon selection criteria to simply require isolated EM clusters in the Jet-20 and combined $e + \mu$ data samples, using only the calorimeter isolation and tracking isolation cuts, $ET4 < 2$ GeV and $\Sigma PT4 < 2$ GeV. In the Jet-20 (combined $e + \mu$) data sample, 64 (30) isolated "loose" EM clusters are found, respectively. We expect a combined $e+\mu$ SM signal passing these cuts of 8.8 ± 0.8 events. Thus, any inaccuracy in the signal subtraction is diluted by approximately a factor of $\sim 3\times$, relative to the previous comparison with the full photon cuts applied. The results of the comparison using relaxed photon selection cuts are shown in Table 41. Again, the agreement between the two probability distributions is reasonably good.

Table 40: QCD Jet Misidentification Probability – All Photon Cuts. The statistical uncertainty associated with each quantity is given. See text for further details.

E_T Range (GeV)	$\mathcal{P}^{J20}_{Jet\rightarrow\text{"}\gamma\text{"}}$	$\mathcal{P}^{W_{e+\mu}}_{Jet\rightarrow\text{"}\gamma\text{"}}$
5 – 6	$0.49 \pm 0.15\%$	$0.41 \pm 0.29\%$
6 – 8	$0.17 \pm 0.07\%$	$0.15 \pm 0.21\%$
8 – 11	$0.07 \pm 0.05\%$	$-0.10 \pm 0.16\%$
11 – 15	$0.06 \pm 0.06\%$	$0.58 \pm 0.53\%$
> 15	$0.00 \,^{+\,0.08}_{-\,0.00}\,\%$	$0.09 \pm 0.21\%$
> 5	$0.17 \pm 0.04\%$	$0.19 \pm 0.11\%$

Table 41: QCD Jet Misidentification Probability – "Loose" Photon Cuts. The statistical uncertainty associated with each quantity is given. See text for further details.

E_T Range (GeV)	$\mathcal{P}^{J20}_{Jet\rightarrow\text{"}\gamma\text{"}}$	$\mathcal{P}^{W_{e+\mu}}_{Jet\rightarrow\text{"}\gamma\text{"}}$
5 – 6	$1.35 \pm 0.27\%$	$0.97 \pm 0.53\%$
6 – 8	$0.76 \pm 0.16\%$	$0.97 \pm 0.48\%$
8 – 11	$0.18 \pm 0.10\%$	$0.19 \pm 0.40\%$
11 – 15	$0.17 \pm 0.13\%$	$1.04 \pm 0.87\%$
> 15	$0.00 \,^{+\,0.08}_{-\,0.00}\,\%$	$0.07 \pm 0.21\%$
> 5	$0.55 \pm 0.07\%$	$0.67 \pm 0.13\%$

E DETERMINATION OF ADDITIONAL BACKGROUNDS IN THE $W + \gamma$ AND $Z + \gamma$ DATA SAMPLES

E.1 $Z + \gamma$ and Z+Jet Backgrounds in the $W + \gamma$ Data Samples

The misidentified $Z + \gamma$ background in the $W + \gamma$ data sample is given by:

$$\mathcal{N}_{ZW\gamma} = \sigma \cdot B(ZW + \gamma)_{cuts} \cdot \int \mathcal{L}_\ell dt \cdot \left(A^\ell_{ZW\gamma} \cdot \epsilon^\ell_{ZW\gamma}\right) \tag{95}$$

where $\sigma \cdot B(ZW + \gamma)_{cuts}$ is the Baur $Z\gamma$ Monte Carlo predicted cross section, obtained from $\sigma \cdot B(Z + \gamma)_{gen}$ for $Z\gamma$ MC events passing the $W\gamma$ event selection cuts, for the $\ell = e$ or μ channels. For the $Z\gamma$ background in the electron $W\gamma$ data sample:

$$A^e_{ZW\gamma} \cdot \epsilon^e_{ZW\gamma} = \epsilon_{zvx} \cdot A^e_{M^T_W} \cdot \left(A^e_{ZW} \cdot T^e \cdot \epsilon^e_{cent_T}\right) \cdot (f^{\gamma_e}_{ZWcem} \cdot A^{\gamma_e}_{ZWcem} \cdot \epsilon^\gamma_{cem}) \tag{96}$$

For the $Z\gamma$ background in the muon $W\gamma$ data sample:

$$A^\mu_{ZW\gamma} \cdot \epsilon^\mu_{ZW\gamma} = \epsilon_{zvx} \cdot A^\mu_{M^T_W} \cdot \left(A^\mu_{ZW} \cdot T^\mu \cdot \epsilon^\mu_{cent_T} \cdot \epsilon^\mu_{cos}\right) \cdot (f^{\gamma_\mu}_{ZWcem} \cdot A^{\gamma_\mu}_{ZWcem} \cdot \epsilon^\gamma_{cem}) \tag{97}$$

where $A^\ell_{ZW} = A^\ell_{ZW\ P_T} \cdot A^\ell_{ZWfid} \cdot A^{\bar{\nu}_\ell}_{ZW\ \not\!\!E_T}$ is the overall kinematic $\times$ geometrical acceptance for single central fiducial leptons associated with $Z\gamma$ events misidentified as $W\gamma$ events for the $\ell = e,\ \mu$ $W\gamma$ data samples. The factor $A^\ell_{ZW\ P_T}$ is the kinematical acceptance for either of the Z decay leptons to pass the common-selection "tight" central fiducial lepton E_T (P_T) > 20 GeV cut. The factor A^ℓ_{ZWfid} is the geometrical acceptance for one of the Z decay leptons associated with $Z\gamma$ events misidentified as $W\gamma$ events to be within the fiducial acceptance of the central EM calorimeter, for electrons, or the fiducial acceptance of the central muon system, for muons. The factor $A^{\bar{\nu}_\ell}_{ZW\ \not\!\!E_T}$ is the kinematic acceptance for the unobserved lepton from Z decay satisfying the $\not\!\!E_T > 20$ GeV cut.

For central photons in misidentified $\ell = e$ or μ $Z\gamma$ events, the factor $f^{\gamma_\ell}_{ZWcem}$ is defined as the fraction of all photons that are central ($|\eta_\gamma| < 1.1$), which are produced in $Z\gamma$ events where the misidentified Z decay leptons pass the W selection requirements and the photon has already satisfied the $E^\gamma_T > 5.0$ GeV and $\Delta R_{\ell\gamma} > 0.7$ requirements. The factor $A^{\gamma_\ell}_{ZWcem} = A^{\gamma_\ell}_{ZWfid\ cem}$ is the overall kinematic $\times$ geometrical acceptance for central fiducial photons associated with $Z\gamma$ events misidentified as $W\gamma$ events for the $\ell = e,\ \mu$ $W\gamma$ data samples, since by our definition of the $\sigma \cdot B(W + \gamma)$ and $\sigma \cdot B(Z + \gamma)$ cross sections, all central photons with Z bosons must intrinsically pass the $E^\gamma_T > 5.0$ GeV and $\Delta R_{\ell\gamma} > 0.7$ angular separation requirements.

The QCD jet background in the electron and muon $Z\gamma$ data samples is given by:

$$\mathcal{N}^{Z_{QCD}}_{bkg} = \sigma \cdot B(Z_\ell) \cdot \int \mathcal{L}_\ell dt \cdot \left(A^\ell_{Z\text{"}\gamma\text{"}} \cdot \epsilon^\ell_{ZW\text{"}\gamma\text{"}}\right) \tag{98}$$

The contribution from inclusive Z+Jet background in the electron and muon $W\gamma$ data samples, where the Z is misidentified as a W boson and a central jet is misidentified as a photon is given by:

$$\mathcal{N}^{ZW_{QCD}}_{bkg} = \sigma \cdot B(Z_\ell) \cdot \int \mathcal{L}_\ell dt \cdot \left(A^\ell_{ZW\text{"}\gamma\text{"}} \cdot \epsilon^\ell_{ZW\text{"}\gamma\text{"}}\right) \tag{99}$$

where $\sigma \cdot B(Z_\ell)$ is the inclusive Z production cross section $\times$ decay branching ratio for the $\ell = e$ or μ channel.

The inclusive Z+Jet background in the electron and muon $W\gamma$ data samples is obtained from:

$$\mathcal{N}_{bkg}^{ZW_{QCD}} = \mathcal{N}_{bkg}^{Z_{QCD}} \cdot \left[\frac{A^{\ell}_{ZW"\gamma"} \cdot \epsilon^{\ell}_{ZW"\gamma"}}{A^{\ell}_{Z"\gamma"} \cdot \epsilon^{\ell}_{Z"\gamma"}} \right] \tag{100}$$

E.2 Tau Lepton QCD Jet Backgrounds in the $W+\gamma$ and $Z+\gamma$ Data Samples

The tau decay contribution to the inclusive W+Jet background in the electron and muon $W+\gamma$ data samples is given by:

$$\mathcal{N}_{bkg}^{W_{QCD}^{\tau}} = \sigma \cdot B(W_{\ell}^{\tau}) \cdot B(\tau \rightarrow \ell\ \bar{\nu}_{\ell}\ \nu_{\tau}) \cdot \int \mathcal{L}_{\ell} dt \cdot \left(A^{\ell}_{W^{\tau}"\gamma"} \cdot \epsilon^{\ell}_{W^{\tau}"\gamma"} \right) \tag{101}$$

The direct $\ell = e$ or μ contributions to the inclusive W+Jet background in the electron/muon $W\gamma$ data samples are given by:

$$\mathcal{N}_{bkg}^{W_{QCD}^{\ell}} = \sigma \cdot B(W_{\ell}) \cdot \int \mathcal{L}_{\ell} dt \cdot \left(A^{\ell}_{W"\gamma"} \cdot \epsilon^{\ell}_{W"\gamma"} \right) \tag{102}$$

where $\sigma \cdot B(W_{\ell})$ is the inclusive W production cross section $\times$ decay branching ratio for $\ell = e$ or μ.

The tau W+Jet background in the electron and muon $W\gamma$ data samples can therefore be obtained from:

$$\mathcal{N}_{bkg}^{W_{QCD}^{\tau}} = \mathcal{N}_{bkg}^{W_{QCD}^{\ell}} \cdot B(\tau \rightarrow \ell\ \bar{\nu}_{\ell}\ \nu_{\tau}) \cdot \left[\frac{A^{\tau}_{W"\gamma"} \cdot \epsilon^{\ell}_{W^{\tau}"\gamma"}}{A^{\ell}_{W"\gamma"} \cdot \epsilon^{\ell}_{W"\gamma"}} \right] \tag{103}$$

References

[1] S.L. Glashow, Nucl. Phys. **22**, 579 (1961); S. Weinberg, Phys. Rev. Lett. **19**, 1264 (1967); A. Salam, in *Elementary Particle Theory: Relativistic Groups and Analyticity (Nobel Symposium No. 8)*, edited by N. Svartholm (Almqvist and Wiksell, Sweden, 1968), p. 367; see also S.L. Glashow, J. Illiopoulous and L. Maiani, Phys. Rev. D**2**, 1285 (1970).

[2] E. Fermi, Z. Phys. **88**, 161 (1934); H. Yukawa, Proc. Phys.-Math. Soc. Jap. **17**, 48 (1935); T.D. Lee and C.N. Yang, Phys. Rev. **119**, 1410 (1960).

[3] R.W. Robinett, Phys. Rev. D**28**, 1185 (1983); G.N. Valenzuela and J. Smith, Phys. Rev. D**31**, 2787 (1985); J. Cortés, K. Hagiwara and F. Herzog, Nucl. Phys. B**278**, 26 (1986).

[4] F.M. Renard, Nucl. Phys. B**196**, 93 (1982).

[5] R. Barbieri, H. Harari and M. Leurer, Phys. Lett. B**141**, 455 (1985); J.P. Eboli, A.V. Olinto, Phys. Rev. D**38**, 3461 (1988).

[6] F. Abe *et al.*, Phys. Rev. Lett. **64**, 152 (1990); F. Abe *et al.*, Phys. Rev. Lett. **68**, 3398 (1992); A. Roodman, Ph.D. thesis, University of Chicago (1991).

[7] F. Abe *et al.*, Phys. Rev. Lett. **62**, 1005 (1989); F. Abe *et al.*, Phys. Rev. D**44**, 29 (1991); F. Abe *et al.*, Phys. Rev. Lett. **69**, 28 (1992); P. Derwent, Ph.D. thesis, University of Chicago (1990); R.L Swartz, Jr., Ph.D. thesis, University of Illinois at Urbana-Champaign (1993).

[8] D. Benjamin, Ph.D. thesis, Tufts University (1993); C. Luchini, Ph.D. thesis, University of Illinois at Urbana-Champaign (1993); M. Roach-Bellino, Ph.D. thesis, Tufts University (1994).

[9] Review of Particle Properties, Phys. Rev. D**45**, V.2, V.3 (1992).

[10] U. Baur and D. Zeppenfeld, Nucl. Phys. B**308**, 127 (1988).

[11] U. Baur and E.L. Berger, Phys. Rev. D**41**, 1476 (1990).

[12] U. Baur and D. Zeppenfeld, Phys. Lett. B**201**, 383 (1988).

[13] T.D. Lee and C.N. Yang, Phys. Rev. **128**, 885 (1962); L.D. Landau and E.M. Lifshitz, *Quantum Mechanics* (Addison-Wesley Publishing Co, Inc., Reading, MA, 1965), p. 262; H. Aronson, Phys. Rev. **186**, 1434 (1969); K.J. Kim and Y.-S. Tsai, Phys. Rev. D**7**, 3710 (1973).

[14] D.R. Yennie, M.M. Lévy and D.G. Ravenhall, Rev. Mod. Phys. **29**, 144 (1957); L. Durand III, P.C. DeCelles and R.B. Marr, Phys. Rev. **126**, 1882 (1962).

[15] K. Hagiwara *et al.*, Nucl. Phys. B**282**, 253 (1987).

[16] C.N. Yang, Phys. Rev. **77**, 242 (1950).

[17] U. Baur and E.L. Berger, Phys. Rev. D**47**, 4889 (1993).

[18] A. Barroso, F. Boudjema, J. Cole and N. Dombey, Z. Phys. C**28**, 149 (1985).

[19] F. Boudjema, private communication.

[20] Our convention for defining the $ZZ\gamma$ transition *moments* from the $ZZ\gamma$ *transitions* is similar to that of ref. [4], except that we keep the factor of electric charge e explicitly in the definition of the transition moments in order to maintain a consistent *overall* definition of the $WW\gamma$ higher-order EM static moments *and* the $ZZ\gamma$ transition moments.

[21] J. M. Cornwall, D. N. Levin and G. Tiktopoulos, Phys. Rev. Lett. **30**, 1268 (1973); Phys. Rev. D**10**, 1145 (1974); C. H. Llewellyn Smith, Phys. Lett. B**46**, 233 (1973); S. D. Joglekar, Ann. of Phys. **83**, 427 (1974).

[22] F. Abe *et al.*, Nucl. Instrum. Methods A**271**, 387 (1988).

[23] F. Snider *et al.*, Nucl. Instrum. Methods A**268**, 75 (1988).

[24] F. Bedeschi *et al.*, Nucl. Instrum. Methods A**268**, 50 (1988).

[25] L. Balka *et al.*, Nucl. Instrum. Methods A**267**, 272 (1988).

[26] S. Bertolucci *et al.*, Nucl. Instrum. Methods A**267**, 301 (1988).

[27] Y. Fukui *et al.*, Nucl. Instrum. Methods A**267**, 280 (1988).

[28] G. Brandenberg *et al.*, Nucl. Instrum. Methods A**267**, 257 (1988).

[29] M.E.B. Franklin, *et al.*, in the proceedings of the 7^{th} *Topical Workshop on Proton-Antiproton Collider Physics*, p. 420, edited by R. Raja, A. Tollestrup and J. Yoh, World Scientific, Singapore (1988).

[30] S. Cihangir *et al.*, Nucl. Instrum. Methods A**267**, 249 (1988).

[31] G. Ascoli *et al.*, Nucl. Instrum. Methods A**267**, 218 (1988).

[32] D. Amidei *et al.*, Nucl. Instrum. Methods A**267**, 51 (1988).

[33] G. Ascoli *et al.*, Nucl. Instrum. Methods A**267**, 272 (1988).

[34] G.W. Foster *et al.*, Nucl. Instr. Methods A**269**, 93 (1988).

[35] D.A. Smith, Ph.D. thesis, the University of Illinois at Urbana-Champaign (1989).

[36] T. Carroll *et al.*, Nucl. Instrum. Methods A**263**, 199 (1988); T. Carroll *et al.*, Nucl. Instrum. Methods A**300**, 552 (1991).

[37] K. Yasuoka *et al.*, Nucl. Instrum. Methods A**267**, 315 (1988).

[38] VEGAS, G. Peter Lepage, J. Comp. Phys. **27**, 192-202, Academic Press (1978); G. Peter Lepage, CLNS-80/447 (1980).

[39] PDFLIB version 4.15, H. Plothow-Besch, Computer Phys. Commun. **75**, 396 (1993); H. Plothow-Besch, CERN Report W5051, (1992).

[40] M. Kobayashi and M. Maskawa, Prog. Theor. Phys. **49**, 652 (1973).

[41] P.N. Harriman, A.D. Martin, R.G. Roberts and W.J. Stirling, Phys. Rev. D**42**, 798 (1990).

[42] The VVJET Monte Carlo, U. Baur, E.W.N. Glover and J.J. van der Bij, Nucl. Phys. **B318**, 106 (1989).

[43] ISAJET Monte Carlo version 6.24, F.E. Paige and S.D. Protopopescu, BNL Technical Report No. 38034, 1986 (unpublished).

[44] PAPAGENO Monte Carlo version 3.12, I. Hinchliffe, (to be published).

[45] PYTHIA version 5.4, T. Sjöstrand, Computer Phys. Commun. **39**, 347 (1986); T. Sjöstrand and M. Bengtsson, Computer Phys. Commun. **43**, 367 (1987); H.-U. Bengtsson and T. Sjöstrand, Computer Phys. Commun. **46**, 43 (1987).

[46] R.G. Wagner, Comp. Phys. Commun. **70**, 15 (1992); see also F.A. Berends, J.P. Revol and R. Kleiss, Z. Phys. C**27**, 155 (1985); F.A. Berends and R. Kleiss, *ibid.* C**27**, 365 (1985).

[47] F. Abe *et al.*, Phys. Rev. D**43**, 2070 (1991); F. Abe *et al.*, Phys. Rev. Lett. **65**, 2243 (1990); W. Trischuk, Ph.D. thesis, Harvard University (1990); P. Schlabach, Ph.D. thesis, University of Illinois at Urbana-Champaign (1990).

[48] F. Abe *et al.*, Phys. Rev. Lett. **63**, 720 (1989); H. Keutelian, Ph.D. thesis, University of Illinois at Urbana-Champaign (1990).

[49] F. Abe *et al.*, Phys. Rev. Lett. **68**, 1104 (1992).

[50] VECBOS Monte Carlo, F.A. Berends, W.T. Giele, H. Kuijf and B. Tausk, Nucl. Phys. B**357**, 32 (1991).

[51] HERWIG Monte Carlo version 5.6, G. Marchesini and B.R. Webber, Nucl. Phys. B**310**, 461 (1988).

[52] Review of Particle Properties, Phys. Rev. D**45**, VI.21, (1992).

[53] U. Baur, S. Errede and J. Ohnemus, Phys. Rev. D**48**, 4103 (1993).

[54] Review of Particle Properties, Phys. Rev. D**45**, III.39, (1992). Note that for the purposes of extracting limits on anomalous couplings, the use of the bounded physical region for $\mathcal{N}_{sig}(V_\ell + \gamma)_{expt}$ and comparing to $\mathcal{N}_{sig}(V_\ell + \gamma)_{pred}$ results in more conservative limits on such couplings than the same method applied to the comparison of $\mathcal{N}_{obs}(V_\ell + \gamma)_{expt}$ *vs.* $\mathcal{N}_{sig}(V_\ell + \gamma)_{pred} + \mathcal{N}_{bkg}(V_\ell + \gamma)_{pred}$.

[55] F. Abe *et al.*, Phys. Rev. Lett. **66**, 2951 (1991); F. Abe *et al.*, Phys. Rev. Lett. **67**, 2937 (1991); B. Winer, Ph.D. thesis, University of California at Berkeley (1991); J. Ng, Ph.D. thesis, Harvard University (1991).

[56] P.B. Arnold and M.H. Reno, Nucl. Phys. B**319**, 37 (1989); P.B. Arnold and R.P. Kauffman, Nucl. Phys. B**349**, 381 (1991).

[57] M. Diemoz, F. Ferroni, E. Longo, and G. Martinelli, Z. Phys. C**39**, 21 (1988).

[58] A.D. Martin, R.G. Roberts and W.J. Stirling, Phys. Lett. B**206**, 327 (1989).

[59] A.D. Martin, R.G. Roberts and W.J. Stirling, Phys. Rev. D**47**, 867 (1993).

[60] J.G. Morfin and Wu-Ki Tung, Z. Phys. C**52**, 13 (1991).

[61] F. Halzen, and K. Mursula, Phys. Rev. Lett. **51**, 857 (1983); K. Hikasa, Phys. Rev. D**29**, 1939 (1984); N.G. Deshpande, *et al.*, Phys. Rev. Lett. **54**, 1757 (1985); A.D. Martin, R.G. Roberts and W.J. Stirling, Phys. Lett. B**189**, 220 (1987); E.L. Berger, F. Halzen, C.S. Kim and S. Willenbrock, Phys. Rev. D**40**, 83 (1989).

[62] The convention we adopted for distinquishing radiative $W \to \ell\nu\gamma$ decay from $W+\gamma$ production is the same as that of Berends and Kleiss, see eqn. 2.13 and accompanying discussion in F.A. Berends and R. Kleiss, Z. Phys. C**27**, 365 (1985). The WZRAD Monte Carlo event generator [46] incorporates the Berends and Kleiss formalism for radiative W/Z decay.

[63] MINUIT, F. James and M. Roos, CERN Report D506, 1988.

[64] The Standard Model process $\bar{p}\,p \to \gamma^*, Z^* \to W^+W^-$ is mediated both by the photon and the Z. In general, for the situation in which *anomalous* W^+W^- pair production is considered, both $WW\gamma$ *and* WWZ anomalous couplings, $\Delta\kappa_\gamma$, λ_γ, $\tilde{\kappa}_\gamma$, $\tilde{\lambda}_\gamma$ and $\Delta\kappa_Z$, λ_Z, $\tilde{\kappa}_Z$, $\tilde{\lambda}_Z$, respectively, must be considered. However, for the $W+\gamma$ process only $WW\gamma$ anomalous couplings are relevant. In our notation of $WW\gamma$ anomalous couplings, we have dropped all reference to the subscript γ throughout this paper.

[65] J. Alitti *et al.*, Phys. Lett. B**241**, 150 (1990).

[66] F. Herzog, Phys. Lett. B**148**, 355 (1984); F. Herzog, *erratum, ibid.* B**155**, 468 (1984); J.C. Wallet, Phys. Rev. D**32**, 813 (1985).

[67] M. Suzuki, Phys. Lett. B**153**, 289 (1985).

[68] P. Méry, S.E. Moubarik, M. Perottet and F.M. Renard, Z. Phys. C**46**, 229 (1990).

[69] G.L. Kane, J. Vidal and C.P. Yuan, Phys. Rev. D**39**, 2617 (1989).

[70] F. Boudjema, K. Hagiwara, C. Hamazaoui and K. Numata, Phys. Rev. D**43**, 2223 (1991).

[71] W.J. Marciano and A. Queijeiro, Phys. Rev. D**33**, 3449 (1986).

[72] J.J. van der Bij, Phys. Rev. D**35**, 1088 (1987).

[73] J.A. Grifols, S. Peris and J. Sola, Intern. J. Mod. Phys. A**3**, 225 (1988).

[74] A. De Rujula *et al.*, Nucl. Phys. B**384**, 31 (1992); P. Hernández and F.J. Vegas, Phys. Lett. B**307**, 116 (1993).

[75] C. Burgess and D. London, Phys. Rev. Lett. **69**, 3428 (1992); C. Burgess and D. London, Phys. Rev. D**48**, 4337 (1993).

[76] K. Hagiwara, S. Ishihara, R. Szalapski, and D. Zeppenfeld, Phys. Lett. B**283**, 353 (1992); K. Hagiwara, S. Ishihara, R. Szalapski, and D. Zeppenfeld, Phys. Rev. D**48**, 2182 (1993).

[77] M.E. Peskin and T. Takeuchi, Phys. Rev. Lett. **65**, 964 (1990); M.E. Peskin and T. Takeuchi, Phys. Rev. D**46**, 381 (1992).

[78] G. Altarelli and R. Barbieri, Phys. Lett. B**253**, 161 (1991); G. Altarelli, R. Barbieri, and S. Jadach, Nucl. Phys. B**369**, 3 (1992).

[79] D. Choudhury, P. Roy, and R. Sinha, TIFR-TH/93-08 preprint (May 1993); C.P. Burgess *et al.*, Mc-Gill-93/14 preprint (June 1993).

[80] J. Alitti, *et al.*, Phys. Lett. B**277**, 194 (1992).

[81] Review of Particle Properties, Phys. Rev. D**45**, VIII.8, (1992).

[82] U. Baur, private communication.

[83] O. Adriani, *et al.*, Phys. Lett. B**297**, 469 (1992). The limit given in this paper is multiplied by 2 here to correct for an error, recently discovered by the authors of Phys. Lett. B**196**, 547 (1987) (A. Barroso, P. Nogueira, and J.C. Romao). The error occurred in the program they wrote to carry out the numerical calculations for their paper which was subsequently used by L3 in its analysis. J.C. Romao, private communication to J. Busenitz.

[84] K.O. Mikaelian, Phys. Rev. D**17**, 750 (1978); K.O. Mikaelian, M.A. Samuel and D. Sahdev, Phys. Rev. Lett. **43**, 746 (1979); R.W. Brown, K.O. Mikaelian and D. Sahdev, Phys. Rev. D**20**, 1164 (1979); T.R. Grose and K.O. Mikaelian, Phys. Rev. D**23**, 123 (1981); C.J. Goebel, F. Halzen and J.P. Leveille, Phys. Rev. D**23**, 2682 (1981); S.J. Brodsky and R.W. Brown, Phys. Rev. Lett. **49**, 966 (1982); M.A. Samuel, Phys. Rev. D**27**, 2724 (1983); R.W. Brown, K.L. Kowalski and S.J. Brodsky, Phys. Rev. D**28**, 624 (1983); R.W. Brown and K.L. Kowalski, Phys. Rev. D**29**, 2100 (1984).

[85] J. Smith, D. Thomas and W.L. van Neerven, Z. Phys. C44, 267 (1989); S. Mendoza, J. Smith and W.L. van Neerven, Phys. Rev. D**47**, 3913 (1993); J. Ohnemus, Phys. Rev. D**47**, 940 (1993); U. Baur, T. Han and J. Ohnemus, Phys. Rev. D**48**, 5140 (1993).

[86] U. Baur, S. Errede and G. Landsberg, to appear in Phys. Rev. D; U. Baur, S. Errede and G. Landsberg, in *The Proceedings of the Workshop on Physics at Current Accelerators and Supercolliders*, p. 211-217, edited by J. Hewett, A. White and D. Zeppenfeld (Argonne, June 2-5, 1993).